Investigating the role of very long chain sphingolipids in pancreatic beta cell demise

Inaugural-Dissertation

zur Erlangung des Doktorgrades
der Mathematisch-Naturwissenschaftlichen Fakultät
der Heinrich-Heine-Universität Düsseldorf

vorgelegt von

Kerstin Grieß
aus Duisburg

Düsseldorf, September 2020

aus dem Institut für Vaskular- und Inselzellbiologie
des Deutschen Diabetes-Zentrums (DDZ)

Gedruckt mit der Genehmigung der
Mathematisch-Naturwissenschaftlichen Fakultät der
Heinrich-Heine-Universität Düsseldorf

Berichterstatter:

1. Prof. Dr. Eckhard Lammert

2. PD Dr. Volker Burkart

Tag der mündlichen Prüfung: 27.11.2020

The main purpose of science is simplicity and as we understand more things, everything is becoming simpler.   Edward Teller

Table of contents

1.   Abstract

Type 2 diabetes (T2D) is characterized by dysfunctional insulin secretion from pancreatic beta cells. Ceramides are suggested to be involved in the development of T2D and might be implicated in beta cell failure. Six individual ceramide synthases (CERS1-6) exist, which attach fatty acids with a specific chain length to a sphingoid base backbone and thus generate distinct ceramide species possessing different biophysical and biochemical properties. Previous studies demonstrated that pharmacological inhibition of ceramide *de novo* synthesis might be a potential therapy to treat metabolic diseases, such as obesity and T2D. However, the role of distinct ceramide species in pancreatic beta cells has not been investigated.

In this thesis, alterations in the sphingolipidome of diabetic pancreatic islets of db/db mice were analyzed using untargeted lipidomics. While long and very long chain ceramide species were elevated in islets from db/db mice, more complex sphingolipids, such as sphingomyelins and hexosylceramides showed an increase in C16:0 species, but a reduction in C24:1 species. This demonstrates that sphingolipid species with distinct acyl chain length are differentially regulated during the development of T2D in islets. Furthermore, the role of very long chain C22-C24 ceramides and sphingolipids were analyzed in pancreatic beta cells *in vivo* and *in vitro* by ablation of *CerS2*. Beta cell specific deletion of *CerS2* and the concomitant reduction in very long chain sphingolipids impaired glucose tolerance and insulin secretion in mice on normal and high fat diet. Consistently, pancreatic beta cells of *CerS2* knockout mice contained less mature insulin due to impaired processing of proinsulin into insulin. Mechanistically, ablation of *CerS2* specifically reduced the number of mature insulin granules and decreased prohormone convertase 1 (PC1, encoded by *Pcsk1*), the rate limiting enzyme for proinsulin processing, while PC2 expression was unaffected. Furthermore, CERS2 deficiency did not alter *Pcsk1* mRNA expression and PC1 degradation, indicating that CERS2 is required for efficient PC1 protein biosynthesis, maturation and/or trafficking along the secretory pathway.

This data demonstrate the importance of CERS2 and very long chain sphingolipids in prohormone processing of pancreatic beta cells and highlight potentially unwanted consequences of global ceramide and sphingolipid inhibition as diabetes treatment.

2.   Introduction

2.1.   The pancreas and pancreatic islets

The pancreas is a crucially important metabolic organ and is involved in energy homeostasis by secreting several digestive enzymes and hormones (Fig.1). It can be divided into three different compartments: the head, body and tail [1]. In fact, its dysfunction plays a role in the development of diabetes. The pancreas can be divided into an exocrine and an endocrine part, both accomplishing different functions. More than 90% of the pancreas consist of exocrine cells, which secrete digestive enzymes into the intestine. The endocrine cells make up only 1-2% of the pancreas and they are clustered in island-like structures, so called islets of Langerhans, which are scattered throughout the whole tissue [1,2]. In non-diabetic human pancreata, a total islet number between 1 and 14.8 million is estimated [2–6]. Human pancreatic islets have a size of 50-500 μm, are composed of 50-3,000 cells and consist of at least five different cell types that secrete specific hormones into the bloodstream that regulate energy homeostasis [1,7]. Glucagon is secreted by alpha cells, insulin is secreted by beta cells, somatostatin is secreted by delta cells, ghrelin is secreted by epsilon cells and pancreatic polypeptide is secreted by PP cells [1,6].
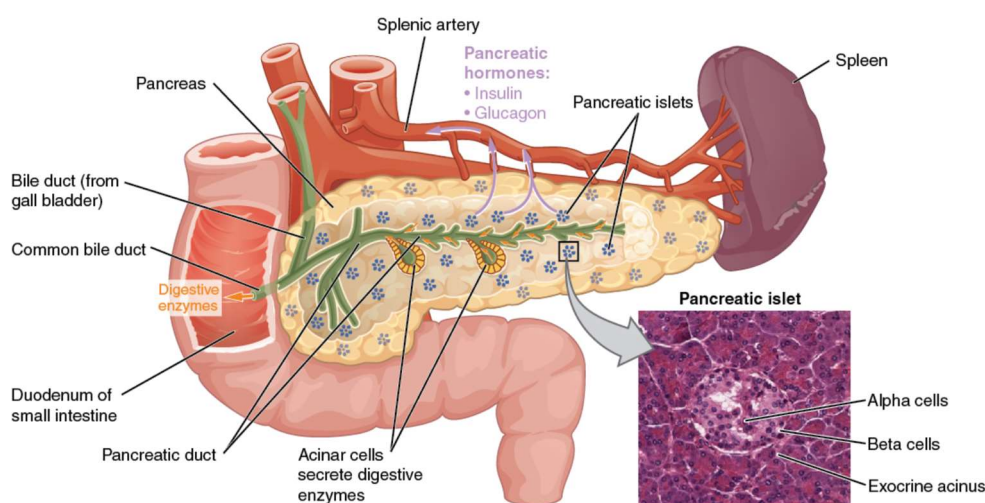
Figure 1: Anatomical structure of the pancreas. The pancreas is located in the upper left abdominal cavity and is divided into an exocrine and endocrine part. Acinar cells, which are part of the exocrine system, secrete digestive enzymes into the duodenum. The islets of Langerans are scattered throughout the whole pancreas and fulfill the endocrine function. Pancreatic islets consist of glucagon secreting alpha cells, insulin secreting beta cells, somatostatin secreting delta cells, ghrelin secreting epsilon cells and pancreatic polypeptide secreting PP cells. Hormones are released into the vascular system and regulate blood glucose homeostasis. The micrograph shows a pancreatic islet, which is embedded in the exocrine tissue. The image is adapted from Human Anatomy and Physiology, an OpenStax College ressource [8].

The most abundant cell type in pancreatic islets are beta cells with a proportion of 50-75% in humans and 60-80% in mice, followed by alpha cells with approximately 25-35% in humans and 15-20% in mice [1,9]. Thus, mice exhibit a higher proportion of beta cells and lower proportion

of alpha cells in pancreatic islets compared to humans [6]. Delta cells account for approximately 10% in human and 5% in mouse islets. The residual two cell types, epsilon and PP cells, compose only less than 1% of the islet [9]. Moreover, the architecture of mouse and human islets is different. In mouse islets, beta cells are localized in the center of the islet while the other cell types are located in the periphery. This organization is also seen in islets from young humans. However, in adult human islets the architecture differs and alpha, beta and delta cells are dispersed throughout the islet, which allows paracrine signaling between the different cell types [1,9–11].

Furthermore, pancreatic islets of mice and humans are both highly vascularized, which allows the cells to respond rapidly to an altered nutritional environment and to secrete hormones into the circulatory system that delivers hormones to the respective target tissues [9]. To regulate hormone secretion from pancreatic islets, mouse and human islets are innervated by autonomic neurons [6,12].

2.2. Diabetes mellitus

Diabetes mellitus is a chronic metabolic disorder, which is characterized by elevated blood glucose levels, called hyperglycemia, and results from insufficient or deficient secretion and/or action of insulin [13,14]. Worldwide, 463 million people have diabetes and the number of diabetic people dramatically increased during the last decades [14]. In 2030 the estimated number of people with diabetes will rise up to 578 million people and may further increase up to 700 million people in 2045 [14]. Therefore, diabetes has attained the status of a pandemic [15]. Chronic hyperglycemia is known to damage a large number of tissues and organs. Therefore, diabetes patients have a higher risk of developing several secondary complications, such as cardiovascular diseases, cancer, retinopathy, neuropathy and nephropathy [13,16–19]. Thus, diabetes is among the top 10 leading causes of death worldwide and 4.2 million people died due to diabetes in 2019 [14]. Besides the higher mortality rate, lower life expectancy and lower quality of life, diabetes also represents a high economic burden for society. Recently, Bommer and colleagues calculated the absolute global costs of diabetes for the year 2015 with an amount of USD 1.32 trillion. Furthermore, they predicted a dramatic increase in the costs of diabetes up to USD 2.12-2.48 trillion in the year 2030 [20].

There are two main types of diabetes mellitus. Type 1 diabetes mellitus (T1D) accounts for 5-10% of all diabetes cases, while the majority is represented with over 90% by type 2 diabetes mellitus (T2D) [13,21,22].

2.2.1. Type 1 diabetes mellitus

T1D is a polygenic disease that is caused by an autoimmune reaction leading to beta cell destruction in the pancreas. Therefore, little amounts or no insulin are secreted from the

pancreas, which results in hypoinsulinemia and consequently hyperglycemia [23]. Despite former designation of T1D as juvenile diabetes, T1D can be diagnosed at any age [14]. A recent study from Thomas and colleagues indicates that 42% of newly diagnosed T1D patients are older than 30 years of age [24]. T1D patients, who are older than 30 years of age, are more difficult to be diagnosed and might be misclassified as T2D patients [17,24,25]. Nevertheless, T1D is the major cause of diabetes in childhood [14]. The etiology of beta cell autoimmunity is still unclear, but most likely results from a complex interplay of genetic and environmental factors [17,21,26]. Genome wide association studies (GWAS) identified more than 60 loci that are associated with increased susceptibilty to T1D. Among those, many polymorphisms are located in the human leukocyte antigen (HLA) region on chromosome 6 and account for approximately 50% of the genetic predisposition [17,27]. In addition to the genetic component, several environmental factors like diet, vitamin D, the microbiome and potentially viruses are involved in the progression of T1D and may trigger islet specific autoimmunity [28,29]. Once autoimmunity is initiated, T1D progression is variable between patients and takes between months to decades [26,30]. At the beginning, T1D patients are asymptomatic with normoglycemia, but two or more autoantibodies against specific beta cell proteins are expressed and can be detected in the circulation. These include autoantibodies against insulin (INS), glutamic acid decarboxylase (GAD), insulinoma associated antigen-2 (IA-2), zinc transporter 8 (ZNT8) and tetraspanin-7 (TSPAN7) [17,26,31]. As the disease progresses, immune cells, such as CD8+ and CD4+ T-cells, CD68+ macrophages and CD20+ B-cells, infiltrate the pancreatic islets and induce beta cell destruction and insulin deficiency [26,32]. Beta cell mass declines over time, presumably non-linear in a relapsing-remitting fashion, and the ability to secrete insulin is eventually lost, leading to glucose intolerance and hyperglycemia [26,30,33]. After the loss of 60-90% of beta cell mass [34–40], insulin supply is insufficient and T1D can be clinically diagnosed by specific symptoms, such as persistant hyperglycemia, weight loss, polyuria, polydipsia and polyphagia [26,30].

2.2.2. Type 2 diabetes mellitus

T2D is a highly heterogenous polygenic disease and the most common form in over 90% of diabetes patients [41,42]. It is characterized by deficient insulin secretion from the pancreatic beta cells in combination with impaired insulin sensitivity, called insulin resistance, in several organs, such as the liver, skeletal muscle and adipose tissue [42,43]. The risk to develop T2D increases with age and is therefore commonly diagnosed in older adults. However, due to the rise in obesity, physical inactivity and unhealthy diets, which are the major environmental risk factors for the development and progression of T2D, it is diagnosed with increasing frequency in children, adolescents and young adults [14,44]. In addition, T2D has a genetic component. Over 400 gene variants were identified by GWAS that are involved in the development of T2D [45].

However, individual gene variants have only small effect sizes and cannot explain the overall risk of T2D [15,45,46].

Overnutrition, and as a consequence obesity, is one of the major risk factors of T2D and is associated with insulin resistance in the liver, skeletal muscle and adipose tissue [47]. Excess food intake results in increased triacylglycerol (TAG) storage in adipocytes, which leads to enlargement and hypertrophy of those cells. Enlarged adipocytes were shown to be less vascularized, resulting in hypoxia and subsequent apoptosis and cell death [45]. Adipocytes start to secrete larger amounts of monocyte chemoattractant protein 1 (MCP1), which promotes the recruitment of macrophages and immune cells to the adipocyte. Tumor necrosis factor α (TNFα), interleukin-1β (IL-1β) and interleukin-6 (IL-6) are released from adipocytes and macrophages and cause a local and systemic low-grade inflammation in obesity [48,49]. Furthermore, lipolysis is increased and TAG synthesis is decreased in dysfunctional adipocytes, which results in the release of glycerol and free fatty acids (FFA, also called non-esterified fatty acids, NEFA) into the circulatory system [45,48]. Elevated levels of lipids in the circulatory system, designated as hyperlipidemia, leads to the accumulation of lipids in peripheral organs, such as the liver, pancreas, skeletal muscle and heart, which can result in organelle dysfunction and insulin resistance in a process called lipotoxicity [47,50,51].

Nevertheless, many obese people that are insulin resistant do not develop T2D. In obese mice and humans, it was shown that in this prediabetic state, pancreatic beta cells can compensate for the higher demand of insulin [43,52,53]. Immunohistological analyses of human pancreata showed that the pancreatic beta cell volume of obese non-diabetic subjects is increased compared to lean subjects [54–56]. Beta cell expansion was also observed in rodents, fed with a high fat diet or in genetic animal models that develop insulin resistance [57–59]. Furthermore, pancreatic beta cells can adapt to such a prediabetic state by increasing insulin biosynthesis and secretion [43,52]. In rodent studies it was demonstrated that even after a short time period of high fed diet feeding, as well as after glucose- or lipidinfusion, beta cell proliferation is induced, which leads to an increase in beta cell mass and hyperinsulinema [59–62]. However, when beta cells cannot sufficiently compensate for the insulin resistance and are dysfunctional, relative hypoinsulinemia leads to reduced systemic glucose uptake from the blood and hyperglycemia occurs. Ongoing hyperglycemia and hyperlipidemia can lead to beta cell toxicity and failure, which subsequently reduce functional beta cell mass [43]. In T2D patients, the beta cell mass is decreased by approximately 30-60% compared to non-diabetic subjects [54,63–65]. However, high variations are observed and some studies detect no differences in beta cell mass of T2D patients [34,66,67]. Furthermore, beta cell loss progressively increases over time after diagnosis [63]. Currently, the underlying mechanisms of beta cell failure are not completely understood and several models have been proposed and debated that do not mutually exclude each other [68].

First, the reduction in beta cell mass can originate from a reduced beta cell number, which results from an imbalance of beta cell proliferation and cell death. It was shown that even between healthy individuals, the pancreatic beta cell mass and presumably beta cell growth is highly variable [63,69]. Thus individuals, who have a lower initial beta cell mass, a lower potential for beta cell regeneration or a compromised capacity for compensation due to genetic and environmental factors, could be more susceptible to T2D [68]. Furthermore, a study from Butler et al. showed that in human pancreata from T2D donors, apoptosis is 3-10 fold increased [54].

Second, it was suggested that beta cells can lose their molecular identity. A study from Talchai and coworkers pointed out by lineage tracing experiments in mice that beta cell loss arises from dedifferentiation of beta cells into more progenitor-like cells and alpha cells, not from beta cell death [70]. Dedifferentiation into progenitor-like cells, alpha cells and delta-like cells was confirmed in *ex vivo* islet studies from human non-diabetic and diabetic donor islets [71]. However, the group of Butler observed only a slight increase in non-hormone expressing endocrine cells in autopsies from T2D human pancreata. Furthermore, this increase is comparitively low in contrast to the loss in beta cell mass. Therefore, they conclude that dedifferentiation and degranulation play only a minor role in humans, and endocrine cells with altered cell identity may partially reflect attempted beta cell regeneration [72].

Third, several factors are thought to contribute to beta cell dysfunction, such as ER stress, oxidative stress, DNA damage, inflammation and glucolipotoxicity [68]. Chronically elevated FFA levels in combination with increased glucose levels affect beta cell function and survival in a process that is designated as glucolipotoxicity [73,74]. Increased insulin biosynthesis is thought to exceed the ER folding capacity, leading to the accumulation of unfolded and misfolded proteins in the ER, which activates the unfolded protein response (UPR) [75]. The UPR is a protective process that attempts to reduce ER stress and restore ER homeostasis by the downregulation of protein synthesis, upregulation of protein degradation and refolding processes that remove misfolded proteins. However, when those mechanisms fail and ER stress remains, apoptosis is induced [76,77]. In T2D patients, ER stress was shown to be present in pancreatic islets by increased expression of ER stress markers on mRNA and protein level [78,79]. Existing ER stress in pancreatic beta cells of T2D patients is associated with an expanded ER [78]. Moreover, insulin biosynthesis and glucose stimulated insulin secretion are impaired in the presence of ER stress [75,78,80,81]. In addition, overnutrition promotes the generation of reactive oxygen species (ROS) including radical superoxide ($O_2^{\bullet-}$), hydrogen peroxide (H_2O_2) and hydroxyl radical ($OH^{\bullet}$) in the electron transport chain of mitochondria [82,83]. Furthermore, cytokines trigger the synthesis of nitric oxide (NO) by inducing the expression of inducible nitric oxide synthase (iNOS) [83]. Pancreatic beta cells have a low antioxidative capacity, which makes them more susceptible to oxidative stress [68,84]. Elevated levels of ROS

can damage nucleotides, proteins as well as lipids and mitochondria, leading to beta cell dysfunction [68,85].

Taken together, T2D is a very heterogeneous disease that is characterized by hyperglycemia due to insulin resistance and beta cell dysfunction presumably leading to a progressive loss of beta cell mass. However, the manifestation of diabetes in individual patients can have distinct reasons, such as insulin resistance, beta cell apoptosis, dysfunctional insulin secretion or impaired insulin biosynthesis.

2.2.3. Other forms

In addition to T1D and T2D other forms of diabetes mellitus exist, such as gestational diabetes mellitus (GDM) and maturity-onset diabetes of the young (MODY). GDM appears during pregnancy and can lead to short- and long-term health risks for the mother, the developing fetus and the offspring during later life [86,87]. MODY is a set of rare monogenetic forms of diabetes mellitus, and results from single mutations in genes that are often involved in beta cell function or development, such as the transcription factors hepatocyte nuclear factor-1-alpha (HNF1A), -4-alpha (HNF4A), -1-beta (HNF1B), glucokinase (GCK), insulin (INS) and pancreatic and duodenal homeobox 1 (PDX1) [13,88].

2.2.4. Diabetes medication

Until today, none of the available medication is able to cure diabetes or prevent, reverse or stop the progression of diabetes over a longer timeframe [14,23,89]. Although some T1D patients secrete low amounts of insulin, it is insufficient to maintain blood glucose levels [22,32]. Therefore, T1D patients require lifelong insulin injections [21]. Recent studies showed that in some cases T2D can be reversed by bariatric surgery, low calorie diets and carbohydrate restriction [90]. T2D can be prevented and improved by lifestyle modifications, such as exercise and diets [91,92]. However, when changes in lifestyle are not sufficient to maintain blood glucose homeostasis, additional drug therapy is necessary [86]. Several medications are on the market, which are divided into distinct groups, depending on their metabolic action. Insulin secretagogues, like sulfonylurea, incretin mimetics, glucagon-like peptide 1 (GLP-1) receptor agonists, dipeptidyl peptidase-4 (DPP-4) inhibitors and meglitinides can increase insulin secretion from the pancreatic beta cells [93,94]. Biguanides (e.g. metformin) and thiazolidinediones belong to the class of insulin sensitizers and increase insulin sensitivity in peripheral tissues [92,94]. Finally, glucourics, like sodium-glucose cotransporter 2 (SGLT2) inhibitors, and alpha glucosidase inhibitors reduce blood glucose levels by decreasing reabsorption of glucose in the renal system or lowering the digestion rate in the intestine [94,95]. Nevertheless, those medications may only delay the progression of diabetes, are not efficient in all patients, lose their efficacy over time and can induce adverse effects [14,96,97]. Therefore, many T2D patients become

dependent on insulin therapy over time [86,95,98,99]. Recently, two research groups defined five different subgroups of diabetes, namely severe autoimmune diabetes (SAID), severe insulin-deficient diabetes (SIDD), severe insulin-resistant diabetes (SIRD), mild obesity-related diabetes (MOD) and mild age-related diabetes (MARD) [100,101]. Consequently, different subtypes of diabetes require distinct medications, which are specially taillored to their needs. Furthermore, new therapeutic drugs need to be discovered that prevent or reverse diabetes progression and protect from pancreatic beta cell loss as well as cardiovascular diseases.

2.3. Glucose metabolism

The maintenance of blood glucose levels within a range of 3.3-5.5 mM is important to ensure normal body functions [102]. Chronically decreased glucose concentrations (hypoglycemia) as well as elevated plasma glucose concentrations (hyperglycemia) are correlated to several acute or long-term complications [16,103–105]. Therefore, blood glucose is tightly regulated by the two hormones glucagon and insulin that have opposing effects. The catabolic hormone glucagon is secreted from alpha cells at low glucose concentrations, leading to glucose production in the liver by glycogenolysis and gluconeogenesis, which results in an increase of blood glucose levels [1,106,107]. In contrast, the anabolic hormone insulin is secreted from pancreatic beta cells when blood glucose levels are high. Insulin promotes glucose uptake into the skeletal muscle as well as adipose tissue by translocation of glucose transporter 4 (GLUT4) to the plasma membrane [108]. Moreover insulin promotes glycogenesis and impairs gluconeogenesis in the liver [109]. These processes result in subsequent decrease of glucose concentration in the blood [1,108]. Furthermore insulin affects lipid metabolism by increasing lipogenesis through the promotion of FFA uptake from the plasma into the liver and adipose tissue and stimulation of triglyceride synthesis and storage [1,110].

2.4. Insulin biosynthesis, maturation and trafficking

Insulin is a peptide hormone and acts as an important messenger molecule to regulate glucose homeostasis and metabolism [1,111]. Many processes like translation, translocation, folding, trafficking, maturation and secretion are involved in the regulated release of insulin and dysfunction of any of these actions can lead to improper insulin secretion and development of diabetes [112–114].

Insulin synthesis starts with the translation of the large, inactive precursor peptide preproinsulin at the rough endoplasmic reticulum that is subsequently translocated into the ER [112,115]. Preproinsulin directly undergoes signal peptide cleavage, followed by folding and disulfide bond formation to form proinsulin in the ER [112]. Proinsulin is then transported in vesicles to the Golgi apparatus and translocates from *cis*- to *trans*-Golgi, where secretory granules are formed possibly by self-organization of membrane lipids [114,116,117]. In this model, proteins aggregate

through a mildly acidic and calcium-enriched environment leading to the interaction of aggregated proteins with cholesterol at the membrane [114]. This interaction causes reorganization of cholesterol-rich microdomains and therefore budding of secretory granules into the regulated secretory pathway [114]. Proinsulin is packed together with other prohormones, proteins and molecules like amylin (IAPP), GABA, chromogranin A (CGA), chromogranin B (CGB), prohormone convertase 1 (PC1), prohormone convertase 2 (PC2) and carboxypeptidase E (CPE), into secretory granules [118]. Proinsulin maturation takes place in the immature granule [114]. For this, granule milieu gets acidified by ATP-driven proton pumps leading to the conversion of proinsulin into insulin and C-peptide by combined action of PC1, PC2 and CPE (see Fig.2), which have an acidic pH optimum [116]. While PC2 preferentially cleaves proinsulin at the C-A junction, PC1 prefers processing of the B-C junction [119–121]. Due to a higher pH optimum and more rapidly enzymatic action of PC1, it is thought that first PC1 cleaves the B-C junction of proinsulin at the C-term of Arg31-Arg32 and subsequent PC2 cleaves the C-A junction of proinsulin at the C-term of Lys64-Arg65 [119,120,122]. CPE removes C-terminal Arg or respectively Lys residues from intermediate processed proinsulin and generates insulin and C-peptide [114,123,124].
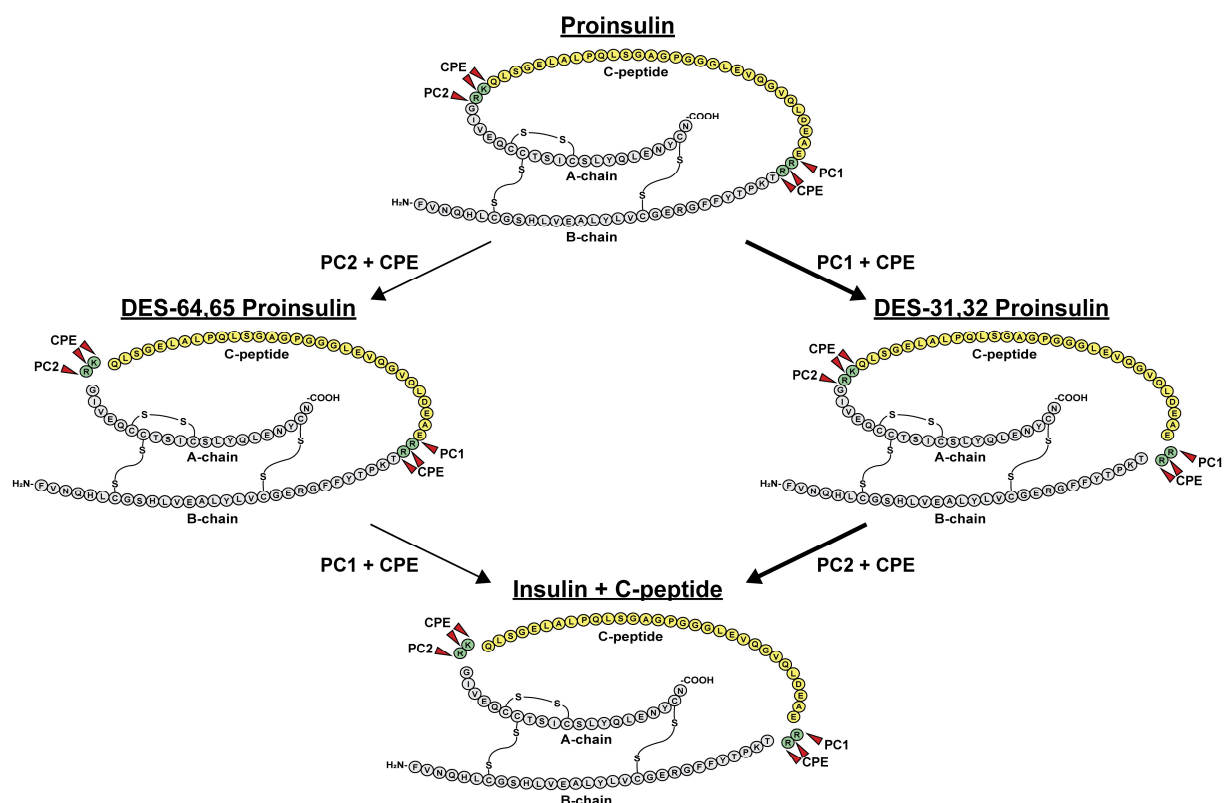
Figure 2: Conversion of human proinsulin into insulin and C-peptide. Shown is the human proinsulin protein sequence with one letter abbreviations and disulfide-bonds. Proinsulin is a single polypeptide precursor of insulin consisting of A- and B-chain (grey) and C-peptide (yellow). Red arrowheads point to cleavage sites of the different enzymes, which are necessary for the conversion into insulin and C-peptide. Proinsulin cleavage takes place in acidified secretory granules by sequential cleavage of PC1, PC2 and CPE. PC1 preferentially cleaves C-terminally of Arg31-Arg32 of the B-C junction, while PC2 is able to cleave C-terminally of Lys64-Arg65 in the A-C junction of proinsulin. After proteolytic cleavage of PC1 or PC2, CPE removes residual basic amino acids at the C-terminus of C-peptide or respectively B-chain leading to the generation of the two intermediates DES-64,65 or DES-31,32

proinsulin. After another round of proteolytic cleavage via PC1 or respectively PC2 and subsequent trimming of residual amino acids by CPE, mature insulin and C-peptide is generated. The pathway on the right site is thought to be more prominent, indicated by bold type arrows. **PC1**= prohormone convertase 1, **PC2**= prohormone convertase 2, **CPE**= carboxypeptidase E.

However, a very recent study questioned this view of proinsulin processing. Ramzy and colleagues reported that PC2 cannot be detected in non-diabetic human pancreatic beta cells by immunofluorescence, suggesting that only PC1 processes proinsulin in humans. Furthermore, due to elevated levels of PC2 in pancreatic beta cells of T2D donors they proposed that mislocalized PC2 expression may contribute to impaired proinsulin processing [125].

Insulin is further crystallized by condensation of six insulin molecules joined with one calcium and two zinc ions and stored in granules until metabolic stimulation and subsequent fusion with the plasma membrane [118]. The most important stimulus for insulin secretion in the beta cell is glucose, but other nutrients like amino acids and fatty acids are able to induce insulin secretion as well [115,126].

2.5. Insulin secretion

Secretion of insulin from pancreatic beta cells is highly stimulated by elevated blood glucose levels (Fig.3). Circulating glucose is taken up from the beta cells by glucose transporters (GLUT), which are highly expressed on the plasma membrane. GLUT2 is encoded by the gene *Slc2a2*, which is the predominant glucose transporter in pancreatic beta cells in rodents. However, human pancreatic beta cells express higher levels of GLUT1 and GLUT3 (encoded by *Slc2a1* and *Slc2a3*) in comparison to GLUT2 [127–129]. After glucose uptake into the beta cell, glucose is metabolized via glycolysis in the cytoplasm leading to the generation of pyruvate and adenosine triphosphate (ATP). Pyruvate enters the mitochondrion and passes through the tricarboxylic acid (TCA) cycle. NADH and $FADH_2$ generated in the TCA cycle are subsequently oxidized and enable ATP production in the respiratory chain [130]. The increased ATP/ADP ratio drives the closure of ATP-sensitive K^+ channels (K_{ATP} channels) and leads to a depolarization of the plasma membrane [131–133]. This leads to opening of voltage dependent Ca^{2+} channels (VDCCs) followed by an increase in intracellular calcium levels. Finally calcium triggers the fusion of granules with the plasma membrane and insulin is released into the circulatory system [7]. In addition to insulin, other hormones and molecules, which are present in secretory granules, like C-peptide, IAPP, ATP, Zn^{2+}, GABA, CGA derived peptides (e.g. betagranin and pancreastatin) and insulin-like growth factor 2 (IGF2) are secreted and affect energy metabolism and glucose homeostasis as well [118].
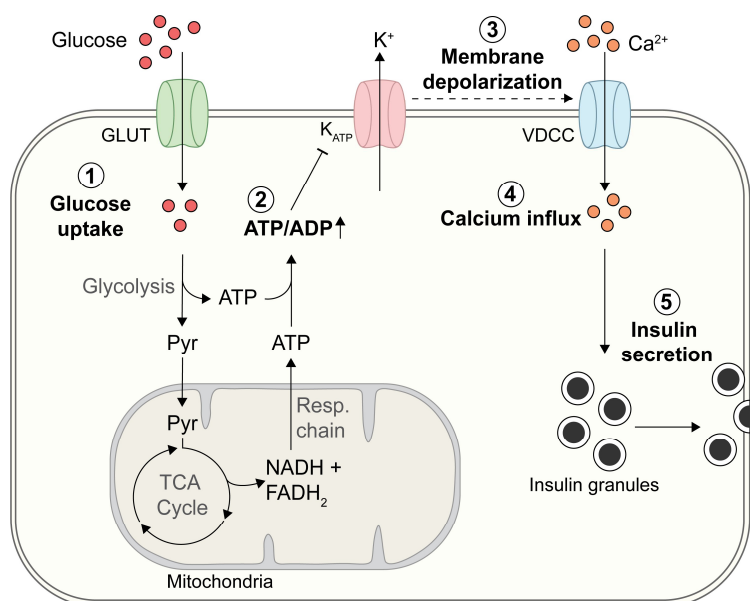
Figure 3: Model for glucose stimulated insulin secretion in pancreatic beta cells. Extracellular glucose is transported into the pancreatic beta cell by glucose transporters (GLUT) and subsequent metabolized to pyruvate (Pyr) via glycolysis in the cytoplasm. Pyruvate enters the tricarboxic acid (TCA) cycle where NADH and $FADH_2$, is generated, which is required for ATP production in the respiratory chain (Resp. chain). Increased ATP/ADP ratios lead to closure of ATP sensitive K_{ATP} channels. Intracellular accumulation of K^+ ions causes a depolarization of the plasma membrane and opens voltage dependent calcium channels (VDCCs). Calcium influx into the beta cell stimulates the fusion of insulin granules with the plasma membrane and secretion of insulin into the circulatory system. The illustration is modified from Rutter et al., 2015 [7].

Insulin secretion occurs in a biphasic manner that originates from the secretion of granules from distinct intracellular pools. The majority of granules (>95%) belongs to the reserve pool, while the rest of granules (<5%) belong to the readily releasable pool (RRP), which are docked to the plasma membrane [114,134]. The transient first phase starts during the first 3-10 minutes after glucose stimulation and releases the majority of insulin vesicles from the RRP. The second phase is slower, but lasts for a longer period of time, which peaks around 1-3 hours and originates from the recruitment of insulin granules of the reserve pool independent of extracellular glucose levels [116]. For the recruitment of granules from the reserve pool to the plasma membrane, also referred as mobilization or priming, granules must undergo several preparatory reactions that are ATP-, Ca^{2+}-, time- and temperature-dependent [135]. A reduction in first phase insulin secretion can be observed in prediabetic patients and is an early sign for the development of T2D [129,136,137]. In T2D patients, the first phase of insulin secretion is almost absent, while the second phase of insulin secretion is reduced [138,139].

2.6.   Sphingolipids and sphingolipid metabolism

Sphingolipids are alongside of glycerolipids and sterols one of the major class of lipids and comprise more than 4,000 distinct species [140–142]. They are integral components of cell membranes and influence not only structural properties of membranes but can also act as signaling molecules, so called bioactive lipids [141,143,144]. Previous studies have shown that

sphingolipids are involved in several cellular processes, like differentiation, apoptosis, growth, inflammation, senescence, migration, adhesion and stress response [144]. All sphingolipids share structural similarities and are composed of a sphingoid base backbone, mostly dihydrosphingosine (d18:0), also known as sphinganine, or sphingosine (d18:1), to which a fatty acid chain with varying length between 14 and 36 carbon atoms (C14-C36) and different head groups can be attached (Fig.4). The assembly of different building blocks leads to a huge diversity in sphingolipids, which can differentially modulate biophysical and biochemical properties of membranes, such as curvature, thickness, charge and fluidity and thereby influence crucial biological functions [142,145–147].
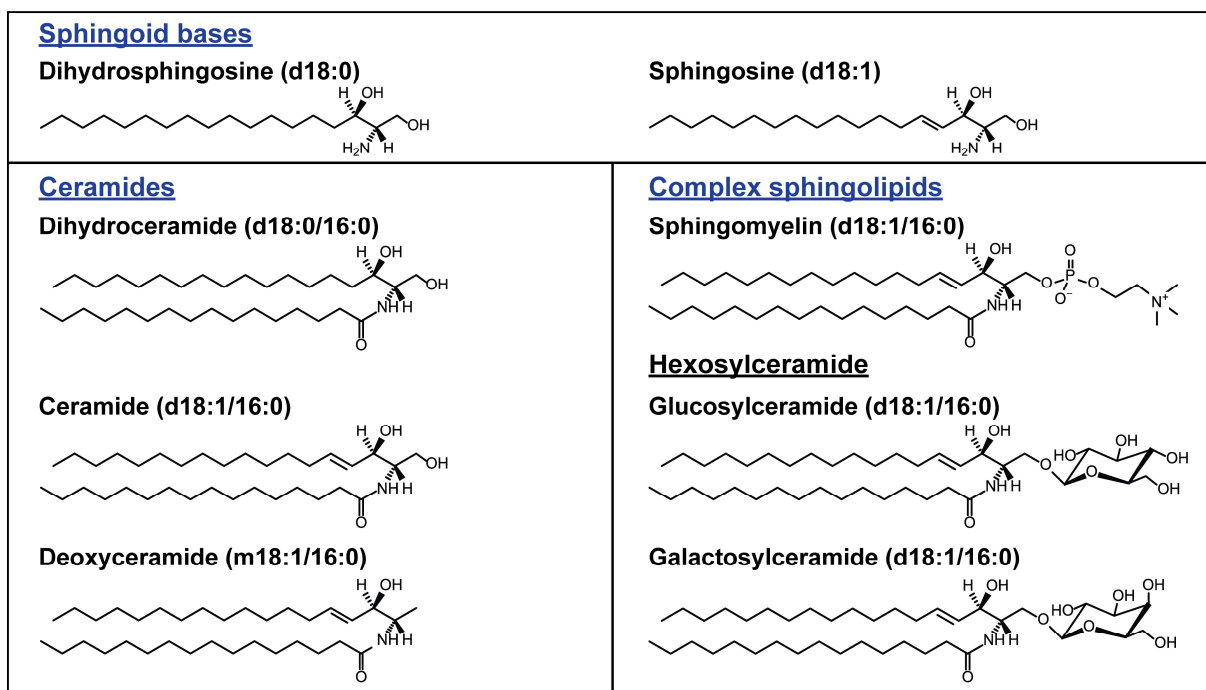
Figure 4: Molecular structures of the most common sphingoid bases and distinct sphingolipids. The sphingoid bases dihydrosphingosine (sphinganine) and sphingosine are the most common used backbones for the generation of dihydroceramides or ceramides by the distinct ceramide synthases. Deoxyceramides are synthesized by using a different backbone, which originates from condensation of L-alanine with palmitoyl-CoA, instead of serine in the *de novo* pathway. Ceramides serve as central metabolites for the generation of complex sphingolipids. For the generation of sphingomyelin, phosphocholine is attached as headgroup to ceramide. Glycosphingolipids are formed by addition of mono- or oligosaccharides to the ceramide backbone. Shown here are the simplest glycosphingolipids, glucosylceramide and galactosylceramide, which are designated as hexosylceramides in this thesis. Glucosylceramides have glucose as headgroup, while galactosylceramides have galactose as headgroup. Attachment of additional mono- or oligosaccharides lead to the generation of very complex and diverse glycosphingolipids, such as ganglioside, globosides and cerebrosides. All sphingolipids shown here have incorporated the C16:0 acyl chain, but due to different ceramide synthases, the fatty acid chain length can differ from C14 to C36. In addition to distinct fatty acid chain lengths, sphingolipids can also differ in their saturation depending on the sphingoid base they use as backbone and the fatty acid they attach. This leads to a huge variety of sphingolipids in the cell. The number in brackets describes the composition of the sphingolipid. m= mono and d=di represent the number of –OH groups in the sphingoid backbone, first number denote which sphingoid base is present and second number display which fatty acid is attached to the sphingoid base backbone.

Ceramides serve as a precursor for more complex sphingolipids and therefore play a central role in the sphingolipid metabolism (Fig.5). They are generated by three different processes in the cell. First, ceramides can be generated by *de novo* synthesis, where new ceramides are

formed from breakdown products of dietary sources in the ER. Second, ceramides can be generated by hydrolysis of sphingomyelin at the plasma membrane. Third, ceramides can be generated by the salvage pathway, in which ceramide is synthesized from sphingosine in the ER after the breakdown of more complex sphingolipids in the endolysosomal pathway [148–150]. Ceramide *de novo* synthesis classically starts with the condensation of palmitoyl-CoA, which originates from the saturated fatty acid palmitate, and the amino acid L-serine to 3-keto-dihydrosphingosine (3-KdhSph). This rate limiting reaction is performed by the enzyme serine palmitoyltransferase (SPT). 3-keto-dihydrosphingosine is directly reduced to the sphingoid base dihydrosphingosine (DhSph), also known as sphinganine, by 3-keto-dihydrosphingosine reductase (KDSR). In the next step, dihydrosphingosine gets N-acylated with a second fatty acid by ceramide synthase (CERS) 1-6 and forms dihydroceramide (DhCer). Importantly, CERS1-6 have high preferences for the fatty acid chain length they use in this reaction and thus generate, depending on the catalyzing CERS isoform, dihydroceramides with defined acyl chain lengths [151,152]. Subsequent trans-double bond formation at position 4-5 by dihydroceramide desaturase 1 (DES1) converts dihydroceramide into bioactive ceramide. Ceramide can be metabolized into more complex sphingolipids. In the ER, ceramide can be converted to galactosylceramide (GalCer) through addition of galactose by the enzyme ceramide galactosyltransferase (CGT), followed by vesicular transport of galactosylceramide to the Golgi [153]. Furthermore, ceramide is transported from the ER to the Golgi by either vesicular trafficking or ceramide transfer protein (CERT). Transport of ceramide by CERT is ATP-dependent and efficiently transports ceramide species with an acyl chain length of C14-C20, but not longer acyl chains [154,155]. Furthermore, CERT mainly delivers ceramides to the Golgi for sphingomyelin (SM) synthesis, while vesicular transport delivers ceramides to the Golgi for the generation of glucosylceramides (GluCer) [143]. Recently, a potential third, non-vesicular mechanism to transport ceramide from ER to Golgi was identified in yeast. Liu and coworkers demonstrated that the protein NVJ2p promotes the formation of ER-Golgi contact sites after ER stress induction and may directly transfer ceramides to the Golgi [156]. Sphingomyelins are the most abundant complex sphingolipids in human cells and are generated by the addition of a phosphocholine headgroup to ceramide via sphingomyelin synthase (SMS) [157]. For the generation of glucosylceramides, glucose is attached to ceramide by glucosylceramide synthase (GCS). Following this, four-phosphate adaptor protein 2 (FAPP2) transports glucosylceramides to the *trans*-Golgi [158]. There, glucosylceramides and galactosylceramides are converted into more complex glycosphingolipids, like lactosides, gangliosides, globosides and cerebrosides through addition of further mono- or oligosaccharides [159,160]. One of those glycosphingolipids is sulfatide, which is generated by sulfation of galactosylceramide via cerebroside sulfotransferase (CST) [157,161]. Most of ceramide is metabolized into sphingomyelin and glucosylceramide in the Golgi, but a part of the ceramide

pool can be additionally converted into ceramide-1-phosphate (C1P) by phosphorylation via ceramide kinase (CERK) at the *trans*-Golgi [157,158]. Ceramide-1-phosphate, sphingomyelin and glycosphingolipids are transported to the plasma membrane, whereas ceramide-1-phosphate is transported by ceramide-1-phosphate transfer protein (CPTP) and the latter two sphingolipids by vesicular trafficking [144,162]. The breakdown of sphingomyelin is catalyzed by sphingomyelinase (SMase), which leads to the generation of ceramide and free phosphorylcholine [143]. Dependent on their pH optimum sphingomyelinases can be classified into acid SMase (aSMase), neutral SMase (nSMase) and alkaline SMase (alkSMase) and are differentially localized in the cell. aSMase is mainly present in the endolysosomes, but can also relocate to the outer leaflet of the plasma membrane, while nSMase is located to the inner leaflet of the plasma membrane [143]. alkSMase is specifically expressed in human intestine and liver [157]. Ceramidases (CDase) are able to cleave the fatty acid from ceramide and generate sphingosine. Five different ceramidases exist, which are divided by their pH optimum into acid CDase (aCDase), neutral CDase (nCDase) and alkaline CDase (alkCDase or ACER), whereas the latter class consist of three different enzymes (ACER1-3) [163]. While nCDase is localized at the plasma membrane, aCDase is localized to the lysosome and ACER1-3 are localized to the ER and/or Golgi [163]. Sphingosine can either be recycled in the salvage pathway to ceramide in the ER, or phosphorylated by sphingosine kinase (SK) 1 or 2 to form sphingosine-1-phosphate (S1P) [143,164,165]. S1P is an important bioactive lipid that can either be secreted and act in an autocrine/paracrine manner by binding to sphingosine-1-phosphate receptors (S1PR) at the plasma membrane or function intracellularly as second messenger [166]. S1P levels in most tissues are low and are tightly regulated not only through its generation via sphingosine kinases, but also through its degradation via sphingosine-1-phosphate lyase (S1P lyase) and sphingosine-1-phosphate phosphatases (S1PP) or other phosphatases [166]. Dephosphorylation of S1P leads to the generation of sphingosine, which can reenter ceramide and sphingolipid biosynthesis in the ER. Ultimately, S1P can be irreversibly cleaved into hexadecanal and phosphoethanolamine by the enzyme S1P lyase, which is located at the ER membrane with its catalytic site in the cytosol [157,167]. This reaction is the final step of sphingolipid degradation and the only known route to leave the sphingolipid metabolism [157,164]. Hexadecanal is converted to palmitoyl-CoA after several steps and can be reused for ceramide *de novo* synthesis or for the synthesis of glycerolipids [144,168,169].

Figure 5: Schematic overview of the sphingolipid metabolism. Sphingolipid synthesis starts with the *de novo* synthesis of ceramides in the ER by the condensation of palmitoyl-CoA and serine. Ceramides are the central backbone for the generation of complex sphingolipids. They are transported either by vesicular trafficking or by CERT to the Golgi, where more complex sphingolipids are synthesized. Glucosylsphingolipids and sphingomyelins are transported to the plasma membrane. The breakdown of complex sphingolipids takes place in the lysosomes and ceramides can be regenerated by the salvage pathway. Sphingolipids can exit the sphingolipid pathway only by the irreversible breakdown of sphingosine-1-phosphate to hexadecanal and phosphoethanolamine via the enzyme sphingosine-1-phosphate lyase. A more detailed description is written in the text. **ER**: endoplasmic reticulum, **SPT**: serine palmitoyltransferase, **3-KdhSph**: 3-keto-dihydrosphingosine, **KDSR**: 3-keto-dihydrosphingosine reductase, **DhSph**: dihydrosphingosine (sphinganine), **CERS**: ceramide synthase, **DhCer**: dihydroceramide, **DES1**: dihydroceramide desaturase 1, **Cer**: ceramide, **CGT**: ceramide galactosyltransferase, **GalCer**: galactosylceramide, **CERT**: ceramide transfer protein, **GCS**: glucosylceramide synthase, **GluCer**: glucosylceramide, **CST**: cerebroside sulfotransferase, **SMS**: sphingomyelin synthase, **CERK**: ceramide kinase, **C1P**: ceramide-1-phosphate, **GSL**: glycosphingolipids, **SM**: sphingomyelin, **aSMase**: acid sphingomyelinase, **nSMase**: neutral sphingomyelinase, **nCDase**: neutral ceramidase, **aCDase**: acid ceramidase, **GCase**: glucocerebrosidase; **Sph**: sphingosine, **SK**: sphingosine kinase, **GCase**: glucocerebrosidase, **S1PP**: sphingosine-1-phosphate phosphatase, **S1P lyase**: sphingosine-1-phosphate lyase. The schematic overview is based on several publications [143,153,168,170,171].

2.7.   Properties of ceramide synthases

Ceramides are the central metabolite in the sphingolipid metabolism and are generated in mammals by a family consisting of six enzymes, CERS1-6, previously known as longevity assurance (LASS) 1-6. *CerS* are differentially expressed in various tissues. For example, *CerS3* is mainly expressed in the skin and the testis, while *CerS2* is almost ubiquitously expressed [151,172]. CERS1-6 primarily reside in the ER as transmembrane proteins and are suggested to have 5-6 transmembrane domains, whereas the catalytic site presumably faces the ER lumen [140,171,173,174]. In addition, several studies demonstrated CERS activity or localization in the mitochondria, the Golgi and the nuclear envelope [175–182]. However, mitochondrial localization of CERS is still unclear, due to insufficient purity after subcellular fragmentation [151]. All CERS possess a C-terminal domain, a Tram/Lag/CLN8 (TLC) domain, a N-terminal domain and a Hox domain, whereby the latter is missing in CERS1, which is more distantly related to the other CERS proteins [151,171,183]. CERS1-6 perform the same reaction and N-acylate (dihydro-) sphingosine with a fatty acid to generate (dihydro-) ceramide, but each CERS has high specificity towards distinct fatty acids with a certain chain length (see Fig.6). The fatty acid moiety of ceramide can vary between 14 and 36 carbon atoms (C14-C36), but long (C16-C20) and very long (C22-C24) ceramides are the most abundant ceramide species in mammals [147,184]. Ultra long ceramides with a chain length ≥26 are only present in a few tissues, like epidermal keratinocytes in the skin or male germ cells in the testis [147,185]. Based on studies using knockout animals, CERS1 primarily attaches fatty acyl-CoAs with a chain length of C18 [186,187], CERS2 attaches longer fatty acyl-CoAs with a chain length of C22-24 [188–191], CERS3 uses acyl-CoAs ≥26 [192], CERS4 adds C18-20 acyl-CoAs to the sphingoid backbone [193] and CERS5 and CERS6 preferentially uses acyl-CoAs with a chain length of C16 [194–197]. Overexpression and knockdown experiments of *CerS* in cell lines partially show additional specificities towards the acyl chain length of CERS. Due to tissue specific expression of CERS and attachment of different fatty acid chain lengths to the sphingoid base backbone, CERS proteins are not redundant. This leads to a complex tissue-specific distribution pattern of ceramides, followed by a large heterogeneity of sphingolipids [198].
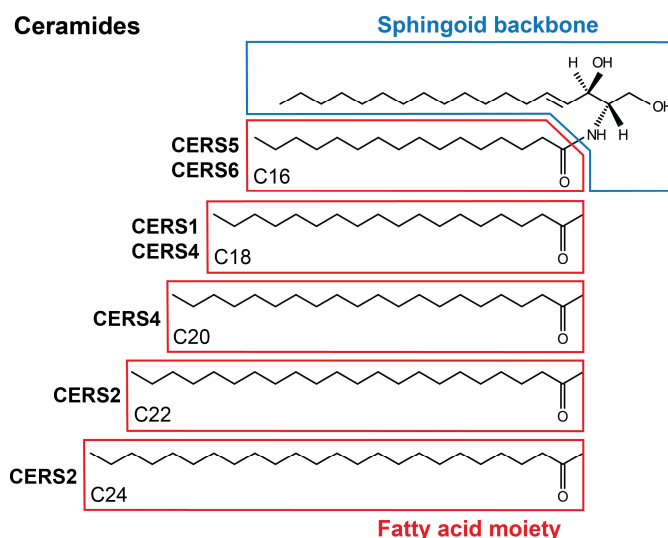
Figure 6: Ceramide synthases generate ceramides with variable acyl chain length. Ceramides consist of a sphingoid backbone (blue) and a second fatty acid (red). All ceramide synthases (CERS), CERS1-6, carry out the same reaction and N-acylate a fatty acid to a sphingoid base, but they possess high specificity towards the acyl chain length they are using in this reaction. In this way, ceramides with different chain length are generated that obtain different biophysical and biochemical properties. CERS5 and CERS6 generate long chain C16 ceramides, while CERS2 generates very long chain ceramides with a fatty acid chain length of C22-C24. The image displays the most abundant ceramide species (C16-C24) in mammals and respective CERS enzymes that are responsible for their generation.

Ceramides are a family of at least 50 closely related molecular species that are highly hydrophobic and can differ in their acyl chain length, hydroxylation and saturation state [143]. Therefore, distinct ceramides possess different biochemical and biophysical properties that affect membrane packing, shape, size and thickness and thus influence biological functions, like vesicle formation, protein interactions and signaling processes [146]. Furthermore, ceramides are located in distinct cellular compartments, such as the ER, Golgi, plasma membrane, mitochondria, nuclei and lysosomes, where they may fulfill different biological functions [143,198].

2.8. Sphingolipids in metabolic diseases

Sphingolipid metabolism in the cell is very complex and is tightly regulated due to the implication in many cellular processes. Dysregulation of sphingolipid biosynthesis and degradation is involved in several pathologies and diseases, such as sphingolipidosis, cancer, Alzheimer's disease, atherosclerosis, cystic fibrosis, and diabetes [144,168,199]. Usually, ceramide levels in the cell are very low and an imbalance can have deleterious effects on cell properties. Increased plasma and tissue ceramide concentration are associated with several metabolic disorders such as diabetes, obesity, fatty liver disease and insulin resistance [144]. Overnutrition and obesity result in elevated circulating levels of lipids (hyperlipidemia), including TAG, DAG, ceramide and FFA, as well as amino acids [200]. The excess of FFA and amino acids provide new substrates for sphingolipid biosynthesis and promote *de novo* synthesis of ceramides by upregulating the expression of SPT and DES1 [201–203]. Furthermore, obesity and insulin resistance are associated with chronic low grade inflammation, which triggers ceramide

biosynthesis and accumulation in skeletal muscle, liver and hypothalamus in human and rodents [141,200,204–206]. Mechanistically, a number of *in vitro* studies demonstrated that the cytokines TNFα and IL-1β upregulate SMase activity, which leads to increased sphingomyelin hydrolysis and ceramide synthesis [207–211]. Furthermore, hyperinsulinemia and TNFα increase SPT activity, resulting in enhanced *de novo* synthesis and subsequent ceramide generation [211,212]. Other stress stimuli, like oxidative stress, growth factors, heat shock or chemotherapeutic reagents are able to increase ceramide synthesis as well [213,214]. In addition, the adipokine adiponectin was shown to increase CDase activity, which hydrolyzes ceramide into sphingosine and a fatty acid [215]. Adiponectin receptors are suggested to possess intrinsic basal CDase activity that is augmented after binding to adiponectin [216]. Plasma levels of adiponectin are reduced in obese and T2D patients potentially leading to increased ceramide levels [217]. Elevated ceramide levels impair insulin signaling in the liver, skeletal muscle and adipocytes by inhibiting protein kinase B (AKT), as well as insulin receptor substrate 1 (IRS1) [149,150,218,219]. Several studies have shown that a reduction in ceramide levels by pharmacolgical inhibition of SPT using myriocin and L-cycloserine *in vivo* and *in vitro* improves insulin signaling, insulin sensitivity and glucose homeostasis in the context of high fat diet, palmitate treatment or obesity [203,219–227]. Moreover, genetic approaches that inhibit ceramide *de novo* synthesis, like heterozygous ablation of *Sptlc2*, one of the subunits from the SPT complex, or heterozygous as well as inducible ablation of *Degs1* (coding for DES1), result in an improved glucose homeostasis and insulin resistance in different organs [226–229]. Although those studies showed an advance in glucose homeostasis and insulin sensitivity after ceramide depletion, global inhibition of sphingolipid metabolism potentially leads to adverse side effects due to their contribution in many cellular signaling pathways [196,197,227]. Homozygous knockout of one of the two SPT subunits, *Sptlc1* or *Sptlc2*, leads to embryonic lethality [228,230,231]. In addition, homozygous DES1 deficiency is partially embryonic lethal and surviving animals display growth retardation and die within 8-10 weeks after birth [227].

Importantly, several studies have demonstrated by knockout of *CerS* that specific ceramide species with defined acylchain length differentially influence cellular functions in various tissues [186,189,192,194,196,232]. Especially long chain C16:0 fatty acids are associated with an increased diabetes risk, while longer C20:0, C22:0 and C24:0 fatty acids are linked to a lower diabetes risk [233–235]. Preventing the synthesis of detrimental ceramide species or modulating beneficial species could be a new therapeutic approach to treat diabetes. CERS, which are characterized by their specificity to use defined fatty acyl chains, represent a potential target [236]. C16:0 ceramides are generated by CERS5 and CERS6, while CERS2 synthesizes C22-C24 ceramide species [184,198]. Previous studies could demonstrate that the reduction of C16:0 ceramides in the liver or adipose tissue by ablation or inhibition of *CerS6 in vivo* protect animals from high fat diet induced obesity, glucose intolerance and improves insulin

sensitivity [196,197,236]. Conversely, it could be shown that an increase in C16:0 ceramide levels, generated by overexpression of CERS6 in primary mouse hepatocytes, is able to inhibit insulin signaling [237]. However, controversial data were published concerning the ablation of *CerS5*, which generates C16:0 ceramides as well. Gosejacob and collegues reported that *CerS5* knockout mice displayed improved glucose tolerance and insulin sensitivity and are protected from high fat diet-induced obesity [195]. In contrast to that, Hammerschmidt and colleagues showed that *CerS5* ablation in mice does not protect from diet induced obesity, hepatic lipid accumulation, insulin resistance and glucose intolerance, demonstrating a specific impact of CERS6 derived sphingolipids [196].

The loss of very long chain ceramides by heterozygous or homozygous knockout of *CerS2* in mice is accompanied with a compensatory increase in C16:0 ceramides and promotes diet induced hepatosteatosis, insulin resistance and glucose intolerance [188,189,191,237,238]. Furthermore, *CerS2* null mice develop myelin sheath defects and cerebellar degeneration [188]

In addition to ceramides, other sphingolipid species, such as sphingomyelins and glycosphingolipids are involved in insulin resistance. Elevation of sphingomyelins at the plasma membrane by overexpression of SMS2 are proposed to promote FFA uptake in the liver, leading to hepatosteatosis, while decreased sphingomyelins at the plasma membrane by the knockout of sphingomyelin synthase 2 (*Sgms2*) protects from high fat diet induced obesity, insulin resistance and fatty liver [228,239,240]. In contrast to this, decreased sphingomyelin levels by ablation of sphingomyelin synthase 1 (*Sgms1*) in mice, which is located in the Golgi, result in impaired glucose homeostasis and hyperglycemia, originating from decreased insulin secretion from pancreatic beta cells [241]. The expression of the ganglioside GM3 is increased after TNFα stimulation suppressing insulin signaling in adipocytes [242]. Knockout of ganglioside GM3 synthase (*St3gal5*) in mice protects from high fat diet induced obesity [243].

In contrast to ceramide, S1P and C1P are considered as pro-survival and anti-apoptotic sphingolipids [244]. It is proposed that the balance of relative amounts of prosurvival S1P and proapoptotic ceramide signals act as a rheostat that determines cellular response and outcome [245].

Those findings indicate that several sphingolipid species, as well as the fatty acid chain length affect glucose homeostasis and demonstrate the importance of proper regulation of sphingolipid metabolism.

2.9.   Sphingolipids in pancreatic beta cells

Lipids and sphingolipids also play an important role in pancreatic beta cell function. At physiological concentrations, FFA serves as an important nutrient that can stimulate insulin secretion in response to glucose [246]. However, in obesity, circulating fatty acids are elevated, the fat mass of the pancreas is potentially increased and lipid droplets in beta cells accumulate,

leading to the assumption that pancreatic beta cells are constantly exposed to high fatty acid concentrations [247–253]. Nevertheless, a recent study from Nowotny and colleagues could not detect a correlation of beta cell function and pancreatic fat content [254].

Chronically elevated FFA levels serve as fuel for the generation of sphingolipids, such as ceramide and are thus implicated in the induction of beta cell dysfunction and apoptosis by the induction of ER stress and ROS production [74,255–258]. Importantly, lipotoxicity is dependent on the chain length, as well as the saturation state of the FFA. *In vitro* studies with beta cell lines, as well as *ex vivo* studies with rodent and human islets report that exposure to the saturated fatty acid palmitate (palmitic acid, C16:0) or soluble ceramide analogues result in increased apoptosis and reduced proliferation, while exposure to unsaturated longer fatty acids, such as oleate (oleic acid, C18:1) is partially protective [259–264]. However, only few studies exist that have analyzed specific alterations of sphingolipid species by manipulating *CerS* in pancreatic islets. Overexpression of CERS4 was shown to increase the generation of C18:0, C22:0 and C24:1 ceramide, which augments glucolipotoxicity-induced beta cell apoptosis in INS1E cells [265]. Conversely, knockdown of *CerS4* inhibited apoptosis in INS1E cells [265]. Ceramide induced apoptosis is associated with mitochondrial dysfunction and increased ROS production, ultimately leading to mitochondrial membrane permeabilization, cytochrome c release and apoptosis [74]. The mechanism how mitochondrial membrane integrity is diminished was extensively debated and controversely discussed. Goñi and coworkers proposed that increased ceramide levels lead to changes in the membrane curvature resulting in membrane destabilization and increased permeabilization [266], while Collombini and coworkers proposed that ceramides form channels with a size of 5-40 nm in the mitochondrial outer membrane (MOM) during early apoptotic events resulting in the release of cytochrome c, ions and other proteins [267]. Inhibtion of ceramide *de novo* synthesis by inhibiting SPT using myriocin or L-cycloserine or inhibiting CERS via fumonisin B1 can partially prevent beta cell apoptosis after lipotoxic stress *in vitro* in beta cell lines and in rodent and human islets *ex vivo* [256,259,262,265,268]. In addition, application of L-cycloserine to prediabetic fa/fa Zucker Diabetic Fatty rats partially protects islets from apoptosis [269].

Furthermore, palmitate or ceramide were shown to reduce insulin biosynthesis *ex vivo* in rodent islets by impairing insulin gene expression and decreasing insulin content [270–272]. In addition, lipotoxicity induced by palmitate or ceramide impairs glucose stimulated insulin secretion in human and MIN6 cells [259,262]. Inhibition of ceramide *de novo* synthesis in beta cell lines, as well as human and rodent islets was sufficient to normalize insulin biosynthesis and partially rescue insulin secretion after palmitate induced ceramide synthesis [262,270].

In addition to ceramides, other sphingolipid species, such as sulfatide, S1P and sphingomyelin can affect beta cell function and survival.

S1P, which is generated by SK1 and SK2 was shown to enhance insulin secretion and protect beta cells from cytokine induced apoptosis [273,274]. However, SK1 and SK2 differ in their cellular localization and SK1 is reported to be pro-survival, while SK2 is described as pro-apoptotic [275]. SK1 knockout mice possess increased apoptosis and decreased beta cell mass, which results in impaired glucose tolerance after lipotoxic stress induction by high fat diet (HFD) [276]. In contrast, SK2 null mice are protected from beta cell apoptosis and retain insulin production after diabetes induction by HFD in combination with streptozotocin (STZ) [277].

Knockout of SMS1 in mice, as well as knockdown or inhibition of SMS1 and SMS2 in INS1 cells, strongly impair glucose stimulated insulin secretion [241,278]. However, SMS2 knockout mice exhibit an improved glucose tolerance and insulin sensitivity [228].

Sulfatide seems to play an important role in the beta cell and reduced sulfatide levels have been implicated in T1D and T2D [161]. It is packed together into secretory granules at the *trans*-Golgi and promotes proinsulin folding and crystallization of insulin into hexamers [279,280]. Furthermore, sulfatide is also located at the plasma membrane, where it regulates insulin secretion in a glucose-dependent manner by activation of K_{ATP}-channels, as well as mediating Ca^{2+}-dependent exocytosis [281].

Those studies demonstrated that sphingolipids differentially affect beta cell survival and function. Especially, ceramide species with different acyl chain length and their function in various organs and pathological diseases are in the focus of research during the last 10-20 years, but the role of distinct CERS and sphingolipid species in pancreatic beta cell remain unclear.

2.10. Aim

Ceramides have been shown to contribute to the development of T2D and are proposed to affect beta cell function and physiology. Although global inhibition of ceramide *de novo* synthesis prevents glucose intolerance and obesity, there are concerns about severe adverse effects due to the importance of sphingolipids for several cellular processes. However, targeting only sphingolipids with certain acyl chain length, ideally those species that are responsible for harmful cellular effects, might be a less serious intervention in cellular physiology. Therefore, CERS1-6, which generate distinct ceramide species with a defined acyl chain length, are in the focus of current research.

Since the role of distinct ceramide and sphingolipid species in pancreatic beta cells is largely unknown, we aimed to identify which sphingolipid species are altered during the development of obesity and T2D by analyzing the islet sphingolipidome in the diabetic db/db mouse model using untargeted lipidomics. Furthermore, we aimed to investigate the role of very long chain ceramides and sphingolipids on glucose homeostasis and beta cell physiology under obesogenic and non-obesogenic conditions *in vivo* and *ex vivo*. Therefore, we generated beta

cell specific *CerS2* knockout mice and analyzed their body weight, blood glucose levels, glucose tolerance, insulin tolerance and insulin secretion on normal and high fat diet. In addition, to uncover the underlying mechanisms, *CerS2* was ablated in the rat beta cell line INS1E and a proteome analysis was conducted.

3. Material and methods

3.1. Mouse experiments

3.1.1. Animal care

All animal procedures were conducted in at the German Diabetes Center in Düsseldorf and were in compliance with protocols approved by local government authorities (Bezirksregierung Düsseldorf, Germany). Mice were housed in groups of 2-6 mice, at 22-24°C with a 12 h light, 12 h dark cycle. Mice were either fed with normal chow diet (ND) containing 62% carbohydrates, 26% protein and 12% fat (ssniff Spezialdiäten, V1126-000) or with high fat diet (HFD) containing 20% carbohydrates, 20% protein and 60% fat (Research Diets, D12492). All animals have unlimited access to drinking water at all times and food was only removed for a specific fasting period if required for experiments. Blood glucose levels and body weight were monitored every week from mice in experimental cohorts. At the end of experiment, mice were sacrificed by cervical dislocation or decapitation.

3.1.2. Mouse models

Dependent on the scientific questions, different mouse models were used in this study. Male BKS.Cg-*Dock7*^{m} +/+ *Lepr*^{db}/J (control) and BKS.Cg-*Dock7*^{m} +/+ *Lepr*^{db}/^{db} (db/db) mice were purchased from the Jackson Laboratory in week 5 and 11 and used for islet isolations after one week of adaptation. db/db mice possess a homozygous mutation in the leptin receptor and become morbidly obese, hyperglycemic and relative hypoinsulinemic [282,283].

To investigate the role of CERS2 in pancreatic beta cells *in vivo* and *ex vivo*, *CerS2* was specifically knocked out in beta cells in mice onto the C57B6/J background. Conditional *CerS2* mice with integrated flanking loxP (flox, fl) sites in front of exon 2 and behind exon 11 were generated and kindly provided by Prof. Dr. Jens C. Brüning from the Max-Planck-Institute for Metabolism Research in Cologne, Germany. Conditional *CerS2* mice were crossbred with the *Ins1*-Cre driver mouse line, which expresses a Cre recombinase under the control of the *Insulin 1* (*Ins1*) promoter [284]. When *Ins1* expression starts, the Cre recombinase specifically eliminates the gene sequence of *CerS2* between the two flanking loxP sites, generating beta cell specific *CerS2* knockout mice. *CerS2*$^{+/+}$, as well as *CerS2*$^{fl/fl}$ mice were generated in parallele by breeding heterozygous *CerS2*$^{fl/+}$ mice with *Ins1*-Cre$^{tg/+}$, *CerS2*$^{fl/+}$ mice and littermates were used for the generation of experimental cohorts in the next breeding. *CerS2*$^{fl/fl}$ mice were mated with *Ins1*-Cre$^{tg/+}$, *CerS2*$^{fl/fl}$ mice to generate beta cell specific *CerS2* knockout mice (*Ins1*-Cre$^{tg/+}$, *CerS2*$^{fl/fl}$, designated as *CerS2*$^{\Delta BKO}$). As control group *CerS2*$^{+/+}$ mice were crossed with *Ins1*-Cre$^{tg/+}$, *CerS2*$^{+/+}$ mice to generate mice that possess the *CerS2* wildtype allele (*Ins1*-Cre$^{tg/+}$, *CerS2*$^{+/+}$, designated as control).

3.1.3. Genotyping

Genotypes of mice were determined by polymerase chain reaction (PCR) using genomic DNA extracted from ear biopsies. In addition, germline deletion was excluded using primers, which detect the deleted allele.

3.1.3.1. Isolation of genomic DNA from ear biopsies

Biopsies from mice were digested in 500 µl lysis buffer (0.1 M Tris pH 8.0, 0.2 M NaCl, 5mM EDTA, 0.4% SDS) for 1 h to over night at 55°C in a shaking thermomixer. DNA was precipitated by adding an equal amount of isopropanol. After centrifugation for 10 min at 12,000x g, DNA was washed with 1 ml of 75% ethanol (EtOH), centrifuged and the dry DNA pellet was subsequently dissolved in 200 µl of double distilled water (ddH$_2$O).

3.1.3.2. Extraction of genomic DNA from mouse organs

For determination of specific *CerS2* deletion in pancreatic beta cells, different organs were isolated from mice. For this, mice were sacrificed by cervical dislocation and pieces of the liver, kidney, heart, adrenal gland, brain, gonadal fat, skeletal muscle from musculus gastrocnemius, lung and tail were extracted and transferred in 1ml lysis buffer (0.1 M Tris pH 8.0, 0.2 M NaCl, 5 mM EDTA, 0.4% SDS). Organs were homogenized using an Ultra Turrax (IKA), which was cleaned with 5% SDS, 70% EtOH and ddH$_2$O between different samples. DNA of homogenates was precipitated by adding an equal amount of isopropanol following centrifugation for 10 min at 12,000x g. Then resulting precipitate was washed with 1 ml EtOH, centrifuged with the same conditions and DNA pellet was dried at 55°C. Dried DNA pellet was dissolved in 200 µl of ddH$_2$O.

Islets were isolated as described later in chapter 3.2.1. On the next day, 15 islets were picked, washed with 1 ml PBS and lyzed in 30 µl QuickExtract DNA Extraction Solution (Epicentre, QE09050). DNA was digested for 6 min at 65°C, follwed by inactivation for 5 min at 95°C and addition of 20 µl ddH$_2$O prior to PCR.

3.1.3.3. Polymerase chain reaction

PCR was used to amplify rapidly specific DNA sequences in a biological sample using specific primers. For the detection of the Cre transgene in the *Ins1* locus and loxP flanked exons of *CerS2* in mouse genome two different PCRs were performed. Tab.1 shows specific primers and expected PCR products.

Table 1: Specific primer sequences for genotyping of *CerS2* and *Ins1*-Cre allele. Expected PCR fragments for the different genotypes are shown. Wt= wildtype; flox= flanked by loxP sites, Δ= delta, tg= transgene.

Primer	Sequence 5´ - 3´	Expected fragments [bp]
CerS2 A	CAGCACCAAGACTCATCACC	*CerS2* Wt: 276
CerS2 B	AAGCCACAACTACAGGTAGG	*CerS2* flox: 567
CerS2 C	ATCTCCTGCCTTGATCTTCC	*CerS2*Δ: 371
Cre A	GGGCAGAGAGGAGGTACTTTG	Wt: 618
Cre B	TTTTTGGTGCTTATTCAAAAGTT	tg: 410
Cre C	GCAAACGGACAGAAGCATTT	

PCR reaction was set up as mastermix and pipetted in a microreaction tube as depicted in Tab.2.

Table 2: Mastermix composition for genotyping PCR of mouse biopsies. Volume is calculated for one reaction. 2x GoTaq G2 Hotstart Green Mastermix was purchased from Promega (M7423).

Component	Volume [µl]
2x GoTaq G2 Hotstart Green Mastermix	5
Primer A (10 µM)	0.5
Primer B (10 µM)	0.5
Primer C (10 µM)	0.5
Template DNA (lysate)	1
ddH$_2$O	2.5
Final volume	10

Reactions were run on a Biometra Trio Thermocycler (Analytik Jena) using the programs depicted in Tab.3 and Tab.4.

Table 3: PCR program for the detection of *CerS2* floxed and *CerS2*Δ alleles.

Step	Temperature [°C]	Time [sec]	Cycle number
Initial denaturation	95	480	1
Denaturation	95	30	
Annealing	60	30	35
Extension	72	60	
Final Extension	72	120	1
Hold	4	∞	1

Table 4: PCR program for the detection of *Ins1*-Cre transgene.

Step	Temperature [°C]	Time [sec]	Cycle number
Initial denaturation	95	320	1
Denaturation	95	60	
Annealing	58	60	35
Extension	72	90	
Final Extension	72	180	1
Hold	4	∞	1

3.1.3.4. Analysis of PCR products on agarose gels

PCR products were analyzed on a 1-2% agarose (VWR, 732-2789DE) gel in 1x TAE buffer (AppliChem, A4686) containing peqGREEN dye (VWR, 732-2960) depending on the expected size of products. Samples were loaded on agarose gels and run for 20-30 min at 120 V in a Sub-Cell GT system (Bio-Rad). As marker, Generuler DNA ladder mix (Thermo Fisher Scientific, SM0332) was loaded. Bands were visualized by a Chemidoc™ XRS imaging system (Bio-Rad).

3.1.4. Determination of blood glucose levels and collection of plasma samples

Tail tips were scratched carefully with a small scissor and blood glucose levels were determined with a drop of blood using a glucometer (Contour®XT, Bayer AG). For collecting plasma, microvette CB 300 LH (Sarstedt, 16.443), which are coated with lithium-heparin were used. After centrifugation for 6 min at 2,000x g, supernatant was frozen at -80°C. Blood collection from control and *CerS2*$^{\Delta BKO}$ mice was performed side by side in the morning or after a specific fasting period to avoid intra-group deviations caused by circadian variations.

3.1.5. Glucose tolerance test

For glucose tolerance test (GTT), mice were fasted for 16 h over night. Body weight of mice was determined and 1 g/kg or 2 g/kg glucose was injected intraperitoneal (i.p.) depending of the cohorte and diet. This corresponds to 5 µl/g or respectively 10 µl/g mouse from the 20% glucose solution (Glucosteril® 20%, Fresenius Kabi). Mice, which did not increase blood glucose levels above 100 mg/dl after glucose injection were excluded from the analysis. Blood glucose levels were determined after 0, 20, 40, 60, 80, 100 and 120 min and plasma was collected at 0, 20 and 120 min.

3.1.6. Insulin tolerance test

For insulin tolerance test (ITT), mice were fasted for 4 h. Body weight was measured and a 0.75 U/kg (male mice on ND) or 0.25 U/kg (female mice on ND) insulin (Insuman Rapid 40 I.U./ml, Sanofi-Aventis) was injected i.p. into mice depending on the cohorte and diet. Stock

solution was prediluted in PBS in such a concentration that 10 µl/g mouse was injected. Blood glucose levels were determined after 0, 20, 40, 60, 80, 100 and 120 min.

3.1.7.   Acid-ethanol extraction of pancreatic proteins

Pancreata were excised carefully from mice and weight was measured for normalization. Pancreata were homogenized in 5 ml of ice-cold acid-ethanol (1.5% HCl in 75% EtOH) using an Ultra-Turrax homogenizer (IKA). After each pancreas, Ultra-Turrax was cleaned sequentially using 5% SDS, 70% EtOH and ddH$_2$O. Samples were incubated over night at -20°C. On the next day, samples were centrifuged for 5 min at maximum speed and supernatant was transferred to a new falcon tube and stored at -20°C until use in Enzyme-linked Immunosorbent Assay (ELISA).

3.1.8.   Extraction of RNA from mouse organs

Pieces of brain, liver, skeletal muscle from musculus gastrocnemius and adipose tissue from gonadal fat were excised and subsequently transferred into tubes containing ceramic beads with the size 0f 1.4 mm (VWR, 432-0356) on dry ice. 1 ml of Trizol (PeqGold Trifast, VWR, 30-2020) was pipetted on organs and tissues were homogenized by Precellys Evolution homogenizer (Bertin Instruments, P000062-PEVO0-A) using the soft protocol (15 sec shaking at 5,800 rpm, waiting 30 sec, 15 sec shaking at 5,800 rpm). Mouse islets were isolated as described in chapter 3.2.1. On the next day, 50 islets were picked, washed with PBS and 1 ml of Trizol was pipetted on islets.

3.2.   *Ex vivo* studies of pancreatic mouse islets

3.2.1.   Isolation and cultivation of pancreatic mouse islets

To isolate pancreatic islets from control and *CerS2*$^{\Delta BKO}$ mice, mice were sacrificed and pancreata were perfused with 2 ml of 2.3 Wünsch Units/ml Liberase™ TL Research Grade (Merck, 5401020001) in RPMI without additives (Gibco by Life Technologies, 11835105). Perfused pancreata were shaken in a waterbath (GFL, 1083) by approximately 100 U/min for 16 min at 37°C. After addition of 50 ml RPMI containing 10% FCS (Gibco by Life Technologies, 10270106), falcons were shaken manually for 30 sec and centrifuged for 3 min at 189x g. Afterwards the pellet was resuspended in 10 ml RPMI medium and transferred through a strainer with a pore size of 420 µm (Sigma-Aldrich, CD1-1KT) into a new falcon tube. The samples were filled up to 50 ml with RPMI and centrifuged for 3 min at 189x g. For segregation of the islets from other tissues, a density gradient was generated using Histopaque with different densities. The pellet was resuspended in 3 ml Histopaque 1119 (Sigma Aldrich, 11191), afterwards 3 ml of Histopaque 1083 (Sigma-Aldrich, 10831), Histopaque 1077 (Sigma-

Aldrich, 10771) and finally RPMI was carefully added. After centrifugation for 20 min at 935x g with ACC and DCC set to 1 (Thermo Fisher Scientific, Heraeus Megafuge 40), islets were collected between the highest two phases and transferred to a new falcon tube. The islets were washed with RPMI medium containing FCS and centrifuged for 5 min at 336x g. Afterwards medium was discarded and cultured in petridishes (LABSOLUTE, TH.Geyer, 7696400) in DMEM media (Gibco by Life Technologies, 31885049) containing 5 mM D-Glucose, 1 mM Na-Pyruvate, 2 mM Glutamax, 0.18 mM 2-mercaptoethanol, 11 mM HEPES, 10% FCS and 1% Pen/Strep (all Gibco by Life Technologies). The islets were incubated at 5% CO_2 at 37°C and were hand-picked on the next day for analysis of pancreatic islets.

3.2.2. Pharmacological treatment of mouse islets

To study protein degradation of PC1, isolated pancreatic mouse islets were treated with 100 nM of the translational inhibitor cycloheximide (CHX) (Sigma-Aldrich, 239765) in full media for different periods of time (0, 0.5, 1, 2.5 and 5 h).

3.2.3. Insulin secretion assay with mouse islets

For functional analysis of pancreatic islets an glucose stimulated insulin secretion assay (GSIS) was performed. From each mouse, 7 islets with similar size were picked in 100 µl media and transferred into a U-shaped 96 well plate (VWR, 734-0955) as triplicates. The islets were washed 3 times with 80 µl KRH buffer (129 mM NaCl, 4.8 mM KCl, 5 mM $NaHCO_3$, 1.2 mM $CaCl_2$, 1.2 mM KH_2PO_4, 1.2 mM $MgSO_4$, 10 mM HEPES and 0.1% BSA in ddH_2O, pH was adjusted to 7.4 with 5 mM NaOH) containing 2 mM glucose and subsequently starved for 1 h at 37°C in 100 µl of the same buffer. Afterwards, islets were stimulated sequentially first with 100 µl low glucose KRH buffer (2 mM glucose) follwed by stimulation with 100 µl high glucose KRH buffer (20 mM glucose) for 1 h at 37°C. 80 µl of low glucose and high glucose supernatants were collected, centrifuged at 4°C and 900x g for 5 min and 50 µl of the supernatant was transferred into new reaction tubes. Islets were dissolved in 250 µl RIPA Buffer (Abcam, ab156034) containing PhosSTOP™ (Sigma-Aldrich, 4906837001) and cOmplete Protease Inhibitor Cocktail (Sigma-Aldrich, 4693132001) and placed on a cell disruptor (Scientific Industries, Digital Disruptor Genie, SI-DD38) for 10 min and 2,500 rpm at 4°C. Cell debris was removed by centrifugation in a tabletop centrifuge (Thermo Fisher Scientific) at 4°C for 10 min at max speed and 100 µl of supernatant was transferred into new reaction tubes. All samples were stored at -20°C until they were used in ELISA.

3.3.   *In vitro* studies in INS1E cells

3.3.1.   Cultivation of INS1E cells

The rat beta cell line INS1E [285] was cultivated in RPMI media (Gibco by Life Technologies, 11835105) containing 11 mM Glucose, 1 mM Na-Pyruvate, 2 mM Glutamax, 0.18 mM 2-mercaptoethanol, 11 mM HEPES, 10% FCS and 1% Pen/Strep (all Gibco by Life Technologies) in an incubator with 5% CO_2 and 37°C. For passaging, INS1E cells were washed with PBS, trypsinized with 0.05% Trypsin for 3 min. Trypsin was neutralized by adding fresh RPMI media. After centrifugation for 3 min at 190x g, cells were resuspended in RPMI media, cell numbers were determined using a Neubauer counting chamber and respective number of INS1E cells was seeded on tissue culture treated plates.

3.3.2.   Pharmacological treatment of INS1E cells

To analyze protein degradation of PC1 in INS1E cells, cells were treated with 100 nM cycloheximide (CHX) for different time periods (0, 1, 3, 5, 7 and 9 h).

3.3.3.   siRNA mediated knockdown in INS1E cells

To analyze the role of specific genes in INS1E cells, knockdown experiments were performed using specific siRNA that target concrete rat mRNAs. As control, non-targeting siRNA (Ambion, 4390844) was used. Sequences are shown in Tab.5.

Table 5: Used siRNA sequences for knockdown experiments in INS1E cells.

siRNA	Company	siRNA ID	Sequence 5' - 3'
Tpst1	Ambion	s143642	GAAGUGGGUUGGGAAGAUA tt
Tpst2	Ambion	s143734	GCUAUGAUCCGUACGCAAA tt
Pcsk1	Ambion	s129182	CGAAUAUUCUCGUAGAGGA tt

siRNA was transfected with a final concentration of 50 nM in INS1E cells using Lipofectamine RNAiMAX reagent (Thermo Fisher Scientific, 13778150). Thus, for double knockdown cells were transfected with 25 nM of each siRNA. For the double knockdown of *Tpst1* and *Tpst2* Opti-MEM (Gibco by Life Technologies, 31985047) was mixed with Lipofectamine RNAiMAX in one reaction tube, while Opti-MEM and the siRNA mix were combined in a second reaction tube. Both tubes were combined in a 1:1 ratio, incubated for 5 min at room temperature (RT) and respective volumes were carefully dropped onto INS1E cells. The pipetting sheme is shown in Tab.6.

Table 6: Transfection protocol for knockdown in INS1E cells. Volume is calculated for one reaction.

Reaction	Supplement	Volume [µl]	
		6 well	24 well
1	Opti-MEM	250	62.5
	Lipofectamine RNAiMAX	6	1.5
2	Opti-MEM	250	62.5
	Ctrl siRNA (50 µM)	2.5	0.625
3	Opti-MEM	250	62.5
	siRNA1 (50 µM)	1.25	0.3125
	siRNA2 (50 µM)	1.25	0.3125
Mix in a 1:1 ratio, incubate 5 min at RT			
RPMI volume [µl]		2000	500
Transfection volume [µl]		500	125

48 h after transfection cells were harvested for respective analysis.

3.3.4. Plasmid transfection in INS1E cells

To analyze the specificity of PC1 antibody, overexpression experiments of PC1 (Origene, MR225451) were performed in INS1E cells using Lipofectamine 2000 (Thermo Fisher Scientific, 10270106). Therefore, Opti-MEM was mixed with Lipofectamine 2000 in one reaction tube, while Opti-MEM and PC1 plasmid were combined in a second reaction tube. Both tubes were combined in a 1:1 ratio, incubated for 5 min at RT and 500 µl of transfection mixture was carefully dropped onto INS1E cells. The pipetting sheme is shown in Tab.7

Table 7: Transfection protocol for protein overexpression in INS1E cells. The volume is calculated for one reaction. X represents the volume, which is required for 2 µg plasmid.

Reaction	Supplement	Volume [µl] for 6 well
1	Opti-MEM	250
	Lipofectamine 2000	6
2	Opti-MEM	250
	Plasmid (2 µg)	X
Mix in a 1:1 ratio, incubate 5 min at RT		
RPMI volume [µl]		2000
Transfection volume [µl]		500

To reduce lipotoxic effects, medium was changed 6 h after the transfection and cells were incubated for 48 h at 37°C until harvesting proteins.

3.3.5. Determination of insulin content in INS1E cells

To ascertain the insulin content in INS1E cells *in vitro*, 200,000 control and *CerS2*$^{\Delta INS1E}$ cells were seeded as triplicates on a 24 well plate. On the next day, cells were washed 3 times with

300 μl of 2 mM glucose containing KRH buffer and starved for 30 min in the same buffer at 37°C. Afterwards, cells were exposed for 1 h at 37°C to low glucose KRH buffer (2 mM glucose) or high glucose KRH buffer (25 mM glucose). The supernatant was discarded and 100 μl RIPA was added to each 24 well dish. INS1E cells were lyzed for 10 min at RT, collected into a reaction tube and disrupted for 10 min at 2,500 rpm in a cell disruptor at 4°C. Cell debris was removed by centrifugation for 10 min at max speed and 4°C and supernatant was transferred into a new reaction. Samples were stored at -20°C until they were used in insulin ELISA.

3.3.6. Celltiter-Glo Assay

ATP levels in INS1E cells were measured by using Celltiter-Glo 2.0 (Promega, G7571). INS1E cells were cultured for 48 h in a 96 well plate. One volume of Celltiter-Glo 2.0 Reagent was added to each wells and plates were shaken for 2 min on a horizontal shaker to induce cell lysis. ATP leads to the oxygenation of luciferin (included in Celltiter-Glo 2.0 mix) to oxyluciferin and release of a luminescent signal, which was measured after 10 min of incubation at RT in a GloMax® Discover Microplate Reader (Promega) using the preset program.

3.3.7. EdU staining

To investigate proliferation in INS1E cells, Click-iT™ Plus EdU Alexa Fluor™ 488 Flow Cytometry Assay Kit (Thermo Fisher Scientific, C10425) was used. INS1E cells were grown in a 6 well dish and treated with 5 μM EdU in full media for 1 h. Following this, staining was performed according to the manufacturer's protocol. EdU incorporation was determined in 10,000 cells with the FACSCalibur Flow Cytometer (BD Biosciences) by measuring fluorescent 488 signal with an 530/30 nm emissionfilter and using following parameters:

Table 8: Parameters for the detection of EdU positive cells by flow cytometry.

Detector	Voltage	Amp Gain	Mode
FSC	E-1	5.0	Lin.
SSC	350	1.0	Lin.
FL1	450	1.0	Log.

Quantification was performed with FlowJo software (Version 10).

3.3.8. Generation of monoclonal knockout cells using the CRISPR/Cas9 system

The clustered regularly interspaced short palindromic repeats (CRISPR)/CRISPR associated 9 (Cas9) system is a relatively new, cheap and fast genome editing tool for the generation of genetically modified organisms. In brief, a guide RNA (gRNA) containing a 20 nt targeting sequence specifically binds to a designated DNA sequence. The Cas9 enzyme binds to a protospacer adjacent motif (PAM) sequence, which is directly next to the targeting site, and

cuts the DNA in this region. Due to error-prone repair mechanism of the cell by non-homologous end joining (NHEJ), small insertions and deletions (Indels) can emerge leading to frameshifts and/or premature stop codons and hence loss of protein in a subset of cells.

In this study, a two-sided cutting strategy was used as described from Bauer and colleagues [286]. Two individual gRNAs were designed that specifically target two different sequences in the gene of interest and result in two double strand breaks. In a subset of transfected cells, reparation of the double strand breaks by NHEJ leads to the loss of the whole DNA sequence between both cutting sites. With this strategy knockout cells can be easily identified by genotyping PCR. A schematic overview of the targeting strategy for *CerS2* is shown in Fig.17A.

3.3.8.1. Transfection of CRISPR/Cas9 plasmids in INS1E cells

For the generation of homozygous *CerS2* and *Pcsk1* INS1E knockout cells (designated as *CerS2*$^{\Delta INS1E}$ or respectively *Pcsk1*$^{\Delta INS1E}$), two different gRNA containing pSpCas9 plasmids with a total amount of 3 µg were cotransfected into INS1E cells using Lipofectamine 2000. *CerS2*$^{\Delta INS1E}$ cells were generated by cotransfection of plasmids that contain gRNAs targeting exon 2 and exon 11, which is the same locus deleted in *CerS2*$^{\Delta BKO}$ mice (see Fig.8A and Fig.17A). For the generation of *Pcsk1*$^{\Delta INS1E}$ cells, gRNA containg plasmids were transfected that target intron 3-4 and intron 5-6. The design and preparation of pSpCas9 plasmids are described from chapter 3.4.2 onwards. Control cells were generated by the transfection with respective non-targeting pSpCas9-control plasmids. Controls of *CerS2*$^{\Delta INS1E}$ cells were transfected with 3 µg of the plasmid pSpCas9(BB)-2A-Puro(PX459) (Addgene, 62988), while controls of *Pcsk1*$^{\Delta INS1E}$ cells were cotransfected with 1.5 µg of each plasmid, pSpCas9(BB)-2A-GFP(PX458) (Addgene, 48138) and pSpCas9(BB)-2A-mcherry(PX458) (kindly provided by Dr. S. Hoffmann from the Institute for Physical Biology at the Heinrich Heine University Düsseldorf, Germany). The transfection was performed as described in chapter 3.3.4 and medium was changed after 6 h to normal cultivation media. Cells were incubated for 48 h at 37°C.

3.3.8.2. Generation of monoclonal INS1E cells

While *CerS2* gRNAs were cloned into plasmids for puromycin selection, *Pcsk1* gRNAs were inserted into plasmids that contain either GFP or mcherry for selection. Therefore, the procedure to generate monoclonal INS1E knockout cell lines slightly differed.

For the generation of *CerS2*$^{\Delta INS1E}$ cells and respective control cells, INS1E cells were treated 48 h after the transfection with 2 µg/ml puromycin (Sigma-Aldrich, P8833) for 7 days. Surviving cells, have taken up the gRNA containing plasmids, transcribed *CerS2* gRNA and the Cas9 enzyme, which potentially leads to double strand breaks in the *CerS2* locus and the generation

of *CerS2*[ΔINS1E] cells. The medium was exchanged every day or every two days with fresh media containing puromycin. After seven days, medium was changed back to normal cultivation media and cells were cultured until reaching a cell confluency of approximately 70-80%. To obtain monoclonal control and *CerS2*[ΔINS1E] cells, cells were trypsinized and seeded in a very low density of 6,000 cells on a p10 dish. Monoclonal cells were cultured for approximately one week until the formation of round colonies, which can be hand-picked under a microscope using a pipette and transferred onto a 96 well plate.

Monoclonal control and *Pcsk1*[ΔINS1E] cells were generated 48 h after transfection. Cells were simultaniously selected and singularized by fluorescence activated cell sorting (FACS) in collaboration with Prof. Dr. Häussinger and Dr. Wammers from the Department of Gastroenterology, Hepatology and Infectious Diseases at the University Hospital in Düsseldorf, Germany. GFP and mcherry double positive cells were directly sorted as single cells into a 96 well plate.

Independent of the selection and separation procedure, monoclonal cells were grown to a monolayer and splitted on two 96 well plates, one of those for further culturing and one for the identification of control and knockout cells by genotyping.

3.3.8.3. Isolation of genomic DNA from INS1E cells

Control and potential knockout INS1E cells in the 96 well plate were washed with PBS and dissolved in 20 μl of QuickExtract DNA Extraction Solution (Epicentre, QE09050). Cell lysis was performed for 6 min at 65°C. Subsequently proteinase activity was inactivated for 2 min at 95°C.

3.3.8.4. Genotyping of monoclonal INS1E cells

DNA of monoclonal cell lines was diluted 1:2 and used in PCR for the identification of wildtype and mutated *CerS2* or respectively *Pcsk1* alleles. Therefore, two different PCR reactions were set up, one for the detection of the knockout allele and one for the detection of the wildtype allele. In both PCRs, the detection of beta actin was used as internal control. Primers used and expected PCR fragment size of *CerS2*[ΔINS1E] and control cells are shown in Tab.9.

Table 9: Genotyping primers used for the detction of *CerS2* Wt and KO alleles in INS1E cells.

Primer	Direction	Sequence 5' - 3'	Expected fragments [bp]
CerS2 A (intron 1-2)	For	TGGCCTTACTTTTCCCTTCC	*CerS2* Wt: 563 *CerS2Δ*: ~301
CerS2 B (intron 2-3)	Rev	GCCCTCCTAACCCTAGATGG	
CerS2 C (exon 11)	Rev	AGCCAAGCCTCCTTTCTACC	
Actb A	For	TAGCCCTCTTTTGTGCCTTG	Control band: 802
Actb B	Rev	CAGGGGCTCCATTTAGACCT	

PCR primers and size of expected fragments for the identification of *Pcsk1*[ΔINS1E] and control cells are displayed in Tab.10.

Table 10: Genotyping primers used for the detction of *Pcsk1* Wt and KO alleles in INS1E cells.

Primer	Direction	Sequence 5' - 3'	Expected fragments [bp]
Pcsk1 A (intron 3-4)	For	GCTGGTGTAAGTGCAGAGGA	*Pcsk1* Wt: 381 *Pcsk1Δ*: ~501
Pcsk1 B (intron 3-4)	Rev	CTATTCCCAGCAGCAAGTCC	
Pcsk1 C (intron 5-6)	Rev	CATCTGAAAGGAGAAGCCAAG	
Actb A	For	TAGCCCTCTTTTGTGCCTTG	Control band: 802
Actb B	Rev	CAGGGGCTCCATTTAGACCT	

PCR reactions were set up as depicted in Tab.11.

Table 11: Pipetting scheme for genotyping of *CerS2* as well as *Pcsk1* Wt and KO alleles in INS1E cells. The volume is calculated for one reaction.

Detection of Wt allele	Detection of KO allele	Volume [µl]
Component		
2x GoTaq G2 Hotstart Green Mastermix	2x GoTaq G2 Hotstart Green Mastermix	5
Primer A (10 µM)	Primer A (10 µM)	0.5
Primer B (10 µM)	Primer C (10 µM)	0.5
Actb A (10 µM)	Actb A (10 µM)	0.5
Actb B (10 µM)	Actb B (10 µM)	0.5
Template DNA (lysate)	Template DNA (lysate)	1
ddH$_2$O	ddH$_2$O	2.5
Final volume [µl]		10

Following PCR program was used to identify control and *CerS2*[ΔINS1E] cells, as well as control and *Pcsk1*[ΔINS1E] cells.

Table 12: Genotyping PCR program for the detection of *CerS2* as well as *Pcsk1* Wt and KO alleles in INS1E cells.

Step	Temperature [°C]	Time [sec]	Cycle number
Initial denaturation	95	180	1
Denaturation	95	30	35
Annealing	58	15	
Extension	72	50	
Final Extension	72	300	1
Hold	4	∞	1

PCR products were analyzed on agarose gels as described in chapter 3.1.3.4.

3.3.8.5. Functional analysis of *CerS2*$^{\Delta INS1E}$ and *Pcsk1*$^{\Delta INS1E}$ cells

Positively identified control and *CerS2*$^{\Delta INS1E}$ clones were cultured seperately and for experiments the same numbers of cells from four different control and *CerS2*$^{\Delta INS1E}$ clones were pooled at the time of seeding into the final dish.

The generation procedure of *Pcsk1*$^{\Delta INS1E}$ cells created only one homozygous mutant clone. Therefore, a pool of three different control clones, two different heterozygous *Pcsk1* (*Pcsk1*$^{+/-}$) clones and the one *Pcsk1*$^{\Delta INS1E}$ clone were used with the same cell number in experiments to identify specificity of the used PC1 antibody.

3.4.   Molecular biology

3.4.1.   Quantification of nucleic acids

DNA and RNA concentrations were determined by measuring the absorption of samples at 260 nm and 280 nm with a Nanophotometer N60 (Implen).

3.4.2.   Generation of CRISPR/Cas9 plasmids

The pSpCas9 plasmids encodes for nearly all needed elements, which are required for sufficient CRISPR/Cas9 dependent induction of double strand breaks, except of the specific gRNA targeting sequence. Therefore, gRNA sequences have to be inserted into the plasmids. Different kinds of pSpCas9 plasmids were used in this thesis for the generation of *CerS2*$^{\Delta INS1E}$ and *Pcsk1*$^{\Delta INS1E}$ cells. *CerS2*$^{\Delta INS1E}$ and control cells were generated by puromycin selection, using the commercially available pSpCas9(BB)-2A-Puro(PX459) V2.0 vector (Addgene, 62988). To distinguish between correct inserted gRNA sequences or undigested and religated plasmid during the cloning procedure, an approximately 100 nt insert (sequence is shown in Tab.13). was integrated into the BbsI restriction site from the original pSpCas9(BB)-2A-Puro(PX459) vector.

Table 13: Inserted sequence into pSpCas9(BB)-2A-Puro(PX459) plasmid. To discriminate between undigested or religated plasmid and correctly inserted gRNA sequence during the cloning procedure an approximately 100 nt sequence was inserted into the pSpCas9(BB)-2A-Puro(PX459) plasmid. The cloning procedure was performed similar as described in the following chapters. In brief, oligonucleotides were annealed, phosphorylated and ligated into the BbsI restriction site of pSpCas9(BB)-2A-Puro(PX459).

	Direction	Sequence 5'- 3'
BbsI insert	For	GACGTCCACCGGGTCTTCGCGGCCGCGATATCGCTAGCGC GATCGCGGCGCGCCGTTTAAACGGATCCTGTACAGAATTC GAAGACCTCTCGAGGAGCT
	Rev	AGCTCCTCGAGAGGTCTTCGAATTCTGTACAGGATCCGTTT AAACGGCGCGCCGCGATCGCGCTAGCGATATCGCGGCCG CGAAGACCCGGTGGACGTC

Cloning procedure was performed similar to the process described below and the plasmid is designated as pSpCas9-2A-Puro-BbsI-insert. *Pcsk1*$^{\Delta INS1E}$ and control cells were generated with another strategy using the expression of fluorescent marker proteins for selection. Therefore, one gRNA was cloned into the commercially available pSpCas9(BB)-2A-GFP(PX458) plasmid (Addgene, 48138) and the second gRNA was cloned into a modified version of this plasmid containing mcherry instead of GFP. This plasmid is termed pSpCas9(BB)-2A-mcherry(PX458) and was kindly provided by Dr. S. Hoffmann from the Institute for Physical Biology at the Heinrich Heine University Düsseldorf, Germany.

3.4.2.1. gRNA design

gRNA sequences specifically targeting *CerS2* and *Pcsk1* were designed using the web application E-CRISP [287] or the CRISPR design tool from IDT (Alt-R® Custom Cas9 crRNA Design Tool, IDT, Coralville, Iowa, USA. Accessed 25 May, 2020. https://eu.idtdna.com/pages/tools). For the gRNA integration into the designated plasmids, overhangs were attached to the 5' end of gRNA sequences as described by the Zhang lab [288]. Tab.14 shows oligonucleotide sequences, which were ordered from Eurogentec and used for the generation of double stranded gRNA fragments.

Table 14: Designed oligonucleotides for the generation of double stranded gRNA targeting *CerS2* and *Pcsk1* in INS1E cells. Underlined sequences designate overhangs for cloning into the pSpCas9 backbone vectors.

gRNA	Target	Direction	Sequence 5´ - 3´
1	*CerS2* exon 2	For	<u>CACCG</u> TCAGCCCAGGTTAAGTTCAC
		Rev	<u>AAAC</u> GTGAACTTAACCTGGGCTGA C
2	*CerS2* exon 11	For	<u>CACCG</u> TCTTAGGATGGTTGTTATTG
		Rev	<u>AAAC</u> CAATAACAACCATCCTAAGA C
1	*Pcsk1* intron 3-4	For	<u>CACC</u> GGTATTTACAAGGTCTTGAC
		Rev	<u>AAAC</u> GTCAAGACCTTGTAAATACC
2	*Pcsk1* intron 5-6	For	<u>CACC</u> TTTACCCGAAGAGGACGTGT
		Rev	<u>AAAC</u> ACACGTCCTCTTCGGGTAAA

3.4.2.2. Annealing and phosphorylation of gRNA oligos

For the generation of double stranded gRNA fragments, complementary oligonucleotides, which contain the gRNA target site information as well as overhangs for the cloning procedure were mixed together for a phosphorylation and annealing reaction according to the following Tab.15.

Table 15: Pipetting scheme for phosphorylation and annealing of gRNA oligonucleotides. The volume is calculated for one reaction.

Component	Volume [µl]
Oligonucleotide 1 (100 µM)	1
Oligonucleotide 2 (100 µM)	1
10x T4 Ligation Buffer (Thermo Fisher Scientific)	1
ddH$_2$O	6.5
T4 PNK (NEB)	0.5
Final volume [µl]	10

Phosphorylation of oligonucleotides was performed for 30 min at 37°C on a heating block. Afterwards, the annealing reaction was performed on a heating block. Oligonucleotides were denaturated for 5 min at 95°C, followed by switching off the heating block and cooling down the samples to RT.

3.4.2.3. Digestion and dephosphorylation of pSpCas9 plasmids

The vector pSpCas9-2A-Puro-BbsI-insert, as well as pSpCas9(BB)-2A-GFP(PX458) and pSpCas9(BB)-2A-mcherry(PX458) were digested using the restriction enzyme BbsI (Thermo Fisher Scientific, FD1014). In addition, to inhibit religation of the plasmid in later performed ligation reaction, digested plasmid was dephosphorylated in the same reaction setup by Fast Alkaline Phosphatase (FastAP) (Thermo Fisher Scientific, EF0654). The reaction setup is shown in Tab.16.

Table 16: Pipetting scheme for the digestion and dephosporylation of pSpCas9 plasmids. The volume is calculated for one reaction. X represents the volume, which is required for 1 µg plasmid, while Y is the amount of ddH$_2$O to fill up the reaction to the final volume.

Component	Volume [µl]
pSpCas9 plasmid (1 µg)	X
FastDigest BbsI	1
FastAP	1
10x FastDigest Buffer	2
ddH$_2$O	Y
Final volume [µl]	20

The reaction was incubated for 30 min at 37°C and digested plasmid was purified using the Monarch PCR&DNA Cleanup Kit (NEB, T1030L).

3.4.2.4. Ligation of gRNA into the pSpCas9 vector

Double stranded gRNA was ligated into the digested pSpCas9-2A-Puro-BbsI-insert vector using the Quick Ligation Kit (NEB, M2200S) and the follwing pipetting scheme in Tab.17.

Table 17: Pipetting scheme for ligation of gRNA oligonucleotide into the backbone vector. Double stranded *CerS2* gRNA1 and *CerS2* gRNA2 were both inserted into the pSpCas9-2A-Puro-BbsI-insert vector. Double stranded *Pcsk1* gRNA1 was ligated in the pSpCas9(BB)-2A-GFP plasmid, while *Pcsk1* gRNA2 was cloned into the pSpCas9(BB)-2A-mcherry plasmid. The volume is calculated for one reaction. X represents the volume, which is required for 50 ng plasmid, while Y is the amount of ddH$_2$O to fill up the reaction to the subtotal volume.

Component	Volume [µl]
BbsI dig. pSpCas9 plasmid (50 ng)	X
Phosphorylated and annealed oligo duplex (1:100)	1
2x Quick Ligase Reaction Buffer	5
ddH$_2$O	Y
Subtotal	10
Quick ligase	1
Final volume [µl]	11

The reaction was incubated for 10 min at RT. Ligation was stopped by transferring samples onto ice.

3.4.2.5. Transformation of competent *E.coli* DH5α cells

For amplification of plasmids, 2 µl of ligation mix was pipetted to 50 µl of competent *E.coli* DH5α cells (Thermo Fisher Scientific, 18265017). After a 30 min incubation on ice, a heatshock was performed for 30 sec at 42°C. Competent cells were incubated on a horizontal shaker for 1 h at 37°C in 1 ml fresh LB medium (AppliChem, A7459,0500G) containing no antibiotics. Afterwards the cells were centrifuged at 100x g for 1 min, supernatant was discarded and resuspended cells were spread in a small volume of LB on LB plates containing 100 µg/ml ampicilin (Sigma-Aldrich, A0166). LB plates were incubated over night at 37°C.

3.4.2.6. Colony PCR

To check if gRNAs were correctly incorporated into plasmids and amplified in *E.coli* cells, a colony PCR was performed. Therefore, one colony was transferred with a pipette tip from the LB plate to 50 µl LB medium. 1 µl of this suspension was used for PCR with specific primers targeting the vector DNA. Primers are shown in Tab.18.

Table 18: Primers for the colony PCR of *E.coli* cells transfected with pSpCas9 plasmids.

Primer	Direction	Sequence 5´ - 3´
pSpCas9	For	TTTCTTGGGTAGTTTGCAGTTT
	Rev	CACGCGCTAAAAACGGACTA

PCR reaction was set up according to the follwing table.

Table 19: Mastermix composition for colony PCR. Volume is calculated for one reaction.

Component	Volume [µl]
2x GoTaq G2 Hotstart Green Mastermix	10
Primer A (10 µM)	1
Primer B (10 µM)	1
Template DNA (colony)	1
ddH$_2$O	7
Final volume	20

Reactions were run in a Thermocycler (Biometra) using the following protocol.

Table 20: Colony PCR program.

Step	Temperature [°C]	Time [sec]	Cycle number
Initial denaturation	95	480	1
Denaturation	95	15	
Annealing	58	15	35
Extension	72	30	
Final Extension	72	300	1
Hold	4	∞	1

PCR products were analyzed on agarose gels as described in chapter 3.1.3.4. *CerS2* gRNA was inserted in the pSpCas9-2A-BbsI-insert plasmid. Therefore, it could be distuinguished between colonies that have taken up undigested plasmid or ligated plasmid containing the gRNA. Due to the cut generated by BbsI, ligation of the gRNA is only possible in the correct direction. Colonies with the correct inserted plasmid generate a PCR product size of approximately 275 nt, while undigested plasmids would generate a PCR fragment of approximately 375 nt. *Pcsk1* gRNA was inserted in pSpCas9(BB)-2A-GFP(PX458) or pSpCas9(BB)-2A-mcherry(PX458), which were not modified by additional insertion of a longer fragment between BbsI cutting sites. Therefore, undigested and ligated plasmid had the same PCR product size of approximately 275 nt. Minipreps of three different colonies of each gRNA construct were inoculated in 3 ml LB medium containing 100 µg/ml ampicillin over night in a bacterial shaker (Thermo Fisher Scientific MaxQ™ 4450) at 200 rpm and 37°C.

3.4.2.7. Extraction of plasmid DNA

Plasmid DNA was isolated from Minipreps using the NucleoSpin Plasmid Miniprep Kit (Macherey-Nagel) according to the manufacturer's protocol. Afterwards, DNA concentrations were measured on a Nanophotometer (Implen) and were send to GATC for Sanger sequencing. Plasmid DNA was checked for correct sequence using A Plasmid Editor (ApE, V2.0.55; University of Utah; Salt Lake City, https://jorgensen.biology.utah.edu/wayned/ape/).

3.4.3. RNA isolation, cDNA synthesis and qPCR

INS1E cells and mouse islets were washed once with PBS and RNA was extracted using Trizol (Peqlab) following the manufacturer's protocol. 200-1000 ng of RNA was transcribed into cDNA using the High-Capacity Reverse Transcription Kit (Thermo Fisher Scientific, 4368813). For the detection of gene expression levels, a quantitative realtime PCR was performed. Therefore, PerfeCTa SYBR Green Fastmix low ROX (Quantabio, 95073-05K) was mixed with cDNA, which was prediluted 1:10 in ddH$_2$O and specific primers as shown in Tab.21.

Table 21: Pipetting scheme for qPCR plate.

Supplement	Volume [µl]
cDNA	4
Primer mix (each 4 µM)	1
SYBR Green Fastmix low ROX (Quantabio)	5
Final volume [µl]	10

Specific primers for mouse and rat target genes are depicted Tab.22.

Table 22: Specific forward and reverse primers for qPCR analysis of gene expression levels.

Gene	Species	Direction	Sequence 5' - 3'
36b4	Rat	For	CGTGATGCCCAGGGAAGACA
		Rev	CCACATTGTCTGCTCCCACA
	Mouse	For	GCCGTGATGCCCAGGGAAGACA
		Rev	CATCTGCTTGGAGCCCACGTTG
Gusb	Rat	For	GCCAATGAGCCTGTCTCTTC
		Rev	TTGCTCACAAAGGTCACAGG
	Mouse	For	GCATCAGAAGCCGATTATCC
		Rev	CAGCCTTCTGGTACTCCTCA
CerS1	Rat	For	TCCTCCTGGTCATGAACATCT
		Rev	GCGCTTCCAGACTGTCGTAT
CerS2	Rat	For	CTATGCCAAAGCCTCAGACC
		Rev	GCAGTCGGGTTTTCTCCTTA
	Mouse	For	GCTAGAAGTGGGAAACGGAGT
		Rev	ACAGGCAGCCATAGTCGTTC

Gene	Species	Direction	Sequence 5' - 3'
CerS4	Mouse	For	ACACGCGCCTCATATTCTTC
		Rev	TCTGTAGCATCACCAAGAGCA
CerS5	Rat	For	TTTTGTATCTTCTGCTACGGAGTC
		Rev	CTGATATGGATAGTTGTACCAGCA
	Mouse	For	AACCCAATGACACCCTTGAG
		Rev	AACCAGCATTGGATTTTTCG
CerS6	Rat	For	CATCCTGGAGCTGTCGTTTT
		Rev	GAAAATGGTTGCAAGGTGGT
	Mouse	For	GTATTTAGCTACGGAGTCCGGT
		Rev	GGATGTAATAGTAGTGAAGGTCAGC
Ins1	Rat	For	GCAAGCAGGTCATTGTTCCA
		Rev	GGTGCTGTTTGACAAAAGCC
	Mouse	For	AGACCATCAGCAAGCAGGTC
		Rev	CTCCCAGAGGGCAAGCAG
Ins2	Rat	For	CGAAGTGGAGGACCCACA
		Rev	CCAGTGCCAAGGTCTGAAG
	Mouse	For	GGAGCGTGGCTTCTTCTACA
		Rev	CAGTGCCAAGGTCTGAAGGT
Pdx1	Rat	For	CAGCCGCGTTCATCTCCCTT
		Rev	TTCTCCTCCGGTTCTGCTGC
	Mouse	For	CCTTTCCCGTGGATGAAAT
		Rev	TGTAGGCAGTACGGGTCCTC
Nkx6.1	Rat	For	TCAGGTCAAGGTCTGGTTCC
		Rev	TCAGTCTCCGAGTCCTGCTT
	Mouse	For	TCAGGTCAAGGTCTGGTTCC
		Rev	CGATTTGTGCTTTTTCAGCA
Slc2a1	Rat	For	CCCCCAGAAGGTAATTGAGG
		Rev	CCAGAGTGTGGTGAGTGTGG
	Mouse	For	CCCCAGAAGGTTATTGAGGA
		Rev	AGAGAGACCAAAGCGTGGTG
Slc2a2	Rat	For	AATGGTCGCCTCGTTCTTTG
		Rev	CATCAAGAGGGCTCCAGTCA
	Mouse	For	TCTGTGTCCAGCTTTGCAGT
		Rev	GAGGGCTCCAGTCAATGAGA
Foxo1	Rat	For	TTCAAGGATAAGGGCGACAG
		Rev	CCAAGAACTTTTCCCAGTTCC
	Mouse	For	GTACGCCGACCTCATCACCA
		Rev	TGCTGTCGCCCTTATCCTTG
Grp78	Rat	For	AGCCCACCGTAACAATCAAG
		Rev	CAGGAGGGATTCCAGTCAGA
	Mouse	For	AAGGAGACTGCTGAGGCGTA
		Rev	CCAGCAATAGTGCCAGCAT
Chop	Rat	For	CGTCGATCATACCATGTTGAA
		Rev	AAAGGCGAAAGGCAGAGACT
	Mouse	For	TTGAGCCTAACACGTCGATT
		Rev	TCAGGTGTGGTGGTGTATGAA

Gene	Species	Direction	Sequence 5' - 3'
Pdia3	Rat	For	GGGCTCATGCTAGTCGAGTT
		Rev	TGGTTGCTGCAGCTTCATAC
	Mouse	For	TATGAAGCTGCAGCAACCAG
		Rev	GGTAGCCACTGACCCCATAC
Grp94	Rat	For	GCTGACCCAAGAGGAAACAC
		Rev	TGGGAAAGTTGATGAACTGAGA
	Mouse	For	AATTGCTGACCCAAGAGGAA
		Rev	TCCAATTCAAGGTAATCAGATGC
Hsp60	Rat	For	GTAAAATTTGGTGCGGATGC
		Rev	GGGACTTCCCCAACTCTGTT
	Mouse	For	CTGTTACAATGGGGCCAAAG
		Rev	AACAGTGACCCCATCTTTTGTT
Erp29	Rat	For	TGCTCCTCTCTGCTCCTCAT
		Rev	TGTCGAACTTCACCAAGACG
	Mouse	For	CCCTTCCCTTGGACACAGT
		Rev	CATAGGGGTACTGGGTGTCG
Hsp70	Rat	For	AGAGCTGCTATGTCGCTGTG
		Rev	GCTGCTCCAACTGAACGATT
	Mouse	For	TGGTGCTGACGAAGATGAAG
		Rev	AGGTCGAAGATGAGCACGTT
Grp170	Rat	For	TGACCTACCAAACGGTGAAG
		Rev	GAGCTTAGCCAGGTGCTCTC
	Mouse	For	GACTAAGGAGGCTGGGATGC
		Rev	TAGCCAGGTGTTCTCGAAGC
Calr	Rat	For	CCCCGATGCGAATATCTATG
		Rev	GCATAGGCCTCATCATTGGT
	Mouse	For	TCCCCCGATGCAAATATCTA
		Rev	TCAAAGATTGTCCCGGACTT
Pcsk1	Rat	For	GAGATACATGGAGGGCCAGA
		Rev	CGGGATCTTCGAGGATGATT
	Mouse	For	TCAAACACAAAAGCCATCCTC
		Rev	TCCAATGCTGAGTCTTTTTGAA
Anxa6	Rat	For	TTTGATGCAAATCAGGATGC
		Rev	AGATCTCCTGCCTCTGCTTG
	Mouse	For	GAGGCTCTGTCCACGACTTC
		Rev	CTGGCAGATCTCCTGCCTCT
Tpst1	Rat	For	ACGCCAATCCCCCTAACTAC
		Rev	TCAGGTAGCTGAAACTCTCCTTT
	Mouse	For	CCATACGCCAATCCTCCTAA
		Rev	TCAGGGAGCTGAAATTCTCC
Tpst2	Rat	For	GCAAATCCACCCAACTATGG
		Rev	CAGATTGGCTGGCGTTTTAT
	Mouse	For	CTTGGCTATGACCCGTATGC
		Rev	CAGATTGGCTGGCGTTTTAT

qPCR was performed on a QuantStudio 7 Flex System (Thermo Fisher Scientific) using the following program:

Table 23: qPCR program for the detection of mRNA expression levels.

Step	Temperature [°C]	Time [sec]	Cycle number
Thermal activation	95	125	1
Denaturation	95	10	40
Annealing	60	30	
Extension	95	15	
Dissociation	60	60	1
Melting curve	95	15	1

Relative expression levels of genes were normalized to the housekeeping gene *36b4* and/or *Gusb*.

3.5. Biochemistry

3.5.1. Protein expression analysis

3.5.1.1. Protein extraction of INS1E cells

To harvest the proteins from INS1E cells, cells and supernatant were collected after trypsinization in a 15 ml falcon tube and centrifuged for 5 min at 336x g at 4°C. The cell pellets were washed once with PBS, centrifuged and cell pellets were resuspended in 30 µl Bioplex Cell Lysis Buffer (Bio-Rad, 171304011) containing one tablet of cOmplete Protease Inhibitor Cocktail. To allow sufficient cell lysis, tubes were shaken subsequently on a cell disruptor for 10 min at 2,500 rpm and 4°C. Samples were stored afterwards at -80°C or directly used for determination of protein concentrations.

3.5.1.2. Protein extraction of mouse islets

An equal amount of mouse islets (50-100) with similar size were picked from wildtype and knockout mice and washed once with PBS containing 0.1% BSA in a 1.5 ml reagent tube. Supernatant was discarded and islets were resuspended in 30 µl of Bioplex Cell Lysis Buffer. For sufficient cell lysis samples were shaken on a cell disruptor for 10 min at 10,000 rpm and 4°C followed by sonication for 6 cycles (30 sec sonication, 30 sec on ice) in an ultrasonic cleaning bath (Elma, Elmasonic P 30 H, 1013737) at 4°C. Islet samples were subsequently boiled for 5 min at 95°C in Laemmli Sample Buffer (Bio-Rad, 1610747) containing 200 µM DTT (AppliChem, A2948).

3.5.1.3. Bicinchoninic acid assay

For the determination of protein concentrations in samples, a bicinchoninic acid (BCA) assay was performed. To generate a standard curve, a BSA standard (Sigma Aldrich, P0914) was diluted in the appropriate lysis buffer with following concentrations: 1000 µg/µl, 500 µg/µl, 250 µg/µl, 125 µg/µl, 62.5 µg/µl, 31.25 µg/µl, 15.625 µg/µl and 0 µg/µl. INS1E lysates from 6 well plates were diluted 1:20, while lysates from 24 well plates were diluted 1:2.5 in respective lysis buffer and 20 µl of each sample, as well as the standard was pipetted in duplicates on a clear 96 well plate. In the next step solution A and B of the BCA Kit (Sigma-Aldrich, BCA1-1KT) were mixed in a 1:50 ratio and 200 µl of this solution was pipetted on samples. After 30 min of incubation at 37°C, absorbance was measured at 562 nm on GloMax Discover Microplate Reader (Promega). Protein concentrations were calculated by the standard curve. Samples of the same experiment were adjusted to equal amounts of protein in Laemmli Sample Buffer containing 200 µM DTT and boiled for 5 min at 95°C on a heating block.

3.5.1.4. SDS-PAGE, western blotting and immunoblot imaging

For the detection of proteins, 3-20 µg of protein and 5 µl of PAGERuler Prestained Protein Ladder (Thermo Fisher Scientific, 26617) was loaded on 4-15% Mini-PROTEAN TGX Stain-Free Precast gels (Bio-Rad, 4568096). Gels were run for approximately 60-90 min at 120 V in Mini-PROTEAN Tetra Vertical Electrophoresis Cell (Bio-Rad) containing 1x Tris/glycine/SDS Running buffer (Bio-Rad, 1610772). Stainfree was activated in gels using Chemidoc XRS imaging system (Bio-Rad). Subsequently proteins were transferred to Immun-Blot Low Fluorescence PVDF membranes (Bio-Rad, 1704274) using the Transblot Turbo Transfer System (Bio-Rad, 1704150) with the mixed molecular weight program (1.3 A, up to 25 V for 7 min). Stainfree was detected on membranes in the Chemidoc XRS imaging system for subseequent protein normalization. Membranes were cut at the level of relevant marker bands and blocked for 1 h at RT in 5% BSA or 5% milk in TBST (for 1 l TBST dilute 2.4 g Tris base, 8.8 g NaCl and 1 ml Tween-20 in ddH$_2$O) depending on the dilution buffer of the primary antibody (see Tab. 24). Afterwards membranes were incubated over night at 4°C with primary antibody.

Table 24: Primary antibodies used on immunoblot.

Antibody	Catalogue number	Supplier	Dilution
CERS2	HPA027262	Sigma Aldrich	1:1,000 in BSA
PC1	11914	Cell Signaling	1:1,000 in milk
PC2	14013	Cell Signaling	1:1,000 in BSA
ANXA6	ab199422	Abcam	1:1,000 in milk
CGA	ab254322	Abcam	1:1,000 in milk
RCAS1	12290	Cell Signaling	1:1,000 in milk
PDI	ab2792	Abcam	1:1,000 in BSA

On the next day, membranes were washed 3 times with TBST followed by incubation for 1 h at RT with the respective secondary antibodies (Tab. 25).

Table 25: Secondary antibodies used on immunoblot.

Antibody	Catalogue number	Supplier	Dilution
Anti-mouse HRP conjugate IgG (H+L)	401253	Calbiochem	1:1,000
Anti-rabbit HRP conjugate IgG (H+L)	401393	Calbiochem	1:1,000

After washing the membranes three times with TBST, membranes were developed on a Chemidoc XRS imaging system (BioRad) using Clarity Western ECL substrate (BioRad, 1705061).

3.5.2. Enzyme-linked immunosorbent assay

3.5.2.1. Insulin ELISA

Insulin was measured using a commercial Rat Insulin ELISA Kit (CrystalChem, 90062) according to the manufacturer's instructions. Dilutions are shown in Tab.26.

Table 26: Dilutions of samples for insulin ELISA. All dilutions were made in provided Sample Diluent (G).

Origin	Condition	Dilution
Mouse islets	Supernatant low glucose	-
	Supernatant high glucose	1:5
	Lysis	1:400
Mouse plasma	-	-
Mouse pancreata	-	1:2,000
INS1E	Lysis	1:20

For pancreatic samples, total insulin content was normalized to total protein concentration as well as pancreas weight. Secreted insulin and content was normalized to total protein content in INS1E cells.

3.5.2.2. Proinsulin ELISA

Proinsulin was measured using a commercial Rat/Mouse Proinsulin ELISA (Mercodia, 10-1232-01) according to the manufacturer's protocol. As recommended, lysates from mouse islets were diluted 1:500 in Diabetes Sample Buffer (Mercodia, 10-1195-01).

3.5.2.3. Glucagon ELISA

Glucagon was measured using a commercial Glucagon ELISA (Mercodia, 10-1281-01) according to the manufacturer's protocol. Dilutions are shown in Tab.27.

Table 27: Dilutions of samples for glucagon ELISA. Appropriate dilutions were previous tested using different buffers and the Calibrator 0 standard. Dilution of mouse islets were made with PBS, while lysates from pancreata were diluted in provided Calibrator 0.

Origin	Condition	Dilution
Mouse islets	Lysis	1:200
Mouse pancreata	-	1:2,000

For pancreatic samples, total glucagon content was normalized to total protein concentration as well as pancreas weight.

3.6. Untargeted lipidomics of pancreatic mouse islets and INS1E cells

To analyze the sphingolipidome in db/db islets, $CerS2^{\Delta BKO}$ islets, as well as in $CerS2^{\Delta INS1E}$ cells and their respective controls, untargeted lipidomics were performed in collaboration with Prof. Thorsten Hornemann and Gergely Karsai from the Institute of Clinical Chemistry at the University Hospital in Zurich. Therefore, 100 islets from four control and four $CerS2^{\Delta BKO}$ animals or respectively db/db animals were pooled, washed with PBS, centrifuged for 5 min at 400x g and supernatant was completely discarded. Islet pellets were stored at -80°C and send to the University Hospital Zurich. 6,000,000 control and $CerS2^{\Delta INS1E}$ cells were seeded on a p10 dish. On the next day, cells were washed with PBS, scraped off in 1 ml PBS and transferred in a reaction tube. After centrifugation for 5 min at 400x g, supernatant was completely discarded and pellet weights were determined for subsequent normalization. Samples were stored at -80°C and were send to the Institute for Clinical Chemistry from the University Hospital in Zurich for analysis.

Lipid extraction was performed as described previously [289]. Shortly, 0.5-5 million cells or 100 islets were suspended in 20 µl PBS, 1 ml of a mixture of methanol: MTBE: chloroform (MMC) 4:3:3 (v/v/v) was added. The MMC mix was fortified with 100 mg/L Butylated hydroxytoluene, 100 pmol/ml of the internal standards (Avanti Polar Lipids): d7-sphinganine (d18:0), d7-sphingosine (d18:1), dihydroceramide (d18:0;12:0), 1-deoxydihydroceramide

(m18:0/12:0), ceramide (d18:1/12:0), 1-deoxyceramide (m18:1/12:0), glucosylceramide (d18:1/8:0), sphingomyelin (18:1/12:0) and 50 pmol/ml d7-sphingosine-1-phosphate, and 2.5 µl/ml of the SPLASH® LIPIDOMIX® Mass Spec Standard (Avanti Polar Lipids). After brief vortexing, the samples were continuously mixed (1,400 rpm) in a thermomixer (Eppendorf) for 20 min at 37°C. Protein precipitation was obtained after centrifugation for 5 min, 16,000x g, 25°C. The single-phase supernatant was collected, dried under liquid nitrogen and stored at -20°C until analysis. Before analysis, the dried lipids were dissolved (40 min at 25°C) in 80 µl MetOH.

Liquid chromatography was done according to [290] with some modifications. The lipids were separated using a C30 Accucore LC column (Thermo Fisher Scientific, 150 mm * 2.1 mm * 2.6 µm) using the following mobile phases; A) Acetonitrile:Water (6:4) with 10 mM ammonium acetate and 0.1% formic acid, B) Isopropanol: Acetonitrile (9:1) with 10 mM ammonium acetate and 0.1% formic acid at a flow rate of 0.26 ml/min. The following gradient was applied:

1. 0.0-0.5 min (isocratic 70% A, 30% B and 10% C),
2. 0.5-2.0 min (ramp 70-57% A, 30-43% B),
3. 2.0-2.10 min (ramp 57-45% A, 43-55% B),
4. 2.1-12.0 min (ramp 45-35% A, 55-65% B),
5. 12.0-18.0 min (ramp 35-15% A, 65-85% B),
6. 18.0-20.0 min (ramp 15-0% A, 85-100% B),
7. 20.0-25.0 min (isocratic 0% A, 100% B),
8. 25.0-25.5 min (ramp 0-70% A, 100-30% B),
9. 25.5-29.5 min (isocratic 70% A, 30% B).

The liquid chromatography was coupled to a hybrid quadrupole-orbitrap mass spectrometer Q-Exactive (Thermo Fisher Scientific, Reinach, BL, Switzerland), samples were analyzed in positive and negative mode using a heated electrospray ionization (HESI) interface. The following parameters were used: spray voltage 3.5 kV, vaporizer temperature of 300°C, sheath gas pressure 20 AU, aux gas 8 AU and capillary temperature of 320°C. The detector was set to an MS2 method using a data dependent acquisition with top10 approach with stepped collision energy between 25 and 30. A full scan from 220 to 3,000 m/z at a resolution of 70,000 was used, while the resolution for MS2 was 17,500. A dynamic exclusion filter was applied which will excludes fragmentation of the same ions for 20 sec.

Identification criteria were:

1. Resolution with an accuracy of 5 ppm from the predicted mass at a resolving power of 140,000 at 200 m/z.
2. Isotopic pattern fitting to expected isotopic distribution.
3. Matching retention time to synthetic standards (if available) and to the in-house database.
4. Fragmentation pattern matching the in-house validated fragmentation database

Quantification of sphingolipids were achieved by comparison to the respective internal standard using a one point calibration. Pooled samples in four concentration were used as quality controls. Mass spectrometric data analysis was performed in Tracefinder software 4.1 (Thermo Fisher Scientific) for peak picking, annotation and matching to the in-house fragmentation database.

3.7.   Proteomics

3.7.1. Sample preparation

For investigation of the underlying mechanism of insufficient insulin availability in *CerS2*[ΔBKO] islets, the proteome was analyzed in *CerS2*[ΔINS1E] cells. Therefore, 6,000,000 control and *CerS2*[ΔINS1E] cells were seeded on a p10 dish and collected one day later in parallele to the lipidomic samples (see chapter 3.6.1). Samples were stored at -80°C and pellets were delivered to the Proteome Analysis Unit from the German Diabetes Center in Düsseldorf, Germany.

3.7.2. Cell lysis

Dry cell pellets were lyzed in denaturing SDS buffer (4% SDS, 100 mM Tris pH8.0, 100 mM DTT, Complete™ and phosphatase inhibitors 2&3 (Sigma Aldrich); 1:5 (w/v)), by 10 strokes through an insulin syringe (needle 26 gauge) followed by sonification (3 times 70%-Pulse 0.09sec_10sec). After centrifugation at 75.000x g for 30 min at 4°C, supernatants were transferred to fresh reaction tubes and protein concentration was determined by direct photometric measurements (nanodrop, Thermo Fisher Scientific).

3.7.3. Protease digest

To purify and concentrate the sample, a protein equivalent of 10 µg was loaded onto a short SDS-PAGE (10% polyacrylamide, 0.5 cm separation distance as previously described [291]). Subsequently, Coomassie blue stained protein bands were excised and subjected to in-gel protease digestion. Therefore, gel slices were alternated washed twice with 25 mM ammonium bicarbonate and 25 mM ammonium bicarbonate and 50% acetonitrile (v/v). Protein reduction

was performed in 65 mM DTT for 15min, shaking at 350 rpm and 50°C. Subsequent alkylation was done in 216 mM Iodacetamide for 15 min in the dark at RT. After washing (25 mM ammonium bicarbonate and 25 mM ammonium bicarbonate and 50% ACN (v/v)), gel slices were shrinked in 100% Acetonitrile. Protein digestion was performed with 400 ng LysC/Trypsin mix (Promega) in 25 mM ammonium bicarbonate and 2% ACN (v/v) over night at 37°C. Resulting peptides were eluted with 1% TFA (v/v) followed by a second elution with 0.1% TFA/90% Acetonitrile (v/v). Peptides were lyophilized and subjected to MS analysis.

3.7.4. Mass spectrometry

Lyophilized peptides were reconstituted in 1% TFA (v/v) supplemented with iRT peptides (Biognosys) and separated by liquid chromatography (Ultimate 3000, Thermo Fisher Scientific) using an EASYspray ion source equipped to an Orbitrap Fusion Lumos mass spectrometer (Thermo Fisher Scientific). Peptides were trapped and desalted on an Acclaim PepMap C18-LC-column (ID: 75 µm, 2 cm length; Thermo Fisher Scientific) and subsequently separated via EASYspray C18 column (ES803; ID: 50 cm x 75 µm inner diameter; Thermo Fisher Scientific) using a 100 min linear gradient from buffer A (0.1% formic acid) to 4-34% buffer B (80% Acetonitrile, 0.1% formic acid) at a flow rate of 300 nl/min followed by a 20 min linear gradient increasing buffer B to 50% and a 1min linear gradient increasing buffer B to 90%. Column temperature was set to 40°C.

MS data for spectral libraries were acquired in DDA (data dependent acquisition) mode. MS spectra were obtained at 120,000 resolution (3 s cycle time), m/z range of 350-1600 and a target value of 4e5 ions, with maximum injection time of 50 ms. For fragmentation precursor selection filter were set to charge state between 2 and 7, dynamic exclusion of 30 s and intensity threshold of 2.5e4. Fragmentation of precursors was done with an isolation window (m/z) 1.2, HCD energy of 32%, Orbitrap resolution of 15,000 and an ion target value of 1.0e5 with maximum injection time of 50 ms.

MS data for label free quantification were acquired in a DIA (data independent acquisition) mode. Full scan MS spectra were obtained at 120,000 resolution, m/z range of 400-1200, and an AGC target value of 5e5 and maximum injection time of 50 ms. Fragmentation was performed with HCD energy of 32% in 28 windows covering the range from 400-1200 (m/z) with a segment width of 29.6 (m/z), Orbitrap resolution of 30,000, AGC target of 1.0e6, scan range from 200-2000 (m/z) and maximal injection time was 60 ms.

3.7.5. Analysis of mass spectrometry data

To calculate protein quantities, single shot DIA runs were processed in Spectronaut Pulsar (Version 13.12.200217, Biognosys) based on MS2 level using factory settings. Spectra were

matched against a project specific spectral library composed out of 44 DDA runs from analogous sample material.

Spectral library was generated in Spectronaut Pulsar (Version 12.0.20491.5) from a Proteome Discoverer result file (Version 2.2.0.388; Thermo Fisher Scientific). Used HTSequest search settings were: enzyme trypsin (full), max missed cleavages 2, peptide length 6-144 modifications: carbamidomethyl (C) (fixed); oxidation (M), acetyl (protein N-term) (dynamic) and FASTA files (Rattus norvegicus TaxID 10116 SwissProt TaxID=10116 (with subtaxonomies, v2017-10-25) and TrEMBL (v2017-10-25)).

For label free quantitative analysis by Spectronaut, identification was done with a q-value cutoff of 0.01, matching against the project specific spectral library (95.235 Precursors) and utilizing FASTA file (reviewed SwissProt and TrEMBL database, rat TaxID 10116 canonical and isoforms, both downloaded from UniProt 07-2018) for Pulsar search. Quantitation was done on MS2 level, area type and global cross run normalization were performed on median. Student's t-test was performed on precursor ion level and protein candidates for regulation were filtered by average log2 ratio greater than or equal to 0.5 and q-value less than or equal to 0.05.

3.8. Electron microscopic analysis of mouse islets

Control and $CerS2^{\Delta BKO}$ islets were isolated as described in chapter 3.2.1. On the next day 50 islets were hand-picked, washed thoroughly 3 times with PBS to remove BSA from media and fixed for 1 h at RT by immersion in 2.5% glutaraldehyde in KRH buffer at pH 7.4, postfixed in 2% osmium tetroxide in 0.19 M sodium cacodylate buffer, pH 7.4, for 30 min, and subsequently stained with 2% uranyl acetate in maleate buffer, pH 4.7. The specimens were dehydrated in graded ethanols and embedded in epoxy resin [292]. Ultrathin sections were picked up onto Formvarcarbon-coated grids, stained with lead citrate, and viewed in a transmission electron microscope (TEM 910; Zeiss Elektronenmikroskopie, Oberkochen, Germany). Morphometric evaluation of insulin containing vesicles in beta cells was manually done using Fiji processing program (ImageJ 1.51w). For quantification, the number of granules was normalized to the beta cell area.

3.9. Computational analysis

3.9.1. Densitometrical analysis

Intensity of western blot bands was measured using Image lab 6.0 software (Bio-Rad). Each band was normalized to total protein amount of the sample detected by stainfree. Stainfree gels contain a proprietary trihalo compound that covalently binds to tryptophan residues in proteins after exposure to UV light and allows for the detection of proteins on the membrane.

3.9.2. Statistical methods

Data was analyzed by unpaired two-tailed t-test, paired two-tailed t-test, multiple t-test or two-way ANOVA using GraphPad Prism (Version 7.05) as described for each figure in the result chapter.

3.10. Personal contributions

The following packages describe the personal contribution for the different methods used in this thesis.

- K. Grieß designed and performed most of the experiments. K. Grieß was supervised by Dr. B.-F. Belgardt (Group leader, Research Group Beta Cell Defects) as well as Prof. Dr. Eckhard Lammert (Institute Director, Institute for Vascular and Islet Cell Biology).

- K. Grieß and C. Schlegel (Research Group Beta Cell Defects) build up the lab and established the majority of the fundamental methods in the Research Group Beta Cell Defects at the German Diabetes Center in Düsseldorf, Germany.

- K. Grieß established the generation of various knockout cell lines, including $CerS2^{\Delta INS1E}$ cells, using the CRISPR/Cas9 system.

- Dr. M. Rieck (Research Group Beta Cell Defects) generated control and $Pcsk1^{\Delta INS1E}$ cells and performed immunoblot experiments. K. Grieß designed gRNA sequences and genotyping primers for the generation and identification of $Pcsk1^{\Delta INS1E}$ cells. FACS sorting was performed in collaboration with Prof. Dr. D. Häussinger and Dr. M. Wammers from the Department of Gastroenterology, Hepatology and Infectious Diseases at the University Hospital in Düsseldorf, Germany.

- K. Grieß, C. Schlegel and S. Cames (Oskar-Minkowski Laboratory) performed *in vivo* experiments with control and $CerS2^{\Delta BKO}$ mice. K. Grieß planned the experiments and supervised C. Schlegel and S. Cames.

- J. Kuboth (Research Group Beta Cell Defects) extracted pancreata of female control and $CerS2^{\Delta BKO}$ mice and conducted the insulin ELISA for the determination of pancreatic insulin content. K. Grieß supervised J. Kuboth and performed the analysis.

- C. Schlegel and Dr. B.-F. Belgardt conducted the perfusion of islets from control and db/db mice. Dr. M. Rieck and K. Grieß isolated islets from control and db/db mice and prepared samples for untargeted lipidomics.

- C. Schlegel and Dr. B.-F. Belgardt conducted the perfusion of islets from $CerS2^{\Delta BKO}$ mice and their respective controls. Dr. M. Rieck and K. Grieß performed CHX experiments with islets from control and $CerS2^{\Delta BKO}$ mice.

- J. Jablonskyj (Research Group Beta Cell Defects) performed the qPCR of $CerS2^{\Delta INS1E}$ cells on ER stress marker during her Master thesis and was supervised by K. Grieß.

- J. Kuboth and C. Schlegel were supervised by K. Grieß and performed the *Tpst1* and *Tpst2* double knockdown experiments.

- Untargeted lipidomics of $CerS2^{\Delta INS1E}$ cells, $CerS2^{\Delta BKO}$ islets, as well as db/db islets and their controls were performed in collaboration with Prof. T. Hornemann and Dr. G. Karsai from the Institute of Clinical Chemistry at the University Hospital in Zurich, Switzerland. Dr. G. Karsai performed the MS measurement, analyzed the raw data and wrote the method part in chapter 3.6 of this thesis. Statistical analysis of the lipidomic data was performed in collaboration with Prof. Dr. O. Kuß from the Institute for Biometrics and Epidemiology at the German Diabetes Center in Düsseldorf, Germany.

- Proteomics were performed in collaboration with Dr. S. Hartwig, Dr. S. Lehr and Prof. Dr. H. Al-Hasani from the Proteome Analysis Unit of the Institute for Clinical Biochemistry and Pathobiochemistry at the German Diabetes Center in Düsseldorf, Germany. S.Hartwig planned and performed proteomics and wrote the method part in chapter 3.7.2 - 3.7.5 of this thesis.

- Electron microscopic analysis of control and $CerS2^{\Delta BKO}$ islets was executed in collaboration with the Dr. J. Weiß, K. Jeruschke and Prof. Dr. H. Al-Hasani from the Cellular Morphology Unit of the Institute for Clinical Biochemistry and Pathobiochemistry at the German Diabetes Center in Düsseldorf, Germany. K. Grieß analyzed and quantified images. J. Weiß wrote the method part in chapter 3.8 of this thesis.

- K. Grieß created the illustrations in this work, if not denoted otherwise. Chemical structures were created with BKchem program (Version 0.13.0).

4.   Results

4.1.   Long and very long chain ceramides accumulate in islets of db/db mice

To identify sphingolipid species in pancreatic islets that are regulated in beta cell dysfunction and development of T2D, 6 and 12 week old male BKS.Cg-*Dock7*[m] +/+ *Lepr*[db/db] (further denoted as db/db) and BKS.Cg-*Dock7*[m] +/+ *Lepr*[db]/J (further denoted as control) mice were used in this study. db/db mice carry a mutation in the gene encoding the leptin receptor and mice with a homozygous deficiency on the BKS background exhibit features of T2D, like hyperphagia, extreme obesity, chronic hyperglycemia and relative hypoinsulinemia [282]. db/db mice at an age of 6 weeks had increased body weights, but exhibited no significantly altered blood glucose levels and reflected a prediabetic state, while mice at an age of 12 weeks were morbidly obese with highly elevated body weight and blood glucose levels and reflected the diabetic state (S.Fig.1A and S.Fig1B).

Untargeted lipidomics of control and db/db islets was performed in collaboration with Prof. Dr. Thorsten Hornemann and and Dr. Gergely Karsai from the Institute of Clinical Chemistry in Zurich, Switzerland [289,293]. Statistical analyses of lipidomic data was conducted without correction for multiple testing in agreement with Prof. Dr. Oliver Kuß from the Institute for Biometrics and Epidemiology at the German Diabetes Center in Düsseldorf and is in line with several published studies [187,196]. Untargeted lipidomics revealed that long chain C16:0 (~135%), C18:0 (~90%) and C20:0 (6 weeks: ~110%; 12 weeks: ~140%) ceramides, as well as very long chain C22:0 (6 weeks: ~150%; 12 weeks: ~110%), C24:0 (6 weeks: ~190%; 12 weeks: ~135%) and C24:1 (6 weeks: ~150%) ceramide species were significantly elevated in islets of db/db mice compared to heterozygous controls (Fig.7A). Thus, total amounts of all ceramide species were increased about 100-150% in islets of 6 and 12 week old db/db mice (Fig.7B).

As ceramide serves as precursor for the generation of more complex sphingolipids, we further investigated sphingomyelins and hexosylceramides, which are directly generated from ceramide, in islets of control and db/db mice. In this thesis, the two simplest glycosphingolipids, galactosylceramides and glucosylceramides are designated as hexosylceramides. As observed for ceramides, C16:0 sphingomyelin and hexosylceramide species were increased in islets from 6 and 12 week old db/db mice compared to control (6 weeks: ~50-60%, 12 weeks: ~35-40%) (Fig.7D and Fig.7G). In contrast, C24:1 sphingomyelins and hexosylceramides were decreased about 50% in islets of 12 week old db/db mice (Fig.7D and Fig.7G). Due to elevated long chain C16:0 species, but decreased very long chain C24:1 species in islets of db/db mice at an age of 12 weeks, total amounts of sphingomyelins and hexosylceramides were equal in islets of db/db mice and controls (Fig.7E and Fig.7H). This suggests that an imbalance

between long and very long chain sphingolipids might contribute to beta cell failure upon the development of diabetes.

To determine if previously described plasma ceramide ratios (C16:0/24:0, C18:0/C24:0, C24:1/C24:0 and C18:0/C16:0) that are reported to positively correlate with increased cardiovascular and other risks, can also be used as marker for beta cell dysfunction in islets, ratios were calculated for ceramides, sphingomyelins and hexosylceramides. However, previously described ratios were not increased, but sometimes even decreased in islets of prediabetic and diabetic mice (S.Fig.2). Due to specifically decreased C24:1 sphingolipid species, ratios of long chain C16:0 to very long chain C24:1 sphingolipid species were additionally calculated in islets of control and db/db mice. The ratio of C16:0/C24:1 ceramides, sphingomyelins as well as hexosylceramides was increased in islets of 12 week old diabetic db/db mice compared to controls (Fig.7C, Fig.7F and Fig.7I). Consequently, this might be an indicator for islet beta cell dysfunction.

To visualize all differentially expressed sphingolipid species in islets of 12 week old diabetic db/db mice compared to controls, the log2 fold change (log2 FC) was calculated for all measured sphingolipids and plotted against their -log10 p-values in a volcano plot. Importantly, very long chain C24:1 sphingolipids are mainly downregulated, while predominantly ceramides with different acyl chain lengths were upregulated in islets of 12 week old db/db mice (Fig.7J). In addition, many of those upregulated species had incorporated the sphingoid base sphingadiene (18:2) as backbone, which comprises two double bonds and results in a bent structure, which might influence membrane structure and lipid microdomain formation [294]. All differentially expressed sphingolipids of the volcano plot in db/db islets of 12 week old mice are displayed in S.Tab.1.

These changes in sphingolipid species led to an increase in total sphingolipids about 40% in 6 week old db/db islets compared to control, while no significant difference was detected in 12 week old db/db mice compared to control (Fig.7K).
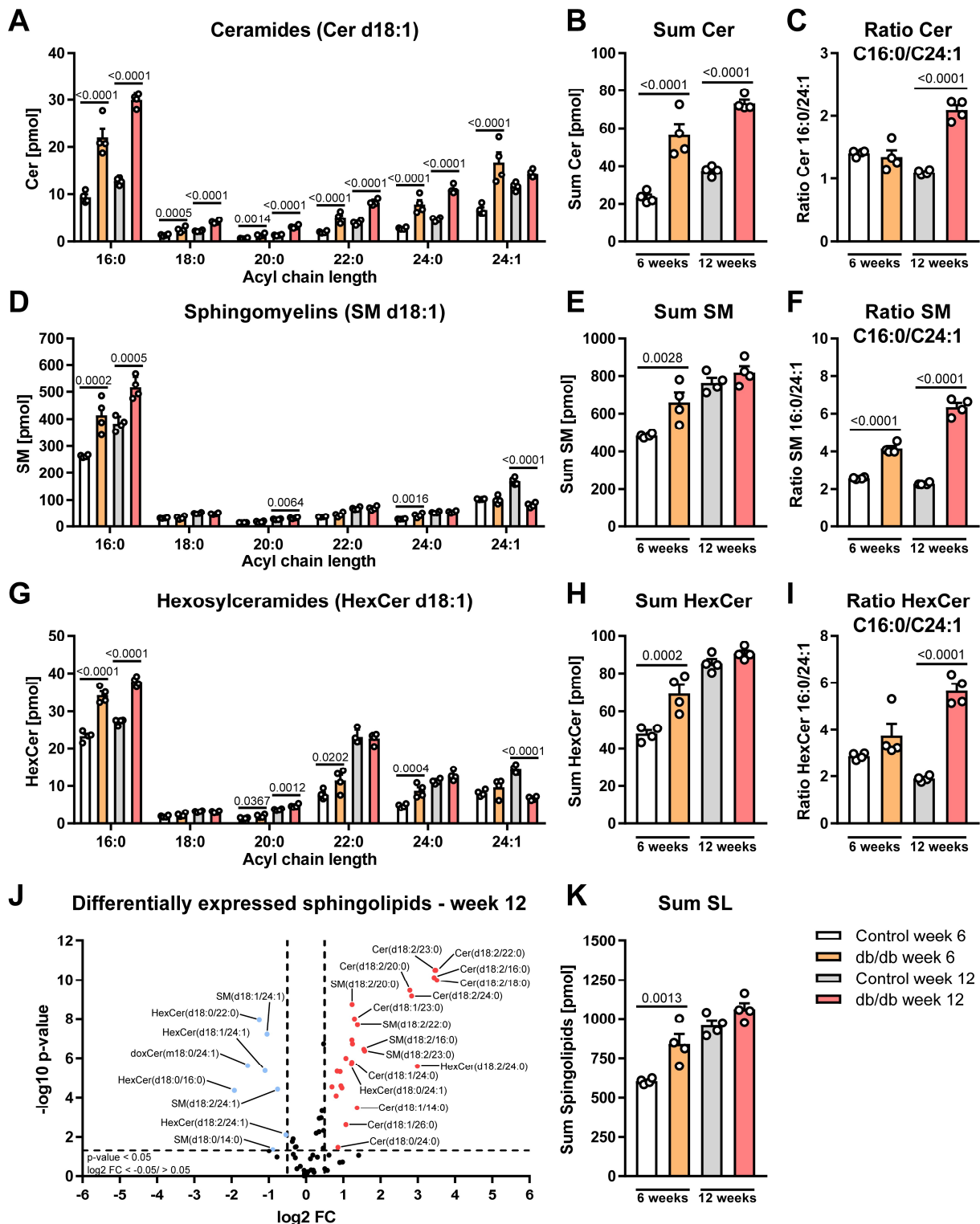
Figure 7: Long and very long chain ceramides are highly elevated, while very long chain C24:1 species of complex sphingolipids are reduced in islets of db/db mice. A) Ceramide, **D)** sphingomyelin and **G)** hexosylceramide species with various acyl chain lengths in islets of 6 and 12 week old control and db/db mice were determined by untargeted lipidomics. **B)** Sum of all ceramide, **E)** sphingomyelin and **H)** hexosylceramide species were calculated in islets from control and db/db mice at an age of 6 and 12 weeks. **C)** Ratio of C16:0 to C24:1 ceramides, **F)** sphingomyelins and **I)** hexosylceramides in control and db/db islets of 6 and 12 week old mice. **J)** Volcano plot shows sphingolipid species which are decreased (blue) or increased (red) in db/db islets. **K)** Sum of all measured sphingolipids in islets of 6 and 12 week old control and db/db mice. n= 4 for control, n= 4 for db/db with pooled islets of 7-8 mice. Shown are means ± SEM and significant p-values. Significance was determined by two-way ANOVA (**A-K**). **SL**= sphingolipid, **Cer**= ceramide, **SM**= sphingomyelin, **HexCer**= hexosylceramide, **doxCer**= deoxyceramide, **m**= monohydroxylated backbone; **d**= dihydroxylated backbone, **18:0**= sphingoid backbone without double bond (e.g. dihydro-ceramide, -sphingomyelin), **18:1**= sphingoid backbone with one double

bond (e.g. ceramide, sphingomyelin), **18:2**= sphingoid backbone with two double bonds (sphingadiene), **FC**= fold change.

4.2. Beta cell specific ablation of *CerS2* does not alter beta cell identity in mice

To analyze the role of CERS2 and its influence on the sphingolipidome in pancreatic beta cells, *CerS2* was specifically ablated in pancreatic beta cells by crossbreeding of two mouse lines: the conditional *CerS2* KO mouse (kindly provided by Prof. Dr. Jens C. Brüning from the Max-Planck-Institute for Metabolism Research in Cologne, Germany) and the *Ins1*-Cre mouse [284]. In the conditional *CerS2* KO mouse, two loxP sites have been inserted in front of exon 2 and behind exon 11 (Fig.8A). Furthermore, the overlapping UTR sequence between *CerS2* and another gene next to the *CerS2* locus (SET domain bifurcated histone lysine methyltransferase 1, *Setdb1*) was duplicated to avoid unspecific effects of 3′ UTR deletion (Fig.8A, conditional *CerS2* KO locus). After crossbreeding those mice with heterozygous *Ins1*-Cre mice, the sequence between both loxP sites is deleted in the offspring as early as insulin expression starts in pancreatic beta cells. Mice possessing the genotype *Ins1*-Cre$^{tg/+}$; *CerS2*$^{fl/fl}$ were used in experiments and are further designated as *CerS2*$^{\Delta BKO}$ mice. For the generation of control mice, *CerS2* Wt littermates were crossed with heterozygous *Ins1*-Cre and offspring mice possessing the genotype *Ins1*-Cre$^{tg/+}$; *CerS2*$^{+/+}$ were used in experiments and designated as control. If not mentioned otherwise, adult male mice at an age of 12-30 weeks were used in experiments.

First, we tested specificity of *CerS2* deletion in pancreatic beta cells. Therefore, DNA from different organs was extracted from *CerS2*$^{\Delta BKO}$ mice and the presence of the *Ins1*-Cre transgene and the deleted locus of *CerS2* (loss of exons 2-11) were detected via PCR. Genotyping of the different organs revealed that *CerS2* ablation (*CerS2Δ*) was only present in pancreatic islets of *CerS2*$^{\Delta BKO}$ mice, while the floxed *CerS2* locus (*CerS2* flox) and the heterozygous *Ins1*-Cre transgene (Cre tg) was detected in all organs (Fig.8B). In addition, *CerS2* mRNA expression was exclusively reduced by approximately 80% in pancreatic islets of *CerS2*$^{\Delta BKO}$ mice compared to controls (Fig.8C). Next, we investigated, if other *CerS* were coregulated after *CerS2* deletion in *CerS2*$^{\Delta BKO}$ islets. Therefore, mRNA expression of *CerS2*, *CerS4*, *CerS5* and *CerS6*, which are the most abundant *CerS* in pancreatic islets, were determined by qPCR in control and *CerS2*$^{\Delta BKO}$ islets. *CerS1* is known to be mainly expressed in brain, skeletal muscle and testis, while *CerS3* is only present in the skin and testis [151]. qPCR revealed specific downregulation of *CerS2* by approximately 80%, while other *CerS* were not regulated on mRNA level in pancreatic islets of *CerS2*$^{\Delta BKO}$ mice (Fig.8D). On protein level, CERS2 was strongly reduced by approximately 70-80% in pancreatic islets from *CerS2*$^{\Delta BKO}$ islets as shown by immunoblot analysis (Fig.8E and Fig.8F). Residual 20-30% of *CerS2* mRNA and CERS2 protein signal most likely originated from other cell types in pancreatic islets, like

alpha cells. To address if *CerS2* deletion alters beta cell function and identity, mRNA expression levels of several beta cell markers (*Ins1*, *Ins2*, *Pdx1*, *Nkx6.1*, *Slc2a1*, *Slc2a2* and *Foxo1*) were examined in control and *CerS2*ᐃBKO islets, but no significant differences were detected (Fig.8G). Due to implication of ER stress on beta cell function during the development of T2D, we additionally analyzed mRNA expression of several ER stress markers (*Pdia3*, *Grp78*, *Grp94*, *Grp170*, *Chop*, *Hsp60*, *Hsp70*, *Erp29*, *Calr*) and observed no significant differences in control and *CerS2*ᐃBKO islets (Fig.8H). In addtition, mRNA expression of *Setdb1* was unaltered after *CerS2* deletion (data not shown).
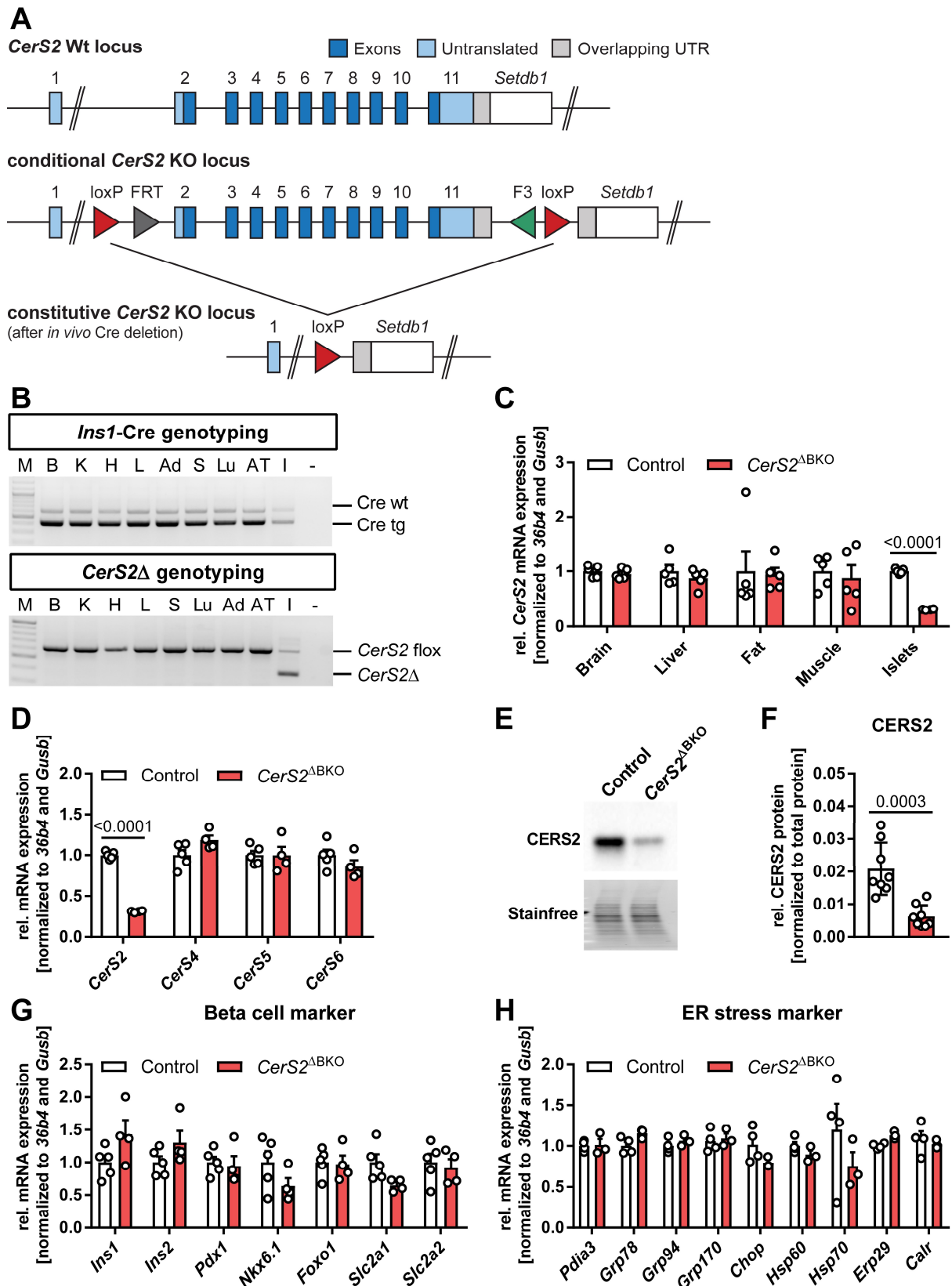
Figure 8: Generation of beta cell specific *CerS2* knockout mice. A) Overview of *CerS2* targeting strategy (modified from Taconic Biosciences documentation sheet). The image illustrates a scheme of the *CerS2* Wt, conditional *CerS2* KO and constitutive *CerS2* KO locus in mice. Conditional *CerS2* mice were generated by insertion of loxP sites in front of exon 2 and behind exon 11. Constitutive *CerS2* KO locus emerged in pancreatic beta cells by breading of conditional *CerS2* mice with the *Ins1*-Cre driver line leading to the deletion of the locus between exon 2 and exon 11. loxP= recognition sequence for Cre recombinase, F3= recognition sequence for Flippase (Flp) recombinase, FRT= recognition sequence for Flp recombinase. **B)** Representative *Ins1*-Cre and *CerS2*Δ genotyping PCR in various mouse organs from *CerS2*^ΔBKO mice. M= marker, B= brain, K= kidney, H= heart, L= liver,

Ad= adrenal gland, S= skeletal muscle, Lu= lung, AT= adipose tissue, I= pancreatic islets, -= H_2O. **C)** qPCR of *CerS2* in various organs from control and *CerS2*[ΔBKO] animals. n= 4-5 for control, n= 5 for *CerS2*[ΔBKO] mice. **D)** Expression of *CerS* in control and *CerS2*[ΔBKO] islets detected by qPCR. n= 5 for control, n= 4 for *CerS2*[ΔBKO] mice. **E)** Representative immunoblot of CERS2 in pancreatic islets of control and *CerS2*[ΔBKO] mice. **F)** Quantification of all performed immunoblots n= 8 experiments. **G)** qPCR of beta cell markers in control and *CerS2*[ΔBKO] islets. n= 5 for control, n= 4 for *CerS2*[ΔBKO] mice. **H)** qPCR of ER stress markers in control and *CerS2*[ΔBKO] islets. n= 4 for control, n= 3 for *CerS2*[ΔBKO] mice. All graphs show mean ± SEM and significant p-values. Significance was determined by multiple t-test corrected with Holm-Sidak method (**C-D**, **G-H**) or Student's unpaired two-tailed t-test (**F**).

4.3.   Very long chain sphingolipids are strongly reduced in *CerS2*[ΔBKO] islets

Next, we asked if beta cell specific ablation of *CerS2* is sufficient to alter the generation of very long chain sphingolipids. Therefore, islets of control and *CerS2*[ΔBKO] islets were analyzed by untargeted lipidomics. Very long chain ceramides with length of C20-C24 were significantly reduced (C20:0 = ~-40%, C22:0 = ~-75%, C24:0 = ~-70%, C24:1 = ~-90%), while shorter species with a chain length from C14-C18 were not significantly changed in islets of *CerS2*[ΔBKO] mice compared to control (Fig.9A). Consequently, the sum of all measured ceramide species in *CerS2*[ΔBKO] islets was significantly reduced by 50% (Fig.9B). In addition, the ratio of C16:0/C24:1 ceramides was strongly upregulated by approximately 12 fold in *CerS2*[ΔBKO] islets compared to control (Fig.9C). We noticed that not only ceramides, but also other sphingolipid species like sphingomyelins and hexosylceramides were altered in pancreatic beta cells after *CerS2* deletion. Very long sphingomyelin species from C20-C26 were significantly reduced (C20:0 = ~-40%, C22:0 = ~-80%, C24:0 = ~-85%, C24:1 = ~-90%, C26:0 = ~-80%) in *CerS2*[ΔBKO] islets, while shorter sphingomyelin species from C14-C18 were not different in comparison to control islets (Fig.9D). However, total amounts of all sphingomyelins only tended to be reduced (p= 0.071), probably due to much higher concentrations of C16 sphingomyelins in comparison to other sphingomyelin species (Fig.9E). Changes in the sphingolipid species resulted in an increased ratio of C16:0/C24:1 sphingomyelin by approximately 10 fold in *CerS2*[ΔBKO] islets (Fig.9F). Moreover, very long chain C22-C26 hexosylceramides were significantly reduced (C22:0 = ~-80%, C24:0 = ~-90%, C24:1 = ~-95%, C26:0 = ~-80%) in *CerS2*[ΔBKO] islets compared to control. Interestingly, long chain C16:0 hexosylceramides were compensatorily increased about two fold in *CerS2*[ΔBKO] islets (Fig.9G). Thus, the ratio of C16:0 to C24:1 hexosylceramides was increased by approximately 40 fold in *CerS2*[ΔBKO] islets, while total amount of hexosylceramides was unaltered (Fig.9H and Fig.9I). When comparing all measured sphingolipid species in islets of control and *CerS2*[ΔBKO] mice, specifically very long chain sphingolipid species, not only ceramides but also sphingomyelins, deoxyceramides and hexosylceramides, were decreased in *CerS2*[ΔBKO] islets (Fig.9J). Furthermore, *CerS2* ablation led to a compensatory upregulation of long chain C16:0 hexosylceramides, as well as C16:0 and C20:0 dihydrodeoxyceramides (Fig.9J). Those changes significantly decreased the sum of all measured sphingolipids by approximately 30% in *CerS2*[ΔBKO] islets compared to control (Fig.9K). All differentially expressed sphingolipids of *CerS2*[ΔBKO] islets are shown in S.Tab.2.
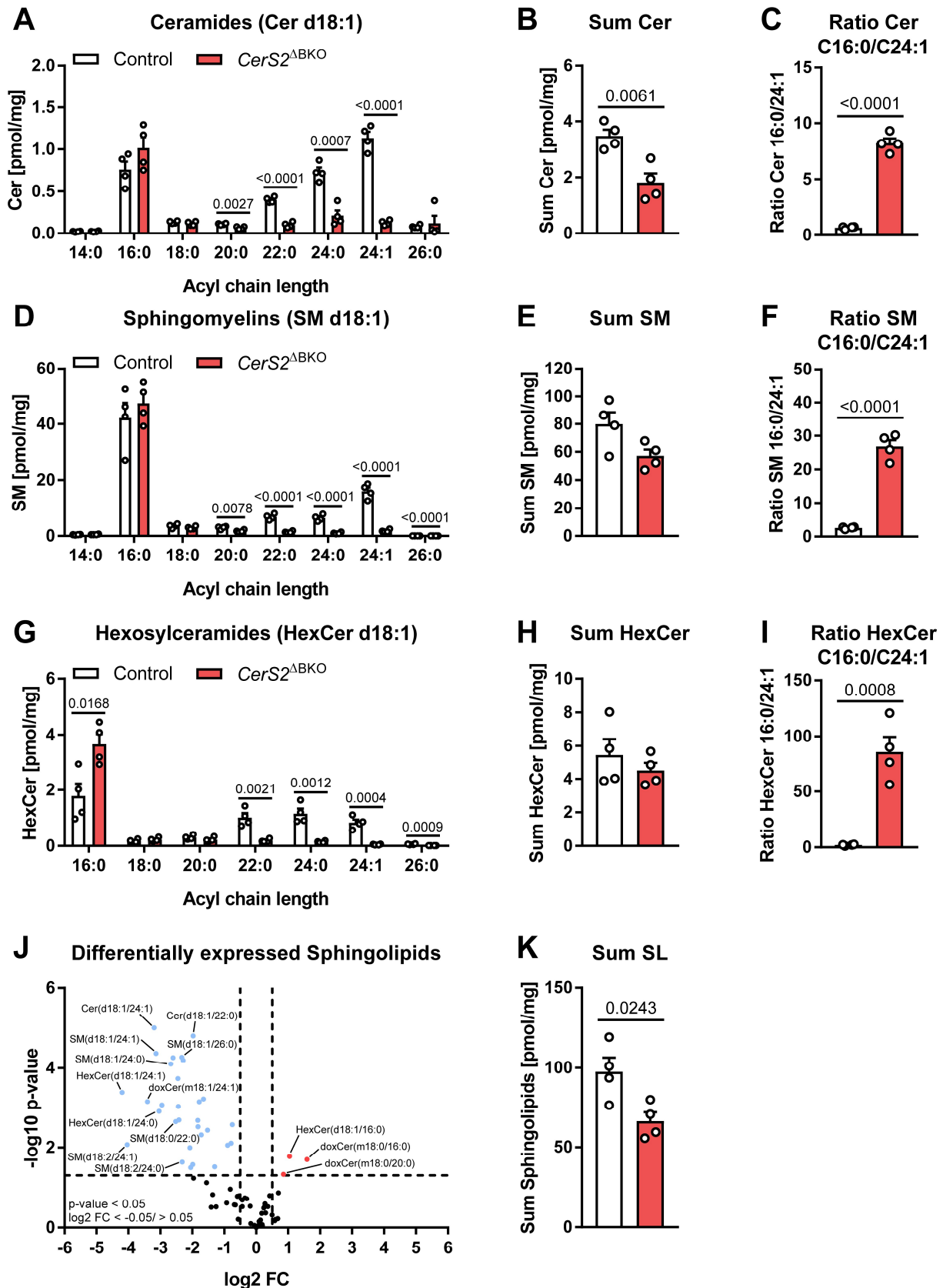
Figure 9: CerS2^ΔBKO islets display an altered sphingolipidome with a reduction in very long sphingolipid species. A) Ceramide, **D)** sphingomyelin and **G)** hexosylceramide species with various acyl chain length in control and *CerS2^ΔBKO* islets determined by untargeted lipidomics. **B)** Sum of all ceramide, **E)** sphingomyelin and **H)** hexosylceramide species were calculated in control and *CerS2^ΔBKO* islets. **C)** Ratio of C16:0 to C24:0 ceramides, **F)** sphingomyelins and **I)** hexosylceramides in control and *CerS2^ΔBKO* islets. **J)** Volcano plot shows sphingolipid species which are decreased (blue) or increased (red) in *CerS2^ΔBKO* islets compared to control. **K)** Sum of all measured sphingolipids in control and *CerS2^ΔBKO* islets. Shown are means ± SEM and significant p-values. n= 4

independent experiments with pooled islets of 4 mice. Significance was determined by Student's unpaired two-tailed t-test (**A-K**). **SL**= sphingolipids, **Cer**= ceramide, **SM**= sphingomyelin, **HexCer**= hexosylceramide **doxCer**= deoxyceramide, **m**= monohydroxylated backbone; **d**= dihydroxylated backbone, **18:0**= sphingoid backbone without double bond (e.g. dihydro-ceramide, -sphingomyelin), **18:1**= sphingoid backbone with one double bond (e.g. ceramide, sphingomyelin), **18:2**= sphingoid backbone with two double bonds (sphingadiene), **FC**= fold change.

4.4. Impaired glucose tolerance in *CerS2*$^{\Delta BKO}$ mice

To analyze if *CerS2* ablation affects beta cell function, *in vivo* experiments with male and female control and *CerS2*$^{\Delta BKO}$ mice fed with a normal diet (ND) were performed from 4 weeks to 20 weeks of age.
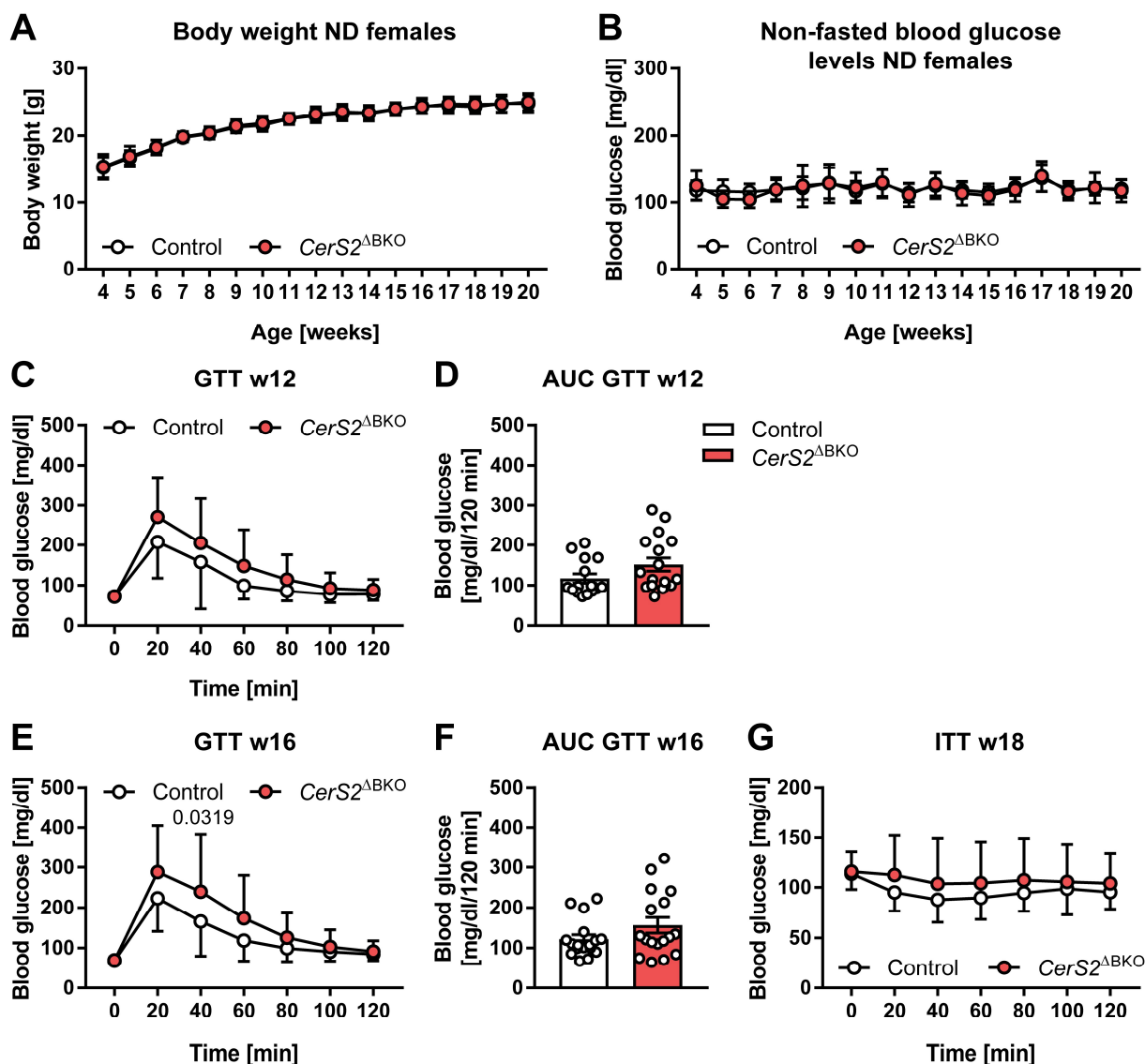
Body weight of male control and *CerS2*$^{\Delta BKO}$ mice was measured weekly and was comparable during 16 weeks of experimental period with an increase about 90% of initial body weight (Fig.10A). In addition, non-fasted blood glucose levels were determined weekly in control and *CerS2*$^{\Delta BKO}$ mice. Blood glucose levels of *CerS2*$^{\Delta BKO}$ mice were similar to control mice and values remained stable around 150 mg/dl over the whole experimental period (Fig.10B). Notably, glucose tolerance tests (GTT) in week 12 and week 16 of age showed impaired glucose tolerance of *CerS2*$^{\Delta BKO}$ mice compared to control mice (Fig.10C and Fig.10F) with significantly increased area under the curve (AUC) by approximately 45% in *CerS2*$^{\Delta BKO}$ mice (Fig.10D and Fig.10G). Plasma insulin concentrations of 12 week old control and *CerS2*$^{\Delta BKO}$ mice were determined during GTT and revealed a significant reduction in plasma insulin concentrations by approximately 70% 20 min after glucose injections in *CerS2*$^{\Delta BKO}$ mice (Fig.10E). Furthermore, insulin sensitivity was comparable during an insulin tolerance test (ITT) in *CerS2*$^{\Delta BKO}$ and control mice (Fig.10H). This indicates that impaired glucose tolerance of *CerS2*$^{\Delta BKO}$ mice results from insufficient insulin secretion after glucose injection. Impaired glucose tolerance, as well as reduced plasma insulin levels were specifically observed in *CerS2*$^{\Delta BKO}$ mice. This does not occur in *CerS5*$^{\Delta BKO}$ and *CerS6*$^{\Delta BKO}$ mice, which lack the enzymes generating long chain C16 ceramides (personal communication Dr. Michael Rieck, DDZ).
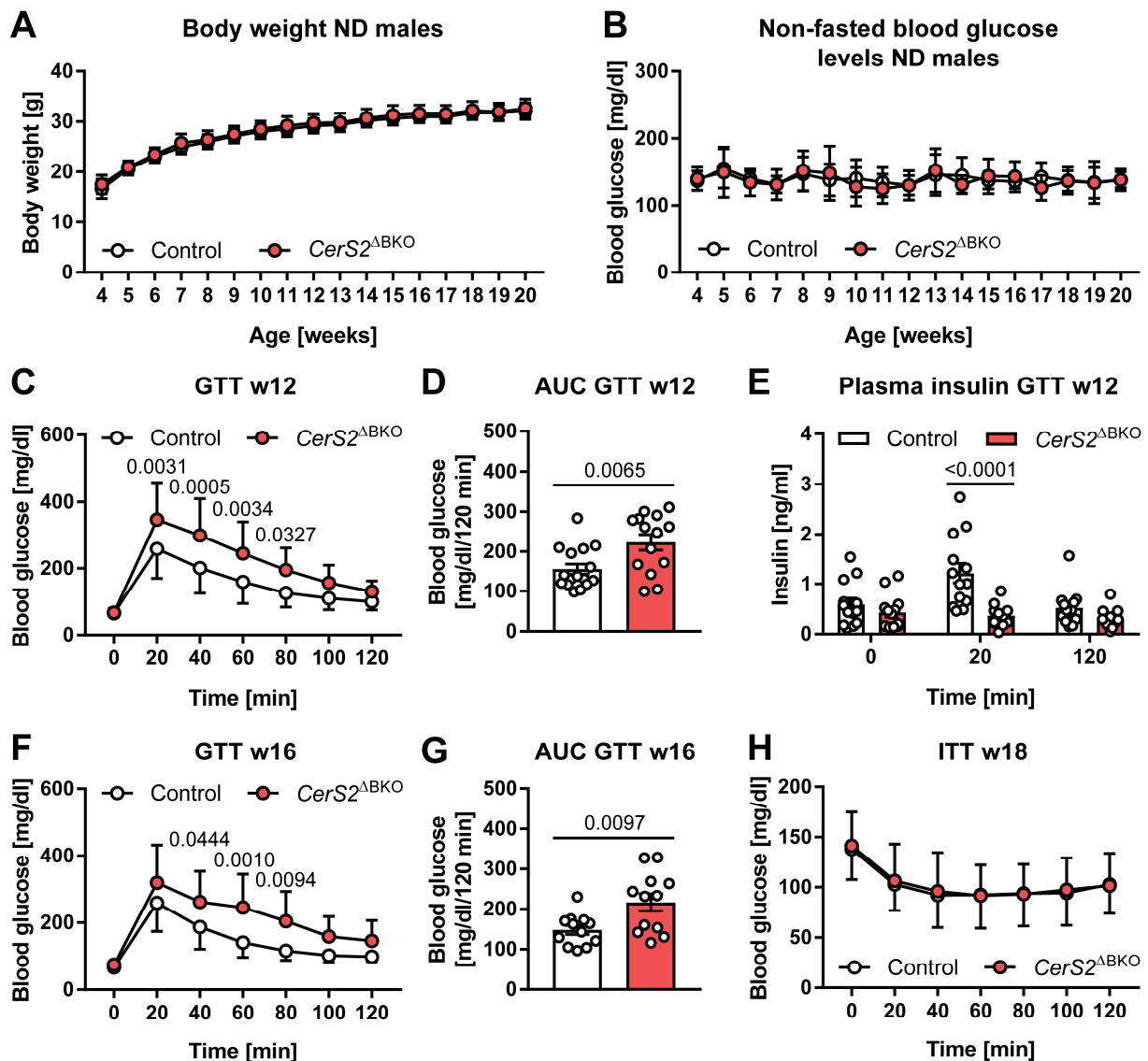
Figure 10: Male CerS2^ΔBKO mice manifest impaired glucose tolerance on normal diet. A) Body weight and **B)** non-fasted blood glucose levels were measured weekly in control and CerS2^ΔBKO mice receiving normal diet (ND). n= 16 for control, n= 16 for CerS2^ΔBKO mice. **C)** In week 12 and **F)** week 16 of age an intraperitoneal glucose tolerance test (GTT) was performed by injection of 2g/kg glucose and **D) and G)** area under the curve was calculated. n= 12-16 for control, n= 12-14 for CerS2^ΔBKO mice. **E)** Plasma insulin concentrations were determined by an insulin ELISA after 0, 20 and 120 min of glucose injection in 12 week old control and CerS2^ΔBKO mice. n= 13 for control, n= 13 for CerS2^ΔBKO mice. **H)** Insulin tolerance test (ITT) was performed by intraperitoneal injection of 0.75 U/kg insulin in week 18 of age in control and CerS2^ΔBKO mice. n= 16 for control, n= 16 for CerS2^ΔBKO mice. Shown are means ± SD (**A-C**, **F**, **H**) or means ± SEM (**D**, **E**, **G**) and significant p-values. Significance was determined by two-way ANOVA corrected with Sidak method (**A-C**, **E**, **F**, **H**) or by Student's unpaired two-tailed t-test (**D**, **G**).

We further investigated if impaired glucose tolerance was also present in female mice after CerS2 ablation. In general, due to higher insulin sensitivity and improved glucose homeostasis, at least partially mediated by higher estrogen levels, female individuals exhibit a reduced incidence to develop T2D in comparison to male subjects [295]. As observed in male mice, body weight and non-fasted blood glucose levels were similar between female control and CerS2^ΔBKO mice (Fig.11A and Fig.11B). Female CerS2^ΔBKO mice exhibited no major impairment of glucose tolerance during the performed GTT in week 12 and 16, but showed a tendentially decreased glucose tolerance compared to control (Fig.11C and Fig.11E). Blood glucose levels

were slightly increased 20 min after glucose injection (p= 0.053), but the calculated AUC was not significantly altered in 12 week old *CerS2*[ΔBKO] mice compared to control (Fig.11C and Fig.11D). Furthermore, 16 week old *CerS2*[ΔBKO] mice showed a slightly impaired glucose tolerance with tendentially increased glucose levels 20 min after glucose injection (p= 0.092) and significantly increased levels 40 min after glucose injection (Fig.11E). However, AUC was not significantly increased (Fig.11F). In addition, insulin tolerance in 18 week old control and *CerS2*[ΔBKO] mice was comparable (Fig.11G).

Figure 11: Female *CerS2*[ΔBKO] mice exhibit only a slightly impaired glucose tolerance on normal diet. A) Body weight and **B)** non-fasted blood glucose levels were measured weekly in control and *CerS2*[ΔBKO] mice receiving a normal diet (ND). n= 17 for control, n= 17 for *CerS2*[ΔBKO] mice. **C)** In week 12 and **E)** week 16 of age an intraperitoneal glucose tolerance test (GTT) was performed by injection of 2g/kg glucose and **D) and F)** area under the curve was calculated. n= 15 for control, n= 15-17 for *CerS2*[ΔBKO] mice. **G)** Insulin tolerance test (ITT) was performed by intraperitoneal injection of 0.25 U/kg insulin in week 18 of age in control and *CerS2*[ΔBKO] mice. n= 17 for control, n= 17 for *CerS2*[ΔBKO] mice. Shown are means ± SD (**A-C**, **E**, **G**) or means ± SEM (**D**, **F**) and significant p-values. Significance was determined by two-way ANOVA corrected with Sidak method (**A-C**, **E**, **G**) or by Student's unpaired two-tailed t-test (**D**, **F**).

To address, if ablation of *CerS2* would aggravate impaired glucose tolerance under obesogenic conditions with chronically elevated insulin levels, mice were fed a high fat diet upon 4 weeks of age. Body weight of male control and *CerS2*[ΔBKO] mice were comparable during experimental period and mice doubled their weight after 8 weeks (Fig.12A). Body weight of mice on HFD was approximately 20-25% increased in comparison to normal diet fed mice at the same age (compare Fig.10A and Fig.12A). Blood glucose levels of control and *CerS2*[ΔBKO] mice remained comparable around 170 mg/dl (Fig.12B). As seen with ND, glucose tolerance was impaired in 12 week old *CerS2*[ΔBKO] mice compared to control (Fig.12C) and calculated AUC was significantly increased by approximately 30% in *CerS2*[ΔBKO] mice (Fig.12D). Consistently, insulin concentrations in plasma of 12 week old *CerS2*[ΔBKO] mice were reduced by 50% 20 min after glucose injections in comparison to control mice (Fig.12E).
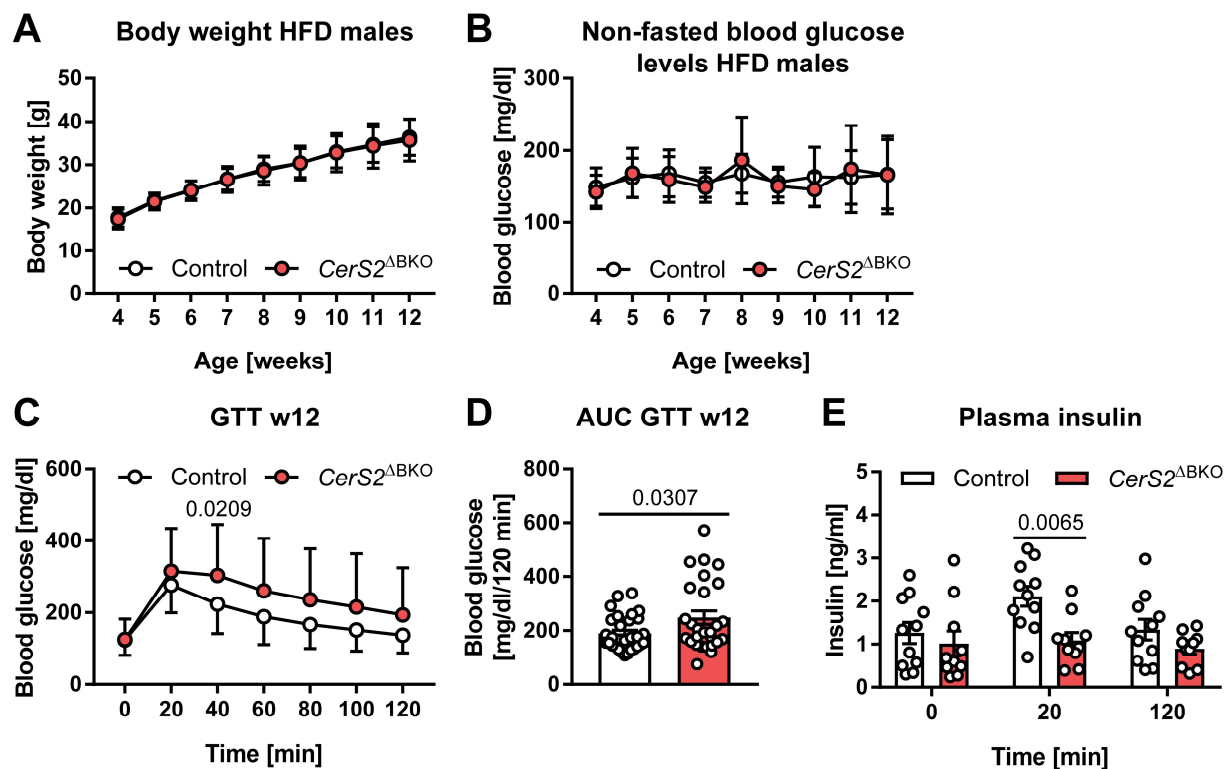
Figure 12: Male *CerS2*[ΔBKO] mice demonstrate impaired glucose tolerance on high fat diet. A) Body weight and **B)** non-fasted blood glucose levels were measured weekly in control and *CerS2*[ΔBKO] mice receiving a high fat diet (HFD) upon week 4 of age. n= 33 for control, n= 30 for *CerS2*[ΔBKO] mice. **C)** In week 12 of age an intraperitoneal glucose tolerance test (GTT) was performed by injection of 1g/kg glucose and **D)** area under the curve was calculated. n= 30 for control, n= 27 for *CerS2*[ΔBKO] mice. **E)** Plasma insulin concentrations were determined by an insulin ELISA after 0, 20 and 120 min of glucose injection in 12 week old control and *CerS2*[ΔBKO] mice. n= 11 for control, n= 10 for *CerS2*[ΔBKO] mice. Shown are means ± SD (**A-C**) or means ± SEM (**D, E**) and significant p-values. Significance was determined by two-way ANOVA corrected with Sidak method (**A-C**, **E**) or by Student's unpaired two-tailed t-test (**D**).

Female control and *CerS2*[ΔBKO] mice exhibited similar body weight and non-fasted blood glucose levels during experimental period on HFD (Fig.13A and Fig.13B). Body weight of control and *CerS2*[ΔBKO] mice increased about 90% during 8 weeks of HFD, which correspond to 20-25% increased weight as compared to females of the same age receiving a ND (compare

Fig.11A and Fig.13A). As observed in ND fed mice, female HFD fed *CerS2^ΔBKO* mice at an age of 12 weeks tended to be more glucose intolerant compared to controls (p= 0.053 at 40 min after glucose injection), which was also detected in the AUC (p=0.094) (Fig.13C and Fig.13D).
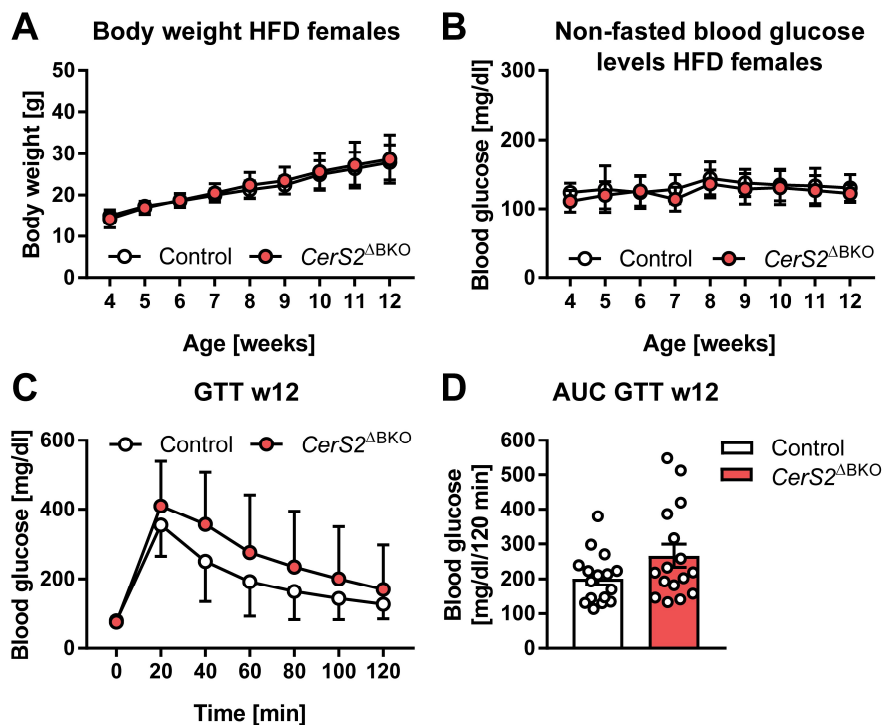

Figure 13: Female *CerS2^ΔBKO* mice displayed no major impairment of glucose tolerance on high fat diet. **A)** Body weight and **B)** non-fasted blood glucose levels were measured weekly in control and *CerS2^ΔBKO* mice receiving high fat diet (HFD) upon week 4 of age. n= 16 for control, n= 17 for *CerS2^ΔBKO* mice. **C)** In week 12 an intraperitoneal glucose tolerance test (GTT) was performed by injection of 2g/kg glucose and **D)** area under the curve was calculated. n= 16 for control, n= 16 for *CerS2^ΔBKO* mice. Shown are means ± SD (**A-C**) or means ± SEM (**D**). Significance was determined by two-way ANOVA corrected with Sidak method (**A-C**) or by Student's unpaired two-tailed t-test (**D**).

Taken together, the data from ND and HFD fed control and *CerS2^ΔBKO* mice showed that ablation of *CerS2* impaired glucose tolerance due to decreased plasma insulin levels independent of diet and especially in male mice.

## 4.5.   Reduced insulin content in *CerS2*$^{\Delta BKO}$ islets and pancreata

To further investigate why insulin levels in plasma of *CerS2*$^{\Delta BKO}$ mice were reduced, islets from adult control and *CerS2*$^{\Delta BKO}$ mice were isolated to perform a glucose stimulated insulin secretion assay (GSIS) (Fig.14A). To this end, seven islets of similar size were consecutively treated for one hour with low glucose concentrations (2 mM), followed by one hour treatment with high glucose concentrations (20 mM). Insulin secretion of control and *CerS2*$^{\Delta BKO}$ islets at low glucose concentration was similar, while after high glucose stimulation *CerS2*$^{\Delta BKO}$ islets secreted approximately 50% less insulin compared to controls (Fig.14B). This could either be explained by a reduction in insulin content, the inability to secrete sufficient amounts of insulin or a combination of both. Considering total insulin content in control and *CerS2*$^{\Delta BKO}$ islets, significantly less insulin (~-35%) was detected in *CerS2*$^{\Delta BKO}$ islets (Fig.14C). In line with this, islets of *CerS2*$^{\Delta BKO}$ mice seemed to be brighter in comparison to control islets, indicating less insulin content (Fig.14A). However, when secreted insulin was normalized to insulin content, insulin secretion of control and *Cer2*$^{\Delta BKO}$ islets was comparable (Fig.14D). Therefore, the primary defect is the decreased insulin content rather than insulin secretion after *CerS2* ablation. Next, we investigated if *CerS2* deletion impairs insulin processing in pancreatic islets. Insulin is synthesized by cleavage of the precursor hormone proinsulin into insulin and C-peptide in the secretory granules of beta cells [111]. Proinsulin content was not significantly changed in *CerS2*$^{\Delta BKO}$ islets compared to controls (Fig.14E). Nevertheless, the calculated ratio of insulin to proinsulin content in *CerS2*$^{\Delta BKO}$ islets was significantly decreased, showing that in *CerS2*$^{\Delta BKO}$ islets more proinsulin is present relative to insulin (Fig.14F). These data indicate that insulin maturation is impaired in *CerS2*$^{\Delta BKO}$ islets. In contrast to insulin, glucagon content in control and *CerS2*$^{\Delta BKO}$ islets was similar (Fig.14G).
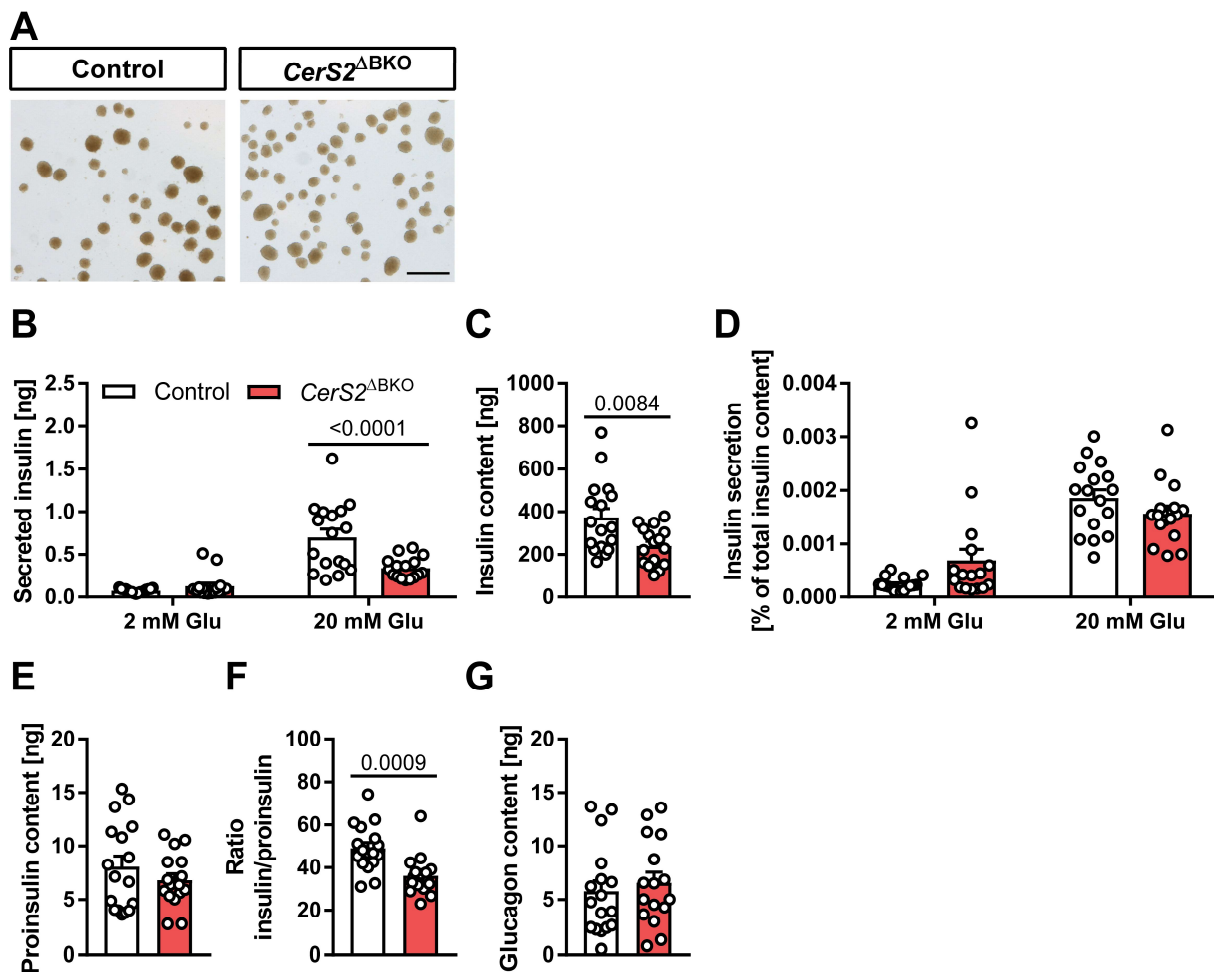
Figure 14: *CerS2*^ΔBKO islets contain reduced amounts of insulin. A) Representative image of islets from control and *CerS2*^ΔBKO mice. Scale bar= 500 μm. **B-D)** Glucose stimulated insulin secretion (GSIS) was performed with seven control and *CerS2*^ΔBKO islets using 2 mM (low) and 20 mM (high) glucose concentrations. Insulin quantity was determined by insulin ELISA. **B)** Secreted insulin after low and high glucose stimulation, **C)** insulin content and **D)** insulin secretion normalized to insulin content was determined in control and *CerS2*^ΔBKO islets. **E)** Proinsulin amount of control and *CerS2*^ΔBKO islets was detected in lysates by proinsulin ELISA and **F)** ratio of insulin to proinsulin was calculated. **G)** Glucagon content in islet lysates was measured via glucagon ELISA. Shown are means ± SEM and significant p-values. Significance was determined by two-way ANOVA corrected with Sidak method (**B**, **D**) or by Student's unpaired two-tailed t-test (**C**, **E-G**). n= 17 for control, n= 16 for *CerS2*^ΔBKO mice from 4 independent experiments.

Since we observed the reduction of insulin content in islets of *CerS2*^ΔBKO mice, we further analyzed insulin content in whole pancreata of control and *CerS2*^ΔBKO mice. Pancreata from adult male and female control and *CerS2*^ΔBKO mice had a similar weight (Fig.15A and Fig.15D). Insulin content in pancreas extracts from male and female control and *CerS2*^ΔBKO mice was determined by insulin ELISA and normalized to protein amount. Pancreata of *CerS2*^ΔBKO mice exhibited significantly less insulin (~-40-45%) compared to controls (Fig.15B and Fig.15E). Normalization of insulin content to pancreas weight revealed similar results (data not shown). As shown before in islets, glucagon content from male control and *CerS2*^ΔBKO pancreata was unchanged (Fig.15C).
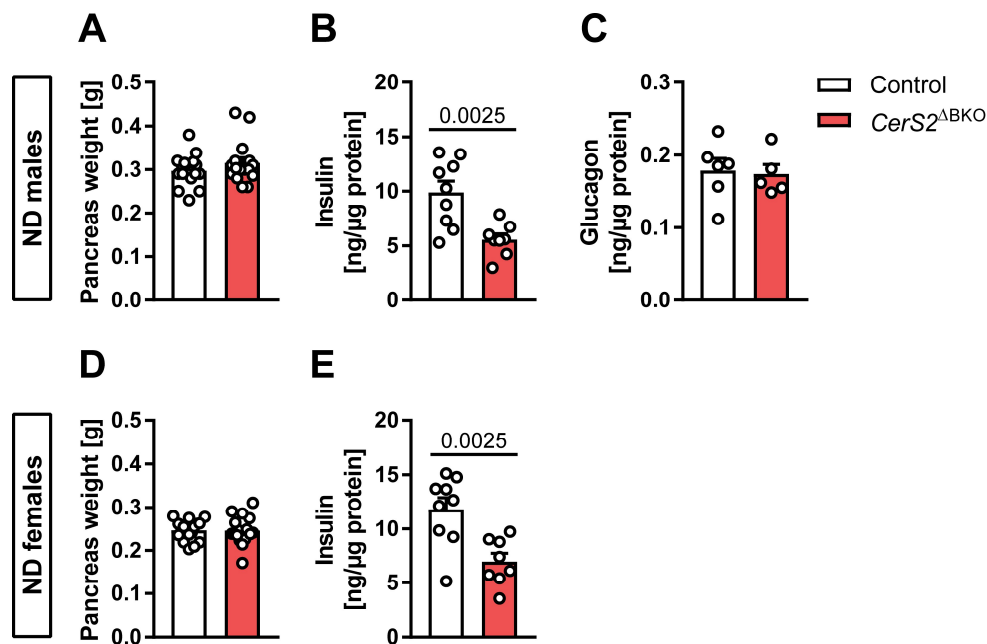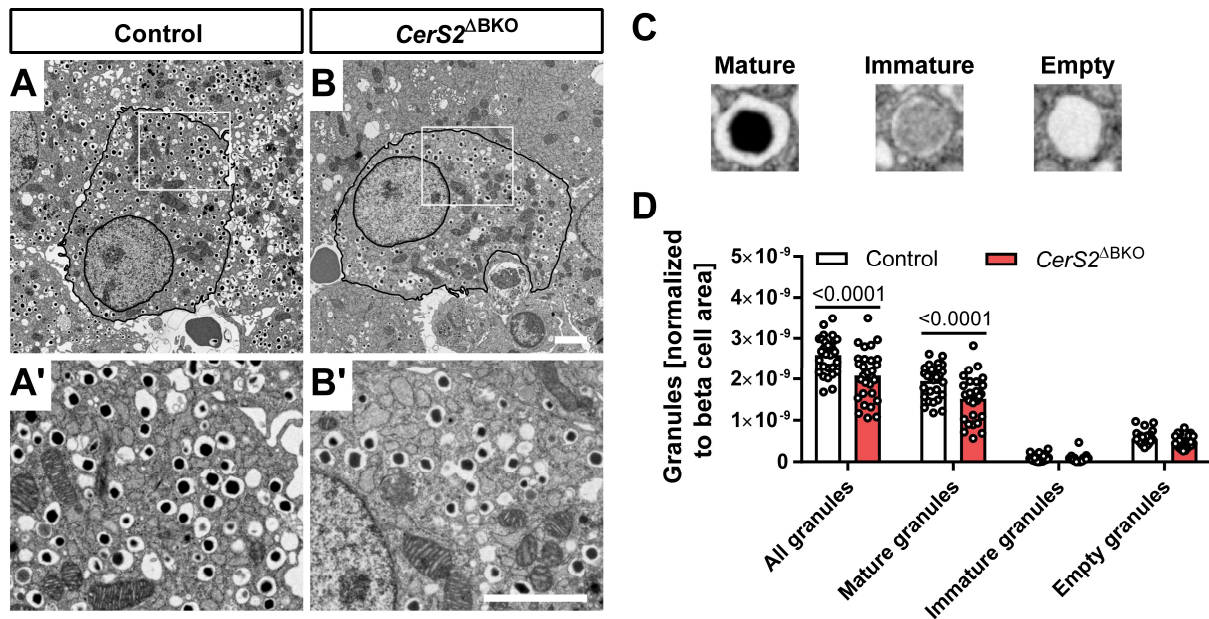
Figure 15: Insulin content is reduced in whole pancreata from *CerS2*^{ΔBKO} mice. A) Pancreatic weight of male and **D)** female mice was measured at the age of 20 weeks. n= 16-17 for control, n= 16-17 for *CerS2*^{ΔBKO} mice. **B)** Insulin content was determined in male and **E)** female pancreas extracts from control and *CerS2*^{ΔBKO} mice using an insulin ELISA and normalized to total protein content. n= 9 for control, n= 8 for *CerS2*^{ΔBKO} mice. **C)** Glucagon content was examined in pancreata from male control and *CerS2*^{ΔBKO} mice by glucagon ELISA and normalized to total protein content. n= 6 for control, n= 5 for *CerS2*^{ΔBKO} mice. Shown are means ± SEM and significant p-values. Significance was determined by Student's unpaired two-tailed t-test (**A-E**).

Taken together, we found that pancreata as well as islets of *CerS2*^{ΔBKO} mice contain less insulin compared to controls. This could explain the decreased insulin secretion after high glucose stimulation from islets *ex vivo* as well as decreased plasma insulin levels *in vivo* leading to impaired glucose tolerance in *CerS2*^{ΔBKO} mice.

4.6. Reduction in mature insulin granules in beta cells of *CerS2*^{ΔBKO} mice

To verify the reduction of insulin content in beta cells of *CerS2*^{ΔBKO} mice, we isolated islets from control and *CerS2*^{ΔBKO} mice and quantified insulin granules by transmission electron microscopy in collaboration with Dr. Jürgen Weiß and Kay Jeruschke from the Cellular Morphology Unit at the German Diabetes Center in Düsseldorf. Representative images of beta cells of control and *CerS2*^{ΔBKO} mice are shown in Fig.16A and Fig.16B and white box indicates magnified area in Fig.16A'and Fig.16B'. Mature, immature and empty insulin granules were counted in consultation with Dr. Jürgen Weiß and representative images are shown in Fig.16C. For quantification, the number of mature, immature, empty and total granules were normalized to beta cell area (black line in Fig.16A and Fig.16B). In beta cells of *CerS2*^{ΔBKO} mice, the number of mature insulin granules was decreased by approximately 20%. Importantly, the amount of immature, as well as empty granules were unaltered in *CerS2*^{ΔBKO} beta cells, leading to a 20% reduction in total granule number (Fig.16D).

Figure 16: Beta cells of CerS2^ΔBKO mice posses less mature insulin granules. A) Representative electron microscopic images of control and **B)** *CerS2*^ΔBKO islets. Black lines surround beta cell and nuclei for the determination of beta cell area. White boxes display the area which is shown with higher magnification in **A')** and **B')**. Scale bars= 2 µm. **C)** Representative images of different kinds of granules within the beta cell. **D)** Quantification of granule number in a beta cell from control and *CerS2*^ΔBKO mice normalized to total beta cell area. n= 29 for control, n= 29 for *CerS2*^ΔBKO beta cells in islets from a pool of 4 mice. Shown are means ± SEM and significant p-values. Significance was determined by two-way ANOVA corrected with Sidak method (**D**).

Taken together, pancreatic beta cells of *CerS2*^ΔBKO mice contain less mature insulin granules compared to controls, which is in line with detected insulin and proinsulin content of islets. The reduction in mature insulin granules leads to less mature insulin content in the pancreatic islets as well as whole pancreata and thus most likely participate in reduced insulin secretion into the plasma, which eventually cause glucose intolerance in *CerS2*^ΔBKO mice.

4.7.   Generation of *CerS2* knockout INS1E cells using the CRISPR/Cas9 system

For mechanistic analyses, we generated a *CerS2* knockout INS1E cell line using the CRISPR/Cas9 system with a two-sided cutting strategy as described by Bauer and colleagues [286]. Thus, almost all exons of *CerS2* were ablated by targeting exon 2 and exon 11 (same exons as in *CerS2*$^{\Delta BKO}$ mice) with specific gRNAs. Monoclonal knockout cells were identified by PCR using specific primers for the *CerS2* wildtype (Wt) and knockout (KO) locus (Fig.17A). As controls, INS1E cells were transfected with the same plasmid containing no gRNA (Addgene, 62988). Four separately cultured monoclonal cell lines were pooled for experiments and *CerS2* knockout cells are further described as *CerS2*$^{\Delta INS1E}$, while *CerS2* wildtype cells are designated as control. *CerS2* knockout was validated in *CerS2*$^{\Delta INS1E}$ cells on mRNA level by qPCR. mRNA expression of *CerS2* was efficiently ablated in *CerS2*$^{\Delta INS1E}$ cells, while other *CerS* were not regulated (Fig.17B). Moreover, CERS2 protein levels were undetectable in immunoblots of *CerS2*$^{\Delta INS1E}$ cells (Fig.17C and Fig.17D). In contrast to *CerS2*$^{\Delta BKO}$ islets, mRNA expression of *Ins2* was significantly upregulated by approximately 50% on mRNA level, while *Nkx6.1* (~-35%), *Pdx1* (~-5%), *Foxo1* (~-10%) and *Slc2a2* (~-25%) were significantliy downregulated (compare Fig.8G and Fig.17E). Next, we analyzed, if *CerS2* ablation in INS1E cells induces beta cell stress by detecting several chaperones as ER stress markers (*Pdia3*, *Grp78*, *Grp94*, *Grp170*, *Chop*, *Hsp60*, *Hsp70*, *Erp29* and *Calr*) via qPCR. Seven of nine ER stress markers were unchanged, but *Chop* (~20%) and *Hsp60* (~30%) were significantly increased in *CerS2*$^{\Delta INS1E}$ cells compared to controls (compare Fig.8H and Fig.17F). To investigate if *CerS2*$^{\Delta INS1E}$ cells possess a defect in insulin biosynthesis, as observed in *CerS2*$^{\Delta BKO}$ islets, *CerS2*$^{\Delta INS1E}$ cells were either treated with low (2 mM) or high (25 mM) glucose concentrations and insulin content was determined by insulin ELISA. Insulin content was slightly, but significantly decreased by 15-20% after low and high glucose stimulation in *CerS2*$^{\Delta INS1E}$ cells compared to control (Fig.17G). However, *Ins2* expression was upregulated in *CerS2*$^{\Delta INS1E}$ cells, but not in *CerS2*$^{\Delta BKO}$ islets, indicating that INS1E cells might partially compensate for decreased insulin content (compare Fig.8G and Fig.17E). Furthermore, *CerS2*$^{\Delta INS1E}$ cells showed comparable proliferation and ATP content compared to controls (Fig.17H and Fig.17I).
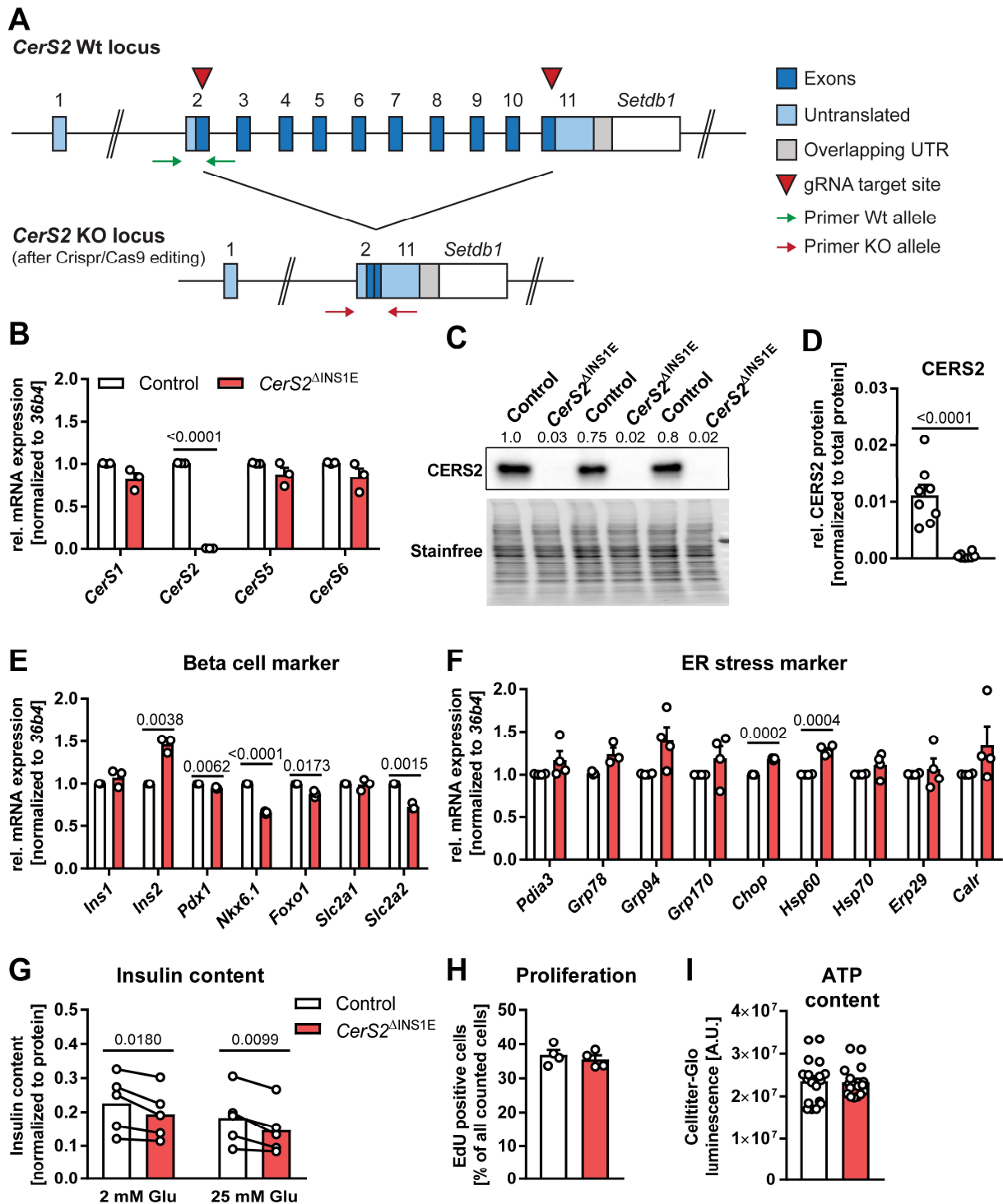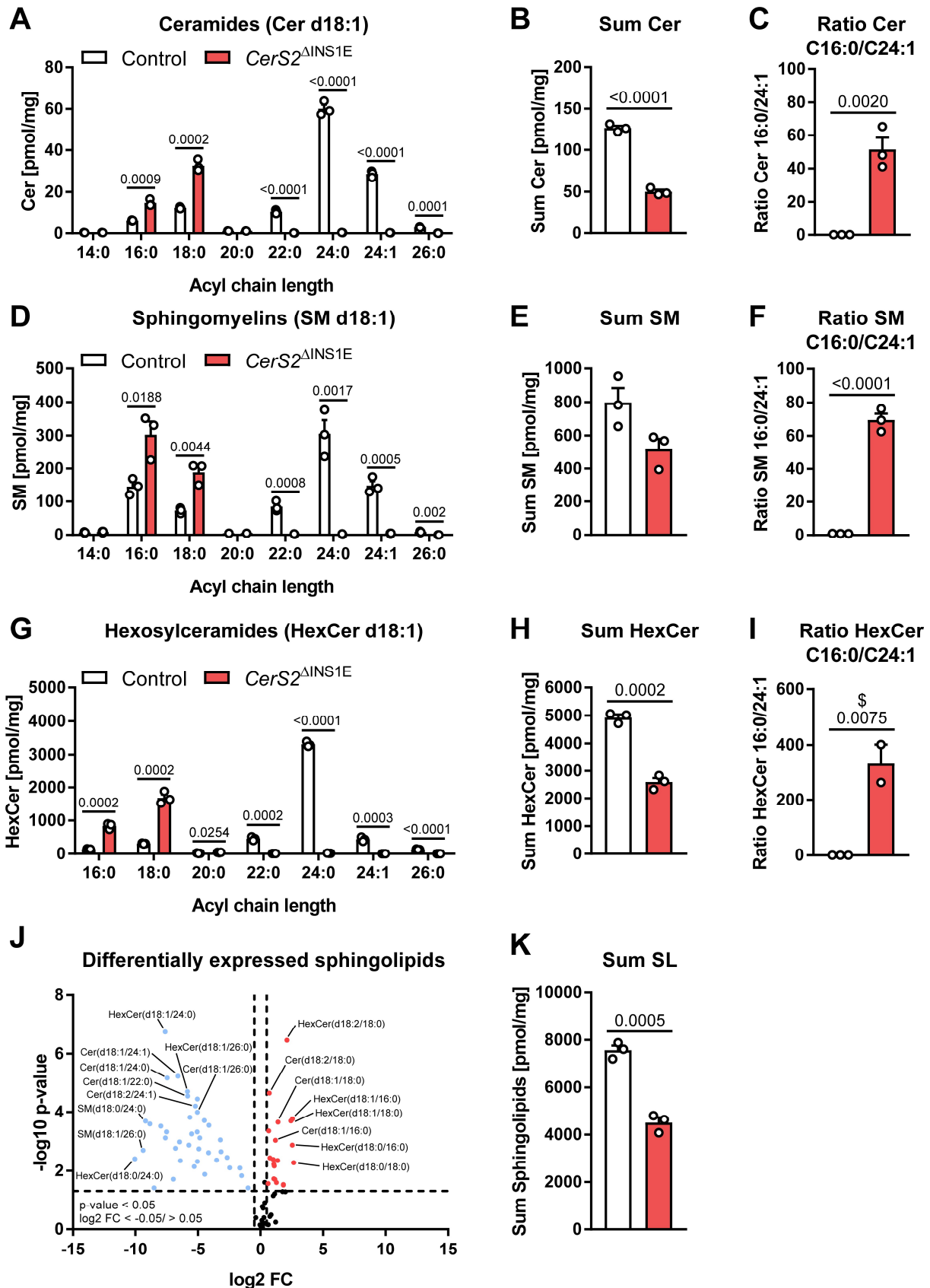
Figure 17: *CerS2*^{ΔINS1E} **cells display a reduction in very long chain ceramide species. A)** Schematic overview of *CerS2* deletion in INS1E cells by the CRISPR/Cas9 system. Shown is the *CerS2* Wt locus with overlapping 3'UTR of *Setdb1* gene and the *CerS2* KO locus generated by double strand breaks in exon 2 and 11 (red arrowheads), leading to the deletion of the same locus as in *CerS2*^{ΔBKO} mice. Genotyping PCR can be performed to identify the Wt locus (green arrows) and KO locus (red arrows). **B)** Relative mRNA expression of different *CerS* in control and *CerS2*^{ΔINS1E} cells. n= 3 independent experiments. **C)** Representative immunoblot for CERS2 in control and *CerS2*^{ΔINS1E} cells. Numbers display quantified intensity of bands and the first control band was set to 1.0. Stainfree was used for normalization of bands to total protein. **D)** Quantification of all performed immunoblots. n= 8 independent experiments. **E)** Relative mRNA expression of different beta cell markers in control and *CerS2*^{ΔINS1E} cells. n= 3 independent experiments. **F)** Relative mRNA expression of different ER stress markers in control and *CerS2*^{ΔINS1E} cells. n= 3-4 independent experiments. **G)** Insulin content was determined in lysates of control and *CerS2*^{ΔINS1E} cells after incubation with low glucose (2mM) or high glucose (25 mM) KRH buffer. Lines connect measurements of control and *CerS2*^{ΔINS1E} cells of the same experiment. n= 5 independent experiments. **H)** Proliferation of control and *CerS2*^{ΔINS1E} cells after 1 hour incubation with 5 μM EdU. n= 4 independent experiments. **I)** Relative ATP content in control and *CerS2*^{ΔINS1E} cells determined by Celltiter-Glo® 2.0 Viability assay. n= 18

independent experiments. Shown are means ± SEM and significant p-values. Significance was determined by multiple t-test corrected with Holm-Sidak method (**B**, **E**, **F**), by two-way ANOVA corrected with Sidak method (**G**) or by Student's unpaired two-tailed t-test (**H**, **I**).

4.8. *CerS2*$^{\Delta INS1E}$ cells phenocopy changes in sphingolipidome of *CerS2*$^{\Delta BKO}$ islets

Next, we analyzed, if the knockout in *CerS2*$^{\Delta INS1E}$ cells was sufficient to alter the sphingolipidome in INS1E cells. *CerS2*$^{\Delta INS1E}$ cells displayed strongly decreased levels of very long chain C22:0, C24:0, C24:1, and C26:0 ceramides (~-95-100%) compared to control (Fig.18A). In contrast to *CerS2*$^{\Delta BKO}$ islets, C20:0 ceramides were unaltered and long chain ceramide species with a length of C16:0 (~130%) and C18:0 (~160%) were compensatorily increased in *CerS2*$^{\Delta INS1E}$ cells (compare Fig.10A and Fig.18A). Although long chain C16:0 and C18:0 ceramides were increased, the dramatic loss of very long chain ceramides resulted in significantly reduction about 60% in overall ceramide levels in *CerS2*$^{\Delta INS1E}$ cells (Fig.18B). These changes in the ceramidome led to 230 fold increase in the ratio of C16:0/C24:1 ceramides in *CerS2*$^{\Delta INS1E}$ cells compared to control (Fig.18C). Then, we analyzed the effect of *CerS2* ablation on more complex sphingolipid species in INS1E cells. Very long C22:0, C24:0. C24:1 and C26:0 sphingomyelins and hexosylceramides were almost completely lost (~-95-100%) in *CerS2*$^{\Delta INS1E}$ cells (Fig.18D and Fig.18G). In addition, long chain C16:0, C18:0 and C20:0 hexosylceramides were compensatorily increased (~2.4-5.9 fold) in *CerS2*$^{\Delta INS1E}$ cells (Fig.18G). However, the sum of all sphingomyelin species was not significantly altered, but tended to be reduced in *CerS2*$^{\Delta INS1E}$ cells (p= 0.059), while total hexosylceramides levels were significantly decreased about 50% (Fig.18E and Fig.18H). Nevertheless, an extreme imbalance of long chain to very long chain sphingomyelins and hexosylceramides was observed by a strong increase in C16:0/C24:1 ratios by approximately 70 fold for sphingomyelins and 1015 fold for hexosylceramides (Fig.18F and Fig.18I). To visualize differentially expressed sphingolipid species in *CerS2*$^{\Delta INS1E}$ cells, the log2 fold changes (log2 FC) of all measured sphingolipids were plotted against their -log10 p-values in a volcano plot. The graph shows specific reductions in several very long chain C22-C26 sphingolipid species such as ceramides, sphingomyelins and hexosylceramides, while primarily long chain C16 and C18 ceramides and hexosylceramides were increased in *CerS2*$^{\Delta INS1E}$ cells compared to control (Fig.18J). Consequently, deletion of *CerS2* in INS1E cells decreased the total amount of all measured sphingolipids by approximately 40% (Fig.18K). All differentially expressed sphingolipids of *CerS2*$^{\Delta INS1E}$ cells are shown in S.Tab.3.

Taken together, *CerS2* ablation in INS1E cells significantly decreased the amount of very long chain sphingolipids species (including ceramides) similar to the phenotype in *CerS2*$^{\Delta BKO}$ islets.

Figure 18: *CerS2*[ΔINS1E] **cells display an altered sphingolipidome with a reduction in very long sphingolipid species. A)** Ceramide, **D)** sphingomyelin and **G)** hexosylceramide species with various acyl chain length in control and *CerS2*[ΔINS1E] cells were determined by untargeted lipidomics. **B)** Sum of all ceramide, **E)** sphingomyelin and **H)** hexosylceramide species were calculated in control and *CerS2*[ΔINS1E] cells. **C)** Ratio of C16:0 to C24:0 ceramides, **F)** sphingomyelins and **I)** hexosylceramides in control and *CerS2*[ΔINS1E] cells. **J)** Volcano plot displays sphingolipid species which were decreased (blue) or increased (red) in *CerS2*[ΔINS1E] cells compared to control. **K)** Sum of all measured sphingolipids in control and *CerS2*[ΔINS1E] cells. Shown are means ± SEM and significant p-values.

n= 3 independent experiments. Significance was determined by Student's unpaired two-tailed t-test (**A-K**). **$**= the ratio of C16:0 to C24:1 hexosylceramides could be calculated in only two samples of *CerS2$^{\Delta INS1E}$* cells due to undetectable C24:1 hexosylceramides in one sample of *CerS2$^{\Delta INS1E}$* cells. **SL**= sphingolipids, **Cer**= ceramide, **SM**= sphingomyelin, **HexCer**= hexosylceramide **doxCer**= deoxyceramide, **m**= monohydroxylated backbone; **d**= dihydroxylated backbone, **18:0**= sphingoid backbone without double bond (e.g. dihydro-ceramide, -sphingomyelin), **18:1**= sphingoid backbone with one double bond (e.g. ceramide, sphingomyelin), **18:2**= sphingoid backbone with two double bonds (sphingadiene), **FC**= fold change.

4.9. Proteome analysis reveals reduced levels of prohormone convertase 1 in *CerS2$^{\Delta INS1E}$* cells

To identify proteins which are differentially expressed in *CerS2$^{\Delta INS1E}$* cells, cell pellets of control and *CerS2$^{\Delta INS1E}$* were collected and analyzed by mass spectrometry in collaboration with Dr. Stefan Lehr and Dr. Sonja Hartwig from the Proteome Analysis Unit of the Institute for Clinical Biochemistry and Pathobiochemistry at the German Diabetes Center. 39 of 5,896 proteins were identified to be differentially expressed, with a q-value < 0.05 and log2 fold change (log2 FC) < -0.5 or > 0.5, in *CerS2$^{\Delta INS1E}$* cells compared to control (Fig.19A). A complete list of differentially expressed proteins in *CerS2$^{\Delta INS1E}$* cells are shown in S.Tab.5. The volcano plot shows all measured proteins in *CerS2$^{\Delta INS1E}$* cells, with significantly downregulated (blue) or upregulated (red) candidate proteins in *CerS2$^{\Delta INS1E}$* cells (Fig.19B). Interestingly, we identified prohormone convertase 1 (PC1, also known as PC1/3 or PCSK1, encoded by the gene *Pcsk1*), which is the rate limiting enzyme for the conversion of proinsulin into insulin, to be downregulated by approximately 35%. Proinsulin is sequentially processed by PC1, PC2 and CPE [114]. In humans, several single nucleotide polymorphisms in *Pcsk1* were identified, which are positively correlated with the development of obesity, increased plasma proinsulin levels and glucose intolerance [296]. Importantly, T2D is characterized by elevated plasma proinsulin levels and an increased proinsulin to insulin ratio [66,297]. Proinsulin into insulin conversion was shown to be almost completely absent in *Pcsk1* null mice, leading to elevated proinsulin levels as well as proinsulin to insulin ratios in the pancreas and plasma [119]. PC2 was shown to be responsible for only one-third of proinsulin processing [119,298]. CPE removes the C-terminal arginine residues of proinsulin and null mice display 50-100% higher proinsulin plasma levels [299].

PC1 itself is translated as an inactive precursor protein in the ER where the signal peptide is directly cleaved off followed by autocatalytic prodomain cleavage, which forms Pro-PC1 with a size of 94 kDa. The prodomain still binds non-covalently to the protein and inhibits its activity [120,300]. After protein folding processes and N-glycosylation of Pro-PC1, it is transferred to the Golgi apparatus. At mildly acidic conditions in the *trans*-Golgi network (pH < 6.4), the prodomain is thought to dissociate from Pro-PC1 leading to the formation of active PC1 with a size of 87 kDa [300,301]. Moreover, PC1 is posttranslationally modified by complex glycosylation and sulfation in the Golgi [300]. Afterwards, 87 kDa PC1 is packed together with proinsulin and other prohormones into immature secretory granules [118]. During the maturation process of

granules, the pH inside the granule is lowered to 5.5 by ATP-dependent proton pumps, which leads to autocatalytic cleavage of the C-terminal domain and formation of a truncated, fully activated 66 and 74 kDa PC1. In comparison to the 87 kDa PC1 protein, the truncated form is more active but less stable [300]. A scheme of the maturation process of PC1 is shown in Fig.19C. To validate the PC1 antibody (Cell signaling, 11914) used in our study to detect the different maturation forms of PC1 in INS1E cells, knockout, knockdown and overexpression experiments were analyzed by immunoblotting. *Pcsk1* knockout cells were generated in collaboration with Dr. Michael Rieck by deletion of exon 4 to exon 6 using the CRISPR/Cas9 system. *Pcsk1* wildtype (control), heterozygous (*Pcsk1*^{+/-}) and homozygous knockout (*Pcsk1*[ΔINS1E]) cells were used for analysis. While the mature, 66 kDa form of PC1 disappeared in immunoblot, detection of the Pro-PC1 form with a size of 94 kDa was reduced in *Pcsk1*^{+/-}, *Pcsk1*[ΔINS1E] and *Pcsk1* knockdown cells, but the signal did not completely disappear (Fig.19D-Fig.19F). Thus, the used antibody specifically detected the mature 66 kDa form of PC1, whereas residual detection of the upper band in *Pcsk1*[ΔINS1E] cells might indicate detection of Pro-PC1 and a non specific band (Fig.19D-Fig.19F). Usage of lower percentage SDS gels could not clearly seperate the unspecific band from the potential Pro-PC1 band (data not shown). Therefore, in further analyses only the mature form of PC1 was quantified in this thesis.
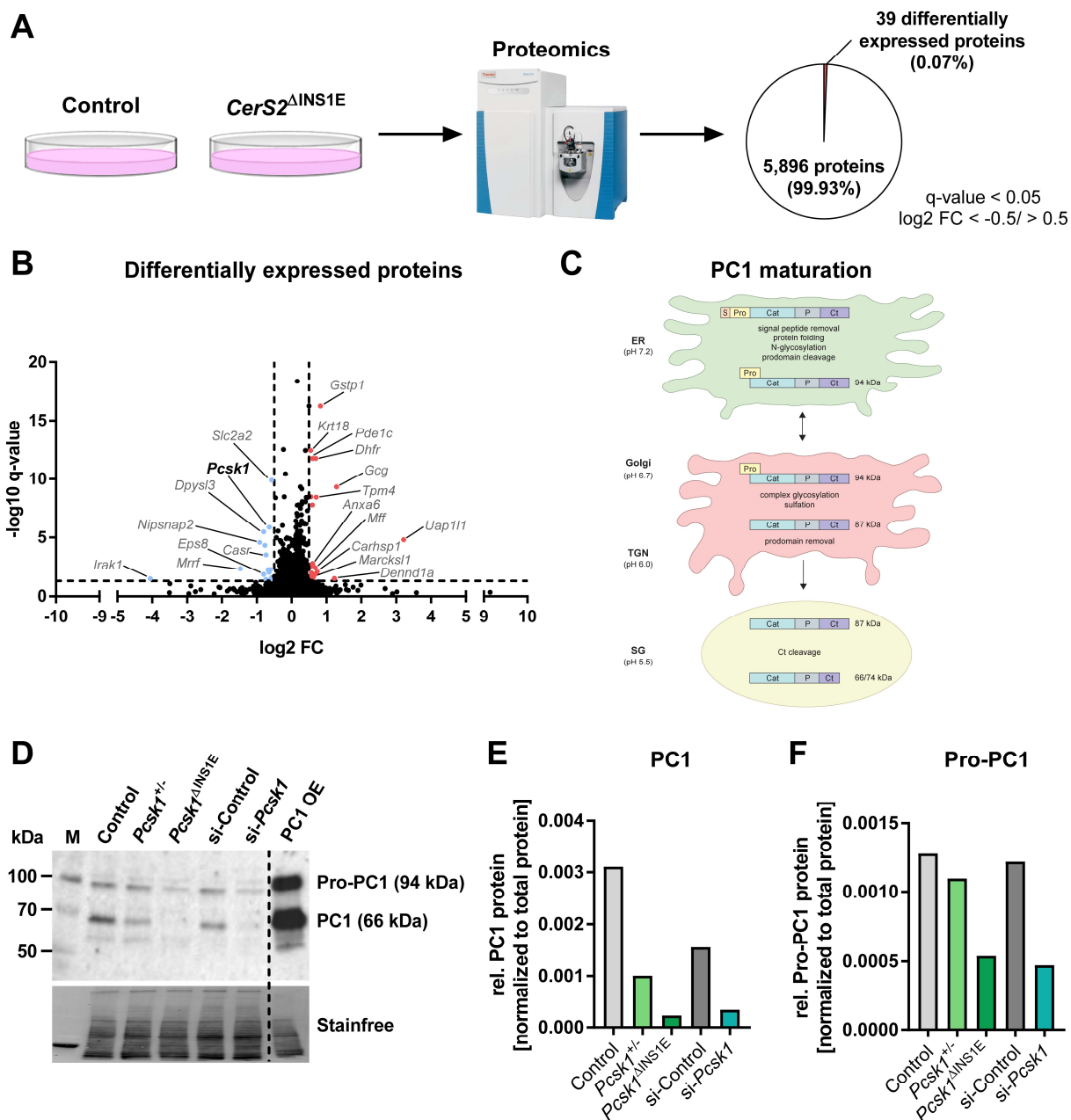
Figure 19: Proteome analysis of control and *CerS2*^ΔINS1E cells reveals a reduction in PC1 expression. A) Control and *CerS2*^ΔINS1E cells were collected from a p10 dish and proteins were analyzed on an Orbitrap (image taken from Thermo Fisher Scientific homepage). Data evaluation on spectronaut discovered 39 differentially expressed proteins with a q-value < 0.05 and log2FC < -0.5 and > 0.5. Some candidate proteins are labeled with the respective gene name. **B)** Volcano plot shows gene names of identified candidate proteins which are downregulated (blue) or upregulated (red) in *CerS2*^ΔINS1E cells. FC= fold change. **C)** Model of PC1 maturation in the regulated secretory pathway. **S**= signal peptide, **Pro**= pro-domain, **Cat**= catabolic domain, **P**= P-domain, **Ct**= C-terminal domain, **TGN**= *trans*-Golgi network, **SG**= secretory granule. Scheme is modified from Stijnen and coworkers [300]. **D)** Immunoblot of PC1 after knockout, knockdown and overexpression of *Pcsk1*. Stainfree was used for normalization of bands to total protein. **E)** Quantification of PC1 and **F)** Pro-PC1 for validation of PC1 antibody (Cell signaling, 11914) in immunoblot.

4.10. Mature PC1 is specifically reduced in *CerS2*[ΔBKO] islets and *CerS2*[ΔINS1E] cells

To validate the findings from the proteome analysis, we further investigated PC1 and annexin A6 (ANXA6) in *CerS2*[ΔINS1E] cells and *CerS2*[ΔBKO] islets. ANXA6 was upregulated in the proteome analysis and previous studies reported that ANXA6 binds to phospholipids in membranes, where it acts as a scaffold protein and is implicated in organization of membrane microdomains, membrane transport and signaling processes [302–304]. In *CerS2*[ΔINS1E] cells, mRNA expression of *Pcsk1* and *Anxa6* was detected by qPCR. *Pcsk1* was significantly downregulated by 40%, while *Anxa6* was upregulated about 60% in *CerS2*[ΔINS1E] cells compared to control (Fig.20A). In addition, ANXA6 protein was significantly increased around 60% in *CerS2*[ΔINS1E] cells (Fig.20B and Fig.20C). In turn, PC1 protein levels were decreased by approximately 60% in *CerS2*[ΔINS1E] cells compared to controls (Fig.20D and Fig.20E).
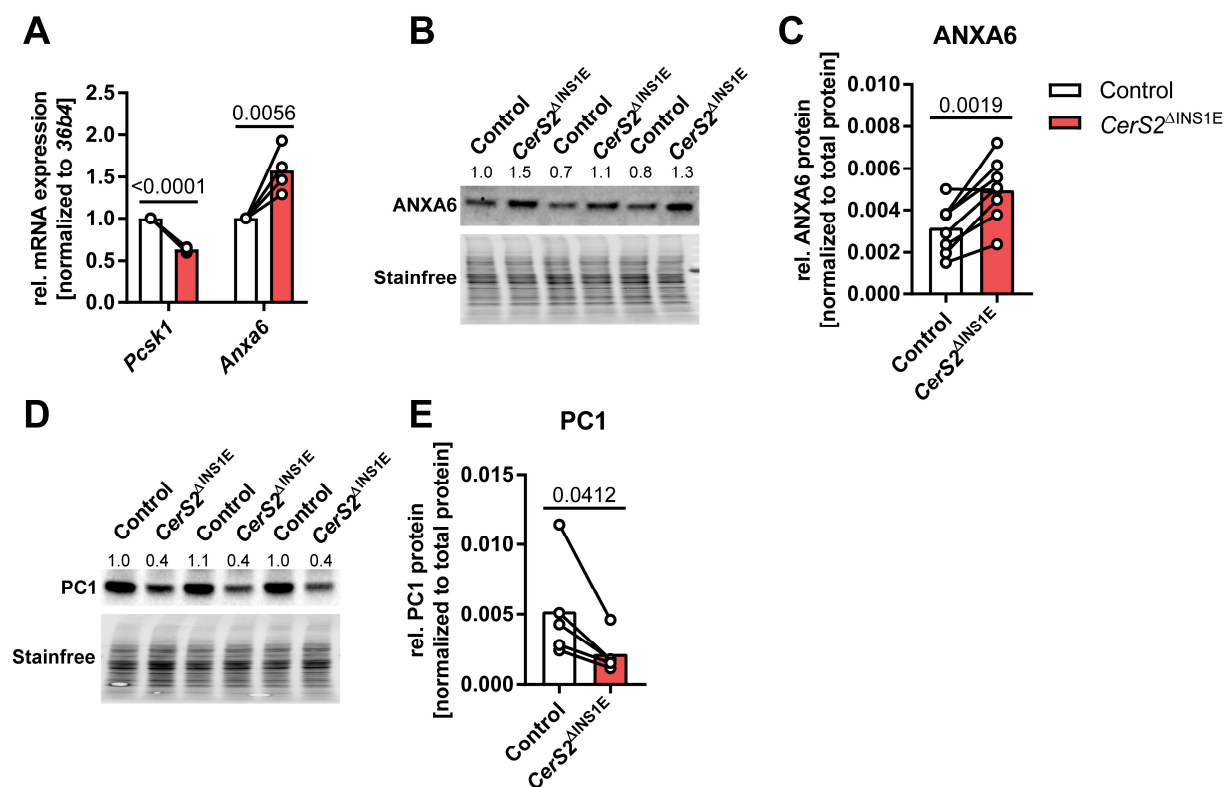
Figure 20: Verification of proteomics by immunoblot reveals decreased PC1 and increased ANXA6 protein in *CerS2*[ΔINS1E] cells. A) Relative mRNA expression of *Pcsk1* and *Anxa6* in control and *CerS2*[ΔINS1E] cells. n= 4 independent experiments. **B)** Representative immunoblot of ANXA6 in control and *CerS2*[ΔINS1E] cells. **C)** Quantification of ANXA6 in control and *CerS2*[ΔINS1E] cells. n= 8 independent experiments. **D)** Representative immunoblot of PC1 in control and *CerS2*[ΔINS1E] cells. **E)** Quantification of PC1 in control and *CerS2*[ΔINS1E] cells. n= 5 independent experiments. Shown are means and significant p-values. Lines connect quantified data from control and *CerS2*[ΔINS1E] cells of the same experiment. Numbers display quantified intensity of bands and first control band was set to 1.0. Stainfree was used for normalization of band intensity to total protein. Significance was determined by by multiple t-test corrected with Holm-Sidak method (**A**) or Student's paired two-tailed t-test (**C**, **E**).

We next asked, if PC1 and ANXA6 protein levels are also changed in control and *CerS2*$^{\Delta BKO}$ islets. First, mRNA expression levels of *Pcsk1* and *Anxa6* were investigated by qPCR, but no difference was detected in control and *CerS2*$^{\Delta BKO}$ islets (Fig.21A). Then, protein levels of PC1 and ANXA6 were determined by immunoblot. In contrast to *CerS2*$^{\Delta INS1E}$ cells, ANXA6 protein was not increased in *CerS2*$^{\Delta BKO}$ islets compared to control (Fig.21B and Fig.21C). However, in line with *CerS2*$^{\Delta INS1E}$ cells, mature PC1 protein was significantly reduced by approximately 40% in *CerS2*$^{\Delta BKO}$ islets compared to control (Fig.21D and Fig.21E).
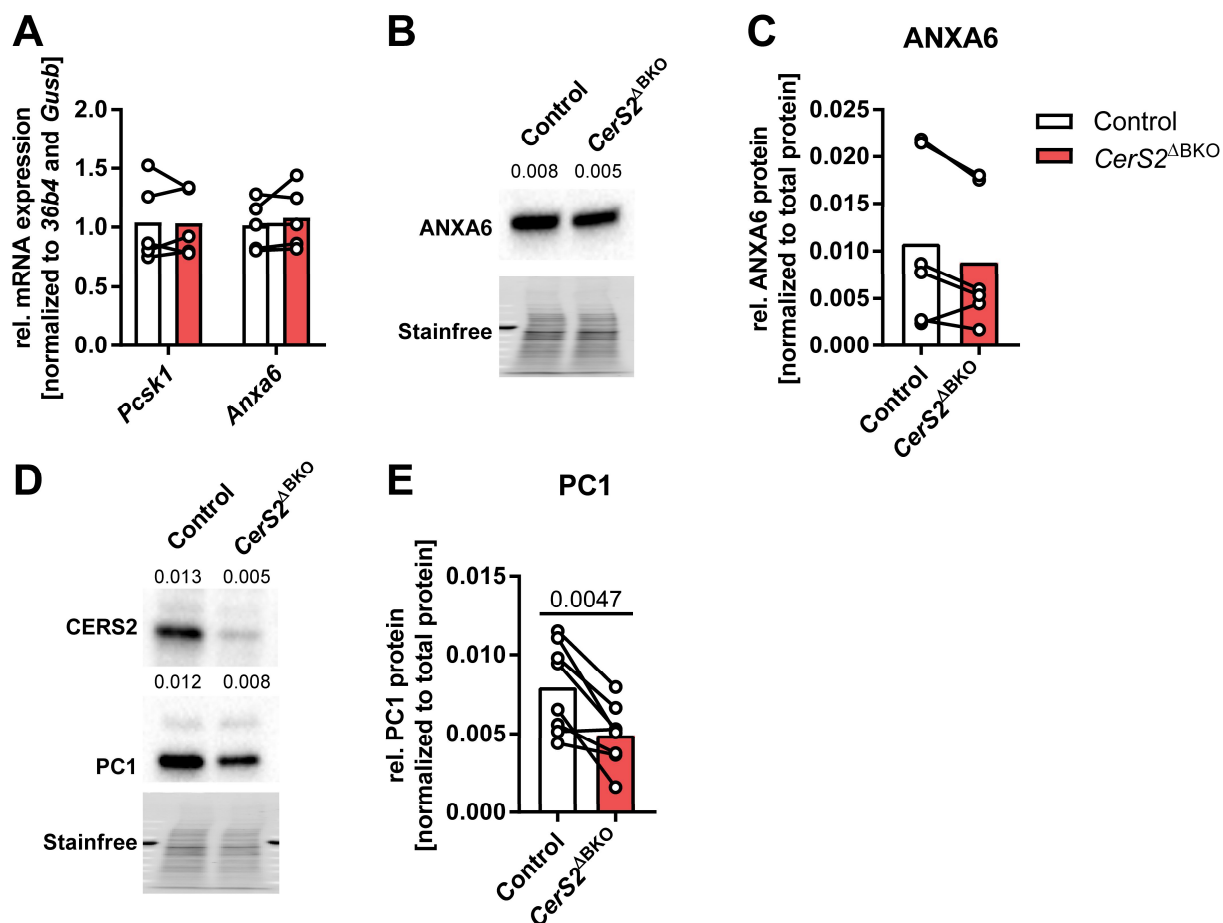
Figure 21: PC1 protein is reduced in *CerS2*$^{\Delta BKO}$ islets. A) Relative mRNA expression of *Pcsk1* and *Anxa6* in control and *CerS2*$^{\Delta BKO}$ islets. n= 5 independent experiments. **B)** Representative immunoblot of ANXA6 in control and *CerS2*$^{\Delta BKO}$ islets. **C)** Quantification of ANXA6 in control and *CerS2*$^{\Delta BKO}$ islets. n= 6 independent experiments. **D)** Representative immunoblot of CERS2 and PC1 in control and *CerS2*$^{\Delta BKO}$ islets. **E)** Quantification of PC1protein in control and CerS2$^{\Delta BKO}$ islets. n= 8 independent experiments. Shown are means and significant p-values. Lines connect quantified data from control and *CerS2*$^{\Delta BKO}$ islets of the same experiment. Numbers in immunoblot display quantified intensity of bands. Stainfree was used for normalization of band intensity to total protein. Significance was determined by by multiple t-test corrected with Holm-Sidak method (**A**) or Student's paired two-tailed t-test (**C**, **E**).

Since PC1 and PC2 consecutively cleave insulin in secretory granules and PC2 maturation occurs in a similar manner as PC1 by autocatalytic cleavage processes, PC2 protein levels were analyzed in *CerS2*$^{\Delta INS1E}$ cells and *CerS2*$^{\Delta BKO}$ islets on immunoblot (Fig.22A and Fig.22C). In contrast to PC1, PC2 was not significantly altered in *CerS2*$^{\Delta INS1E}$ cells as well as in *CerS2*$^{\Delta BKO}$

islets compared to controls (Fig.22B and Fig.22D). CPE was not analyzed in this thesis due to unavailability of specific antibodies.
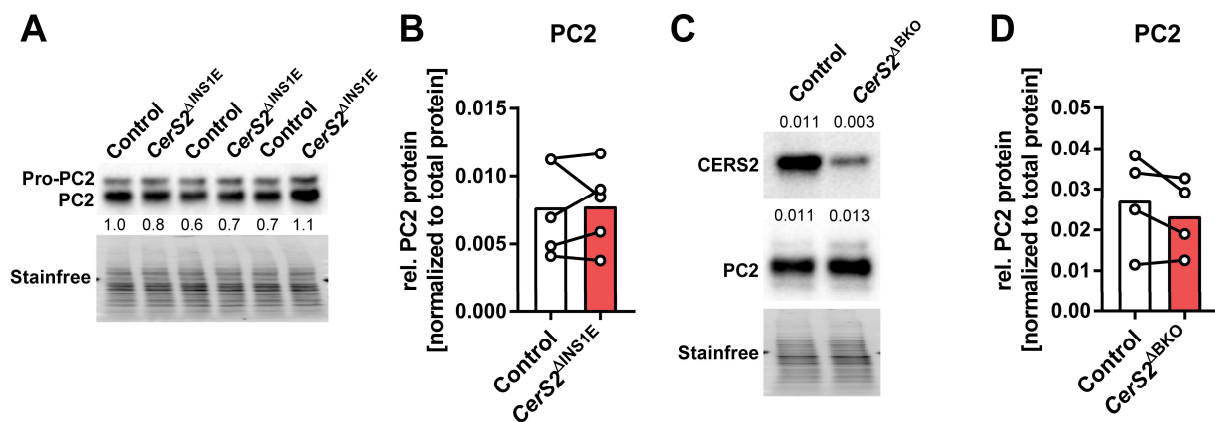
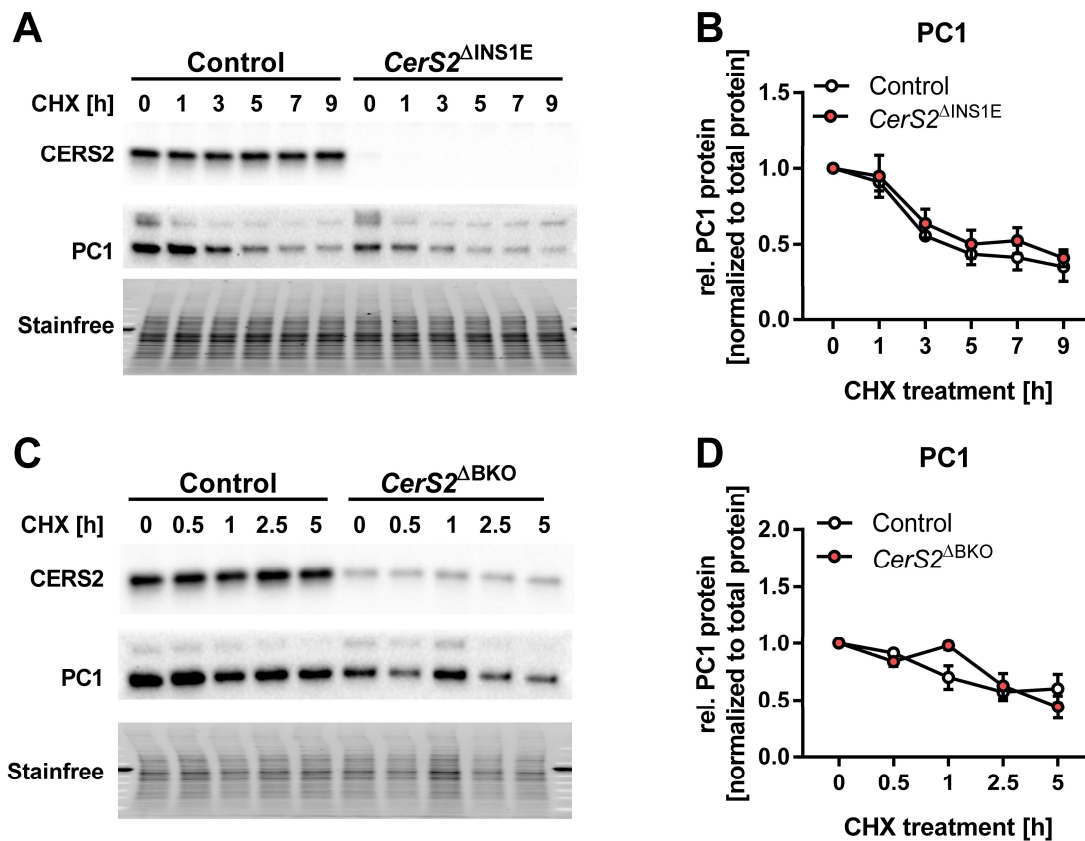**Figure 22: PC2 protein is unaltered in *CerS2*ᐃINS1E cells and *CerS2*ᐃBKO islets. A)** Representative immunoblot of PC2 in control and *CerS2*ᐃINS1E cells. **B)** Quantification of PC2 in control and *CerS2*ᐃINS1E cells. n= 5 independent experiments. **C)** Representative immunoblot of CERS2 and PC2 in control and *CerS2*ᐃBKO islets. **D)** Quantification of PC2 in control and *CerS2*ᐃBKO islets. n= 4 independent experiments. Shown are means and significant p-values. Lines connect quantified data from control and *CerS2*ᐃINS1E cells or respectively *CerS2*ᐃBKO islets of the same experiment. Numbers in imunoblot display quantified intensity of bands normalized to total protein detected by Stainfree. For INS1E experiments, the first control band was set to 1.0. Significance was determined by Student's paired two-tailed t-test (**B**, **D**).

Taken together, we confirmed specific reduction of PC1, but not PC2 protein in *CerS2*ᐃINS1E cells and *CerS2*ᐃBKO islets compared to controls. This potentially leads to decreased insulin content in pancreatic islets as well as whole pancreata, causing an impaired glucose tolerance due to lower plasma insulin concentrations in *CerS2*ᐃBKO mice.

4.11. Unaltered degradation of PC1 in *CerS2*ᐃINS1E cells and *CerS2*ᐃBKO islets

To investigate why mature PC1 protein is decreased after *CerS2* ablation, degradation of PC1 was analyzed in *CerS2*ᐃINS1E cells and *CerS2*ᐃBKO islets by inhibiting the translation of proteins using 100 nM cycloheximide (CHX). INS1E cells and islets were treated with CHX and PC1 degradation was monitored for several hours by immunoblot analysis (Fig.23A-Fig.23D). As mature PC1 protein is decreased after *CerS2* deletion in INS1E cells and islets, time point zero was set to one. Quantifications of immunoblots showed comparable PC1 degradation kinetics in *CerS2*ᐃINS1E cells as well as *CerS2*ᐃBKO islets compared to control (Fig.23B and Fig.23D). Consequently, PC1 reduction after *CerS2* ablation is not caused by increased PC1 degradation. Therefore, reduced PC1 protein levels could arise from maturation defects of PC1 due to mislocalization or malfunctions in posttranslational processing of the protein. Another possibility would be that more PC1 is secreted from beta cells. However, this is unlikely due to unchanged secretory capacities of *CerS2*ᐃBKO islets (see Fig.14D). Lastly, translation of PC1 could be dysfunctional after *CerS2* ablation.

Figure 23: PC1 degradation is unaltered in *CerS2*[ΔINS1E] cells and *CerS2*[ΔBKO] islets. A) Representative immunoblot of CERS2 and PC1 in control and *CerS2*[ΔINS1E] cells treated with 100 nM cycloheximide (CHX) for several hours. **B)** Quantification of PC1 in control and *CerS2*[ΔINS1E] cells. n= 4 independent experiments. **C)** Representative immunoblot of CERS2 and PC1 in control and *CerS2*[ΔBKO] islets treated with 100 nM cycloheximide (CHX) for several hours. **D)** Quantification of PC1 in control and *CerS2*[ΔBKO] islets. n= 3 independent experiments. Shown are means ± SEM. Significance was determined by two-way ANOVA corrected by Sidak meththod (**B**, **D**).
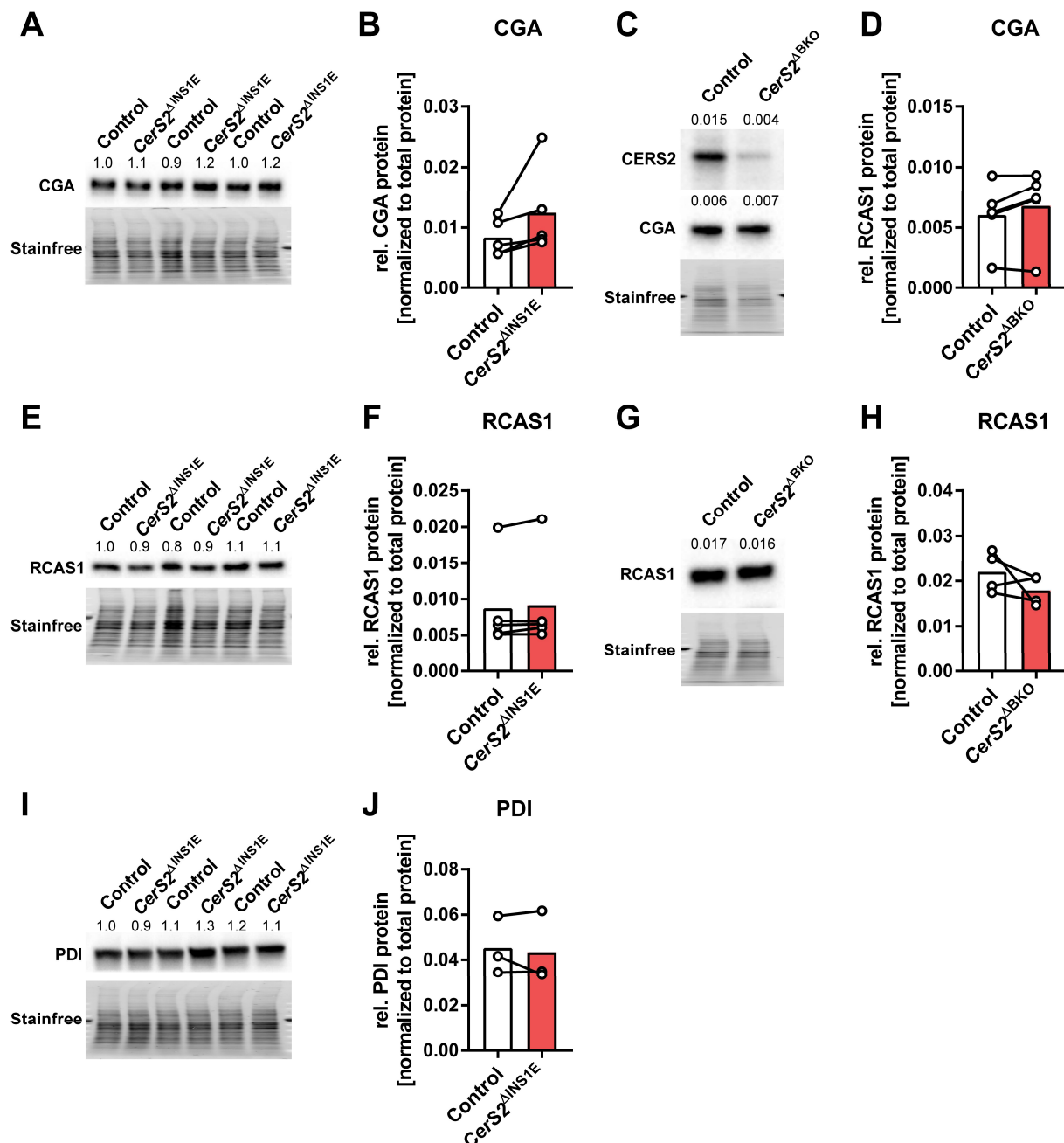
4.12. *CerS2* deletion does not affect protein expression of different organelle markers

To investigate if cellular architecture is altered after *CerS2* deletion and thus potentially change PC1 localization and maturation, we examined different marker proteins for Golgi, ER and secretory vesicles by immunoblot in control and *CerS2*[ΔINS1E] cells and *CerS2*[ΔBKO] islets.

We used protein disulfide isomerase (PDI, also known as P4HB) as a marker protein for the ER, receptor binding cancer antigen expressed on SiSo cells (RCAS1) as a marker protein for the Golgi and chromogranin A (CGA) as a marker protein for secretory granules.

PDI resides in the ER, where it interacts with proinsulin and supports sufficient folding and formation of three native disulfide bonds in proinsulin [305,306]. RCAS1 is a transmembrane protein, predominantly expressed in the Golgi and shuttles between the ER-Golgi compartment and *cis*-Golgi [307,308]. In addition RCAS1 was shown to negatively regulate vesicle trafficking from ER to Golgi [308]. CGA is present in secretory granules and is suggested to be involved in granule biogenesis and cargo sorting to the secretory pathway [118,309,310].

Immunoblots showed no significant differences in expression of CGA (Fig.24A-Fig.24D) and RCAS1 (Fig.24E-Fig.24H) in CerS2$^{\Delta INS1E}$ cells as well as CerS2$^{\Delta BKO}$ islets compared to controls In addition, PDI protein levels were unaltered in CerS2$^{\Delta INS1E}$ cells (Fig.24I-Fig.24J). This indicates that organelle markers are unchanged after *CerS2* deletion. Furthermore, PDI protein is increased during ER stress [311–313]. Unchanged expression of PDI protein at basal conditions, as well as unchanged mRNA expression of seven of nine ER stress markers depicted in Fig.8H for *CerS2*$^{\Delta BKO}$ islets and Fig.17F for *CerS2*$^{\Delta INS1E}$ cells, indicate normal ER homeostasis after *CerS2* deletion. In addition, equal levels of RCAS1, CGA and PC2 protein suggest that specifically PC1 reduction is involved in impaired insulin processing and secretion.

Figure 24: Ablation of *CerS2* does not affect protein expression of different organelle marker. A) Representative immunoblot of secretory granule marker CGA in control and *CerS2*[ΔINS1E] cells or **C)** control and *CerS2*[ΔBKO] islets. **B)** Quantification of CGA in control and *CerS2*[ΔINS1E] cells or **D)** control and *CerS2*[ΔBKO] islets. n= 5 independent experiments. **E)** Representative immunoblot of Golgi marker RCAS1 in control and *CerS2*[ΔINS1E] cells or **G)** control and *CerS2*[ΔBKO] islets. **F)** Quantification of RCAS1 in control and *CerS2*[ΔINS1E] cells or **H)** control and *CerS2*[ΔBKO] islets. n= 4-5 independent experiments. **I)** Representative immunoblot of ER marker PDI in control and *CerS2*[ΔINS1E] cells. **J)** Quantification of PDI in control and *CerS2*[ΔINS1E] cells. n= 3 independent experiments. Shown are means and significant p-values. Lines connect quantified data from control and *CerS2*[ΔINS1E] cells or respectively control and *CerS2*[ΔBKO] islets of the same experiment. Numbers in imunoblot display quantified intensity of bands normalized to total protein detected by Stainfree. For INS1E experiments first control band was set to 1.0. Significance was determined by Student's paired two-tailed t-test (**B, D, F, H, J**).

4.13. Inhibition of sulfation by knockdown of *Tpst1* and *Tpst2* increases mature PC1 protein levels

During maturation, Pro-PC1 is N-glycosylated and sulfated, which is supposed to affect the maturation process of PC1 and thus its activity [300,314,315]. Tyrosine sulfations are very common posttranslational modifications and are responsible for protein-protein interactions, protein stability, intracellular trafficking and proteolytical processing of secreted proteins [316,317]. Tyrosine sulfation of Pro-PC1 occurs in the *trans*-Golgi complex and is predicted at Tyr701 due to undetectable sulfation after C-terminal cleavage of PC1 in secretory granules [314,318]. However, the role of posttranslational Pro-PC1 sulfation is unknown.

In order to analyze, if inhibition of posttranslational sulfation alters PC1 protein expression or maturation, we simultaneously knocked down the two tyrosylprotein sulfotransferase (*Tpst*) isoforms *Tpst1* and *Tpst2* in INS1E cells. These are the only known enzymes that transfer sulfate to tyrosine residues [319]. qPCR revealed efficient knockdown of *Tpst1* and *Tpst2* by approximately 80% (Fig.25A). Notably, inhibition of sulfation by *Tpst1* and *Tpst2* double knockdown was able to enhance mature PC1 protein by approximately 55% (Fig.25B and Fig.25C). To investigate, if *Tpst1* and *Tpst2* expression is altered after ablation of *CerS2*, qPCR was performed. However, no difference in expression of *Tpst1* and *Tpst2* was detected in *CerS2*$^{\Delta INS1E}$ cells and *CerS2*$^{\Delta BKO}$ islets compared to controls (Fig.25D and Fig.25E), indicating that altered tyrosine sulfation is probably not the cause for reduced PC1 levels in CERS2 deficient beta cells. Nonetheless, further analysis of TPST protein levels in *CerS2*$^{\Delta INS1E}$ cells and *CerS2*$^{\Delta BKO}$ islets will clarify the contribution of tyrosine sulfation after *CerS2* ablation.
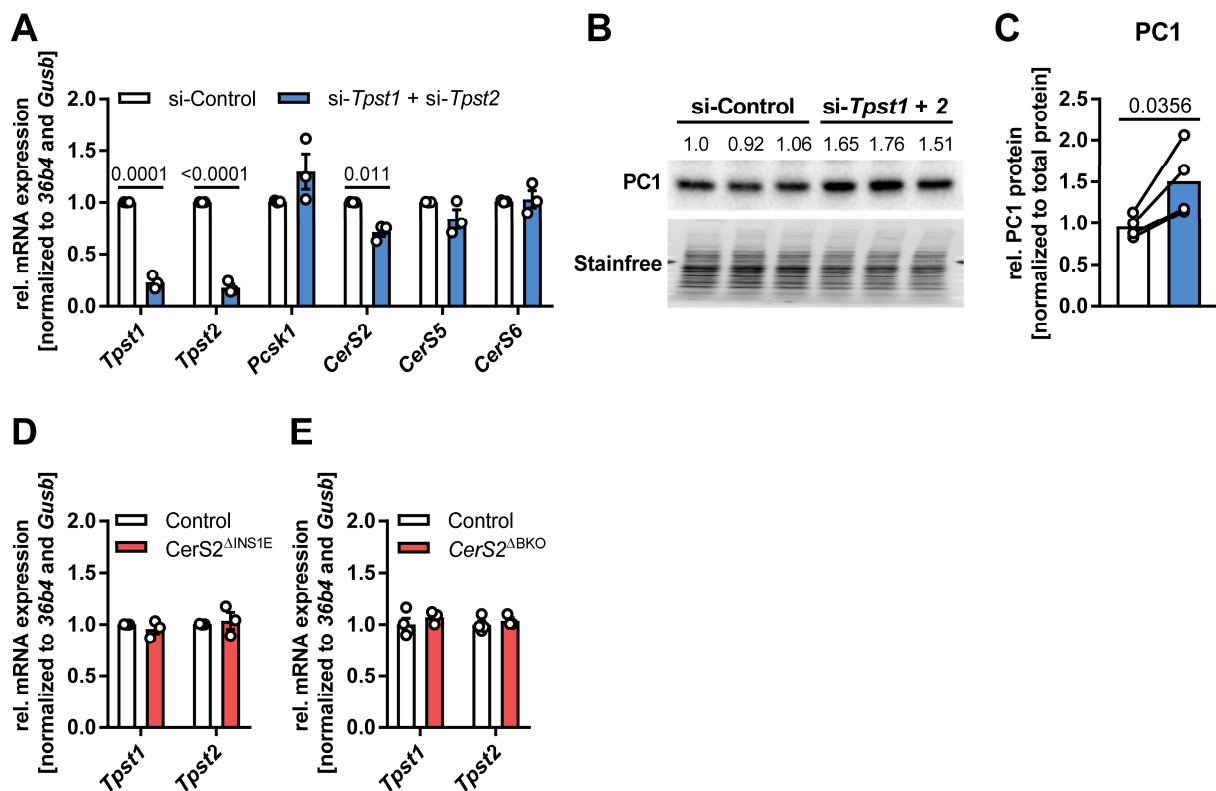
Figure 25: Inhibition of posttranslational sulfation of proteins by downregulation of *Tpst1* and *Tpst2* increases mature PC1 protein levels. A) Relative mRNA expression of genes after double knockdown of *Tpst1* and *Tpst2* (each 25 nM) for 48 hours. n= 3 independent experiments. B) Representative immunoblot of PC1 after *Tpst1* and *Tpst2* double knockdown (each 25 nM) for 48 hours. C) Quantification of PC1 protein after double knockdown of *Tpst1* and *Tpst2* (each 25 nM) for 48 hours. n= 4 independent experiments. D) Relative mRNA expression of *Tpst1* and *Tpst2* in control and *CerS2*$^{\Delta INS1E}$ cells. n= 3 independent experiments. E) Relative mRNA expression of *Tpst1* and *Tpst2* in control and *CerS2*$^{\Delta INS1E}$ cells. n= 4 independent experiments. Shown are means ± SEM and significant p-values. Significance was determined by multiple t-test corrected with Holm-Sidak method (A, D-E) or by Student's paired two-tailed t-test (C).

5.   Discussion

Sphingolipids are an important and diverse class of lipids that are structural components of cell membranes and act as signaling molecules [143]. Due to their implication in several cellular processes and diseases, sphingolipids are in focus of many studies and beneficial or harmful properties have been attributed to specific sphingolipid species [144]. Sphingolipid biosynthesis starts in the ER by *de novo* generation of ceramides, which are the central metabolite for production of complex sphingolipids. Importantly, six different enzymes, CERS1-6, specifically generate ceramide species with varying fatty acid chain length ranging between 14 and 36 carbon atoms (C16-C36) [184]. Especially long C16 ceramides, generated by CERS5 and CERS6, are associated with harmful effects on cellular function and physiology, such as apoptosis and development of insulin resistance, while very long C24 ceramides, generated by CERS2, are proposed to have cell protective effects [197,198,236,237,320]. However, the role of different CERS and long and very long chain ceramides as well as sphingolipid species in pancreatic beta cells are largely unknown. Therefore, we analyzed in this thesis which sphingolipid species are altered in islets of diabetic db/db mice and further investigated the role of very long chain ceramide and sphingolipid species in beta cells by beta cell specific ablation of *CerS2* in mice, as well as in the rat beta cell line INS1E.

5.1.   Accumulation of ceramides and sphingadiene containing sphingolipids might contribute to beta cell dysfunction during the development of T2D

Alterations in sphingolipids are associated with several diseases, such as diabetes, and contribute to cellular dysfunctions [217,258,321]. Previous studies have mainly analyzed sphingolipids in plasma and distinct organs, such as the liver, skeletal muscle and adipose tissue, in humans or mice. However, alterations in sphingolipids during the development of obesity and T2D in pancreatic islets and thus their potential involvement in beta cell dysfunction have not been investigated so far. Therefore, db/db mice were used in this study. These mice develop obesity, insulin resistance, relative hyperinsulinemia and marked hyperglycemia, closely resembling the progression of T2D in humans [282,322,323]. Using 6 week old, prediabetic (obese, but normoglycemic) and 12 week old diabetic (obese and hyperglycemic) db/db mice, we identified that long and very long chain ceramides (d18:1) as well as sphingadiene containing ceramides and sphingomyelins (d18:2) accumulate in islets during development of T2D (Fig.7J and S.Tab.1).

To date, only a small number of publications exist that investigated sphingolipids with a specific chain length in beta cells or pancreatic islets. Former studies have mainly analyzed a limited number of sphingolipid species *in vitro* in pancreatic beta cell lines or *ex vivo* in mouse and human islets, which were treated with palmitate to study lipotoxicity. Although there were some differences between distinct studies, palmitate treatment leads to the accumulation of several

ceramide species in mouse islets, INS1 and MIN6 cells. Most experiments demonstrated that palmitate treatment increased C18:0 and 20:0 ceramides in mouse islets, INS-1 and MIN6 cells, while in some other *in vitro* studies C16:0, C22:0, C24:0 or C24:1 ceramide species were additionally increased [262,265,324]. However, ceramides were not significantly altered in human islets treated with palmitate for three or seven days [325]. Ceramides are the best studied sphingolipids and were shown to contribute to beta cell dysfunction and apoptosis. *In vitro* and *ex vivo* studies in beta cell lines as well as in human and rodent islets demonstrated that ceramide accumulation induced by e.g. palmitate or ceramide treatment leads to reduced insulin gene expression, impaired insulin biosynthesis, decreased insulin content, impaired insulin secretion and increased apoptosis [258–260,262,270,272,326–328]. Furthermore, inhibition of ceramide de novo synthesis by myriocin, fumonisin B1 or L-cycloserine partially rescues lipotoxicity induced apoptosis *in vitro*, *ex vivo* and *in vivo* [259,260,262,265,268,269,329,330].

While the effects of ceramides on cellular physiology were extensively studied, the function and relevance of sphingadienes and sphingadiene containing sphingolipids are largely unknown and often not analyzed [293,331]. Sphingadienes are the second most abundant sphingoid backbone in human plasma and contain an additional *cis* double bond, which leads to a bent structure [293,331]. As other sphingoid backbones, sphingadienes can be used in the sphingolipid metabolism to generate sphingadiene containing ceramides with almost the same efficiency [294]. However, metabolization of sphingadiene containing ceramides into other sphingolipids was shown to be slower than ceramide [331]. Furthermore, sphingadiene-1-phosphate is less susceptible to degradation by S1P lyase [294]. In pancreatic islets sphingadiene containing sphingolipids (d18:2) were much less present in comparison to sphingolipids which have a sphingosine backbone (d18:1). Very recently, two independent research groups identified the fatty acid desaturase 3 (FADS3), which is localized in the ER and predicted to also localize in mitochondria, to be responsible for inserting the second double bond into the sphingoid backbone [293,294,332]. The introduced kink is proposed to reduce the packing density of membranes [331]. FADS3 deficient mice displayed no major abnormalities and have normal survival, growth and fertility rate [333]. However, glucose tolerance, insulin sensitivity and insulin secretion under normal and obesogenic conditions were not analyzed in those mice so far. Previous studies showed that sphingadienes inhibit translocation of AKT from the cytosol to the plasma membrane, leading to increased apoptosis and autophagy in neuroblastoma and HeLa cells [334,335]. Thus, we suggest that accumulation of sphingadiene containing ceramides and sphingomyelins contribute to beta cell dysfunction and apoptosis, but further anaylses are required to analyze the role of FADS3 and resulting sphingadiene species in beta cells.

Furthermore, we detected that specifically C24:1 sphingomyelins and hexosylceramides were decreased in islets of db/db mice at an age of 12 weeks, leading to an increased ratio of

C16:0/C24:1 and an imbalance of long and very long chain sphingolipids during the development of hyperglycemia (Fig.7). Palmitate treated MIN6 cells were found to have elevated levels of C18:0 sphingomyelins, but decreased levels of C24:0 and C24:1 sphingomyelins in one study and unchaged levels in another study [324,330]. In contrast, several glucosylceramides, including C16:0, C18:0, C20:0, C22:0, C24:0 and C24:1, were increased after palmitate treatment in MIN6 cells, while no alterations were detected in mouse islets [324,330]. In addition, contradictory data was observed for sphingomyelins. Moreover, palmitate treatment of human islets led to significantly increased C24:1 sphingomyelin, while no difference in sphingomyelin species was present in mouse islets after palmitate treatment [324,325]. However, palmitate treatment *in vitro* and *ex vivo* cannot fully reflect the complexicity of diabetes development *in vivo*, which involves the crosstalk between different organs as well as their interaction with exogenous factors. In this study, islets of db/db mice were collected six hours after islet isolation for lipidome analysis without culturing them for several days in media, which might better represent the physiological state. Previous studies have shown that distinct ceramide ratios (e.g. C16:0/C24:0 and C18:0/C16:0) can be used to predict the development of cardiovascular complications or T2D [336]. Based on previously described plasma ceramide ratios, we calculated distinct ratios of different sphingolipids for pancreatic islets. Our analysis suggests that increased C16:0/C24:1 ratios might be an indicator for diabetes-associated beta cell dysfunction at least in mouse islets. It would be interesting to see if this ratio is also altered in other tissues of different diabetic mouse models as well as in human biopsies and associates with diabetes.

5.2. Beta cell specific *CerS2* knockout mice and *CerS2* knockout INS1E cells are viable

Previous studies using CERS deficient mice revealed that ceramides and sphingolipids with varying acyl chain length have diverse and tissue specific roles in several biological processes, such as cerebellar development, glucose metabolism, hair follicle cycling and maintenance of skin barrier function [198]. However, the role of distinct CERS and sphingolipids with varying chain length in pancreatic beta cell physiology are almost completely unknown. The conventional knockout of *CerS2* in mice almost ablates C22-C24 sphingolipids and leads to myelin sheath defects, cerebellar degeneration and hepatic defects, such as hepatocarcinomas [188,189,232]. Since we aimed to analyze the role of *CerS2* specifically in beta cells, conditional *CerS2* knockout mice were used in this study. Regarding the Cre-loxP system in beta cells, several disadvantages have been reported for distinct beta cell specific Cre driver lines. The previously described *Ins2*-Cre lines, also known as rat insulin promoter (RIP)-Cre lines, were shown to additionally express the Cre recombinase in the brain [337–340]. Furthermore, heterozygous Cre recombinase expression *per se* altered glucose tolerance, pancreatic islet

mass and islet size in *Ins2*-Cre animals when compared to wildtype mice [341,342]. Moreover, inducible mouse insulin promoter (MIP)-Cre[ERT] mice were shown to express human growth hormone (hGH) from the mini-gene, which is commonly used as polyadenylation sequence in many transgenic constructs [343,344]. Therefore, MIP-Cre[ERT] expressing mice exhibited increased pancreatic insulin content as well as beta cell mass and were protected from hyperglycemia induced by high fat diet and STZ treatment [343,344]. In the inducible *Ins1*-Cre[ERT2] mice, Cre-loxP recombination took place in 60-70% of beta cells only [284]. Hence, in this thesis, conditional *CerS2* mice were crossbred with the *Ins1*-Cre driver line, which expresses the Cre recombinase specifically in beta cells as shown on DNA as well as on RNA level in at least five different tissues (Fig.8B and Fig.8C) [284]. While no differences in weight gain and glucose tolerance between wildtype and heterozygous *Ins1*-Cre mice were reported in the original study [284], control and *CerS2*[ΔBKO] mice used in this study were all heterozygous for the *Ins1*-Cre allele. No littermates could be used in experimental cohorts, due to the fact that only every 8th animal would have the correct genotype (male *Ins1*-Cre[tg/+] knock-in, *CerS2*^{fl/fl} or male *Ins1*-Cre[tg/+] knock-in, *CerS2*^{+/+}, respectively). Thus, wildtype breedings and mutant breedings were set up individually. To exclude genetic drift between wildtype and mutant breedings, all breedings were set up from one pool of mice generated by crossbreeding of heterozygous animals of the same generation.

A previous study reported that conditional deletion of the homeodomain or mutation of the catalytic domain in *CerS2* in mice on a C57BL6/J background reduced the number of born homozygous transgenic offspring from an expected Mendelian ratio of 25% to 17%, which might result from premature death during late embryonic development or more likely immediately after birth [345]. In contrast, conventional *CerS2* null mice on a mixed background of 129S4/SvJae and C57BL/6 were born with normal Mendelian ratios [189], suggesting that the genetic background was responsible for the observed discrepancy. Moreover, on a C57BL6/J background less than 10% of born offspring from heterozygous breedings were *CerS2* null mice (personal communication with Dr. Michael Rieck, DDZ). However, the exact reason of premature death and the impact of genetic background remain unclear. Furthermore, whole body *CerS2* knockout mice exhibited significantly reduced body weight and size, independent of the used background [189,320,345]. Herein, we report that beta cell specific *CerS2* knockout mice are viable and possess similar body weights as controls.

In addition, we successfully generated monoclonal *CerS2* knockout INS1E cells, which are a suitable model for analyzing beta cell physiology *in vitro*, by deleting the same exons as in our mouse model using the CRISPR/Cas9 system (Fig.17). Multiple clones of *CerS2*[ΔINS1E] cells were viable and possessed similar proliferation rates and ATP content as control cells (Fig.17). Furthermore, *CerS2* ablation did not induce significant levels of apoptosis in *CerS2*[ΔINS1E] cells as well as *CerS2*[ΔBKO] islets, at least at unstressed conditions (data not shown). This differs

from previous observations in livers from conventional *CerS2* null mice, in which proliferation, but also apoptosis was increased in 30 days old mice [232]. On the other hand, *CerS2* knockdown *in vitro* in SMS-KCNR neuroblastoma cells decreased cell growth due to cell cycle arrest, without affecting apoptosis [346]. This might indicate that CERS2 or very long chain sphingolipids differentially regulate proliferation and apoptosis in distinct tissues. To further clarify the role of CERS2 in proliferation in usually rarely dividing adult primary pancreatic beta cells, beta cell proliferation can be studied by treating *CerS2*^ΔBKO islets with the small molecule harmine or the insulin receptor antagonist S961 [229,347–349].

In *CerS2*^ΔBKO islets, 20-30% of residual *CerS2* mRNA or CERS2 protein could be detected, which likely derives from non-beta cells in the islets (Fig.8C-Fig.8F). Indeed, *CerS2* is the highest expressed *CerS* in alpha, beta, delta, epsilon and PP cells in humans [350].

CERS are regulated by various mechanisms, such as at epigenetic, transcriptional, posttranscriptional and posttranslational level [351]. In this thesis, we demonstrated that specifically *CerS2* mRNA expression was strongly reduced in islets of *CerS2*^ΔBKO mice, as well as in *CerS2*^ΔINS1E cells, without changing the expression of other *CerS* (Fig.8D and Fig.17B). In contrast, previous studies have shown, that knockdown or knockout of *CerS2 in vitro* and *in vivo* leads to compensatory upregulation of *CerS5* and/or *CerS6*, for example in the liver [189,237,346,352,353]. Indeed, counterregulation of *CerS* seems to be organ and cell type specific. While no coregulation of other *CerS* was observed in adipose tissue, *CerS4* expression was exclusively downregulated in skeletal muscle of conventional *CerS2* knockout mice [352]. In addition, *CerS* expression was shown to be regulated by various stressors *in vitro* [351]. However, in INS1E cells or pancreatic mouse islets, treatment with distinct diabetogenic stress types, such as lipotoxicity (palmitate), glucotoxicity (high glucose), ER stress (tunicamycin), oxidative stress (DetaNO) or DNA damage (STZ) did not or only mildly altered *CerS* mRNA expression (data not shown). This indicates that CERS are rather regulated at posttranslational level than on transcriptional level in pancreatic beta cells. Moreover, several studies reported that mRNA expression of *CerS* did not always correlate with CERS protein levels, CERS activity or corresponding ceramide acyl chain lengths [172,346,354,355]. CERS activity and stability is influenced by posttranslational modifications, such as glycosylations and phosphorylations, and interactions with other proteins and lipids, which might promote rapid alterations in CERS activity after several stress stimuli [351,354]. It was shown that CERS form hetero- and homodimers with each other, which influence their activity [351]. For example, CERS2 forms heterodimers with CERS4, CERS5 or CERS6, which leads to increased activity of CERS2 [351,354,356]. In the liver of *CerS2* null mice CERS activity towards C18-C24 fatty acyl-CoAs was shown to be significantly decreased indicating reduced CERS4 activity [188]. In contrast, CERS activity towards very long C22-C24 fatty acyl-CoAs was specifically reduced in the brain of *CerS2* null mice [188]. This argues for organ specific differences of fatty acyl usage

or activity of various CERS. However, how the lack of CERS2 influences the activity of other CERS is largely unknown and sphingolipidome analyses are necessary to determine the final outcome.

5.3.   CERS2 is required for maintaining the balance between long and very long chain sphingolipids in beta cells

In this study, we demonstrated that CERS2 is essential for the generation of very long chain sphingolipids with an acyl chain length of C22-C26 in islets from *CerS2*ΔBKO mice, as well as *CerS2*ΔINS1E cells (Fig.9 and Fig.18). This is in line with previous studies, which have analyzed the sphingolipidome in the liver, brain and kidney of heterozygous and homozygous *CerS2* knockout mice [188,189,232]. In addition, C20:0 ceramides and sphingomyelins were decreased in *CerS2*ΔBKO islets. This demonstrates that CERS2 either may be able to generate C20:0 ceramides as well, or that the lack of CERS2 decreases CERS4 protein levels or activity in *CerS2*ΔBKO islets, since *CerS4* mRNA expression was not altered in *CerS2*ΔBKO islets (Fig.8D). Unaltered CerS4 mRNA expression was also observed in the liver of *CerS2* null mice [189]. In contrast, *CerS4* mRNA expression was undetectable using two different primer pairs by qPCR analysis in INS1E cells (own observations). More importantly, we showed that long chain C16:0 sphingolipids, except for hexosylceramides and dihydrodeoxyceramides, were not significantly altered in *CerS2*ΔBKO islets (Fig.9 and S.Tab.2). However, remaining *CerS2* expression in non-beta cells might partially conceal the total increase of C16:0 ceramides in pancreatic beta cells of *CerS2*ΔBKO islets. In contrast, C16:0 and C18:0 sphingolipids were increased in *CerS2*ΔINS1E cells compared to control (Fig.18 and S.Tab.3). Previous studies demonstrated that C16:0 ceramides were strongly increased in the liver, brain and kidney after deletion of *CerS2* in mice or in several cell lines after knockdown of *CerS2* [188,189,191,232,346,353]. Moreover, heterozygous *CerS2* knockout mice exhibited increased C16:0 ceramide levels in the liver when fed with a HFD [237,238]. Inhibition of ceramide *de novo* synthesis using the SPT inhibitor myriocin prevented triglyceride accumulation and liver steatosis in heterozygous *CerS2* knockout mice, leading to the assumption that mainly the increase in C16:0 ceramides, not the decrease in very long chain ceramides is responsible for the pathology [237].

The strong reduction in very long chain sphingolipids in *CerS2*ΔBKO islets and *CerS2*ΔINS1E cells decreased the total amount of several sphingolipid classes, as well as total amount of all measured sphingolipids (Fig.9 and Fig.18), raising the question if cellular fatty acid uptake is altered, or if not, where the residual long chain fatty acids not used for sphingolipid synthesis are utilized in the cell. Several studies reported that the sphingoid base sphinganine strikingly accumulates in the liver of heterozygous and homozygous *CerS2* knockout mice [189,232,237]. We observed significantly elevated sphinganine levels in *CerS2*ΔINS1E cells, but no difference was detected in *CerS2*ΔBKO islets (S.Tab.2 and S.Tab.3). However, the increase in

sphinganine (~3.6 fold) in $CerS2^{\Delta INS1E}$ cells was quite low when compared to the 50 fold increase in liver of $CerS2$ null mice [189,232,237]. Furthermore, not all sphingolipids, e.g. very complex glycosphingolipids or S1P, could be detected in this thesis for technical reasons and might be increased in CERS2 deficient islets or INS1E cells. In addition, ablation of $CerS2$ might decrease SPT activity or increase S1P lyase activity through secondary effects. However, alterations in SPT and S1P lyase activity after $CerS2$ ablation have not been examined in this or other studies. Moreover, sphingolipid metabolism is closely linked to glycerolipid and sterol metabolism and sphingolipids can be eventually processed into complex lipids, such as TAG, DAG, cholesteryl ester and phospholipids [245]. However, some glycerophospholipid species, like lysophosphatidylcholine, phosphatidylcholine and phosphatidylethanolamine, are actually decreased in $CerS2^{\Delta BKO}$ islets compared to controls (S.Fig.3A and S.Tab.4). In addition, the sum of all measured phosphatidylglycerols was decreased, while total amounts of all measured lipids were not significantly altered in islets from $CerS2^{\Delta BKO}$ mice compared to controls (S.Fig.3B and S.Fig.3C). A previous study showed that total amounts of glycerophospholipids were unaltered in the liver of 30 day old $CerS2$ null mice [189]. Therefore, the uptake of fatty acyl-CoAs may be decreased or fatty acyl-CoAs potentially not used for sphingolipid biosynthesis have to be metabolized by another pathway in $CerS2^{\Delta BKO}$ islets. Fatty acyl-CoAs can additionally be catabolized for energy production by mitochondrial fatty acid beta oxidation, which is the major pathway for fatty acid degradation [357]. However, we did not detect any changes in ATP levels in $CerS2^{\Delta INS1E}$ cells under unstressed conditions (Fig.17I) and thus impaired fatty acid degradation by β-oxidation is unlikely. Previous studies demonstrated that elevated C16 ceramide levels in the liver of homozygous $CerS2$ knockout mice or HFD fed heterozygous $CerS2$ knockout mice impair mitochondrial fatty acid oxidation in the liver by inhibiting complex II and complex IV of the electron transport chain in mitochondria [191,237]. This in turn promote accumulation of triglycerides in the liver of HFD fed heterozygous $CerS2$ knockout and leads to hepatosteatosis [237]. Due to non-significantly altered C16:0 ceramides and triglyceride levels in $CerS2^{\Delta BKO}$ islets, we assume that beta oxidation is not impaired, at least at unstressed conditions. Nevertheless, further experiments are necessary to verify the role of CERS2 and very long chain sphingolids in mitochondrial function of pancreatic beta cells.

5.4. *CerS2* ablation does not induce overall beta cell dedifferentiation or UPR stress activation

Several mechanisms are thought to contribute to beta cell demise in T2D. One major proposed mechanism for the loss of functional beta cell mass is that beta cells lose their identity and dedifferentiate and/or transdifferentiate into progenitor-like cells or non-beta cells [43,358]. In T2D, beta cell markers, such as PDX1, NKX6.1, GLUT2, FOXO1 and INS were shown to be reduced

in human pancreatic islets, although others do not find evidence for significant beta cell dedifferentiation [66,71,72,359]. In this study, we demonstrated that *CerS2* ablation did not alter beta cell identity in *CerS2*[ΔBKO] islets (Fig.8G). However, *CerS2*[ΔINS1E] cells show partially reduced mRNA expression of beta cell identity markers, such as *Nkx6.1* and *Slc2a2* (Fig.17E). NKX6.1 was shown to be important for maintaining beta cell function and regulates insulin biosynthesis, insulin secretion and beta cell proliferation [360]. In addition, NKX6.1 acts as transcriptional regulator of several genes invoved in beta cell processes, including *Slc2a2*, which was shown to be downregulated in pancreatic islets of *Nkx6.1* knockout mice [360]. *Slc2a2* encodes for the glucose transporter GLUT2, and knockout of *Slc2a2* led to impaired glucose stimulated insulin secretion, insulin biosynthesis and hyperglycemia [361–363]. Thus, decreased mRNA levels of *Slc2a2* might be dependent on decreased *Nkx6.1* mRNA expression. In addition, a previous study demonstrated that palmitate induced ceramide synthesis inhibits insulin gene expression at transcriptional level by decreasing insulin promoter activity after glucose stimulation [270]. Although *Nkx6.1* and *Slc2a2* were downregulated in *CerS2*[ΔINS1E] cells, *Ins2* mRNA expression was significantly upregulated (Fig.17E), indicating that INS1E cells can partially compensate for the loss of CERS2 by an unknown mechanism. However, it has to be considered that INS1E cells are an immortalized cell line originating from radiation-induced rat insulinoma [285,364], which can partially behave different from primary beta cells. For example, INS1E cells exhibit high proliferation rates, while primary pancreatic beta cells rarely proliferate [54,365]. Moreover, INS1E cells contain only 20% of native insulin content from pancreatic islets [364]. Therefore, results from primary pancreatic islets of *CerS2*[ΔBKO] mice better reflect the situation *in vivo*, suggesting that CERS2 rather does not play an important role in beta cell identity.

In addition, ER stress is thought to contribute to beta cell dysfunction and apoptosis in T2D. Chronically elevated blood glucose levels leads to upregulation of insulin biosynthesis, which presumably exceed the ER folding capacity. Furthermore, FFA, such as palmitate are suggested to deplete calcium levels in the ER and inhibit ER to Golgi transport [366]. Consequently misfolded and unfolded proteins accumulate in the ER resulting in ER stress and activation of the UPR, which aims to restore ER homeostasis by several mechanisms, including the upregulation of chaperones and protein processing enzymes [367]. Unresolved ER stress further induce beta cell apoptosis by activation of c-Jun N-terminal kinase (JNK) or C/EBP homology protein (CHOP) [366]. In addition, palmitate treatment leads to the accumulation of ceramides in the ER, which is usually present in low concentrations, leading to cellular dysfunction [146,324].

We demonstrated that ablation of *CerS2* does not induce ER stress in beta cells. In *CerS2*[ΔBKO] islets, mRNA expression of nine ER stress markers were unchanged, while in *CerS2*[ΔINS1E] cells two of them (*Chop* and *Hsp60*) were increased by 1.2 to 1.3 fold (Fig.8H and Fig.17F). In comparison, chemical ER stress induction in INS1E cells by thapsigargin and tunicamycin

leads to an upregulation of *Chop* by approximately 10 fold after 6 hours and thus to the activation of the UPR (own experience, unpublished data). This demonstrates that no major ER stress is present in *CerS2*$^{\Delta INS1E}$ cells. Indeed, the UPR is even decreased in *CerS2*$^{\Delta INS1E}$ cells compared to controls after thapsigargin treatment (unpublished data). However, we cannot exclude that UPR activation is dysfunctional in *CerS2*$^{\Delta INS1E}$ cells due to the contribution of sphingolipids in membrane composition, which may modify protein interactions at those sites.

In contrast, previous studies have shown that downregulation of *CerS2* in Hep3B, MCF-7 and SMS-KCNR cell lines induces ER stress indicated by upregulation of the UPR including pEIF2A, pPERK, GRP78 and CHOP [238,346]. Furthermore, heterozygous deletion of *CerS2* leads to a stronger ER stress response in the liver when fed with a HFD [238]. Conversely, CERS2 overexpression in primary mouse hepatocytes or Hep3B cells strongly decreased UPR activation [238,368].

The discrepancy of ER stress induction after *CerS2* ablation in our and other studies might be partially explained by a strong increase in C16:0 ceramides in conventional *CerS2* knockout mice, which was not observed in our study using conditional *CerS2* knockout mice (Fig.9A). C16:0 ceramides are thought to be pro-apoptotic and treatment with C16:0 ceramides, as well as CERS6 overexpression, but not CERS5 overexpression, leads to increased activation of UPR proteins after palmitate treatment in Hep3B cells [238]. Interestingy, a recent study demonstrated that specifically CERS6 derived C16:0 sphingolipids, but not CERS5 derived C16:0 sphingolipids are able to bind GRP78 (also known as BIP), which is the master regulator of the UPR [196,369].

To further analyze the role of CERS2 in pancreatic beta cells during ER stress, the Akita mouse model could be bred with *CerS2*$^{\Delta BKO}$ mice. The Akita mouse possesses a mutation in the *Ins2* gene, which leads to the accumulation of misfolded proinsulin in the ER and subsequent ER stress. As a result, Akita mice progressively lose beta cell mass due to apoptosis and develop overt diabetes [81,322].

5.5.   CERS2 is necessary for proinsulin processing

The present study showed that CERS2 deficiency decreased the amount of secretory granules in pancreatic beta cells of *CerS2*$^{\Delta BKO}$ mice, whereby specifically the numbers of mature insulin granules, but not immature and empty granules, were reduced (Fig.16). This was confirmed in lysates of *CerS2*$^{\Delta BKO}$ islets by insulin and proinsulin ELISA (Fig.14C and Fig.14E) and is in line with a previous study, which reported that mature insulin granules were decreased, while immature insulin granules were unaltered in pancreatic beta cells of T2D patients compared to non-diabetic individuals [370]. Due to unaltered glucagon levels in islets and pancreata of *CerS2*$^{\Delta BKO}$ mice (Fig.14G and Fig.15C), as well as similar efficiencies of pancreatic islet

isolations, we suggest that CerS2$^{\Delta BKO}$ mice possess a similar number of islets in the pancreas with a similar composition of alpha and beta cells. However, immunohistological analyses of pancreatic islets will be necessary to determine islet number, composition and size in pancreata of CerS2$^{\Delta BKO}$ mice. A reduction of insulin content by 35%, but similar glucagon levels were also detected in human pancreata of T2D patients compared to non-diabetic individuals [371]. Insulin depletion in T2D has been speculated to originate from several mechanisms, including impaired insulin transcription, decreased insulin mRNA stability, increased insulin degradation, decreased insulin granule biogenesis, basal hypersecretion of insulin, impaired proinsulin processing and sorting [372–374]. In this study we demonstrated that transcription of *Ins1* and *Ins2* was not decreased after *CerS2* ablation (Fig.8G and Fig.17E). Moreover, increased endoplasmic-reticulum-associated degradation (ERAD) activated by the UPR is unlikely due to non-existent ER stress in CERS2 deficient islets and INS1E cells (Fig.8H and Fig.17F). However, other degradation mechanisms like proteosomal degradation or lysosomal degradation of insulin cannot be excluded and could be further investigated by the detection of insulin after inhibiting translation with cycloheximid. Furthermore, basal insulin secretion was unaltered in CerS2$^{\Delta BKO}$ islets (Fig.14B) as well as in glucose tolerance tests of CerS2$^{\Delta BKO}$ mice (Fig.10E and Fig.12E). Importantly, the present study demonstrated for the first time that CERS2 is essential to process proinsulin into insulin in pancreatic beta cells, which takes place in secretory granules by sequential cleavage of proinsulin by PC1, PC2 and CPE [114]. We observed decreased ratios of insulin to proinsulin in CerS2$^{\Delta BKO}$ islets (Fig.14F), which is a hallmark of T2D [113] and points towards impaired processing of proinsulin into insulin. Furthermore, we identified prohormone convertase 1 (PC1, encoded by *Pcsk1*), which is the major enzyme for processing proinsulin into insulin, as significantly reduced in CerS2$^{\Delta BKO}$ islets and CerS2$^{\Delta INS1E}$ cells (Fig.19B, S.Tab.3, Fig.20D-E and Fig.21D-E).

The loss of either *Pcsk1* or *Pcsk2* results in impaired prohormone processing and insulin synthesis with elevations in plasma proinsulin levels [119,298,375]. However, studies with *Pcsk1* and *Pcsk2* null mice have demonstrated a more important role of PC1 in proinsulin processing compared to PC2 [119,298]. While combined action of PC1 and PC2 in insulin synthesis was extensively investigated in mice, a very recent study demonstrated that PC1, but not PC2 is present in healthy human pancreatic beta cells and is responsible for insulin biosynthesis [125]. This study underlines the importance of PC1 in proinsulin processing in pancreatic beta cells. Although PC1 and PC2 are generated by similar processes, no reduction in mature PC2 was observed in CerS2$^{\Delta INS1E}$ cells and CerS2$^{\Delta BKO}$ islets (Fig.22). Therefore, *CerS2* ablation seems to specifically impair the generation of mature PC1.

In humans, homozygous or combined heterozygous mutations in *Pcsk1* that lead to PC1 deficiency are rare disorders [300]. Dependent on the pathogenic variant, imbalanced prohormone processing results in an array of metabolic dysfunctions, including early onset of

obesity, several enteroendocrine malfunctions and impaired glucose homeostasis, due to increased circulating proinsulin levels, elevated proinsulin to insulin ratios and impaired glucose tolerance [122,300,376]. In patients with PC1 deficiency, diabetes mellitus is usually not an early clinical manifestation, but can arise later, at least partially due to beta cell exhaustion [300]. In addition, several SNPs have been identified in the *Pcsk1* gene that are linked to obesity, elevated proinsulin levels, increased proinsulin to insulin ratios, postprandial hypoglycemia and impaired glucose tolerance [113,300,377–381].

The present study demonstrated that *Pcsk1* transcription (Fig.21A) and PC1 degradation (Fig.23C-D) were unaltered in *CerS2*[ΔBKO] islets and thus not responsible for reduced PC1 protein levels. These experiments point to dysfunctional PC1 translation or maturation. Maturation of PC1 takes place in the ER, Golgi and finally in secretory granules. Several calcium and pH dependent processes are involved in maturation and activation of PC1 protein, such as autocatalytical cleavage, posttranslational modification by glycosylation as well as sulfation and protein trafficking [296,300]. In this study, we analyzed tyrosyl sulfations as one potential mechanism for PC1 maturation. Sulfation of Pro-PC1 takes place in the *trans*-Golgi network and is predicted at Tyr701 [314,318]. However, the role of Pro-PC1 sulfation is still unknown. In general, tyrosine sulfations are very common posttranslational modifications of many secretory or plasma membrane proteins that are thought to be important for protein-protein interactions, intracellular trafficking, stability and proteolytic processing of secreted proteins [316,317]. The two tyrosyl sulfotransferases (TPST), TPST1 and TPST2, are integral membrane glycoproteins that are localized in the *trans*-Golgi network and are the only enzymes, which are able to transfer sulfate from the sulfate donor 3′-phosphoadenosine-5′-phosphosulfate (PAPS) to tyrosine residues of target proteins [317,319,365]. In this study, we surprisingly observed that sulfation of PC1 might inhibit its maturation or trafficking to secretory granules, as indicated by increased PC1 levels after double knockdown of *Tpst1* and *Tpst2* in INS1E cells (Fig.25B-C). Since insulin secretion was not analyzed after *Tpst1* and *Tpst2* double knockdown in INS1E cells, accumulation of PC1 due to impaired insulin secretion ability cannot be excluded. In addition, many other proteins might exist, which can be sulfated by TPST1 and TPST2 [365] and might influence Pro-PC1 processing. Furthermore, mRNA expression of *Tpst1*, as well as *Tpst2* were neither upregulated in *CerS2*[ΔINS1E] cells nor in *CerS2*[ΔBKO] islets (Fig.25D-E). Therefore, altered sulfation of PC1 seems not to be the cause for reduced PC1 protein levels after *CerS2* ablation. Further analyses of TPST1 and TPST2 protein levels in CERS2 deficient islets and INS1E cells will reveal a potential impact of sulfations on PC1 maturation. Moreover, additional experiments have to be performed to show direct sulfation of Pro-PC1 in control and CERS2 deficient cells.

In addition, PC1 is glycosylated in the ER and the Golgi, which affects folding, autocatalytic cleavage, trafficking as well as stability and thus activation of PC1 [314,315]. Previous studies have

shown that PC1 in mice contains three potential glycosylation sites at Asn173, Asn401 and Asn645, whereby only glycosylation of Asn173 is important for autocatalytic cleavage of Pro-PC1 and ER exit [300,315,382]. This site was shown to be glycosylated in humans as well [383]. Further experiments have to be performed to identify if glycosylations in PC1 are altered after *CerS2* ablation, which may lead to less mature PC1 and ultimately insulin processing.

Beside posttranslational modifications, calcium levels as well as proper pH in distinct organelles are important for PC1 activation. However, unaltered processing of mature PC2 in *CerS2*[ΔINS1E] cells and *CerS2*[ΔBKO] islets suggest no striking changes in calcium levels or pH after *CerS2* deletion, but further analysis of organelle specific calcium or pH levels might be useful. Previous studies reported that several SNPs in *Pcsk1* leads to decreased secretion of PC1 and intracellular mislocalization [381,383–386]. Furthermore, some SNPs in *Pcsk1* result in ER retention of PC1, which is associated with increased ER stress [381,384–386]. Although ER stress is not present in *CerS2*[ΔINS1E] cells and *CerS2*[ΔBKO] islets, biophysical properties of membranes might be altered after *CerS2* deletion, which influence localization of PC1. Park and colleagues observed suppressed insulin receptor and AKT phosphorylation in the liver of *CerS2* null mice and showed that translocation of the insulin receptor was impaired in *CerS2* knockout mice indicated by the inability of translocation into detergent resistant membranes. They hypothesized that depletion of very long chain sphingolipids alters biophysical properties of membranes, which prevents translocation of the insulin receptor into lipid rafts [352]. This shows that trafficking of proteins or hormones might be affected after *CerS2* ablation. Moreover, PC1 interacts with membrane lipids at the *trans*-Golgi network, which sorts PC1 to secretory granules [387–391]. Indeed, it is controversely discussed, if PC1 is a transmembrane protein, although it does not possess a predicted transmembrane amino acid sequence [389,390,392,393]. Since PC1 is also secreted from cells, the existence of a transmembrane domain is highly unlikely, as it can detach from membranes as peripheral membrane protein [318,394–398]. Concerning the localization of PC1, the AG Belgardt is currently analyzing PC1 localization by immunohistological analyses with different organelle markers for ER, Golgi and secretory granules. This experiment will determine whether PC1 is mislocalized in the ER or Golgi after ablation of *CerS2*. In addition, PC1 secretion has to be analyzed in CERS2 deficient islets to exclude that decreased levels of PC1 results from increased PC1 secretion.

Heterozygous *Pcsk1* mice possess elevated proinsulin levels, but also increased levels of insulin in pancreatic extracts [119]. This is in contrast to our study. Although PC1 protein is decreased by approximately 40% in *CerS2*[ΔBKO] islets, specifically mature insulin granules seemed to be reduced after *CerS2* deletion, without significant alterations in immature or empty granules (Fig.16 and Fig.21D-E). Unaltered amounts of immature insulin granules in beta cells of *CerS2*[ΔBKO] mice compared to PC1 deficient mice might originate either from increased secretion of immature granules or decreased biogenesis of secretory granules. Based on

similar proinsulin levels in pancreatic islets (Fig.14E) and plasma of *CerS2*^ΔBKO mice (S.Fig.4), similar insulin secretion ability of *CerS2*^ΔBKO islets (Fig.14D), as well as the inability to sufficiently increase plasma insulin levels during GTT (Fig.10E and Fig.12E), increased secretion of immature and mature insulin granules of *CerS2*^ΔBKO islets is highly unlikely. However, elevated secretion of empty granules, which might arise from dysfunctional sorting to secretory granules, cannot be excluded with the performed experiments in this study.

Furthermore, *Pcsk1* null mice appear to be able to generate significant amounts of immature secretory granules [119]. For this reason, it is unlikely that decreased levels of PC1 in *CerS2*^ΔBKO islets are responsible for the reduction in secretory granules. Since PC1 maturation is dependent on secretory granules, we conclude that residual PC1 in pancreatic islets of *CerS2*^ΔBKO mice is at least partially able to synthesize mature insulin in present secretory granules, but is additionally restricted by the reduced number of insulin granules in beta cells of *CerS2*^ΔBKO mice. Therefore, it is possible that *Cers2* ablation alters biophysical membrane properties, which impairs granule biogenesis at the *trans*-Golgi network, leading to insufficient PC1 maturation, as well as proinsulin processing and insulin synthesis. However, the regulation of insulin granule formation at the *trans*-Golgi network is not completely understood. A recent study demonstrated an essential role for the protein Vgf nerve growth factor inducible (VGF) in granule biogenesis [373]. Beta cell specific deletion of *Vgf* in mice strongly reduces the size and amount of secretory granules, which further decreases insulin content in pancreatic islets and leads to glucose intolerance due to insufficient insulin secretion [373]. This demonstrates the importance of functional insulin granule formation and replenishment of granules stores in glucose homeostasis and development of diabetes. However, immunoblot analyses of different organelle markers, such as RCAS1 for Golgi, CGA for secretory granules and PDI for ER, as well as mature PC2 protein were unchanged after *CerS2* deletion (Fig.22 and Fig.24), suggesting that organelles itself might be not affected from *CerS2* ablation. Furthermore, EM images of *CerS2*^ΔBKO islets do not suggest gross abnormalities in organelle structure, but further analyses have to be performed to exclude organelle dysfunctions as a consequence of potential alterations in membrane microarchitecture, turnover or curvature. Moreover, since non-fasted blood glucose levels are similar in *CerS2*^ΔBKO mice, there is not a massive defect in beta cell function under unstressed conditions.

Herein, we demonstrated that deficient proinsulin processing leads to decreased mature insulin in pancreatic beta cells (Fig.16) as well as insulin content in islets (Fig.14C) and pancreata in *CerS2*^ΔBKO mice (Fig.15B and Fig.15E). This further results in strongly decreased glucose stimulated insulin secretion of pancreatic islets (Fig.14B) and lower plasma insulin levels after glucose injections (Fig.10E and Fig.12E), which is responsible for impaired glucose tolerance in *CerS2*^ΔBKO mice, independent of diet and sex (Fig.10-Fig.13). However, the phenotype in male *CerS2*^ΔBKO mice was much stronger than in female *CerS2*^ΔBKO mice

(compare Fig.10 with Fig.11 and Fig.12 with Fig.13). It is well known and accepted that sex affects the pathogenesis of metabolic disorders, including diabetes. Previous studies have shown that estrogen signaling protects beta cells from apoptosis and increases insulin biosynthesis as well as insulin secretion in female mice [399–401]. Thus, to observe a stronger glucose intolerance in female mice, insulin signaling needs to be further disturbed for example by crossing CerS2^ΔBKO mice with insulin resistant ob/ob mice or treating CerS2^ΔBKO mice with the insulin receptor antagonist S961.

While glucose intolerance in CerS2^ΔBKO mice was not associated with insulin resistance (Fig.10H and Fig.11G), previous studies using conventional heterozygous or homozygous CerS2 knockout mice demonstrated that glucose intolerance derived from insulin resistance in the liver [237,238,352]. CerS2 ablation was shown to specifically impair insulin signaling in the liver, while no significant changes were observed in serum insulin levels after glucose injection, as well as insulin secretion from pancreatic beta cells after high glucose stimulation [352]. Nonetheless, the authors did not measure pancreatic insulin content. Moreover, CerS2 null mice lack CERS2 in all cells during embryogenesis and display hypoglycemia, decreased body weights and remarkable defects in the liver and brain [188,189,232,352]. Moreover, these mice were studied on a mixed background. These differences impede the comparability of the two mouse models and might explain the divergent findings from our study using beta cell specific knockout mice.

Importantly, a common missense mutation in more than 20% of Europeans exist in the CerS2 gene (rs267738), which leads to the substitution of glutamine to alanine at position 115 and is associated with indicators for insulin resistance and glucose intolerance, such as HbA1c [237,402,403]. However, functional studies of this polymorphism are missing and its relevance for the development of diabetes is unknown. Therefore, it might be interesting to analyze the impact of this gene variant on pancreatic beta cell physiology.

Furthermore, a previous study reported that mice with BALB/c background were partially protected from glucose intolerance and insulin resistance after receiving HFD feeding in comparison to four other glucose intolerant and insulin resistant mouse strains [404]. This is correlated with enhanced CERS2 protein levels, higher CERS2 activity and elevated very long chain C24 sphingolipids in the liver of BALB/c mice compared to other mouse strains [368]. In accordance, CERS2 overexpression in primary mouse hepatocytes improves insulin signaling, which indicates a protective role of very long chain sphingolipids in glucose tolerance and insulin resistance in the liver [368]. Thus, it would be interesting to study, if overexpression of CERS2 in pancreatic beta cells leads to increased mature PC1 protein levels and/or numbers of secretory granules and thereby additionally improves glucose tolerance.

5.6. Inhibition of global ceramide synthesis as diabetes therapy might impair proinsulin processing and insulin secretion in pancreatic beta cells

Accumulation of ceramides in distinct tissues are associated with increased lipotoxicity and cellular dysfunctions and might contribute to the development of diabetes. Previous studies demonstrated that inhibition of ceramide *de novo* synthesis by chemical inhibition of SPT using myriocin prevents the development of glucose intolerance and insulin resistance *in vivo* in obese mice and rats [203,225–227]. This is accompanied by improved insulin signaling in the liver, adipose tissue and skeletal muscle, reduced body weight gain, enhanced energy expenditure and oxygen consumption [203,225–227]. Moreover, inducible ablation of *Degs1* protected from glucose intolerance, insulin resistance and hepatic steatosis in adult ob/ob and HFD fed mice [229]. Therefore, it is suggested that global inhibition of ceramide synthesis might be a potential therapy to treat metabolic disorders, such as diabetes and obesity [227,229]. However, there are concerns about potential adverse side effects that could appear from global ceramide inhibition in distinct tissues. In mice, homozygous ablation of either *Sptlc1* or *Sptlc2* is embryonic lethal [226,230,231]. Furthermore, homozygous knockout of *Degs1* leads to partially embryonic lethality and surviving litters are growth retarded and die within the first two weeks [227]. In humans, a homozygous *Degs1* variant was identified, which leads to DES1 deficiency and is responsible for hypomyelination and degeneration of the nervous system [289]. Moreover, ablation of *CerS1* was shown to cause cerebellar neurodegeneration [405], *CerS2* deletion is associated with hepatocarcinomas, myelin sheath defects and cerebellar degeneration [188] and ablation of *CerS3* leads to lethal skin barrier dysfunction [192]. In addition, our study provides novel insights in the essential role of CERS2 and very long chain sphingolipids in generating mature insulin granules. Thus, global inhibition of ceramide *de novo* synthesis as diabetes treatment might cause unwanted consequences on beta cell function as well. For this reason, targeting sphingolipids with a specific chain length for example by manipulating *CerS6*, which generates harmful C16:0 sphingolipids, might be a better therapeutic strategy. The role of CERS5 and CERS6 and the impact of C16 sphingolipid depletion on pancreatic beta cell physiology, which has not been examined so far, is currently under investigation in the AG Belgardt. This study might be an important contribution for the individualized treatment of T2D, which has recently been classified in several subgroups by two different research groups [100,101], underscoring the need for personalized therapies.

5.7. Conclusion

The results of this thesis demonstrate an important role of sphingolipids with different chain lengths in pancreatic beta cell physiology. We provide new insights in alterations of the sphingolipidome in pancreatic islets of db/db mice during the development of T2D and show that increased levels of long and very long chain ceramides, as well as sphingadiene

containing ceramides and sphingomyelins, might contribute to beta cell dysfunction during T2D development. Furthermore, we demonstrate that previously reported ratios of plasma ceramides are not suitable as marker for pancreatic beta cell dysfunction during diabetes; instead we nominate the C16:0/C24:1 ratio as possible indicator for diabetes-associated dysfunctions in islet tissue.

We further analyzed the role of CERS2 and very long chain sphingolipids in beta cell function and physiology by beta cell specific ablation of *CerS2* in mice and INS1E cells. The present study demonstrates an essential role for CERS2 and very long chain sphingolipids in prohormone processing in pancreatic beta cells. Ablation of *CerS2* and concomitant reduction in very long chain sphingolipids lowered the amount of insulin secretory granules and decreased mature PC1 protein in pancreatic beta cells. Consequently, reduced proinsulin processing decreases glucose stimulated insulin secretion and impairs glucose tolerance in CERS2 deficient mice.
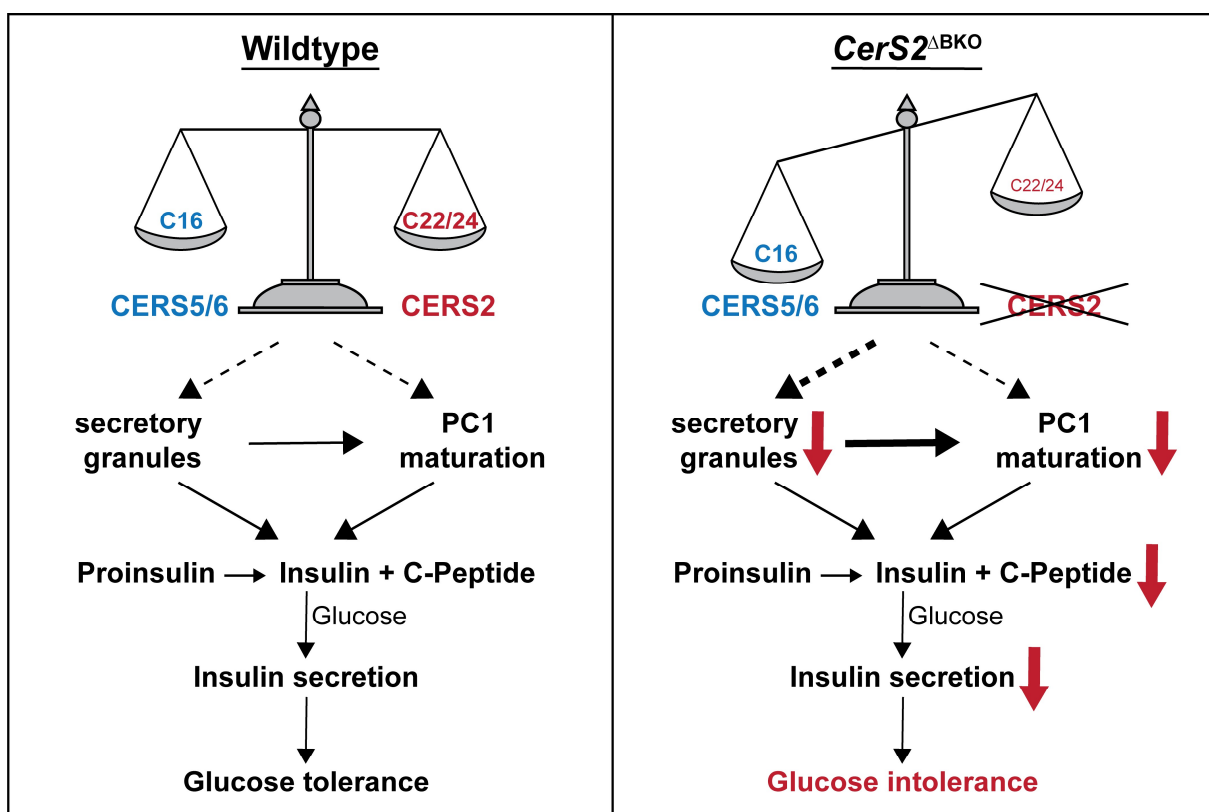
Figure 26: Proposed mechanism of beta cell dysfunction after ablation of *CerS2*. Beta cell specific deletion of *CerS2* strongly decrease very long C22 and C24 sphingolipid species. The imbalance of long C16 and very long C22/24 sphingolipids leads to a reduction in secretory insulin granules and mature PC1 protein. Maturation of PC1 takes place in secretory granules and therefore is dependent on granule biogenesis. Decreased amounts of secretory granules and mature PC1 further result in reduced conversion of proinsulin into insulin and C-peptide. Consequently, pancreatic beta cells contain less mature insulin granules and secrete less insulin after glucose stimulation, which leads to glucose intolerance in *CerS2*ΔBKO mice.

6.   Outlook

This study provided new insights into the role of CERS2 and CERS2 derived very long chain sphingolipids in pancreatic beta cells. CERS2 was identified to be implicated in glucose homeostasis and glucose tolerance by regulating the formation of mature insulin in secretory granules. In *CerS2*$^{\Delta BKO}$ islets, PC1 protein was shown to be specifically decreased without changing *Pcsk1* mRNA levels. Therefore, decreased mature PC1 generation likely emerges from a defect between translation and maturation of PC1 protein in secretory granules. However, an open question is how very long chain sphingolipids can regulate the maturation of PC1 protein, which might be relevant during the development of diabetes. Do very long chain sphingolipids directly interact with PC1 and support autocatalytical cleavage and maturation of PC1 or are they important for PC1 trafficking? Another open question is, if reduced mature PC1 protein levels are a primary defect or rather a secondary result of defective granule biogenesis after depletion of very long chain sphingolipids.

While previous studies demonstrated a beneficial effect of reduced C16:0 ceramide levels in several tissues, the impact of C16:0 ceramide depletion by ablation of *CerS5*, *CerS6* or *CerS5*/*CerS6* in pancreatic beta cells is still unknown. Furthermore, global inhibition of ceramide de novo synthesis is proposed as novel diabetes treatment, but it remain unclear, how deletion of all of the prominent *CerS* (*CerS2*/*CerS5*/*CerS6*) would influence pancreatic beta cell physiology. Analyzing the function of distinct CERS and concomitantly sphingolipids with varying chain length in pancreatic beta cells will verify, if those approaches might be useful as novel diabetes therapy. Furthermore, the relevance of CERS in human pancreatic islets has to be clarified via adenoviral mediated knockdown of *CerS* and overexpression of CERS. Another open question is, how distinct CERS derived sphingolipids can differentially impact beta cell function and physiology. Which are the sphingolipid interacting proteins that mediate distinct cellular destinies? Analyzing specific sphingolipid interaction partners by photoactivatable and clickable sphingosine (PACS) [196,406] will elucidate underlying mechanisms and might indicate sphingolipid specific localizations that contribute to cellular dysfunctions.

7.   List of abbreviations

Symbols and numbers

Δ	delta
3'	three prime end of DNA sequences
36b4	Acidic ribosomal phosphoprotein p 0
3-KdhSph	3-keto-dihydrosphingosine
5'	five prime end of DNA sequences

A

A	adenosine
alkCDase	acid ceramidase
ACN	acetonitrile
Actb	beta actin
ADP	adenosine diphosphate
AGC	automatic gain control
AKT	proteinkinase B
alkCDase (ACER1-3)	alkaline ceramidase 1-3
alkSMase	alkaline sphingomyelinase
ANOVA	analysis of variance
Anxa6	annexin A6
aSMase	acid sphingomyelinase
ATP	adenosine triphosphate
A.U.	arbitrary unit
AUC	area under the curve

B

BCA	bicinchoninic acid
bp	base pair
BSA	bovine serum albumin V

C

C	cytosine
C14-36	acyl chain length with 14-36 carbon atoms
C1P	ceramide-1-phosphate
Ca^{2+}	calcium ion
$CaCl_2$	calcium chloride
Calr	calreticulin
Cas9	CRISPR associated protein 9

CD	cluster of differentiation
CDase	ceramidase
cDNA	complementary DNA
CE	cholesteryl ester
Cer	ceramide
CERK	ceramide kinase
CerS1-6	ceramide synthase 1-6
CERT	ceramide transporter
CGA	chromogranin A
CGB	chromogranin B
CGT	ceramide galactosyltransferase
Chop	C/EBP homology protein
CHX	cycloheximide
CoA	coenzyme A
CO_2	carbon dioxide
CPE	carboxy peptidase E
CPTP	ceramide-1-phosphate transfer protein
Cre	causes recombination (site specific recombinase from phage P1)
CRISPR	clustered regularly interspaced short palindromic repeats
CST	cerebroside sulfotransferase

D

d18:0	sphinganine, sphingoid backbone without double bond
d18:1	sphingosine, sphingoid backbone with one double bond
d18:2	sphingadiene, sphingoid backbone with two double bond
DAG	diacylglycerol
DDA	data dependent aquisition
ddH_2O	double distilled water
DDZ	German Diabetes Center
Degs1	dihydroceramide desaturase 1 (encodes for DES1)
DES1	dihydroceramide desaturase 1 (encoded by Degs1)
DetaNO	diethylenetriamine nitric oxide
DH5α	competent *E.coli* cells
DhCer	dihydroceramide
DhSph	dihydrosphingosine, also known as sphinganine
DIA	data independent acquisition
DMEM	dulbeccos modified eagle medium
DNA	desoxyribonucleic acid

doxCer	deoxyceramide
DPP-4	dipeptidyl peptidase-4
DTT	Dithiothreitol

E

E.coli	escherichia coli
e.g.	*exempli gratia*
ECL	enhanced chemiluminescence
EDTA	ethylendiamine tetraacetate
EdU	5-ethynyl-2'-deoxyuridine
EIF2A	eukaryotic translation initiation factor 2A
ELISA	enzyme-linked immunosorbent assay
ER	endoplasmic reticulum
ERAD	endoplasmic-reticulum-associated degradation
Erp29	endoplasmic reticulum protein 29
EtOH	ethanol

F

FACS	fluorescence activated cell sorting
FADH$_2$	flavin adenin dinucleotide
FADS3	fatty acid desaturase 3
FAPP2	four-phosphate adaptor protein 2
FastAP	fast alkaline phosphatase
FC	fold change
FCS	fetal calf serum
FFA	free fatty acids (also known as NEFA)
Fig.	figure
Floxed/fl	loxP flanked
For	forward
Foxo1	forkhead-O transcription factor 1
FSC	forward side scatter

G

G	guanine
GABA	γ-aminobutyric acid
GAD	glutamic acid decarboxylase
GalCer	galactosylceramide
GCase	glucocerebrosidase
GCK	glucokinase

GCS	glucosylceramide synthase
GDM	gestational diabetes
GFP	green fluorescent protein
GLP-1	glucagon-like peptide 1
GluCer	glucosylceramide
GLUT1-4	glucose transporter 1-4
gRNA	guide RNA
Grp78	glucose-regulated protein 78 kDa
Grp94	heat shock protein 90 kDa beta member 1
Grp170	glucose-regulated protein 170
GSIS	glucose stimulated insulin secretion
GSL	glycosphingolipids
GTT	glucose tolerance test
Gusb	glucoronidase beta
GWAS	genome wide association studies

H

H_2O_2	hydrogen peroxide
H+L	heavy and light chain
HbA1c	glycated hemoglobin
HCD	higher-energy collisional dissociation
HCl	hydrochloric acid
HeLa	Henrietta Lacks (human epithelial cell line)
Hep3B	human hepatocellular carcinoma cell line
HEPES	N-2-hydroxyethylpiperazine-N'-2-ethansulforic acid
HESI	heated electrospray ionization
HexCer	hexosylceramide
HFD	high fat diet
hGH	human growth hormone
HLA	human leukocyte antigen
HNF1A	hepatocyte nuclear factor 1-alpha
HNF4A	hepatocyte nuclear factor 1-alpha
HNF1B	hepatocyte nuclear factor 1-beta
HRP	horseradish peroxidase
Hsp60	heat shock 60 kDa protein 1
Hsp70	heat shock 70 kDa protein 4

I

IA-2	insulinoma associated antigen
IAPP	amylin
IGF2	insulin-like growth factor 2
IgG	Immunoglobulin G
IL-1β	interleukin-1beta
IL-6	interleukin-6
Indel	insertion or deletion
iNOS	inducible nitric oxide synthase
Ins1-2	insulin 1-2
INS-1/INS1E	rat pancreatic beta cell line
i.p.	intraperitoneal
IRS1	insulin receptor substrate 1
iRT	indexed retention time
ITT	insulin tolerance test
I.U.	international unit

J

JNK	Jun N-terminal kinase

K

K^+	potassium ion
K_{ATP}	ATP-dependent potassium channels
KCl	potassium chloride
kDa	kilodalton
KDSR	3-keto sphinganine reductase
KH_2PO_4	potassium dihydrogenphosphate
KO	knockout
KRH	krebs-ringer HEPES

L

LASS1-6	longevity assurance 1-6
LB	lysogeny broth
loxP	locus of cross over in phage P1 (recognition sequence for Cre)
LPC	lysophosphatidylcholine

M

MARD	mild age-related diabetes
MCF-7	Michigan cancer foundation-7 (human epithelial cell line)
MCP1	monocyte chemoattractant protein 1

MetOH	methanol
MgSO$_4$	magnesium sulfate
MIN6	mouse pancreatic cell line
MIP	mouse insulin promoter
MMC	methanol:MTBE:chloroform
MOD	mild obesity-related diabetes
MODY	maturity-onset diabetes of the young
MOM	mitochondrial outer membrane
mRNA	messenger RNA
MS	mass spectrometry
MS2	second stage of mass spectrometry
MTBE	methyl-tert-butylether
m/z	mass-to-charge-ratio

N

NaCl	sodium chloride
NADH	nicotinamide adenine dinucleotide
NaHCO3	sodium bicarbonate
NaOH	sodium hydroxide
nCDase	neutral ceramidase
NEFA	non-esterified fatty acids (also known as FFA)
ND	normal diet
NHEJ	non-homologous end-joining
Nkx6.1	NK6 homeobox 1
NO	nitric oxide
nSMase	neutral sphingomyelinase
nt	nucleotide
NVJ2P	lipid-binding ER protein, enriched at nucleus-vacuolar junctions (NVJ)

O

O2$^{\cdot-}$	radical oxide
OE	overexpression
OH$^{\cdot}$	hydroxyl radical

P

PACS	photoactivatable and clickable sphingosine
PAGE	polyacrylamide gel electrophoresis
PAM	protospacer adjacent motif

PAPS	3′-phosphoadenosine-5′-phosphosulfate
PBS	phosphate buffered saline
PC	phosphatidylcholine
PC1	prohormone convertase 1 (encoded by Pcsk1)
PC2	prohormone convertase 2
PCR	polymerase chain reaction
Pcsk1	prohormone convertase 1 (encodes for PC1)
PDI	protein disulfid isomerase
Pdia3	protein disulfide isomerase family A member 3
PDX1	pancreatic and duodenal homeobox 1
PE	phosphatidylethanolamine
Pen/Strep	Penicillin/Streptomycin
PERK	PRK-like ER kinase
PG	phosphatidylglycerol
PI	phosphatidylinositol
PP	pancreatic polypeptide
ppm	parts per million
PS	phosphatidylserine
Pyr	pyruvate
PVDF	polyvinylidene fluoride

Q

qPCR	quantitative realtime PCR

R

RCAS1	receptor binding cancer antigen expressed on SiSo cells
Rev	reverse
RIP	rat insulin promoter
RIPA	radio immunoprecipitation assay buffer
RNA	ribonucleic acid
ROS	reactive oxygen species
RRP	readily releasable pool
rpm	revolutions per minute
RPMI	Roswell park memorial institute cell culture medium
RT	room temperature

S

S1P	sphingosine-1-phosphate
S1PP	sphingosine-1-phosphate phosphatases

S1PR	sphingosine-1-phosphate receptor
SAID	severe autoimmune diabetes
SD	standard deviation
SDS	sodiumdodecylsulfate
SEM	standard error of the mean
Setdb1	SET domain bifurcated histone lysine methyltransferase 1
S.Fig.	supplementary figure
SG	secretory granule
SGLT2	sodium-glucose cotransporter 2
Sgms1-2	sphingomyelin synthase 1-2 (encodes for SMS1-2)
SIDD	severe insulin-deficient diabetes
SIRD	severe insulin-resistant diabetes
siRNA	small interfering RNA
SK1-2	sphingosine kinase 1-2
SL	sphingolipids
Slc2a1-3	solute carrier family 2 member 1-3 (coding for GLUT1-3)
SM	sphingomyelin
SMase	sphingomyelinase
SMS1-2	sphingomyelin synthase 1-2
SMS-KCNR	human neuroblastoma cell line
SNP	single nucleotide polymorphism
Sph	sphingosine
SPT	serine palmitoyltransferase
Sptlc1-2	serine Palmitoyltransferase Long Chain Base Subunit 1-2
St3gal5	ST3 Beta-Galactoside Alpha-2,3-Sialyltransferase 5
S.Tab.	supplementary table
STZ	streptozotocin

T

T	tyrosine
T1D	type 1 diabetes mellitus
T2D	type 2 diabetes mellitus
Tab.	table
TAE	tris-acetic acid EDTA buffer
TAG	triacylglycerol
TaxID	taxonomic identifier
TBST	tris buffered saline with tween
TCA	tricarboxylic acid cycle

TEM	transmission electron microscope
TFA	trifluoroacetic acid
tg	transgene
TGN	*trans*-Golgi network
TLC domain	Tram/Lag/CLN8 domain
TNFα	tumor necrosis factor alpha
TPST1-2	tyrosylprotein sulfotransferase 1-2
TrEMBL	translated EMBL nucleotide sequence data library
Tris	2-amino-2-(hydroxymethyl-)1,3-propandiole
TSPAN-7	tetraspanin-7

U

U	unit
UPR	unfolded protein response
USD	U.S. dollar
UTR	untranslated region
UV	ultraviolet

V

VDCC	voltage-dependent calcium channels
Vgf	Vgf nerve growth factor inducible
v/v	volume per volume
v/v/v	volume per volume per volume

W

w/v	weight per volume
Wt	wildtype

X

x g	times gravity

Z

Zn^{2+}	zinc ion
ZNT8	zinc transporter 8

8. Figure index

9.   Table index

10. References

1. Röder, P. V., Wu, B., Liu, Y. & Han, W. Pancreatic regulation of glucose homeostasis. *Exp. Mol. Med.* **48**, e219–e219 (2016).
2. Rorsman, P. & Braun, M. Regulation of Insulin Secretion in Human Pancreatic Islets. *Annu. Rev. Physiol.* **75**, 155–179 (2013).
3. Da Silva Xavier, G. The Cells of the Islets of Langerhans. *J. Clin. Med.* **7**, 54 (2018).
4. Saito, K., Iwama, N. & Takahashi, T. Morphometrical Analysis on Topographical Difference in Size Distribution, Number and Volume of Islets in the Human Pancreas. *Tohoku J. Exp. Med.* **124**, 177–86 (1978).
5. Ionescu-Tirgoviste, C. *et al.* A 3D map of the islet routes throughout the healthy human pancreas. *Sci. Rep.* **5**, 14634 (2015).
6. Dolenšek, J., Rupnik, M. S. & Stožer, A. Structural similarities and differences between the human and the mouse pancreas. *Islets* **7**, e1024405 (2015).
7. Rutter, G. A., Pullen, T. J., Hodson, D. J. & Martinez-Sanchez, A. Pancreatic β-cell identity, glucose sensing and the control of insulin secretion. *Biochem. J.* **466**, 203–218 (2015).
8. Betts, J. G. *et al.* Anatomy & Physiology. *OpenStax,* 764–769. Houston, Texas (2013). Access for free at https://openstax.org/books/anatomy-and-physiology/pages/1-introduction; Section URL: https://openstax.org/books/anatomy-andphysiology/pages/17-9-the-endocrine-pancreas
9. Noguchi, G. M. & Huising, M. O. Integrating the inputs that shape pancreatic islet hormone release. *Nat. Metab.* **1**, 1189–1201 (2019).
10. Brissova, M. *et al.* Assessment of Human Pancreatic Islet Architecture and Composition by Laser Scanning Confocal Microscopy. *J. Histochem. Cytochem.* **53**, 1087–1097 (2005).
11. Cabrera, O. *et al.* The unique cytoarchitecture of human pancreatic islets has implications for islet cell function. *Proc. Natl. Acad. Sci.* **103**, 2334–2339 (2006).
12. Rodriguez-Diaz, R. *et al.* Innervation Patterns of Autonomic Axons in the Human Endocrine Pancreas. *Cell Metab.* **14**, 45–54 (2011).
13. Ashcroft, F. M. & Rorsman, P. Diabetes Mellitus and the β Cell: The Last Ten Years. *Cell* **148**, 1160–1171 (2012).
14. International Diabetes Federation. *IDF Diabetes Atlas, 9th edn.* Brussels, Belgium (2019). Available at: https://www.diabetesatlas.org.
15. Unnikrishnan, R., Pradeepa, R., Joshi, S. R. & Mohan, V. Type 2 Diabetes: Demystifying the Global Epidemic. *Diabetes* **66**, 1432–1442 (2017).
16. Marcovecchio, M. L. Complications of Acute and Chronic Hyperglycemia. *US Endocrinol.* **13**, 17 (2017).
17. DiMeglio, L. A., Evans-Molina, C. & Oram, R. A. Type 1 diabetes. *Lancet* **391**, 2449–2462 (2018).
18. Alkayyali, S. & Lyssenko, V. Genetics of diabetes complications. *Mamm. Genome* **25**, 384–400 (2014).
19. Collins, K. K. The Diabetes-Cancer Link. *Diabetes Spectr.* **27**, 276–280 (2014).
20. Bommer, C. *et al.* Global Economic Burden of Diabetes in Adults: Projections From 2015 to 2030. *Diabetes Care* **41**, 963–970 (2018).
21. Beauchamp, G. & Haller, M. J. Can We Prevent Type 1 Diabetes? *Curr. Diab. Rep.* **15**, 1–8 (2015).
22. Kahanovitz, L., Sluss, P. M. & Russell, S. J. Type 1 Diabetes—A Clinical Perspective. *Point Care J. Near-Patient Test. Technol.* **16**, 37–40 (2017).
23. Katsarou, A. *et al.* Type 1 diabetes mellitus. *Nat. Rev. Dis. Prim.* **3**, 17016 (2017).
24. Thomas, N. J. *et al.* Frequency and phenotype of type 1 diabetes in the first six decades of life: a cross-sectional, genetically stratified survival analysis from UK Biobank. *Lancet Diabetes Endocrinol.* **6**, 122–129 (2018).

25. Thomas, N. J. *et al.* Type 1 diabetes defined by severe insulin deficiency occurs after 30 years of age and is commonly treated as type 2 diabetes. *Diabetologia* **62**, 1167–1172 (2019).

26. Regnell, S. E. & Lernmark, Å. Early prediction of autoimmune (type 1) diabetes. *Diabetologia* **60**, 1370–1381 (2017).

27. Noble, J. A. Immunogenetics of type 1 diabetes: A comprehensive review. *J. Autoimmun.* **64**, 101–112 (2015).

28. Rewers, M. & Ludvigsson, J. Environmental risk factors for type 1 diabetes. *Lancet* **387**, 2340–2348 (2016).

29. Zheng, P., Li, Z. & Zhou, Z. Gut microbiome in type 1 diabetes: A comprehensive review. *Diabetes. Metab. Res. Rev.* **34**, e3043 (2018).

30. Insel, R. A. *et al.* Staging Presymptomatic Type 1 Diabetes: A Scientific Statement of JDRF, the Endocrine Society, and the American Diabetes Association. *Diabetes Care* **38**, 1964–1974 (2015).

31. McLaughlin, K. A. *et al.* Identification of Tetraspanin-7 as a Target of Autoantibodies in Type 1 Diabetes. *Diabetes* **65**, 1690–1698 (2016).

32. Atkinson, M. A., Eisenbarth, G. S. & Michels, A. W. Type 1 diabetes. *Lancet* **383**, 69–82 (2014).

33. von Herrath, M., Sanda, S. & Herold, K. Type 1 diabetes as a relapsing–remitting disease? *Nat. Rev. Immunol.* **7**, 988–994 (2007).

34. Chen, C., Cohrs, C. M., Stertmann, J., Bozsak, R. & Speier, S. Human beta cell mass and function in diabetes: Recent advances in knowledge and technologies to understand disease pathogenesis. *Mol. Metab.* **6**, 943–957 (2017).

35. Leete, P. *et al.* Differential Insulitic Profiles Determine the Extent of β-Cell Destruction and the Age at Onset of Type 1 Diabetes. *Diabetes* **65**, 1362–1369 (2016).

36. Klöppel, G., Drenck, C. R., Oberholzer, M. & Heitz, P. U. Morphometric evidence for a striking B-cell reduction at the clinical onset of type 1 diabetes. *Virchows Arch. A Pathol. Anat. Histopathol.* **403**, 441–452 (1984).

37. Klinke, D. J. Age-Corrected Beta Cell Mass Following Onset of Type 1 Diabetes Mellitus Correlates with Plasma C-Peptide in Humans. *PLoS One* **6**, e26873 (2011).

38. Lernmark, Å. *et al.* Heterogeneity of islet pathology in two infants with recent onset diabetes mellitus. *Virchows Arch.* **425**, 631–640 (1995).

39. Butler, A. E. *et al.* Modestly increased beta cell apoptosis but no increased beta cell replication in recent-onset type 1 diabetic patients who died of diabetic ketoacidosis. *Diabetologia* **50**, 2323–2331 (2007).

40. Butler, P. C., Meier, J. J., Butler, A. E. & Bhushan, A. The replication of β cells in normal physiology, in disease and for therapy. *Nat. Clin. Pract. Endocrinol. Metab.* **3**, 758–768 (2007).

41. Pearson, E. R. Type 2 diabetes: a multifaceted disease. *Diabetologia* **62**, 1107–1112 (2019).

42. Zheng, Y., Ley, S. H. & Hu, F. B. Global aetiology and epidemiology of type 2 diabetes mellitus and its complications. *Nat. Rev. Endocrinol.* **14**, 88–98 (2018).

43. Christensen, A. A. & Gannon, M. The Beta Cell in Type 2 Diabetes. *Curr. Diab. Rep.* **19**, 81 (2019).

44. Lascar, N. *et al.* Type 2 Diabetes in Adolescents and Young Adults. *lancet. Diabetes Endocrinol.* **6**, 69–80 (2018).

45. Roden, M. & Shulman, G. I. The integrative biology of type 2 diabetes. *Nature* **576**, 51–60 (2019).

46. Mahajan, A. *et al.* Refining the accuracy of validated target identification through coding variant fine-mapping in type 2 diabetes. *Nat. Genet.* **50**, 559–571 (2018).

47. Czech, M. P. Insulin action and resistance in obesity and type 2 diabetes. *Nat. Med.* **23**, 804–814 (2017).

48. Guilherme, A., Virbasius, J. V., Puri, V. & Czech, M. P. Adipocyte dysfunctions linking obesity to insulin resistance and type 2 diabetes. *Nat. Rev. Mol. Cell Biol.* **9**, 367–377 (2008).

49. Smith, U. & Kahn, B. B. Adipose tissue regulates insulin sensitivity: role of adipogenesis, de novo lipogenesis and novel lipids. *J. Intern. Med.* **280**, 465–475 (2016).

50. Skyler, J. S. *et al.* Differentiation of Diabetes by Pathophysiology, Natural History, and Prognosis. *Diabetes* **66**, 241–255 (2017).

51. Mittra, S., Bansal, V. S. & Bhatnagar, P. K. From a glucocentric to a lipocentric approach towards metabolic syndrome. *Drug Discov. Today* **13**, 211–218 (2008).

52. Prentki, M. & Nolan, C. J. Islet β cell failure in type 2 diabetes. *J. Clin. Invest.* **116**, 1802–12 (2006).

53. Sachdeva, M. M. & Stoffers, D. A. Minireview: Meeting the Demand for Insulin: Molecular Mechanisms of Adaptive Postnatal ß-Cell Mass Expansion. *Mol. Endocrinol.* **23**, 747–758 (2009).

54. Butler, A. E. *et al.* β-Cell Deficit and Increased -Cell Apoptosis in Humans With Type 2 Diabetes. *Diabetes* **52**, 102–110 (2003).

55. Hanley, S. C. *et al.* β-Cell Mass Dynamics and Islet Cell Plasticity in Human Type 2 Diabetes. *Endocrinology* **151**, 1462–1472 (2010).

56. Saisho, Y. *et al.* β-cell mass and turnover in humans: effects of obesity and aging. *Diabetes Care* **36**, 111–7 (2013).

57. Hull, R. L. *et al.* Dietary-fat-induced obesity in mice results in beta cell hyperplasia but not increased insulin release: evidence for specificity of impaired beta cell adaptation. *Diabetologia* **48**, 1350–1358 (2005).

58. Jetton, T. L. *et al.* Mechanisms of Compensatory -Cell Growth in Insulin-Resistant Rats: Roles of Akt Kinase. *Diabetes* **54**, 2294–2304 (2005).

59. Mosser, R. E. *et al.* High-fat diet-induced β-cell proliferation occurs prior to insulin resistance in C57Bl/6J male mice. *Am. J. Physiol. Metab.* **308**, E573–E582 (2015).

60. Steil, G. M. *et al.* Adaptation of β-cell mass to substrate oversupply: enhanced function with normal gene expression. *Am. J. Physiol. Metab.* **280**, E788–E796 (2001).

61. Alonso, L. C. *et al.* Glucose Infusion in Mice: A New Model to Induce β-Cell Replication. *Diabetes* **56**, 1792–1801 (2007).

62. Stamateris, R. E., Sharma, R. B., Hollern, D. A. & Alonso, L. C. Adaptive β-cell proliferation increases early in high-fat feeding in mice, concurrent with metabolic changes, with induction of islet cyclin D2 expression. *Am. J. Physiol. Metab.* **305**, E149–E159 (2013).

63. Rahier, J., Guiot, Y., Goebbels, R. M., Sempoux, C. & Henquin, J. C. Pancreatic β-cell mass in European subjects with type 2 diabetes. *Diabetes, Obes. Metab.* **10**, 32–42 (2008).

64. Sakuraba, H. *et al.* Reduced beta-cell mass and expression of oxidative stress-related DNA damage in the islet of Japanese Type II diabetic patients. *Diabetologia* **45**, 85–96 (2002).

65. Inaishi, J. *et al.* Effects of Obesity and Diabetes on α- and β-Cell Mass in Surgically Resected Human Pancreas. *J. Clin. Endocrinol. Metab.* **101**, 2874–2882 (2016).

66. Cohrs, C. M. *et al.* Dysfunction of Persisting β Cells Is a Key Feature of Early Type 2 Diabetes Pathogenesis. *Cell Rep.* **31**, 107469 (2020).

67. Rahier, J., Goebbels, R. M. & Henquin, J. C. Cellular composition of the human diabetic pancreas. *Diabetologia* **24**, 366–371 (1983).

68. Swisa, A., Glaser, B. & Dor, Y. Metabolic Stress and Compromised Identity of Pancreatic Beta Cells. *Front. Genet.* **08**, 1–11 (2017).

69. Meier, J. J. *et al.* β-Cell Replication Is the Primary Mechanism Subserving the Postnatal Expansion of -Cell Mass in Humans. *Diabetes* **57**, 1584–1594 (2008).

70. Talchai, C., Xuan, S., Lin, H. V., Sussel, L. & Accili, D. Pancreatic β Cell Dedifferentiation as a Mechanism of Diabetic β Cell Failure. *Cell* **150**, 1223–1234 (2012).

71. Cinti, F. *et al.* Evidence of β-Cell Dedifferentiation in Human Type 2 Diabetes. *J. Clin. Endocrinol. Metab.* **101**, 1044–1054 (2016).

72. Butler, A. E. *et al.* β-Cell Deficit in Obese Type 2 Diabetes, a Minor Role of β-Cell Dedifferentiation and Degranulation. *J. Clin. Endocrinol. Metab.* **101**, 523–532 (2016).

73. Poitout, V. & Robertson, R. P. Glucolipotoxicity: Fuel Excess and β-Cell Dysfunction. *Endocr. Rev.* **29**, 351–366 (2008).

74. Véret, J. *et al.* Roles of Sphingolipid Metabolism in Pancreatic β Cell Dysfunction Induced by Lipotoxicity. *J. Clin. Med.* **3**, 646–662 (2014).

75. Back, S. H. & Kaufman, R. J. Endoplasmic Reticulum Stress and Type 2 Diabetes. *Annu. Rev. Biochem.* **81**, 767–793 (2012).

76. Hetz, C. & Papa, F. R. The Unfolded Protein Response and Cell Fate Control. *Mol. Cell* **69**, 169–181 (2018).

77. Evans-Molina, C., Hatanaka, M. & Mirmira, R. G. Lost in Translation: ER Stress and the Decline of β -cell Health in Diabetes Mellitus. *Diabetes, Obes. Metab.* **15**, 159–169 (2013).

78. Marchetti, P. *et al.* The endoplasmic reticulum in pancreatic beta cells of type 2 diabetes patients. *Diabetologia* **50**, 2486–2494 (2007).

79. Laybutt, D. R. *et al.* Endoplasmic reticulum stress contributes to beta cell apoptosis in type 2 diabetes. *Diabetologia* **50**, 752–763 (2007).

80. Lipson, K. L. *et al.* Regulation of insulin biosynthesis in pancreatic beta cells by an endoplasmic reticulum-resident protein kinase IRE1. *Cell Metab.* **4**, 245–254 (2006).

81. Izumi, T. *et al.* Dominant Negative Pathogenesis by Mutant Proinsulin in the Akita Diabetic Mouse. *Diabetes* **52**, 409–416 (2003).

82. Supale, S., Li, N., Brun, T. & Maechler, P. Mitochondrial dysfunction in pancreatic β cells. *Trends Endocrinol. Metab.* **23**, 477–487 (2012).

83. Newsholme, P., Keane, K. N., Carlessi, R. & Cruzat, V. Oxidative stress pathways in pancreatic β-cells and insulin-sensitive cells and tissues: importance to cell metabolism, function, and dysfunction. *Am. J. Physiol. Physiol.* **317**, C420–C433 (2019).

84. Hasnain, S. Z., Prins, J. B. & McGuckin, M. A. Oxidative and endoplasmic reticulum stress in β-cell dysfunction in diabetes. *J. Mol. Endocrinol.* **56**, R33–R54 (2016).

85. Kupsco, A. & Schlenk, D. Oxidative Stress, Unfolded Protein Response, and Apoptosis in Developmental Toxicity. *Int. Rev. Cell Mol. Biol.* **317**, 1–66 (2015).

86. American Diabetes Association. Standars of Medical Care in Diabetes - 2020. **43**, (2020).

87. Johns, E. C., Denison, F. C., Norman, J. E. & Reynolds, R. M. Gestational Diabetes Mellitus: Mechanisms, Treatment, and Complications. *Trends Endocrinol. Metab.* **29**, 743–754 (2018).

88. Misra, S. & Owen, K. R. Genetics of Monogenic Diabetes: Present Clinical Challenges. *Curr. Diab. Rep.* **18**, 141 (2018).

89. van Ommen, B. *et al.* From Diabetes Care to Diabetes Cure—The Integration of Systems Biology, eHealth, and Behavioral Change. *Front. Endocrinol. (Lausanne).* **8**, 1–19 (2018).

90. Hallberg, S. J., Gershuni, V. M., Hazbun, T. L. & Athinarayanan, S. J. Reversing Type 2 Diabetes: A Narrative Review of the Evidence. *Nutrients* **11**, 766 (2019).

91. Schellenberg, E. S., Dryden, D. M., Vandermeer, B., Ha, C. & Korownyk, C. Lifestyle Interventions for Patients With and at Risk for Type 2 Diabetes: A Systematic Review and Meta-analysis. *Ann. Intern. Med.* **159**, 543 (2013).

92. Chaudhury, A. *et al.* Clinical Review of Antidiabetic Drugs: Implications for Type 2 Diabetes Mellitus Management. *Front. Endocrinol. (Lausanne).* **8**, (2017).

93. Seino, S., Sugawara, K., Yokoi, N. & Takahashi, H. β-Cell signalling and insulin secretagogues: A path for improved diabetes therapy. *Diabetes, Obes. Metab.* **19**, 22–29 (2017).

94. Tan, S. Y. *et al.* Type 1 and 2 diabetes mellitus: A review on current treatment approach and gene therapy as potential intervention. *Diabetes Metab. Syndr. Clin. Res. Rev.* **13**, 364–372 (2019).

95. Nathan, D. M. *et al.* Medical Management of Hyperglycemia in Type 2 Diabetes: A Consensus Algorithm for the Initiation and Adjustment of Therapy: A consensus statement of the American Diabetes Association and the European Association for the Study of Diabetes. *Diabetes Care* **32**, 193–203 (2009).

96. Marín-Peñalver, J. J., Martín-Timón, I., Sevillano-Collantes, C. & Cañizo-Gómez, F. J. del. Update on the treatment of type 2 diabetes mellitus. *World J. Diabetes* **7**, 354 (2016).

97. Razavi-Nematollahi, L. & Ismail-Beigi, F. Adverse Effects of Glycemia-Lowering Medications in Type 2 Diabetes. *Curr. Diab. Rep.* **19**, 132 (2019).

98. Inzucchi, S. E. *et al.* Progression to insulin therapy among patients with type 2 diabetes treated with sitagliptin or sulphonylurea plus metformin dual therapy. *Diabetes, Obes. Metab.* **17**, 956–964 (2015).

99. Gentile, S. *et al.* Five-Year Predictors of Insulin Initiation in People with Type 2 Diabetes under Real-Life Conditions. *J. Diabetes Res.* **2018**, 1–10 (2018).

100. Ahlqvist, E. *et al.* Novel subgroups of adult-onset diabetes and their association with outcomes: a data-driven cluster analysis of six variables. *Lancet Diabetes Endocrinol.* **6**, 361–369 (2018).

101. Zaharia, O. P. *et al.* Risk of Diabetes-Associated Diseases in Subgroups of Patients With Recent-Onset Diabetes: A 5-year Follow-Up Study. *lancet. Diabetes Endocrinol.* **7**, 684–694 (2019).

102. Güemes, M., Rahman, S. A. & Hussain, K. What is a normal blood glucose? *Arch. Dis. Child.* **101**, 569–574 (2016).

103. Alsahli, M. & Gerich, J. E. Hypoglycemia. *Endocrinol. Metab. Clin. North Am.* **42**, 657–676 (2013).

104. Ashish, R. K. & Kunjan, D. R. Impact of Hypoglycemia on Brain Metabolism During Diabetes. *Mol. Neurobiol.* **55**, 9075–9088 (2018).

105. Brownlee, M. The Pathobiology of Diabetic Complications: A Unifying Mechanism. *Diabetes* **54**, 1615–1625 (2005).

106. Jiang, G. & Zhang, B. B. Glucagon and regulation of glucose metabolism. *Am. J. Physiol. Metab.* **284**, E671–E678 (2003).

107. Adeva-Andany, M. M., Funcasta-Calderón, R., Fernández-Fernández, C., Castro-Quintela, E. & Carneiro-Freire, N. Metabolic effects of glucagon in humans. *J. Clin. Transl. Endocrinol.* **15**, 45–53 (2019).

108. Khan, A. H. & Pessin, J. E. Insulin regulation of glucose uptake: a complex interplay of intracellular signalling pathways. *Diabetologia* **45**, 1475–83 (2002).

109. Taniguchi, C. M., Emanuelli, B. & Kahn, C. R. Critical nodes in signalling pathways: insights into insulin action. *Nat. Rev. Mol. Cell Biol.* **7**, 85–96 (2006).

110. Yaribeygi, H., Farrokhi, F. R., Butler, A. E. & Sahebkar, A. Insulin resistance: Review of the underlying molecular mechanisms. *J. Cell. Physiol.* **234**, 8152–8161 (2019).

111. Boland, B. B., Rhodes, C. J. & Grimsby, J. S. The dynamic plasticity of insulin production in β-cells. *Mol. Metab.* **6**, 958–973 (2017).

112. Liu, M. *et al.* Biosynthesis, structure, and folding of the insulin precursor protein. *Diabetes, Obes. Metab.* **20**, 28–50 (2018).

113. Chen, Y.-C., Taylor, A. J. & Verchere, C. B. Islet prohormone processing in health and disease. *Diabetes, Obes. Metab.* **20**, 64–76 (2018).

114. Hou, J. C., Min, L. & Pessin, J. E. Insulin granule biogenesis, trafficking and exocytosis. *Vitam. Horm.* **80**, 473–506 (2009).

115. Fu, Z., Gilbert, E. R. & Liu, D. Regulation of Insulin Synthesis and Secretion and Pancreatic Beta-Cell Dysfunction in Diabetes. *Curr. Diabetes Rev.* **9**, 25–53 (2013).

116. Vakilian, M., Tahamtani, Y. & Ghaedi, K. A review on insulin trafficking and exocytosis. *Gene* **706**, 52–61 (2019).

117. Tanguy, E. *et al.* Lipids implicated in the journey of a secretory granule: from biogenesis to fusion. *J. Neurochem.* **137**, 904–912 (2016).

118. Suckale, J. & Solimena, M. The insulin secretory granule as a signaling hub. *Trends Endocrinol. Metab.* **21**, 599–609 (2010).

119. Zhu, X. *et al.* Severe block in processing of proinsulin to insulin accompanied by elevation of des-64,65 proinsulin intermediates in islets of mice lacking prohormone convertase 1/3. *Proc. Natl. Acad. Sci.* **99**, 10299–10304 (2002).

120. Goodge, K. A. & Hutton, J. C. Translational regulation of proinsulin biosynthesis and proinsulin conversion in the pancreaticβ-cell. *Semin. Cell Dev. Biol.* **11**, 235–242 (2000).

121. Rhodes, C. J., Lincoln, B. & Shoelson, S. E. Preferential Cleavage of des-31,32-Proinsulin over Intact Proinsulin by the Insulin Secretory Granule Type II Endopeptidase. Implication of a Favored Route for Prohormone Processing. *J. Biol. Chem.* **267**, 22719–27 (1992).

122. O'Rahilly, S. *et al.* Brief Report: Impaired Processing of Prohormones Associated with Abnormalities of Glucose Homeostasis and Adrenal Function. *N. Engl. J. Med.* **333**, 1386–1391 (1995).

123. Davidson, H. W. & Hutton, J. C. The insulin-secretory-granule carboxypeptidase H. Purification and demonstration of involvement in proinsulin processing. *Biochem. J.* **245**, 575–582 (1987).

124. Steiner, D. F. The proprotein convertases. *Curr. Opin. Chem. Biol.* **2**, 31–39 (1998).

125. Ramzy, A., Asadi, A. & Kieffer, T. J. Revisiting Proinsulin Processing: Evidence That Human β-Cells Process Proinsulin With Prohormone Convertase (PC) 1/3 but Not PC2. *Diabetes* **69**, 1451–1462 (2020).

126. Newsholme, P., Brennan, L. & Bender, K. Amino Acid Metabolism, β-Cell Function, and Diabetes. *Diabetes* **55**, S39–S47 (2006).

127. Pingitore, A. *et al.* Dynamic Profiling of Insulin Secretion and ATP Generation in Isolated Human and Mouse Islets Reveals Differential Glucose Sensitivity. *Cell. Physiol. Biochem.* **44**, 1352–1359 (2017).

128. McCulloch, L. J. *et al.* GLUT2 (SLC2A2) is not the principal glucose transporter in human pancreatic beta cells: Implications for understanding genetic association signals at this locus. *Mol. Genet. Metab.* **104**, 648–653 (2011).

129. Prentki, M., Matschinsky, F. M. & Madiraju, S. R. M. Metabolic Signaling in Fuel-Induced Insulin Secretion. *Cell Metab.* **18**, 162–185 (2013).

130. Jitrapakdee, S., Wutthisathapornchai, A., Wallace, J. C. & MacDonald, M. J. Regulation of insulin secretion: role of mitochondrial signalling. *Diabetologia* **53**, 1019–1032 (2010).

131. Ashcroft, F. M., Harrison, D. E. & Ashcroft, S. J. H. Glucose induces closure of single potassium channels in isolated rat pancreatic β-cells. *Nature* **312**, 446–448 (1984).

132. Cook, D. L. & Hales, N. Intracellular ATP directly blocks K+ channels in pancreatic B-cells. *Nature* **311**, 271–273 (1984).

133. Meissner, H. P. & Schmelz, H. Membrane Potential of Beta-Cells in Pancreatic Islets. *Pflügers Arch. Eur. J. Physiol.* **351**, 195–206 (1974).

134. Rorsman, P. *et al.* The Cell Physiology of Biphasic Insulin Secretion. *Physiology* **15**, 72–77 (2000).

135. Rorsman, P. & Renström, E. Insulin granule dynamics in pancreatic beta cells. *Diabetologia* **46**, 1029–45 (2003).

136. Huang, M. & Joseph, J. W. Assessment of the Metabolic Pathways Associated With Glucose-Stimulated Biphasic Insulin Secretion. *Endocrinology* **155**, 1653–1666 (2014).

137. Gerich, J. E. Is Reduced First-Phase Insulin Release the Earliest Detectable Abnormality in Individuals Destined to Develop Type 2 Diabetes? *Diabetes* **51**, S117–S121 (2002).

138. Seino, S., Shibasaki, T. & Minami, K. Dynamics of insulin secretion and the clinical implications for obesity and diabetes. *J. Clin. Invest.* **121**, 2118–2125 (2011).

139. Wang, Z. & Thurmond, D. C. Mechanisms of biphasic insulin-granule exocytosis - roles of the cytoskeleton, small GTPases and SNARE proteins. *J. Cell Sci.* **122**, 893–903 (2009).

140. Tidhar, R. & Futerman, A. H. The complexity of sphingolipid biosynthesis in the endoplasmic reticulum. *Biochim. Biophys. Acta - Mol. Cell Res.* **1833**, 2511–2518 (2013).

141. Chaurasia, B. & Summers, S. A. Ceramides – Lipotoxic Inducers of Metabolic Disorders. *Trends Endocrinol. Metab.* **26**, 538–550 (2015).

142. Harayama, T. & Riezman, H. Understanding the diversity of membrane lipid composition. *Nat. Rev. Mol. Cell Biol.* **19**, 281–296 (2018).

143. Hannun, Y. A. & Obeid, L. M. Principles of bioactive lipid signalling: lessons from sphingolipids. *Nat. Rev. Mol. Cell Biol.* **9**, 139–150 (2008).

144. Hannun, Y. A. & Obeid, L. M. Sphingolipids and their metabolism in physiology and disease. *Nat. Rev. Mol. Cell Biol.* **19**, 175–191 (2018).

145. Carreira, A. C., Ventura, A. E., Varela, A. R. P. & Silva, L. C. Tackling the biophysical properties of sphingolipids to decipher their biological roles. *Biol. Chem.* **396**, 597–609 (2015).

146. Zelnik, I. D., Ventura, A. E., Kim, J. L., Silva, L. C. & Futerman, A. H. The role of ceramide in regulating endoplasmic reticulum function. *Biochim. Biophys. Acta - Mol. Cell Biol. Lipids* **1865**, 158489 (2020).

147. Castro, B. M., Prieto, M. & Silva, L. C. Ceramide: A simple sphingolipid with unique biophysical properties. *Prog. Lipid Res.* **54**, 53–67 (2014).

148. Kogot-Levin, A. & Saada, A. Ceramide and the mitochondrial respiratory chain. *Biochimie* **100**, 88–94 (2014).

149. Hassan, R. H., Bourron, O. & Hajduch, E. Defect of insulin signal in peripheral tissues: Important role of ceramide. *World J. Diabetes* **5**, 244 (2014).

150. Aburasayn, H., Al Batran, R. & Ussher, J. R. Targeting ceramide metabolism in obesity. *Am. J. Physiol. Metab.* **311**, E423–E435 (2016).

151. Levy, M. & Futerman, A. H. Mammalian ceramide synthases. *IUBMB Life* **62**, NA-NA (2010).

152. Park, J.-W., Park, W.-J. & Futerman, A. H. Ceramide synthases as potential targets for therapeutic intervention in human diseases. *Biochim. Biophys. Acta - Mol. Cell Biol. Lipids* **1841**, 671–681 (2014).

153. Sandhoff, R. & Sandhoff, K. Emerging concepts of ganglioside metabolism. *FEBS Lett.* **592**, 3835–3864 (2018).

154. Hanada, K. *et al.* Molecular machinery for non-vesicular trafficking of ceramide. *Nature* **426**, 803–809 (2003).

155. Kumagai, K. *et al.* CERT Mediates Intermembrane Transfer of Various Molecular Species of Ceramides. *J. Biol. Chem.* **280**, 6488–6495 (2005).

156. Liu, L.-K., Choudhary, V., Toulmay, A. & Prinz, W. A. An inducible ER–Golgi tether facilitates ceramide transport to alleviate lipotoxicity. *J. Cell Biol.* **216**, 131–147 (2017).

157. Gault, C. R., Obeid, L. M. & Hannun, Y. A. An overview of sphingolipid metabolism: from synthesis to breakdown. *Adv. Exp. Med. Biol.* **688**, 1–23 (2010).

158. Maceyka, M. & Spiegel, S. Sphingolipid metabolites in inflammatory disease. *Nature* **510**, 58–67 (2014).

159. D'Angelo, G., Capasso, S., Sticco, L. & Russo, D. Glycosphingolipids: synthesis and functions. *FEBS J.* **280**, 6338–6353 (2013).

160. Deevska, G. M. & Nikolova-Karakashian, M. N. The twists and turns of sphingolipid pathway in glucose regulation. *Biochimie* **93**, 32–38 (2011).

161. Buschard, K., Blomqvist, M., Osterbye, T. & Fredman, P. Involvement of sulfatide in beta cells and type 1 and type 2 diabetes. *Diabetologia* **48**, 1957–1962 (2005).

162. Simanshu, D. K. *et al.* Non-vesicular trafficking by a ceramide-1-phosphate transfer protein regulates eicosanoids. *Nature* **500**, 463–467 (2013).

163. Coant, N., Sakamoto, W., Mao, C. & Hannun, Y. A. Ceramidases, roles in sphingolipid metabolism and in health and disease. *Adv. Biol. Regul.* **63**, 122–131 (2017).

164. Futerman, A. H. & Riezman, H. The ins and outs of sphingolipid synthesis. *Trends Cell Biol.* **15**, 312–318 (2005).

165. Pitson, S. M. Regulation of sphingosine kinase and sphingolipid signaling. *Trends Biochem. Sci.* **36**, 97–107 (2011).

166. Spiegel, S. & Milstien, S. The outs and the ins of sphingosine-1-phosphate in immunity. *Nat. Rev. Immunol.* **11**, 403–415 (2011).

167. Ikeda, M., Kihara, A. & Igarashi, Y. Sphingosine-1-phosphate lyase SPL is an endoplasmic reticulum-resident, integral membrane protein with the pyridoxal 5′-phosphate binding domain exposed to the cytosol. *Biochem. Biophys. Res. Commun.* **325**, 338–343 (2004).

168. Hla, T. & Dannenberg, A. J. Sphingolipid Signaling in Metabolic Disorders. *Cell Metab.* **16**, 420–434 (2012).

169. Nakahara, K. *et al.* The Sjögren-Larsson Syndrome Gene Encodes a Hexadecenal Dehydrogenase of the Sphingosine 1-Phosphate Degradation Pathway. *Mol. Cell* **46**, 461–471 (2012).

170. Espaillat, M. P., Shamseddine, A. A., Adada, M. M., Hannun, Y. A. & Obeid, L. M. Ceramide and sphingosine-1-phosphate in cancer, two faces of the sphinx. *Transl. Cancer Res.* **4**, 484–499 (2015).

171. Mullen, T. D., Hannun, Y. A. & Obeid, L. M. Ceramide synthases at the centre of sphingolipid metabolism and biology. *Biochem. J.* **441**, 789–802 (2012).

172. Laviad, E. L. *et al.* Characterization of ceramide synthase 2: tissue distribution, substrate specificity, and inhibition by sphingosine 1-phosphate. *J. Biol. Chem.* **283**, 5677–84 (2008).

173. Tidhar, R. *et al.* Eleven residues determine the acyl chain specificity of ceramide synthases. *J. Biol. Chem.* **293**, 9912–9921 (2018).

174. Riebeling, C., Allegood, J. C., Wang, E., Merrill, A. H. & Futerman, A. H. Two Mammalian Longevity Assurance Gene (LAG1) Family Members, trh1 and trh4 , Regulate Dihydroceramide Synthesis Using Different Fatty Acyl-CoA Donors. *J. Biol. Chem.* **278**, 43452–43459 (2003).

175. Shimeno, H. *et al.* Partial Purification and Characterization of Sphingosine N-Acyltransferase (ceramide synthase) from Bovine Liver Mitochondrion-Rich Fraction. *Lipids* **33**, 601–5 (1998).

176. Sridevi, P. *et al.* Stress-induced ER to Golgi translocation of ceramide synthase 1 is dependent on proteasomal processing. *Exp. Cell Res.* **316**, 78–91 (2010).

177. Min, J. *et al.* (Dihydro)ceramide Synthase 1 Regulated Sensitivity to Cisplatin Is Associated with the Activation of p38 Mitogen-Activated Protein Kinase and Is Abrogated by Sphingosine Kinase 1. *Mol. Cancer Res.* **5**, 801–812 (2007).

178. Venkataraman, K. *et al.* Upstream of Growth and Differentiation Factor 1 (uog1), a Mammalian Homolog of the Yeast Longevity Assurance Gene 1 (LAG1), Regulates N-Stearoyl-sphinganine (C18-(Dihydro)ceramide) Synthesis in a Fumonisin B1-independent Manner in Mammalian Cells. *J. Biol. Chem.* **277**, 35642–9 (2002).

179. Mizutani, Y., Kihara, A. & Igarashi, Y. Mammalian Lass6 and its related family members regulate synthesis of specific ceramides. *Biochem. J.* **390**, 263–271 (2005).

180. White-Gilbertson, S. *et al.* Ceramide synthase 6 modulates TRAIL sensitivity and nuclear translocation of active caspase-3 in colon cancer cells. *Oncogene* **28**, 1132–1141 (2009).

181. Yu, J. *et al.* JNK3 Signaling Pathway Activates Ceramide Synthase Leading to Mitochondrial Dysfunction. *J. Biol. Chem.* **282**, 25940–25949 (2007).

182. Senkal, C. E. *et al.* Role of human longevity assurance gene 1 and C18-ceramide in chemotherapy-induced cell death in human head and neck squamous cell carcinomas. *Mol. Cancer Ther.* **6**, 712–722 (2007).

183. Holmes, R., Barron, K. & Krupenko, N. Ceramide Synthase 6: Comparative Analysis, Phylogeny and Evolution. *Biomolecules* **8**, 111 (2018).

184. Sassa, T., Hirayama, T. & Kihara, A. Enzyme Activities of the Ceramide Synthases CERS2–6 Are Regulated by Phosphorylation in the C-terminal Region. *J. Biol. Chem.* **291**, 7477–7487 (2016).

185. Sandhoff, R. Very long chain sphingolipids: Tissue expression, function and synthesis. *FEBS Lett.* **584**, 1907–1913 (2010).

186. Ginkel, C. *et al.* Ablation of Neuronal Ceramide Synthase 1 in Mice Decreases Ganglioside Levels and Expression of Myelin-associated Glycoprotein in Oligodendrocytes. *J. Biol. Chem.* **287**, 41888–41902 (2012).

187. Turpin-Nolan, S. M. *et al.* CerS1-Derived C18:0 Ceramide in Skeletal Muscle Promotes Obesity-Induced Insulin Resistance. *Cell Rep.* **26**, 1-10.e7 (2019).

188. Imgrund, S. *et al.* Adult Ceramide Synthase 2 (CERS2)-deficient Mice Exhibit Myelin Sheath Defects, Cerebellar Degeneration, and Hepatocarcinomas. *J. Biol. Chem.* **284**, 33549–33560 (2009).

189. Pewzner-Jung, Y. *et al.* A Critical Role for Ceramide Synthase 2 in Liver Homeostasis: I. Alterations in Lipid Metabolic Pathways. *J. Biol. Chem.* **285**, 10902–10 (2010).

190. Ben-David, O. *et al.* Encephalopathy Caused by Ablation of Very Long Acyl Chain Ceramide Synthesis May Be Largely Due to Reduced Galactosylceramide Levels. *J. Biol. Chem.* **286**, 30022–30033 (2011).

191. Zigdon, H. *et al.* Ablation of Ceramide Synthase 2 Causes Chronic Oxidative Stress Due to Disruption of the Mitochondrial Respiratory Chain. *J. Biol. Chem.* **288**, 4947–4956 (2013).

192. Jennemann, R. *et al.* Loss of ceramide synthase 3 causes lethal skin barrier disruption. *Hum. Mol. Genet.* **21**, 586–608 (2012).

193. Ebel, P. *et al.* Ceramide synthase 4 deficiency in mice causes lipid alterations in sebum and results in alopecia. *Biochem. J.* **461**, 147–158 (2014).

194. Ebel, P. *et al.* Inactivation of Ceramide Synthase 6 in Mice Results in an Altered Sphingolipid Metabolism and Behavioral Abnormalities. *J. Biol. Chem.* **288**, 21433–21447 (2013).

195. Gosejacob, D. *et al.* Ceramide Synthase 5 Is Essential to Maintain C 16:0 -Ceramide Pools and Contributes to the Development of Diet-induced Obesity. *J. Biol. Chem.* **291**, 6989–7003 (2016).

196. Hammerschmidt, P. *et al.* CerS6-Derived Sphingolipids Interact with Mff and Promote Mitochondrial Fragmentation in Obesity. *Cell* **177**, 1536-1552.e23 (2019).

197. Turpin, S. M. *et al.* Obesity-Induced CerS6-Dependent C16:0 Ceramide Production Promotes Weight Gain and Glucose Intolerance. *Cell Metab.* **20**, 678–686 (2014).

198. Turpin-Nolan, S. M. & Brüning, J. C. The role of ceramides in metabolic disorders: when size and localization matters. *Nat. Rev. Endocrinol.* **16**, 224–233 (2020).

199. Canals, D. & Hannun, Y. A. Novel Chemotherapeutic Drugs in Sphingolipid Cancer Research. in *Handbook of experimental pharmacology* vol. 215 211–238 (2013).

200. Newgard, C. B. *et al.* A Branched-Chain Amino Acid-Related Metabolic Signature that Differentiates Obese and Lean Humans and Contributes to Insulin Resistance. *Cell Metab.* **9**, 311–326 (2009).

201. Hu, W., Ross, J., Geng, T., Brice, S. E. & Cowart, L. A. Differential Regulation of Dihydroceramide Desaturase by Palmitate versus Monounsaturated Fatty Acids: Implications for Insulin Resistance. *J. Biol. Chem.* **286**, 16596–16605 (2011).

202. Bikman, B. T., Summers, S. A., Bikman, B. T. & Summers, S. A. Ceramides as modulators of cellular and whole- body metabolism. *J. Clin. Invest.* **121**, 4222–4230 (2011).

203. Yang, G. *et al.* Central role of ceramide biosynthesis in body weight regulation, energy metabolism, and the metabolic syndrome. *Am. J. Physiol. Metab.* **297**, E211–E224 (2009).

204. Choi, S. & Snider, A. J. Sphingolipids in High Fat Diet and Obesity-Related Diseases. *Mediators Inflamm.* **2015**, 1–12 (2015).

205. Holland, W. L. *et al.* Lipid-induced insulin resistance mediated by the proinflammatory receptor TLR4 requires saturated fatty acid–induced ceramide biosynthesis in mice. *J. Clin. Invest.* **121**, 1858–1870 (2011).

206. Tsigos, C. *et al.* Circulating tumor necrosis factor alpha concentrations are higher in abdominal versus peripheral obesity. *Metabolism* **48**, 1332–1335 (1999).

207. Colell, A., Morales, A., Fernández-Checa, J. C. & García-Ruiz, C. Ceramide generated by acidic sphingomyelinase contributes to tumor necrosis factor-α-mediated apoptosis in human colon HT-29 cells through glycosphingolipids formation. *FEBS Lett.* **526**, 135–141 (2002).

208. Wiegmann, K., Schütze, S., Machleidt, T., Witte, D. & Krönke, M. Functional Dichotomy of Neutral and Acidic Sphingomyelinases in Tumor Necrosis Factor Signaling. *Cell* **78**, 1005–15 (1994).

209. Dressler, K. A., Mathias, S. & Kolesnick, R. N. Tumor Necrosis Factor-α Activates the Sphingomyelin Signal Transduction Pathway in a Cell-Free System. *Science* **255**, 1715–8 (1992).

210. Singh, I., Pahan, K., Khan, M. & Singh, A. K. Cytokine-mediated Induction of Ceramide Production Is Redox-sensitive. *J. Biol. Chem.* **273**, 20354–20362 (1998).

211. Samad, F., Hester, K. D., Yang, G., Hannun, Y. A. & Bielawski, J. Altered Adipose and Plasma Sphingolipid Metabolism in Obesity: A Potential Mechanism for Cardiovascular and Metabolic Risk. *Diabetes* **55**, 2579–87 (2006).

212. Memon, R. A. *et al.* Endotoxin and Cytokines Increase Hepatic Sphingolipid Biosynthesis and Produce Lipoproteins Enriched in Ceramides and Sphingomyelin. *Arterioscler. Thromb. Vasc. Biol.* **18**, 1257–1265 (1998).

213. Yabu, T. *et al.* Stress-induced ceramide generation and apoptosis via the phosphorylation and activation of nSMase1 by JNK signaling. *Cell Death Differ.* **22**, 258–273 (2015).

214. Hannun, Y. A. & Luberto, C. Ceramide in the eukaryotic stress response. *Trends Cell Biol.* **10**, 73–80 (2000).

215. Holland, W. L. *et al.* The Pleiotropic Actions of Adiponectin are Initiated via Receptor-Mediated Activation of Ceramidase Activity. *Nat. Med.* **17**, 55–63 (2011).

216. Vasiliauskaité-Brooks, I. *et al.* Structural insights into adiponectin receptors suggest ceramidase activity. *Nature* **544**, 120–123 (2017).

217. Iqbal, J., Walsh, M. T., Hammad, S. M. & Hussain, M. M. Sphingolipids and Lipoproteins in Health and Metabolic Disorders. *Trends Endocrinol. Metab.* **28**, 506–518 (2017).

218. Stratford, S., Hoehn, K. L., Liu, F. & Summers, S. A. Regulation of Insulin Action by Ceramide: Dual Mechanisms Linking Ceramide Accumulation to the Inhibition of Akt/protein Kinase B. *J. Biol. Chem.* **279**, 36608–15 (2004).

219. Hage Hassan, R. *et al.* Sustained Action of Ceramide on the Insulin Signaling Pathway in Muscle Cells. *J. Biol. Chem.* **291**, 3019–3029 (2016).

220. Powell, D. J., Turban, S., Gray, A., Hajduch, E. & Hundal, H. S. Intracellular ceramide synthesis and protein kinase Cζ activation play an essential role in palmitate-induced insulin resistance in rat L6 skeletal muscle cells. *Biochem. J.* **382**, 619–29 (2004).

221. Pickersgill, L., Litherland, G. J., Greenberg, A. S., Walker, M. & Yeaman, S. J. Key Role for Ceramides in Mediating Insulin Resistance in Human Muscle Cells. *J. Biol. Chem.* **282**, 12583–12589 (2007).

222. Watson, M. L., Coghlan, M. & Hundal, H. S. Modulating serine palmitoyl transferase (SPT) expression and activity unveils a crucial role in lipid-induced insulin resistance in rat skeletal muscle cells. *Biochem. J.* **417**, 791–801 (2009).

223. Blachnio-Zabielska, A. U., Chacinska, M., Vendelbo, M. H. & Zabielski, P. The Crucial Role of C18-Cer in Fat-Induced Skeletal Muscle Insulin Resistance. *Cell. Physiol. Biochem.* **40**, 1207–1220 (2016).

224. Mahfouz, R. *et al.* Characterising the Inhibitory Actions of Ceramide upon Insulin Signaling in Different Skeletal Muscle Cell Models: A Mechanistic Insight. *PLoS One* **9**, e101865 (2014).

225. Ussher, J. R. *et al.* Inhibition of De Novo Ceramide Synthesis Reverses Diet-Induced Insulin Resistance and Enhances Whole-Body Oxygen Consumption. *Diabetes* **59**, 2453–2464 (2010).

226. Chaurasia, B. *et al.* Adipocyte Ceramides Regulate Subcutaneous Adipose Browning, Inflammation, and Metabolism. *Cell Metab.* **24**, 820–834 (2016).

227. Holland, W. L. *et al.* Inhibition of Ceramide Synthesis Ameliorates Glucocorticoid-, Saturated-Fat-, and Obesity-Induced Insulin Resistance. *Cell Metab.* **5**, 167–179 (2007).

228. Li, Z. *et al.* Reducing Plasma Membrane Sphingomyelin Increases Insulin Sensitivity. *Mol. Cell. Biol.* **31**, 4205–4218 (2011).

229. Chaurasia, B. *et al.* Targeting a ceramide double bond improves insulin resistance and hepatic steatosis. *Science (80-.).* **365**, 386–392 (2019).

230. Ohta, E. *et al.* Analysis of Development of lesions in Mice with Serine Palmitoyltransferase (SPT) Deficiency -Sptlc2 Conditional Knockout Mice-. *Exp. Anim.* **58**, 515–24 (2009).

231. Alexaki, A. *et al.* De Novo Sphingolipid Biosynthesis Is Required for Adipocyte Survival and Metabolic Homeostasis. *J. Biol. Chem.* **292**, 3929–3939 (2017).

232. Pewzner-Jung, Y. *et al.* A Critical Role for Ceramide Synthase 2 in Liver Homeostasis II. Insights Into Molecular Changes Leading to Hepatopathy. *J. Biol. Chem.* **285**, 10911–10923 (2010).

233. Forouhi, N. G. *et al.* Differences in the prospective association between individual plasma phospholipid saturated fatty acids and incident type 2 diabetes: the EPIC-InterAct case-cohort study. *Lancet Diabetes Endocrinol.* **2**, 810–818 (2014).

234. Ma, W. *et al.* Prospective association of fatty acids in the de novo lipogenesis pathway with risk of type 2 diabetes: the Cardiovascular Health Study. *Am. J. Clin. Nutr.* **101**, 153–163 (2015).

235. Lemaitre, R. N. *et al.* Plasma phospholipid very-long-chain saturated fatty acids and incident diabetes in older adults: the Cardiovascular Health Study. *Am. J. Clin. Nutr.* **101**, 1047–1054 (2015).

236. Raichur, S. *et al.* The role of C16:0 ceramide in the development of obesity and type 2 diabetes: CerS6 inhibition as a novel therapeutic approach. *Mol. Metab.* **21**, 36–50 (2019).

237. Raichur, S. *et al.* CerS2 Haploinsufficiency Inhibits β-Oxidation and Confers Susceptibility to Diet-Induced Steatohepatitis and Insulin Resistance. *Cell Metab.* **20**, 687–695 (2014).

238. Kim, Y.-R. *et al.* Hepatic triglyceride accumulation via endoplasmic reticulum stress-induced SREBP-1 activation is regulated by ceramide synthases. *Exp. Mol. Med.* **51**, 1–16 (2019).

239. Li, Y. *et al.* Sphingomyelin Synthase 2 Activity and Liver Steatosis: An Effect of Ceramide Peroxisome Proliferator-Activated Receptor γ2 Suppression. *Arterioscler. Thromb. Vasc. Biol.* **33**, 1513–1520 (2013).

240. Mitsutake, S. *et al.* Dynamic Modification of Sphingomyelin in Lipid Microdomains Controls Development of Obesity, Fatty Liver, and Type 2 Diabetes. *J. Biol. Chem.* **286**, 28544–28555 (2011).

241. Yano, M. *et al.* Mitochondrial Dysfunction and Increased Reactive Oxygen Species Impair Insulin Secretion in Sphingomyelin Synthase 1-null Mice. *J. Biol. Chem.* **286**, 3992–4002 (2011).

242. Tagami, S. *et al.* Ganglioside GM3 Participates in the Pathological Conditions of Insulin Resistance. *J. Biol. Chem.* **277**, 3085–3092 (2002).

243. Yamashita, T. *et al.* Enhanced insulin sensitivity in mice lacking ganglioside GM3. *Proc. Natl. Acad. Sci.* **100**, 3445–3449 (2003).

244. Pralhada Rao, R. *et al.* Sphingolipid Metabolic Pathway: An Overview of Major Roles Played in Human Diseases. *J. Lipids* **2013**, 1–12 (2013).

245. Breslow, D. K. & Weissman, J. S. Membranes in Balance: Mechanisms of Sphingolipid Homeostasis. *Mol. Cell* **40**, 267–279 (2010).

246. McGarry, J. D. & Dobbins, R. L. Fatty acids, lipotoxicity and insulin secretion. *Diabetologia* **42**, 128–138 (1999).

247. Charles, M. A. *et al.* The role of non-esterified fatty acids in the deterioration of glucose tolerance in Caucasian subjects: results of the Paris Prospective Study. *Diabetologia* **40**, 1101–1106 (1997).

248. Mathur, A. *et al.* Nonalcoholic fatty pancreas disease. *HPB* **9**, 312–318 (2007).

249. Gerst, F. *et al.* Metabolic crosstalk between fatty pancreas and fatty liver: effects on local inflammation and insulin secretion. *Diabetologia* **60**, 2240–2251 (2017).

250. Singh, R. G. *et al.* Ectopic fat accumulation in the pancreas and its clinical relevance: A systematic review, meta-analysis, and meta-regression. *Metabolism* **69**, 1–13 (2017).

251. Saisho, Y. *et al.* Pancreas Volumes in Humans from Birth to Age One Hundred Taking Into Account Sex, Obesity, and Presence of Type-2 Diabetes. *Clin. Anat.* **20**, 933–42 (2007).

252. Dai, C. *et al.* Stress-impaired transcription factor expression and insulin secretion in transplanted human islets. *J. Clin. Invest.* **126**, 1857–1870 (2016).

253. Vernier, S. *et al.* β-cell metabolic alterations under chronic nutrient overload in rat and human islets. *Islets* **4**, 379–392 (2012).

254. Nowotny, B. *et al.* Circulating triacylglycerols but not pancreatic fat associate with insulin secretion in healthy humans. *Metabolism* **81**, 113–125 (2018).

255. Zabielski, P., Błachnio-Zabielska, A. U., Wójcik, B., Chabowski, A. & Górski, J. Effect of plasma free fatty acid supply on the rate of ceramide synthesis in different muscle types in the rat. *PLoS One* **12**, e0187136 (2017).

256. Lupi, R. *et al.* Prolonged Exposure to Free Fatty Acids Has Cytostatic and Pro-Apoptotic Effects on Human Pancreatic Islets: Evidence that β-Cell Death Is Caspase Mediated, Partially Dependent on Ceramide Pathway, and Bcl-2 Regulated. *Diabetes* **51**, 1437–1442 (2002).

257. Ly, L. D. *et al.* Oxidative stress and calcium dysregulation by palmitate in type 2 diabetes. *Exp. Mol. Med.* **49**, e291–e291 (2017).

258. Boslem, E., Meikle, P. J. & Biden, T. J. Roles of ceramide and sphingolipids in pancreatic β-cell function and dysfunction. *Islets* **4**, 177–187 (2012).

259. Maedler, K., Oberholzer, J., Bucher, P., Spinas, G. A. & Donath, M. Y. Monounsaturated Fatty Acids Prevent the Deleterious Effects of Palmitate and High Glucose on Human Pancreatic β-Cell Turnover and Function. *Diabetes* **52**, 726–733 (2003).

260. Maedler, K. *et al.* Distinct Effects of Saturated and Monounsaturated Fatty Acids on β-Cell Turnover and Function. *Diabetes* **50**, 69–76 (2001).

261. Kharroubi, I. *et al.* Free Fatty Acids and Cytokines Induce Pancreatic β-Cell Apoptosis by Different Mechanisms: Role of Nuclear Factor-κB and Endoplasmic Reticulum Stress. *Endocrinology* **145**, 5087–5096 (2004).

262. Manukyan, L., Ubhayasekera, S. J. K. A., Bergquist, J., Sargsyan, E. & Bergsten, P. Palmitate-Induced Impairments of β-Cell Function Are Linked With Generation of Specific Ceramide Species via Acylation of Sphingosine. *Endocrinology* **156**, 802–812 (2015).

263. Karaskov, E. *et al.* Chronic Palmitate But Not Oleate Exposure Induces Endoplasmic Reticulum Stress, Which May Contribute to INS-1 Pancreatic β-Cell Apoptosis. *Endocrinology* **147**, 3398–3407 (2006).

264. Sommerweiss, D., Gorski, T., Richter, S., Garten, A. & Kiess, W. Oleate rescues INS-1E β-cells from palmitate-induced apoptosis by preventing activation of the unfolded protein response. *Biochem. Biophys. Res. Commun.* **441**, 770–776 (2013).

265. Véret, J. *et al.* Ceramide synthase 4 and de novo production of ceramides with specific N-acyl chain lengths are involved in glucolipotoxity-induced apoptosis of INS-1 β-cells. *Biochem. J.* **438**, 177–189 (2011).

266. Alonso, A. & Goñi, F. M. The Physical Properties of Ceramides in Membranes. *Annu. Rev. Biophys.* **47**, 633–654 (2018).

267. Colombini, M. Ceramide channels and mitochondrial outer membrane permeability. *J. Bioenerg. Biomembr.* **49**, 57–64 (2017).

268. Shimabukuro, M., Zhou, Y.-T., Levi, M. & Unger, R. H. Fatty acid-induced β cell apoptosis: A link between obesity and diabetes. *Proc. Natl. Acad. Sci.* **95**, 2498–2502 (1998).

269. Shimabukuro, M. *et al.* Lipoapoptosis in Beta-cells of Obese Prediabetic fa/fa Rats. *J. Biol. Chem.* **273**, 32487–32490 (1998).

270. Kelpe, C. L. *et al.* Palmitate Inhibition of Insulin Gene Expression Is Mediated at the Transcriptional Level via Ceramide Synthesis. *J. Biol. Chem.* **278**, 30015–30021 (2003).

271. Hagman, D. K., Hays, L. B., Parazzoli, S. D. & Poitout, V. Palmitate Inhibits Insulin Gene Expression by Altering PDX-1 Nuclear Localization and Reducing MafA Expression in Isolated Rat Islets of Langerhans. *J. Biol. Chem.* **280**, 32413–32418 (2005).

272. Sjöholm, Å. Ceramide inhibits pancreatic β-cell insulin production and mitogenesis and mimics the actions of interleukin-1β. *FEBS Lett.* **367**, 283–286 (1995).

273. Cantrell Stanford, J. *et al.* Sphingosine 1-Phosphate (S1P) Regulates Glucose-stimulated Insulin Secretion in Pancreatic Beta Cells. *J. Biol. Chem.* **287**, 13457–13464 (2012).

274. Laychock, S. G., Sessanna, S. M., Lin, M. H. & Mastrandrea, L. D. Sphingosine 1-phosphate affects cytokine-induced apoptosis in rat pancreatic islet β-cells. *Endocrinology* **147**, 4705–4712 (2006).

275. Maceyka, M. *et al.* SphK1 and SphK2, Sphingosine Kinase Isoenzymes with Opposing Functions in Sphingolipid Metabolism. *J. Biol. Chem.* **280**, 37118–37129 (2005).

276. Qi, Y. *et al.* Loss of sphingosine kinase 1 predisposes to the onset of diabetes via promoting pancreatic β-cell death in diet-induced obese mice. *FASEB J.* **27**, 4294–4304 (2013).

277. Song, Z. *et al.* Sphingosine kinase 2 promotes lipotoxicity in pancreatic β-cells and the progression of diabetes. *FASEB J.* **33**, 3636–3646 (2019).

278. Subathra, M., Qureshi, A. & Luberto, C. Sphingomyelin Synthases Regulate Protein Trafficking and Secretion. *PLoS One* **6**, e23644 (2011).

279. Osterbye, T. *et al.* Sulfatide promotes the folding of proinsulin, preserves insulin crystals, and mediates its monomerization. *Glycobiology* **11**, 473–479 (2001).

280. Buschard, K. *et al.* Sulfatide Preserves Insulin Crystals Not by Being Integrated in the Lattice but by Stabilizing Their Surface. *J. Diabetes Res.* **2016**, 1–4 (2016).

281. Buschard, K. *et al.* Sulfatide Controls Insulin Secretion by Modulation of ATP-sensitive K+-Channel Activity and Ca2+-Dependent Exocytosis in Rat Pancreatic β-Cells. *Diabetes* **51**, 2514–2521 (2002).

282. Kleinert, M. *et al.* Animal models of obesity and diabetes mellitus. *Nat. Rev. Endocrinol.* **14**, 140–162 (2018).

283. King, A. J. F. The use of animal models in diabetes research. *Br. J. Pharmacol.* **166**, 877–894 (2012).

284. Thorens, B. *et al.* Ins1 Cre knock-in mice for beta cell-specific gene recombination. *Diabetologia* **58**, 558–565 (2015).

285. Merglen, A. *et al.* Glucose Sensitivity and Metabolism-Secretion Coupling Studied during Two-Year Continuous Culture in INS-1E Insulinoma Cells. *Endocrinology* **145**, 667–678 (2004).

286. Bauer, D. E., Canver, M. C. & Orkin, S. H. Generation of Genomic Deletions in Mammalian Cell Lines via CRISPR/Cas9. *J. Vis. Exp.* 1–21 (2014) doi:10.3791/52118.

287. Heigwer, F., Kerr, G. & Boutros, M. E-CRISP: fast CRISPR target site identification. *Nat. Methods* **11**, 122–123 (2014).

288. Ran, F. A. *et al.* Genome engineering using the CRISPR-Cas9 system. *Nat. Protoc.* **8**, 2281–2308 (2013).

289. Karsai, G. *et al.* DEGS1-associated aberrant sphingolipid metabolism impairs nervous system function in humans. *J. Clin. Invest.* **129**, 1229–1239 (2019).

290. Narváez-Rivas, M. & Zhang, Q. Comprehensive untargeted lipidomic analysis using core–shell C30 particle column and high field orbitrap mass spectrometer. *J. Chromatogr. A* **1440**, 123–134 (2016).

291. Hartwig, S. *et al.* Exosomal Proteins Constitute an Essential Part of the Human Adipose Tissue Secretome. *Biochim. Biophys. acta. Proteins proteomics* **1867**, 140172 (2019).

292. Spurr, A. R. A low-viscosity epoxy resin embedding medium for electron microscopy. *J. Ultrastruct. Res.* **26**, 31–43 (1969).

293. Karsai, G. *et al.* FADS3 is a Δ14Z sphingoid base desaturase that contributes to gender differences in the human plasma sphingolipidome. *J. Biol. Chem.* **295**, 1889–1897 (2020).

294. Jojima, K., Edagawa, M., Sawai, M., Ohno, Y. & Kihara, A. Biosynthesis of the anti-lipid-microdomain sphingoid base 4,14-sphingadiene by the ceramide desaturase FADS3. *FASEB J.* **34**, 3318–3335 (2020).

295. Tramunt, B. *et al.* Sex differences in metabolic regulation and diabetes susceptibility. *Diabetologia* **63**, 453–461 (2020).

296. Ramos-Molina, B., Martin, M. G. & Lindberg, I. PCSK1 Variants and Human Obesity. in *Physiology & behavior* vol. 176 47–74 (2016).

297. Yoshioka, N., Kuzuya, T., Matsuda, A., Taniguchi, M. & Iwamoto, Y. Serum proinsulin levels at fasting and after oral glucose load in patients with Type 2 (non-insulin-dependent) diabetes mellitus. *Diabetologia* **31**, 355–360 (1988).

298. Furuta, M. *et al.* Incomplete Processing of Proinsulin to Insulin Accompanied by Elevation of Des-31,32 Proinsulin Intermediates in Islets of Mice Lacking Active PC2. *J. Biol. Chem.* **273**, 3431–3437 (1998).

299. Cawley, N. X. *et al.* The Carboxypeptidase E Knockout Mouse Exhibits Endocrinological and Behavioral Deficits. *Endocrinology* **145**, 5807–5819 (2004).

300. Stijnen, P., Ramos-Molina, B., O'Rahilly, S. & Creemers, J. W. M. PCSK1 Mutations and Human Endocrinopathies: From Obesity to Gastrointestinal Disorders. *Endocr. Rev.* **37**, 347–71 (2016).

301. Lee, S., Prodhomme, E. & Lindberg, I. Prohormone convertase 1 (PC1) processing and sorting: effect of PC1 propeptide and proSAAS. *J. Endocrinol.* **182**, 353–364 (2004).

302. Enrich, C. *et al.* Annexin A6—Linking Ca2+ signaling with cholesterol transport. *Biochim. Biophys. Acta - Mol. Cell Res.* **1813**, 935–947 (2011).

303. Grewal, T. *et al.* Annexin A6—A multifunctional scaffold in cell motility. *Cell Adh. Migr.* **11**, 288–304 (2017).

304. Cornely, R., Rentero, C., Enrich, C., Grewal, T. & Gaus, K. Annexin A6 is an Organizer of Membrane Microdomains to Regulate Receptor Localization and Signalling. *IUBMB Life* **63**, 1009–1017 (2011).

305. Rajpal, G., Schuiki, I., Liu, M., Volchuk, A. & Arvan, P. Action of Protein Disulfide Isomerase on Proinsulin Exit from Endoplasmic Reticulum of Pancreatic β-Cells. *J. Biol. Chem.* **287**, 43–47 (2012).

306. Jang, I. *et al.* PDIA1/P4HB is required for efficient proinsulin maturation and ß cell health in response to diet induced obesity. *Elife* **8**, 1–22 (2019).

307. Engelsberg, A. *et al.* The Golgi Protein RCAS1 Controls Cell Surface Expression of Tumor-associated O -Linked Glycan Antigens. *J. Biol. Chem.* **278**, 22998–23007 (2003).

308. Wolf, J. *et al.* Role of EBAG9 protein in coat protein complex I-dependent glycoprotein maturation and secretion processes in tumor cells. *FASEB J.* **24**, 4000–4019 (2010).

309. Machado, J. D. *et al.* Chromogranins A and B as Regulators of Vesicle Cargo and Exocytosis. *Cell. Mol. Neurobiol.* **30**, 1181–1187 (2010).

310. Kim, T., Tao-Cheng, J.-H., Eiden, L. E. & Loh, Y. P. Chromogranin A, an "On/Off" Switch Controlling Dense-Core Secretory Granule Biogenesis. *Cell* **106**, 499–509 (2001).

311. Plaisance, V. *et al.* Endoplasmic Reticulum Stress Links Oxidative Stress to Impaired Pancreatic Beta-Cell Function Caused by Human Oxidized LDL. *PLoS One* **11**, e0163046 (2016).

312. Wang, X., Olberding, K. E., White, C. & Li, C. Bcl-2 proteins regulate ER membrane permeability to luminal proteins during ER stress-induced apoptosis. *Cell Death Differ.* **18**, 38–47 (2011).

313. Kranz, P. *et al.* PDI is an essential redox-sensitive activator of PERK during the unfolded protein response (UPR). *Cell Death Dis.* **8**, e2986–e2986 (2017).

314. Benjannet, S. *et al.* Comparative biosynthesis, covalent post-translational modifications and efficiency of prosegment cleavage of the prohormone convertases PC1 and PC2: Glycosylation, sulphation and identification of the intracellular site of prosegment cleavage of PC1 and P. *Biochem. J.* **294**, 735–743 (1993).

315. Zandberg, W. F., Benjannet, S., Hamelin, J., Pinto, B. M. & Seidah, N. G. N-Glycosylation controls trafficking, zymogen activation and substrate processing of proprotein convertases PC1/3 and subtilisin kexin isozyme-1. *Glycobiology* **21**, 1290–1300 (2011).

316. Mishiro, E., Sakakibara, Y., Liu, M.-C. & Suiko, M. Differential Enzymatic Characteristics and Tissue-Specific Expression of Human TPST-1 and TPST-2. *J. Biochem.* **140**, 731–737 (2006).

317. Corbeil, D. & Huttner, W. B. Tyrosine Sulfation. in *Encyclopedia of Biological Chemistry* vol. 4 463–466 (Elsevier, 2013).

318. Boudreault, A. *et al.* Molecular Characterization, Enzymatic Analysis, and Purification of Murine Proprotein Convertase-1/3 (PC1/PC3) Secreted from Recombinant Baculovirus-Infected Insect Cells. *Protein Expr. Purif.* **14**, 353–366 (1998).

319. Westmuckett, A. D., Hoffhines, A. J., Borghei, A. & Moore, K. L. Early postnatal pulmonary failure and primary hypothyroidism in mice with combined TPST-1 and TPST-2 deficiency. *Gen. Comp. Endocrinol.* **156**, 145–153 (2008).

320. Park, W.-J. *et al.* Hepatic fatty acid uptake is regulated by the sphingolipid acyl chain length. *Biochim. Biophys. Acta - Mol. Cell Biol. Lipids* **1841**, 1754–1766 (2014).

321. Cowart, L. A. Sphingolipids: players in the pathology of metabolic disease. *Trends Endocrinol. Metab.* **20**, 34–42 (2009).

322. King, A. & Bowe, J. Animal models for diabetes: Understanding the pathogenesis and finding new treatments. *Biochem. Pharmacol.* **99**, 1–10 (2016).

323. Dalbøge, L. S. *et al.* Characterisation of Age-Dependent Beta Cell Dynamics in the Male db/db Mice. *PLoS One* **8**, e82813 (2013).

324. Boslem, E. *et al.* Alteration of Endoplasmic Reticulum Lipid Rafts Contributes to Lipotoxicity in Pancreatic β-Cells. *J. Biol. Chem.* **288**, 26569–26582 (2013).

325. Roomp, K. *et al.* Combined lipidomic and proteomic analysis of isolated human islets exposed to palmitate reveals time-dependent changes in insulin secretion and lipid metabolism. *PLoS One* **12**, e0176391 (2017).

326. Guo, J. *et al.* Blockage of ceramide metabolism exacerbates palmitate inhibition of pro-insulin gene expression in pancreatic β-cells. *Mol. Cell. Biochem.* **338**, 283–290 (2010).

327. Zhou, Y. P. & Grill, V. Long Term Exposure to Fatty Acids and Ketones Inhibits B-Cell Functions in Human Pancreatic Islets of Langerhans. *J. Clin. Endocrinol. Metab.* **80**, 1584–90 (1995).

328. Karunakaran, U., Moon, J. S., Lee, H. W. & Won, K. C. CD36 initiated signaling mediates ceramide-induced TXNIP expression in pancreatic beta-cells. *Biochim. Biophys. Acta - Mol. Basis Dis.* **1852**, 2414–2422 (2015).

329. Lupi, R. *et al.* Prolonged Exposure to Free Fatty Acids Has Cytostatic and Pro-Apoptotic Effects on Human Pancreatic Islets: Evidence that β-Cell Death Is Caspase Mediated, Partially Dependent on Ceramide Pathway, and Bcl-2 Regulated. *Diabetes* **51**, 1437–1442 (2002).

330. Boslem, E. *et al.* A lipidomic screen of palmitate-treated MIN6 β-cells links sphingolipid metabolites with endoplasmic reticulum (ER) stress and impaired protein trafficking. *Biochem. J.* **435**, 267–276 (2011).

331. Couttas, T. A. *et al.* A Novel Function of Sphingosine Kinase 2 in the Metabolism of Sphinga-4,14-Diene Lipids. *Metabolites* **10**, 236 (2020).

332. Park, W. J., Kothapalli, K. S. D., Reardon, H. T., Kim, L. Y. & Brenna, J. T. Novel fatty acid desaturase 3 (FADS3) transcripts generated by alternative splicing. *Gene* **446**, 28–34 (2009).

333. Zhang, J. Y. *et al.* Fads3 modulates docosahexaenoic acid in liver and brain. *Prostaglandins, Leukot. Essent. Fat. Acids* **123**, 25–32 (2017).

334. Fyrst, H. *et al.* Natural Sphingadienes Inhibit Akt-Dependent Signaling and Prevent Intestinal Tumorigenesis. *Cancer Res.* **69**, 9457–9464 (2009).

335. Zhao, P. *et al.* Sphingadienes show therapeutic efficacy in neuroblastoma in vitro and in vivo by targeting the AKT signaling pathway. *Invest. New Drugs* **36**, 743–754 (2018).

336. Kurz, J., Parnham, M. J., Geisslinger, G. & Schiffmann, S. Ceramides as Novel Disease Biomarkers. *Trends Mol. Med.* **25**, 20–32 (2019).

337. Covey, S. D. *et al.* The pancreatic β cell is a key site for mediating the effects of leptin on glucose homeostasis. *Cell Metab.* **4**, 291–302 (2006).

338. Kubota, N. *et al.* Insulin receptor substrate 2 plays a crucial role in β cells and the hypothalamus. *J. Clin. Invest.* **114**, 917–927 (2004).

339. Song, J., Xu, Y., Hu, X., Choi, B. & Tong, Q. Brain Expression of Cre Recombinase Driven by Pancreas-Specific Promoters. *Genesis* **48**, 628–34 (2010).

340. Wicksteed, B. *et al.* Conditional Gene Targeting in Mouse Pancreatic -Cells: Analysis of Ectopic Cre Transgene Expression in the Brain. *Diabetes* **59**, 3090–3098 (2010).

341. Lee, J.-Y. *et al.* RIP-Cre Revisited, Evidence for Impairments of Pancreatic β-Cell Function. *J. Biol. Chem.* **281**, 2649–2653 (2006).

342. Pomplun, D., Florian, S., Schulz, T., Pfeiffer, A. & Ristow, M. Alterations of Pancreatic Beta-cell Mass and Islet Number due to Ins2 -controlled Expression of Cre Recombinase: RIP-Cre Revisited; Part 2. *Horm. Metab. Res.* **39**, 336–340 (2007).

343. Carboneau, B. A., Le, T. D. V., Dunn, J. C. & Gannon, M. Unexpected effects of the MIP-Cre ER transgene and tamoxifen on β-cell growth in C57Bl6/J male mice. *Physiol. Rep.* **4**, e12863 (2016).

344. Oropeza, D. *et al.* Phenotypic Characterization of MIP-CreERT 1Lphi Mice With Transgene-Driven Islet Expression of Human Growth Hormone. *Diabetes* **64**, 3798–3807 (2015).

345. Bickert, A. *et al.* Inactivation of ceramide synthase 2 catalytic activity in mice affects transcription of genes involved in lipid metabolism and cell division. *Biochim. Biophys. Acta - Mol. Cell Biol. Lipids* **1863**, 734–749 (2018).

346. Spassieva, S. D., Mullen, T. D., Townsend, D. M. & Obeid, L. M. Disruption of ceramide synthesis by CerS2 down-regulation leads to autophagy and the unfolded protein response. *Biochem. J.* **424**, 273–283 (2009).

347. Wang, P. *et al.* Induction of human pancreatic beta cell replication by inhibitors of dual specificity tyrosine regulated kinase. *Nat Med.* **21**, 383–388 (2015).

348. Schäffer, L. *et al.* A novel high-affinity peptide antagonist to the insulin receptor. *Biochem. Biophys. Res. Commun.* **376**, 380–383 (2008).

349. Shirakawa, J. *et al.* Insulin Signaling Regulates the FoxM1/PLK1/CENP-A Pathway to Promote Adaptive Pancreatic β Cell Proliferation. *Cell Metab.* **25**, 868-882.e5 (2017).

350. Segerstolpe, Å. *et al.* Single-Cell Transcriptome Profiling of Human Pancreatic Islets in Health and Type 2 Diabetes. *Cell Metab.* **24**, 593–607 (2016).

351. Wegner, M.-S., Schiffmann, S., Parnham, M. J., Geisslinger, G. & Grösch, S. The enigma of ceramide synthase regulation in mammalian cells. *Prog. Lipid Res.* **63**, 93–119 (2016).

352. Park, J.-W. *et al.* Ablation of Very Long Acyl Chain Sphingolipids Causes Hepatic Insulin Resistance in Mice Due to Altered Detergent-Resistant Membranes. *Hepatology* **57**, 525–532 (2013).

353. Mullen, T. D. *et al.* Selective knockdown of ceramide synthases reveals complex interregulation of sphingolipid metabolism. *J. Lipid Res.* **52**, 68–77 (2011).

354. Laviad, E. L., Kelly, S., Merrill, A. H. & Futerman, A. H. Modulation of Ceramide Synthase Activity via Dimerization. *J. Biol. Chem.* **287**, 21025–21033 (2012).

355. Schiffmann, S. *et al.* Ceramide metabolism in mouse tissue. *Int. J. Biochem. Cell Biol.* **45**, 1886–1894 (2013).

356. Mesicek, J. *et al.* Ceramide synthases 2, 5, and 6 confer distinct roles in radiation-induced apoptosis in HeLa cells. *Cell. Signal.* **22**, 1300–1307 (2010).

357. Houten, S. M., Violante, S., Ventura, F. V. & Wanders, R. J. A. The Biochemistry and Physiology of Mitochondrial Fatty Acid β-Oxidation and Its Genetic Disorders. *Annu. Rev. Physiol.* **78**, 23–44 (2016).

358. Moin, A. S. M. & Butler, A. E. Alterations in Beta Cell Identity in Type 1 and Type 2 Diabetes. *Curr. Diab. Rep.* **19**, 83 (2019).

359. Guo, S. *et al.* Inactivation of specific β cell transcription factors in type 2 diabetes. *J. Clin. Invest.* **123**, 3305–3316 (2013).

360. Taylor, B. L., Liu, F.-F. & Sander, M. Nkx6.1 is essential for maintaining the functional state of pancreatic beta cells. *Cell Rep.* **4**, 1262–75 (2013).

361. Guillam, M.-T. *et al.* Early diabetes and abnormal postnatal pancreatic islet development in mice lacking Glut-2. *Nat. Genet.* **17**, 327–330 (1997).

362. Guillam, M. T., Dupraz, P. & Thorens, B. Glucose Uptake, Utilization, and Signaling in GLUT2-Null Islets. *Diabetes* **49**, 1485–91 (2000).

363. Thorens, B. A gene knockout approach in mice to identify glucose sensors controlling glucose homeostasis. *Pflügers Arch. - Eur. J. Physiol.* **445**, 482–490 (2003).

364. Asfari, M. *et al.* Establishment of 2-Mercaptoethanol-Dependent Differentiated Insulin-Secreting Cell Lines. *Endocrinology* **130**, 167–178 (1992).

365. Moore, K. L. The Biology and Enzymology of Protein Tyrosine O-Sulfation. *J. Biol. Chem.* **278**, 24243–24246 (2003).

366. Fonseca, S. G., Gromada, J. & Urano, F. Endoplasmic reticulum stress and pancreatic β-cell death. *Trends Endocrinol. Metab.* **22**, 266–274 (2011).

367. Volchuk, A. & Ron, D. The endoplasmic reticulum stress response in the pancreatic β-cell. *Diabetes, Obes. Metab.* **12**, 48–57 (2010).

368. Montgomery, M. K. *et al.* Regulation of glucose homeostasis and insulin action by ceramide acyl-chain length: A beneficial role for very long-chain sphingolipid species. *Biochim. Biophys. Acta - Mol. Cell Biol. Lipids* **1861**, 1828–1839 (2016).

369. Park, W. & Park, J. The role of sphingolipids in endoplasmic reticulum stress. *FEBS Lett.* 1873-3468.13863 (2020) doi:10.1002/1873-3468.13863.

370. Masini, M. *et al.* Ultrastructural morphometric analysis of insulin secretory granules in human type 2 diabetes. *Acta Diabetol.* **49**, 247–252 (2012).

371. Henquin, J.-C., Ibrahim, M. M. & Rahier, J. Insulin, glucagon and somatostatin stores in the pancreas of subjects with type-2 diabetes and their lean and obese non-diabetic controls. *Sci. Rep.* **7**, 11015 (2017).

372. Pasquier, A. *et al.* Lysosomal degradation of newly formed insulin granules contributes to β cell failure in diabetes. *Nat. Commun.* **10**, 3312 (2019).

373. Stephens, S. B. *et al.* The Prohormone VGF Regulates β Cell Function via Insulin Secretory Granule Biogenesis. *Cell Rep.* **20**, 2480–2489 (2017).

374. Kebede, M. A. *et al.* SORCS1 is necessary for normal insulin secretory granule biogenesis in metabolically stressed β cells. *J. Clin. Invest.* **124**, 4240–4256 (2014).

375. Zhu, X. *et al.* Disruption of PC1/3 expression in mice causes dwarfism and multiple neuroendocrine peptide processing defects. *Proc. Natl. Acad. Sci.* **99**, 10293–10298 (2002).

376. Jackson, R. S. *et al.* Obesity and impaired prohormone processing associated with mutations in the human prohormone convertase 1 gene. *Nat. Genet.* **16**, 303–306 (1997).

377. Benzinou, M. *et al.* Common nonsynonymous variants in PCSK1 confer risk of obesity. *Nat. Genet.* **40**, 943–945 (2008).

378. Nead, K. T. *et al.* Contribution of common non-synonymous variants in PCSK1 to body mass index variation and risk of obesity: a systematic review and meta-analysis with evidence from up to 331 175 individuals. *Hum. Mol. Genet.* **24**, 3582–3594 (2015).

379. Heni, M. *et al.* Association of obesity risk SNPs in PCSK1 with insulin sensitivity and proinsulin conversion. *BMC Med. Genet.* **11**, 86 (2010).

380. Philippe, J. *et al.* A nonsense loss-of-function mutation in PCSK1 contributes to dominantly inherited human obesity. *Int. J. Obes.* **39**, 295–302 (2015).

381. Löffler, D. *et al.* Functional and clinical relevance of novel and known PCSK1 variants for childhood obesity and glucose metabolism. *Mol. Metab.* **6**, 295–305 (2017).

382. Seidah, N. G. *et al.* Cloning and Primary Sequence of a Mouse Candidate Prohormone Convertase PC1 Homologous to PC2, Furin, and Kex2: Distinct Chromosomal Localization and Messenger RNA Distribution in Brain and Pituitary Compared to PC2. *Mol. Endocrinol.* **5**, 111–122 (1991).

383. Creemers, J. W. M. *et al.* Heterozygous Mutations Causing Partial Prohormone Convertase 1 Deficiency Contribute to Human Obesity. *Diabetes* **61**, 383–390 (2012).

384. Blanco, E. H., Ramos-Molina, B. & Lindberg, I. Revisiting PC1/3 mutants: Dominant-negative effect of endoplasmic reticulum-retained mutants. *Endocrinology* **156**, 3625–3637 (2015).

385. Stijnen, P. *et al.* Endoplasmic reticulum-associated degradation of the mouse PC1/3-N222D hypomorph and human PCSK1 mutations contributes to obesity. *Int. J. Obes.* **40**, 973–981 (2016).

386. Muhsin, N. I. A., Bentley, L., Bai, Y., Goldsworthy, M. & Cox, R. D. A novel mutation in the mouse Pcsk1 gene showing obesity and diabetes. *Mamm. Genome* **31**, 17–29 (2020).

387. Blazquez, M., Docherty, K. & Shennan, K. Association of prohormone convertase 3 with membrane lipid rafts. *J. Mol. Endocrinol.* **27**, 107–116 (2001).

388. Jutras, I., Seidah, N. G. & Reudelhuber, T. L. A Predicted α-Helix Mediates Targeting of the Proprotein Convertase PC1 to the Regulated Secretory Pathway. *J. Biol. Chem.* **275**, 40337–40343 (2000).

389. Arnaoutova, I. *et al.* The Prohormone Processing Enzyme PC3 Is a Lipid Raft-Associated Transmembrane Protein. *Biochemistry* **42**, 10445–10455 (2003).

390. Lou, H. *et al.* The transmembrane domain of the prohormone convertase PC3: A key motif for targeting to the regulated secretory pathway. *Mol. Cell. Endocrinol.* **267**, 17–25 (2007).

391. Dikeakos, J. D. *et al.* Functional and structural characterization of a dense core secretory granule sorting domain from the PC1/3 protease. *Proc. Natl. Acad. Sci.* **106**, 7408–7413 (2009).

392. Stettler, H., Suri, G. & Spiess, M. Proprotein Convertase PC3 Is Not a Transmembrane Protein. *Biochemistry* **44**, 5339–5345 (2005).

393. Cawley, N. X., Sridhar, M., Hong, H. & Loh, P. Exploring the membrane topology of prohormone convertase 1 in AtT20 Cells: in situ analysis by immunofluorescence microscopy. *F1000Research* **1**, 9 (2012).

394. Rufaut, N. W., Brennan, S. O., Hakes, D. J., Dixon, J. E. & Birch, N. P. Purification and Characterization of the Candidate Prohormone-processing Enzyme SPC3 Produced in a Mouse L Cell Line. *J. Biol. Chem.* **268**, 20291–8 (1993).

395. Zhou, Y. & Lindberg, I. Enzymatic Properties of Carboxyl-terminally Truncated Prohormone Convertase 1 (PC1/SPC3) and Evidence for Autocatalytic Conversion. *J. Biol. Chem.* **269**, 18408–13 (1994).

396. Jean, F. *et al.* Enzymic characterization of murine and human prohormone convertase-1 (mPC1 and hPC1) expressed in mammalian GH4C1 cells. *Biochem. J.* **292**, 891–900 (1993).

397. Hoshino, A. & Lindberg, I. *Peptide Biosynthesis: Prohormone Convertases 1/3 and 2. Colloquium Series on Neuropeptides* vol. 1 (Biota Publishing, 2012).

398. Fricker, L. D. Neuropeptide Biosynthesis-Prohormone convertases 1/3 and 2. in *Neuropeptides and Other Bioactive Peptides: From Discovery to Function* 41–42 (Biota Publishing, 2012).

399. Zhou, Z. *et al.* Estrogen receptor α protects pancreatic β-cells from apoptosis by preserving mitochondrial function and suppressing endoplasmic reticulum stress. *J. Biol. Chem.* **293**, 4735–4751 (2018).

400. Le May, C. *et al.* Estrogens protect pancreatic β-cells from apoptosis and prevent insulin-deficient diabetes mellitus in mice. *Proc. Natl. Acad. Sci. U. S. A.* **103**, 9232–7 (2006).

401. Mauvais-Jarvis, F. Role of Sex Steroids in β Cell Function, Growth, and Survival. *Trends Endocrinol. Metab.* **27**, 844–855 (2016).

402. Summers, S. A. Could Ceramides Become the New Cholesterol? *Cell Metab.* **27**, 276–280 (2018).

403. Wheeler, E. *et al.* Impact of common genetic determinants of Hemoglobin A1c on type 2 diabetes risk and diagnosis in ancestrally diverse populations: A transethnic genome-wide meta-analysis. *PLOS Med.* **14**, e1002383 (2017).

404. Montgomery, M. K. *et al.* Mouse strain-dependent variation in obesity and glucose homeostasis in response to high-fat feeding. *Diabetologia* **56**, 1129–1139 (2013).

405. Zhao, L. *et al.* A Deficiency of Ceramide Biosynthesis Causes Cerebellar Purkinje Cell Neurodegeneration and Lipofuscin Accumulation. *PLoS Genet.* **7**, e1002063 (2011).

406. Haberkant, P. *et al.* Bifunctional Sphingosine for Cell-Based Analysis of Protein-Sphingolipid Interactions. *ACS Chem. Biol.* **11**, 222–230 (2016).

11. Supplement

11.1. Supplementary tables

11.1.1. Differentially expressed sphingolipids

S.Table 1 to Figure 7: Differentially expressed sphingolipids in pancreatic islets from 12 week old db/db mice compared to controls. Shown are differentially expressed sphingolipids of the volcano plot with p value < 0.05 and log2 FC < -0.05 or > 0.05. p-value was calculated from all measured sphingolipids by two-way ANOVA.

Sphingolipid	Concentration [pmol] (Mean ± SD)		p-value	Change [%]
	Control	db/db		
Cer(d18:0/24:0)	0.058 ± 0.023	0.105 ± 0.035	3.35E-02	81.25
Cer(d18:1/14:0)	0.078 ± 0.012	0.203 ± 0.015	3.38E-04	159.19
Cer(d18:1/16:0)	12.769 ± 0.756	29.983 ± 1.403	1.22E-07	134.81
Cer(d18:1/18:0)	2.183 ± 0.147	4.119 ± 0.322	4.88E-06	88.72
Cer(d18:1/20:0)	1.302 ± 0.121	3.092 ± 0.321	1.91E-07	137.53
Cer(d18:1/22:0)	3.938 ± 0.433	8.274 ± 0.593	1.03E-06	110.13
Cer(d18:1/23:0)	0.757 ± 0.053	1.865 ± 0.178	9.95E-09	146.52
Cer(d18:1/24:0)	4.671 ± 0.398	10.973 ± 0.866	1.64E-06	134.90
Cer(d18:1/26:0)	0.136 ± 0.060	0.285 ± 0.041	2.44E-03	109.92
Cer(d18:2/16:0)	0.205 ±0.033	2.219 ± 0.176	7.31E-11	984.46
Cer(d18:2/18:0)	0.057 ± 0.038	0.655 ± 0.061	1.03E-10	1042.03
Cer(d18:2/20:0)	0.095 ± 0.011	0.654 ± 0.069	3.33E-10	591.70
Cer(d18:2/22:0)	0.238 ± 0.018	2.660 ± 0.117	3.06E-11	1019.11
Cer(d18:2/23:0)	0.036 ± 0.006	0.395 ± 0.041	3.06E-11	1003.11
Cer(d18:2/24:0)	0.281 ± 0.014	2.010 ± 0.168	6.59E-10	615.37
Cer(d18:2/24:1)	3.205 ± 0.272	6.132 ± 0.380	2.61E-05	91.36
doxCer(m18:0/24:1)	0.012 ± 0.002	0.004 ± 0.001	2.41E-06	-66.23
HexCer(d18:0/16:0)	0.222 ± 0.044	0.059 ± 0.035	4.28E-05	-73.64
HexCer(d18:0/20:0)	0.018 ± 0.014	0	2.55E-03	-100.00
HexCer(d18:0/22:0)	0.079 ± 0.007	0.033 ± 0.006	1.06E-08	-58.07
HexCer(d18:0/24:1)	0.526 ± 0.034	1.226 ± 0.174	2.02E-06	133.18
HexCer(d18:1/24:1)	14.376 ± 1.051	6.706 ± 0.502	4.35E-06	-53.35
HexCer(d18:2/24:0)	0.024 ± 0.016	0.190 ± 0.035	2.61E-06	695.26
HexCer(d18:2/24:1)	1.953 ± 0.145	1.347 ± 0.206	7.82E-03	-31.04
SM(d18:0/14:0)	0.012 ± 0.003	0.006 ± 0.004	4.38E-02	-46.04
SM(d18:0/23:0)	0.067 ± 0.006	0.118 ± 0.021	8.37E-05	75.63
SM(d18:0/24:0)	0.184 ± 0.011	0.360 ± 0.065	3.30E-05	95.21
SM(d18:1/24:1)	168.498 ± 12.856	81.680 ± 8.594	6.19E-08	-51.53
SM(d18:2/16:0)	3.141 ± 0.493	9.231 ± 1.046	3.55E-07	193.88
SM(d18:2/18:0)	1.619 ± 0.134	2.625 ± 0.240	2.87E-05	62.15
SM(d18:2/20:0)	0.880 ± 0.093	2.079 ± 0.103	1.82E-09	136.21
SM(d18:2/22:0)	1.601 ± 0.087	4.174 ± 0.463	2.07E-08	160.71
SM(d18:2/23:0)	0.331 ± 0.040	0.985 ± 0.175	4.34E-07	197.57
SM(d18:2/24:0)	5.273 ± 0.302	9.403 ± 0.742	4.68E-06	78.34
SM(d18:2/24:1)	39.416 ± 4.197	23.253 ± 3.960	3.75E-05	-41.01

S.Table 2 to Figure 9: Differentially expressed sphingolipids in *CerS2*^{ΔBKO} islets compared to control.
Shown are differentially expressed sphingolipids of the volcano plot with p-value < 0.05 and log2 FC < -0.05 or
> 0.05. p-value was calculated from all measured sphingolipids by Student's unpaired two-tailed t-test.

Sphingolipid	Concentration [pmol/mg] (Mean ± SD)		p-value	Change [%]
	Control	*CerS2*^{ΔBKO}		
Cer(d18:0/24:1)	0.0089 ± 0.0021	0.0025 ± 0.0012	2.12E-03	-71.82
Cer(d18:1/20:0)	0.1093 ± 0.0089	0.0649 ± 0.0158	2.71E-03	-40.61
Cer(d18:1/22:0)	0.3976 ± 0.0347	0.1010 ± 0.0322	1.58E-05	-74.61
Cer(d18:1/23:0)	0.1080 ± 0.0148	0.0375 ± 0.0269	3.69E-03	-65.29
Cer(d18:1/24:0)	0.7287 ± 0.1072	0.2112 ± 0.1232	7.24E-04	-71.02
Cer(d18:1/24:1)	1.1356 ± 0.1456	0.1241 ± 0.0317	9.90E-06	-89.07
Cer(d18:2/24:0)	0.0345 ± 0.0179	0.0083 ± 0.0060	3.19E-02	-75.94
doxCer(m18:0/16:0)	0.0028 ± 0.0010	0.0084 ± 0.0034	2.01E-02	200.75
doxCer(m18:0/20:0)	0.0018 ± 0.0006	0.0033 ± 0.0010	4.69E-02	80.74
doxCer(m18:0/24:1)	0.0028 ± 0.0009	0.0008 ± 0.0002	4.83E-03	-69.74
doxCer(m18:1/24:1)	0.0074 ± 0.0021	0.0007 ± 0.0002	7.09E-04	-90.57
HexCer(d18:1/16:0)	1.7812 ± 0.8933	3.6609 ± 0.7175	1.68E-02	105.53
HexCer(d18:1/22:0)	1.0128 ± 0.3135	0.1889 ± 0.0572	2.07E-03	-81.35
HexCer(d18:1/23:0)	0.1348 ± 0.0381	0.0174 ± 0.0045	8.65E-04	-87.08
HexCer(d18:1/24:0)	1.1538 ± 0.3534	0.1400 ± 0.0344	1.25E-03	-87.87
HexCer(d18:1/24:1)	0.8320 ± 0.2237	0.0453 ± 0.0141	4.17E-04	-94.55
HexCer(d18:1/26:0)	0.0548 ± 0.0147	0.0101 ± 0.0022	9.43E-04	-81.56
SM(d18:0/20:0)	0.0214 ± 0.0020	0.0115 ± 0.0048	8.80E-03	-46.23
SM(d18:0/22:0)	0.0741 ± 0.0230	0.0129 ± 0.0071	2.26E-03	-82.61
SM(d18:0/23:0)	0.0058 ± 0.0017	0.0017 ± 0.0004	3.03E-03	-71.74
SM(d18:0/24:0)	0.0206 ± 0.0039	0.0066 ± 0.0017	6.14E-04	-68.21
SM(d18:0/24:1)	0.0729 ± 0.0100	0.0120 ± 0.0067	5.53E-05	-83.53
SM(d18:1/20:0)	2.9727 ± 0.5122	1.7200 ± 0.3819	7.79E-03	-42.14
SM(d18:1/22:0)	6.7742 ± 1.0401	1.3861 ± 0.3449	6.37E-05	-79.54
SM(d18:1/23:0)	1.4439 ± 0.2818	0.2634 ± 0.0700	1.86E-04	-81.76
SM(d18:1/24:0)	6.4202 ± 1.1081	1.0076 ± 0.2839	7.93E-05	-84.31
SM(d18:1/24:1)	15.9950 ± 2.6470	1.8147 ± 0.4830	4.29E-05	-88.65
SM(d18:1/26:0)	0.0594 ± 0.0084	0.0118 ± 0.0042	5.37E-05	-80.16
SM(d18:2/20:0)	0.1277 ± 0.0428	0.0518 ± 0.0327	3.06E-02	-59.39
SM(d18:2/22:0)	0.3264 ± 0.1566	0.0822 ± 0.0600	2.69E-02	-74.81
SM(d18:2/23:0)	0.0888 ± 0.0336	0.0210 ± 0.0145	1.01E-02	-76.29
SM(d18:2/24:0)	0.4740 ± 0.2400	0.0948 ± 0.0723	2.32E-02	-80.00
SM(d18:2/24:1)	5.0699 ± 2.4607	0.3081 ± 0.2771	8.50E-03	-93.92

S.Table 3 to Figure 18: Differentially expressed sphingolipids in *CerS2*^{ΔINS1E} cells compared to control.
Shown are differentially expressed sphingolipids of the volcano plot with p-value < 0.05 and log2 FC < -0.05 or
> 0.05. p-value was calculated by Student's unpaired two-tailed t-test.

Sphingolipid	Concentration [pmol/mg] (Mean ± SD)		p-value	Change [%]
	Control	*CerS2*^{ΔINS1E}		
Cer(d18:0/18:0)	4.272 ± 1.823	9.474 ± 1.554	1.98E-02	121.77
Cer(d18:0/22:0)	2.343 ± 0.912	0.106 ± 0.026	1.32E-02	-95.49
Cer(d18:0/23:0)	0.252 ± 0.056	0.040 ± 0.019	3.48E-03	-84.30
Cer(d18:0/24:0)	6.147 ± 1.306	0.115 ± 0.033	1.32E-03	-98.12
Cer(d18:0/24:1)	4.935 ± 2.244	0.039 ± 0.006	1.95E-02	-99.21
Cer(d18:0/26:0)	0.353 ± 0.082	0.124 ± 0.050	1.46E-02	-64.88
Cer(d18:1/16:0)	6.456 ± 0.217	14.748 ± 1.613	9.09E-04	128.44
Cer(d18:1/18:0)	12.438 ± 0.439	32.597 ± 2.714	2.21E-04	162.08
Cer(d18:1/22:0)	10.623 ± 0.846	0.187 ± 0.030	2.84E-05	-98.24
Cer(d18:1/23:0)	3.719 ± 0.627	0.081 ± 0.026	5.54E-04	-97.81
Cer(d18:1/24:0)	60.127 ± 3.380	0.342 ± 0.057	6.77E-06	-99.43
Cer(d18:1/24:1)	28.621 ± 1.541	0.293 ± 0.043	5.81E-06	-98.98
Cer(d18:1/26:0)	3.056 ± 0.328	0.093 ± 0.053	1.02E-04	-96.97
Cer(d18:2/18:0)	1.728 ± 0.047	2.793 ± 0.066	2.25E-05	61.58
Cer(d18:2/22:0)	1.928 ± 0.243	0.086 ± 0.011	1.95E-04	-95.54
Cer(d18:2/23:0)	0.520 ± 0.118	0.017 ± 0.005	1.78E-03	-96.74
Cer(d18:2/24:0)	12.759 ± 2.108	0.070 ± 0.012	4.78E-04	-99.45
Cer(d18:2/24:1)	4.590 ± 0.443	0.124 ± 0.009	6.29E-05	-97.29
doxCer(m18:0/20:0)	0.019 ± 0.005	0.038 ± 0.003	4.08E-03	102.72
doxCer(m18:0/22:0)	0.139 ± 0.029	0.044 ± 0.016	8.03E-03	-68.25
doxCer(m18:0/23:0)	0.034 ± 0.007	0.017 ± 0.007	3.89E-02	-49.89
doxCer(m18:0/24:0)	0.532 ± 0.115	0.060 ± 0.022	2.22E-03	-88.81
doxCer(m18:0/24:1)	0.145 ± 0.040	0.026 ± 0.012	7.90E-03	-81.76
doxSB(m18:0)	0.274 ± 0.088	0.969 ± 0.358	3.10E-02	253.07
HexCer(d18:0/16:0)	61.997 ± 24.539	361.596 ± 60.050	1.32E-03	483.24
HexCer(d18:0/18:0)	40.133 ± 16.833	252.459 ± 64.302	5.21E-03	529.05
HexCer(d18:0/22:0)	69.717 ± 39.677	0.190 ± 0.329	3.86E-02	-99.73
HexCer(d18:0/24:0)	203.064 ± 58.559	0.192 ± 0.333	3.88E-03	-99.91
HexCer(d18:0/24:1)	335.945 ± 94.137	0	3.48E-03	-100.00
HexCer(d18:1/16:0)	142.195 ± 12.467	837.202 ± 87.922	1.71E-04	488.77
HexCer(d18:1/18:0)	311.661 ± 10.365	1678.656 ± 181.975	2.03E-04	438.62
HexCer(d18:1/20:0)	17.660 ± 10.720	42.735 ± 6.392	2.54E-02	141.99
HexCer(d18:1/22:0)	457.090 ± 55.514	9.127 ± 2.230	1.52E-04	-98.00
HexCer(d18:1/23:0)	122.946 ± 10.201	3.717 ± 0.868	3.57E-05	-96.98
HexCer(d18:1/24:0)	3305.826 ± 75.257	16.713 ± 3.592	1.83E-07	-99.49
HexCer(d18:1/24:1)	438.638 ± 64.601	1.748 ± 1.706	3.04E-04	-99.60
HexCer(d18:1/26:0)	134.759 ± 9.679	2.357 ± 1.482	1.97E-05	-98.25
HexCer(d18:2/16:0)	166.948 ± 28.549	254.718 ± 34.505	2.74E-02	52.57
HexCer(d18:2/18:0)	27.809 ± 1.873	119.833 ± 1.630	3.53E-07	330.92
HexCer(d18:2/22:0)	31.327 ± 3.668	0	1.22E-04	-100.00
HexCer(d18:2/24:0)	342.087 ± 63.601	1.748 ± 1.706	7.55E-04	-99.49
HexCer(d18:2/24:1)	71.372 ± 10.082	0.155 ± 0.269	2.57E-04	-99.78

Sphingolipid	Concentration [pmol/mg] (Mean ± SD)		p-value	Change [%]
	Control	*CerS2*[ΔINS1E]		
SB(d18:0)	0.626 ± 0.218	2.230 ± 0.812	2.98E-02	256.41
SM(d18:0/14:0)	1.013 ± 0.141	1.695 ± 0.132	3.59E-03	67.39
SM(d18:0/16:0)	51.262 ± 12.077	109.019 ± 15.295	6.82E-03	112.67
SM(d18:0/18:0)	65.978 ± 14.598	137.497 ± 18.071	5.96E-03	108.40
SM(d18:0/22:0)	22.324 ± 6.623	0.260 ± 0.066	4.48E-03	-98.83
SM(d18:0/23:0)	1.619 ± 0.387	0.091 ± 0.007	2.39E-03	-94.39
SM(d18:0/24:0)	38.248 ± 5.098	0.065 ± 0.010	2.04E-04	-99.83
SM(d18:0/24:1)	30.857 ± 6.190	0.348 ± 0.091	1.03E-03	-98.87
SM(d18:0/26:0)	0.773 ± 0.165	0	1.25E-03	-100.00
SM(d18:1/16:0)	145.079 ± 24.394	302.639 ± 67.170	1.88E-02	108.60
SM(d18:1/18:0)	72.808 ± 8.403	188.428 ± 33.526	4.41E-03	158.80
SM(d18:1/22:0)	84.883 ± 15.335	2.910 ± 0.832	7.61E-04	-96.57
SM(d18:1/23:0)	19.454 ± 5.767	0.584 ± 0.178	4.79E-03	-97.00
SM(d18:1/24:0)	305.447 ± 70.034	2.754 ± 0.862	1.70E-03	-99.10
SM(d18:1/24:1)	147.886 ± 23.729	4.438 ± 1.280	4.73E-04	-97.00
SM(d18:1/26:0)	9.102 ± 2.197	0.014 ± 0.010	2.01E-03	-99.85
SM(d18:2/18:0)	5.901 ± 0.429	9.263 ± 0.340	4.42E-04	56.97
SM(d18:2/22:0)	5.906 ± 1.022	0.642 ± 0.115	8.93E-04	-89.12
SM(d18:2/23:0)	1.283 ± 0.345	0.113 ± 0.038	4.31E-03	-91.18
SM(d18:2/24:0)	33.792 ± 11.289	0.854 ± 0.248	7.22E-03	-97.47
SM(d18:2/24:1)	9.879 ± 1.350	0.562 ± 0.087	2.83E-04	-94.31

S.Table 4: Differentially expressed glycerolipids in *CerS2*^{ΔBKO} islets compared to control. Shown are differentially expressed glycerolipids of the volcano plot with p-value < 0.05 and log2 FC < -0.05 or > 0.05. p-value was calculated from all measured sphingolipids by Student's unpaired two-tailed t-test.

| Lipid	Concentration [pmol/mg] (Mean ± SD)		p-value	Change [%]
	Control	*CerS2*^{ΔBKO}		
LPC(18:3)	0.413 ± 0.057	0.251 ± 0.082	1.79E-02	-39.22
LPC(20:0)	0.059 ± 0.012	0.039 ± 0.008	3.79E-02	-33.50
LPC(20:3)	0.499 ± 0.108	0.249 ± 0.069	7.98E-03	-49.98
LPC(22:4)	0.013 ± 0.004	0.007 ± 0.002	4.07E-02	-43.26
PC(31:0)	0.967 ± 0.271	0.591 ± 0.108	4.23E-02	-38.82
PC(32:0)	12.457 ± 3.848	7.630 ± 0.814	4.95E-02	-38.75
PC(33:0)	0.671 ± 0.156	0.350 ± 0.064	8.80E-03	-47.84
PC(34:0)	3.941 ± 0.674	2.112 ± 0.335	2.82E-03	-46.40
PC(36:0)	0.162 ± 0.028	0.087 ± 0.013	3.00E-03	-46.07
PC(37:4)	1.574 ± 0.376	1.012 ± 0.175	3.52E-02	-35.70
PC(38:6)	4.336 ± 0.902	2.735 ± 0.384	1.71E-02	-36.92
PC(39:4)	0.229 ± 0.050	0.124 ± 0.024	9.06E-03	-45.81
PC(39:6)	0.122 ± 0.020	0.079 ± 0.011	8.99E-03	-35.39
PC(40:8)	0.304 ± 0.043	0.210 ± 0.049	2.75E-02	-30.91
PC(41:6)	0.018 ± 0.004	0.010 ± 0.001	6.19E-03	-47.09
PE(34:1)	3.128 ± 0.827	2.038 ± 0.295	4.76E-02	-34.83
PE(36:1)	4.515 ± 0.687	2.230 ± 0.432	1.34E-03	-50.60
PE(38:3)	2.048 ± 0.355	1.264 ± 0.218	9.37E-03	-38.28
PE(40:6)	4.986 ± 1.226	2.639 ± 0.583	1.35E-02	-47.08
PE(40:8)	0.194 ± 0.121	0.041 ± 0.030	2.78E-02	-37.55
PG(36:1)	1.683 ± 0.294	0.933 ± 0.214	6.19E-03	-44.57
TAG(44:2)	0.164 ± 0.061	0.071 ± 0.046	4.95E-02	-57.00

11.1.2. Differentially expressed proteins

S.Table 5 to Figure 19: Differentially expressed proteins in *CerS2*$^{\Delta INS1E}$ cells compared to control. Shown are gene names, protein IDs from UniProt, change in percent and q-value of all significantly regulated proteins in *CerS2*$^{\Delta INS1E}$ cells with log2 FC< -0.5 or > 0.5 and q-value < 0.05.

Gene	UniProt ID	q-value	Change [%]
Irak1	B2RYH5	3.32E-02	-93.99
Mrrf	Q5RKI9	4.67E-03	-63.99
Nipsnap2	Q5RK08	2.64E-05	-47.14
Eps8	F1M3L7	1.42E-02	-42.70
Dpysl3	Q62952; Q62952-2	3.37E-06	-42.60
Pygl	P09811	4.67E-05	-41.25
Gyg1	A0A0G2JXP1; F8WFR6; O08730	3.83E-02	-39.98
Casr	P48442; Q80ZA8	3.06E-04	-39.88
S100a4	P05942	5.63E-03	-37.43
Fam174b	A0A096MJT8; D4A4W1	4.80E-02	-37.27
Ptov1	Q5U2W6	9.52E-03	-36.17
Pcsk1	A0A0G2JX54; P28840	1.35E-06	-35.92
Syngr2	M0R446; O54980	5.41E-03	-34.30
Slc2a2	A0A0G2K1J9; P12336; Q68FZ1	1.28E-10	-32.86
Nipbl	A0A0G2K0J4	2.64E-02	-32.85
Bad	O35147	3.65E-02	-31.97
Lgmn	Q5PPG2; Q9R0J8	2.50E-02	43.24
Krt42	Q6IFU7	3.13E-03	44.45
Krt18	Q5BJY9	3.68E-13	46.12
Dbn1	A0A0H2UHL9; C6L8E0; Q07266; Q07266-2	3.32E-09	46.30
Grn	F1LMP7; G3V8V1; P23785; Q6IN42	3.77E-02	47.35
Vars2	A0A0H2UHY0;Q6MG21	1.08E-02	48.47
Kcmf1	B2RZ97	1.73E-02	48.68
Pon2	Q6AXM8	1.66E-08	51.34
Anxa6	P48037; Q6IMZ3	2.19E-03	51.58
Slc26a2	O70531	1.61E-03	51.63
Pde1c	A0A0G2KAI1	1.73E-12	51.92
Atp9b	Q5XFX3	3.15E-02	52.14
Mis12	F2Z3S0; Q7TQ72	2.17E-02	55.07
Creld2	Q4G063	1.46E-02	55.76
Mff	A0A0G2K2M2; A0A0G2KAL9; A0A0H2UHM6; Q4KM98	3.82E-03	59.70
Dhfr	B0BMV8; Q920D2	1.73E-12	61.89
Marcksl1	A0A0G2K613; Q9EPH2	1.29E-02	62.57
Tpm4	P09495	3.66E-09	62.81
Carhsp1	Q9WU49	8.89E-03	66.34
Gstp1	B6DYQ7; P04906	5.72E-17	76.86
Dennd1a	F1M241	3.15E-02	133.78
Gcg	G3V6P5; P06883	4.83E-10	144.90
Uap1l1	B5DEH4	1.58E-05	828.80

11.2. Supplementary figures

11.2.1. Additional data for mouse studies
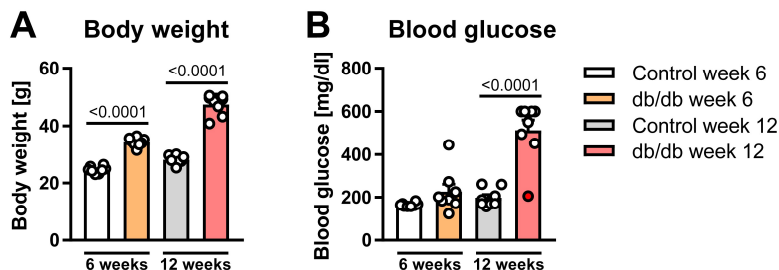
S.Figure 1 to Figure 7: db/db mice are obese and diabetic at an age of 12 weeks. A) Body weight and **B)** non-fasted blood glucose levels of control and db/db mice were measured in week 6 and 12. The red dot highlights the blood glucose level of one db/db mice, which was excluded for the lipidome analysis due to non-elevated blood glucose levels. n= 8 for control, n= 8 for db/db mice. Shown are means ± SEM and significant p-values. Significance was determined by two-way ANOVA (**A** and **B**).
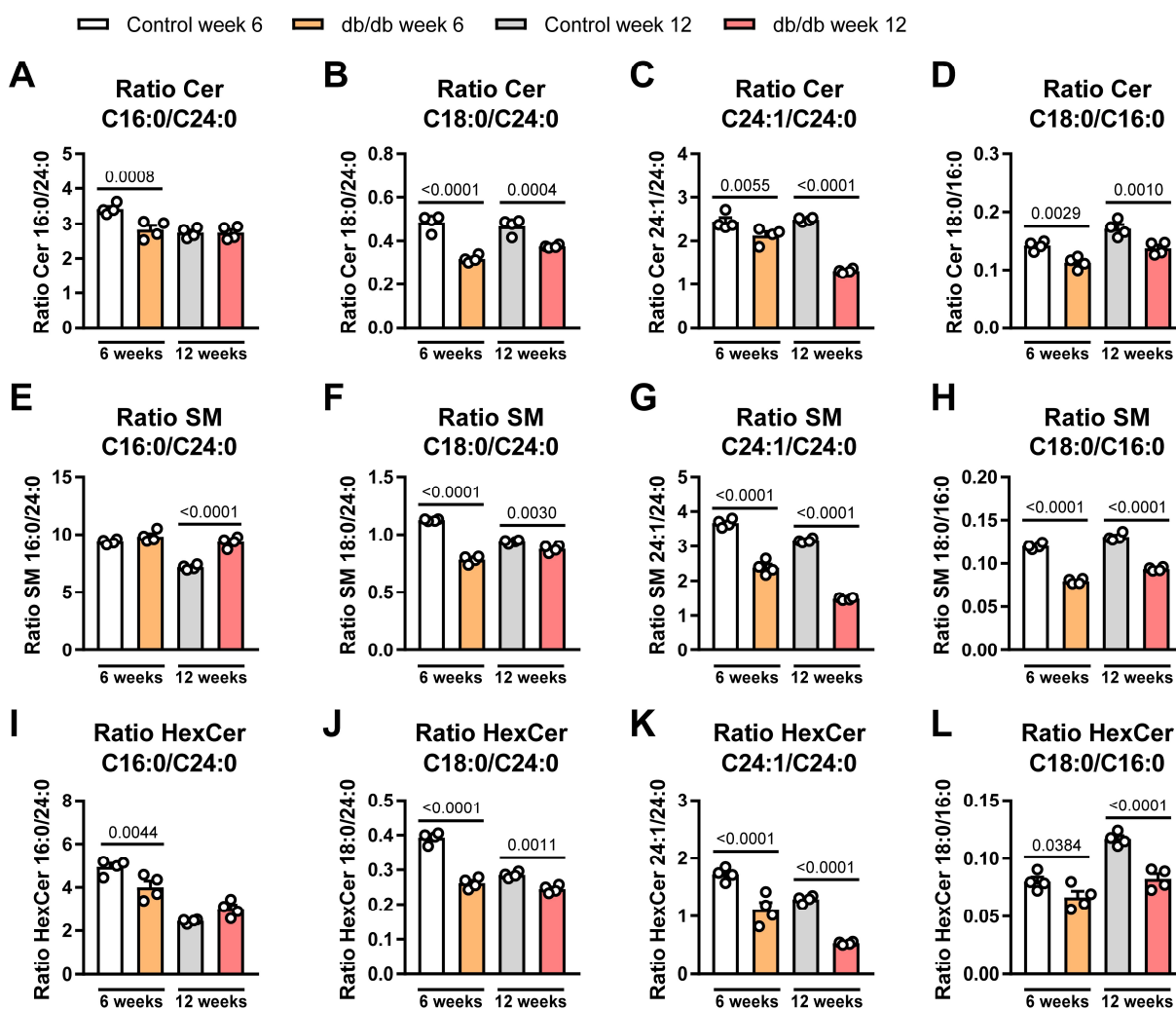
S.Figure 2 to Figure 7: Distinct sphingolipid ratios in islets of control and db/db mice at an age of 6 and 12 weeks. A) Ratio of C16:0/C24:0 ceramide, **E)** sphingomyelin and **I)** hexosylceramide in islets of 6 and 12 week old control and db/db mice. **B)** Ratio of C18:0/C24:0 ceramide, **F)** sphingomyelin and **J)** hexosylceramide in islets of control and db/db mice at an age of 6 and 12 weeks. **C)** Ratio of C24:1/C24:0 ceramide, **G)** sphingomyelin and **K)**

hexosylceramide in islets of control and db/db mice at an age of 6 and 12 weeks. **D)** Ratio of C18:0/C16:0 ceramide, **H)** sphingomyelin and **L)** hexosylceramide in islets of 6 and 12 week old control and db/db mice. n= 4 for control, n= 4 for db/db islets. Shown are means ± SEM and significant p-values. Significance was determined by two-way ANOVA (**A-L**).

A   **Differentially expressed Glycerolipids and Sterols**

B

C   **Sum Lipids**
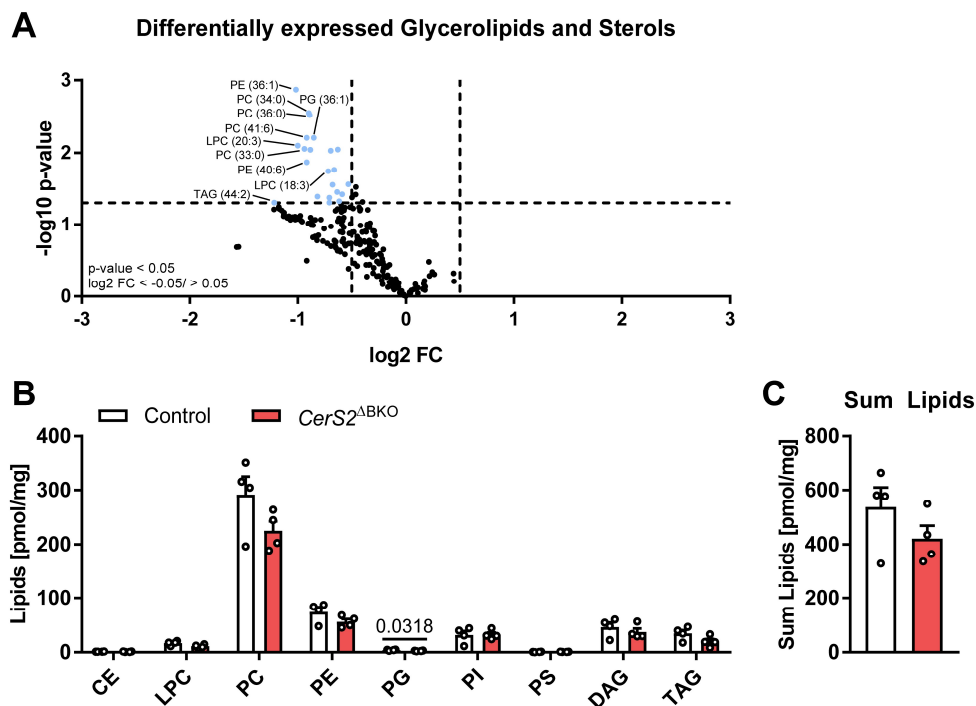
S.Figure 3: Some glycerolipid species are reduced in *CerS2*^ΔBKO^ islets. A) Volcano plot of all measured glycerolipids and sterols in *CerS2*^ΔBKO^ islets compared to control. **B)** Sum of distinct lipid species in control and *CerS2*^ΔBKO^ islets. **C)** Sum of all measured glycerolipids and sterols in control and *CerS2*^ΔBKO^ islets. Shown are means ± SEM and significant p-values. n= 4 for control, n= 4 for *CerS2*^ΔBKO^ islets. Significance was determined by Student's unpaired two-tailed t-test (**A-C**). **CE**= cholesteryl ester, **LPC**= lysophosphatidylcholine, **PC**= phosphatidylcholine, **PE**= phosphatidylethanolamine, **PG**= phosphatidylglycerol, **PI**= phosphatidylinositol, **PS**= phosphatidylserine, **DAG**= diacylglycerol, **TAG**= triacylglycerol.

A   **Plasma proinsulin ND males w20**
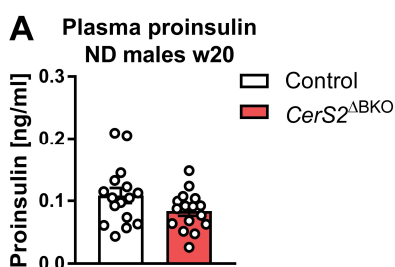
S.Figure 4: Plasma proinsulin levels are unaltered in *CerS2*^ΔBKO^ mice. A) Fasted plasma proinsulin levels of control and *CerS2*^ΔBKO^ mice fed with a ND at the age of 20 weeks. n= 16 for control, n= 16 for *CerS2*^ΔBKO^ mice. Shown is the mean ± SEM. Significance was determined by Student's unpaired two-tailed t-test.

11.2.2. Unedited western blots

Shown are unedited western blot images with overlying protein marker images, which were used as representative immunoblots in this thesis.
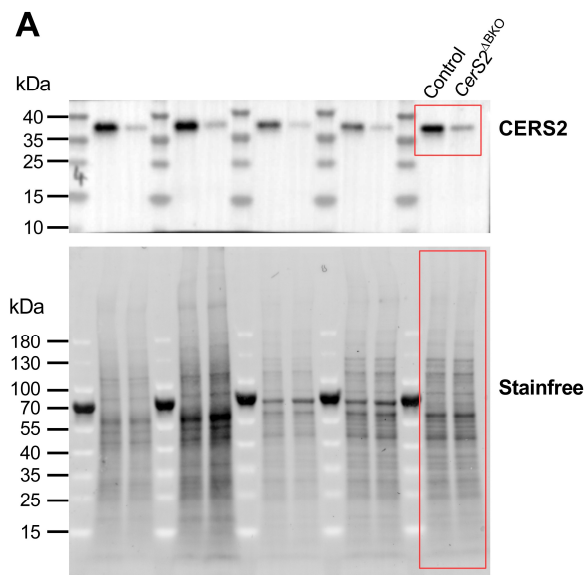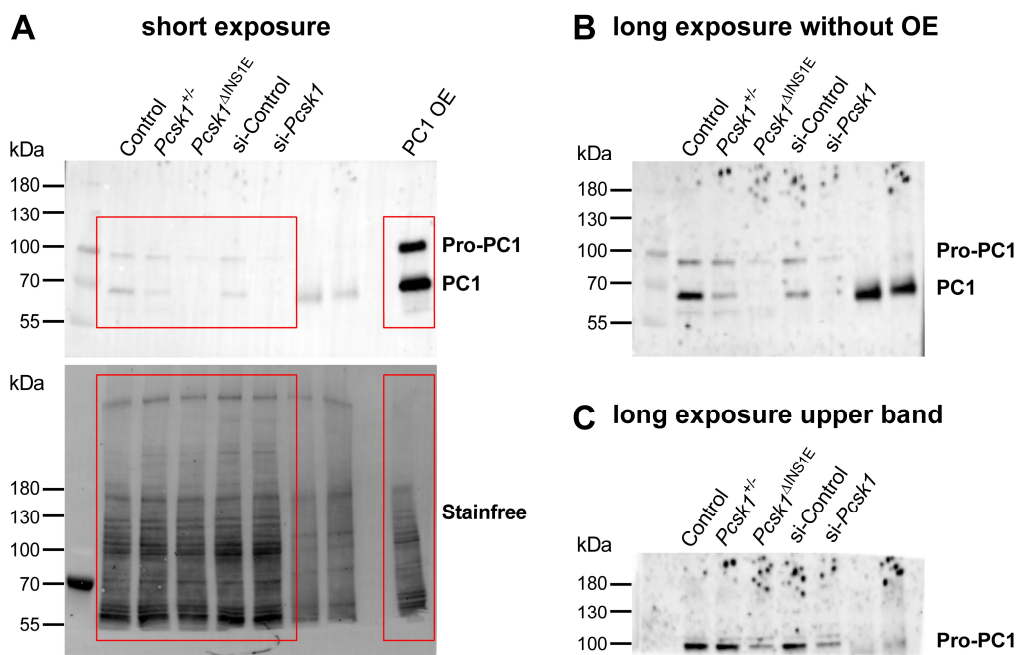

S.Figure 5 to Figure 8: Overlay of CERS2 immunoblot with protein marker image and Stainfree image, which was used for normalization to total protein. The molecular weight is shown in kDa and red boxes display regions of representative immunoblot images used in this thesis.
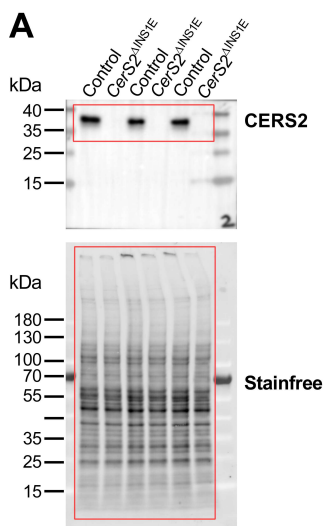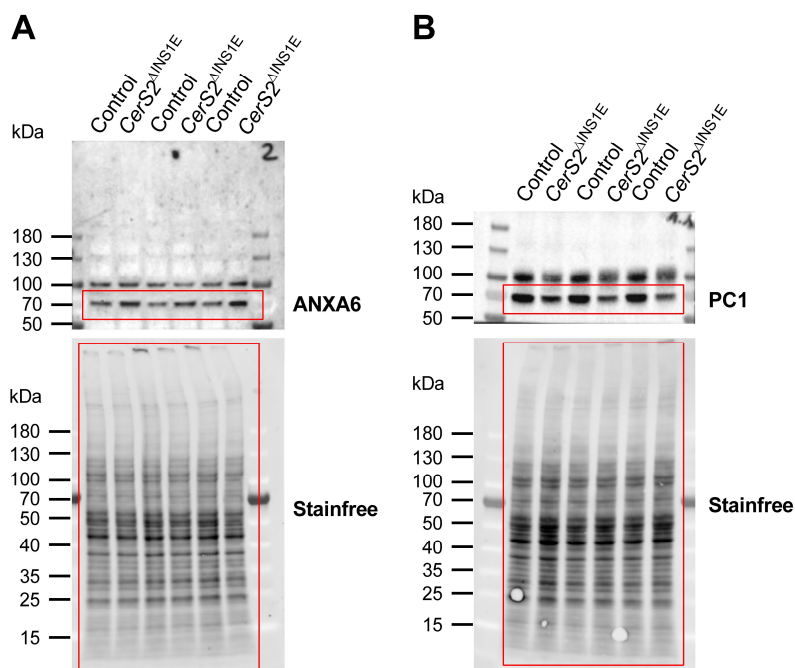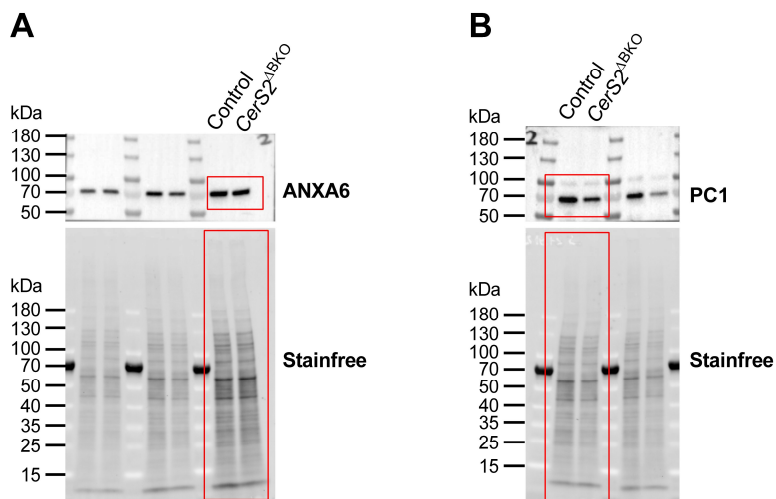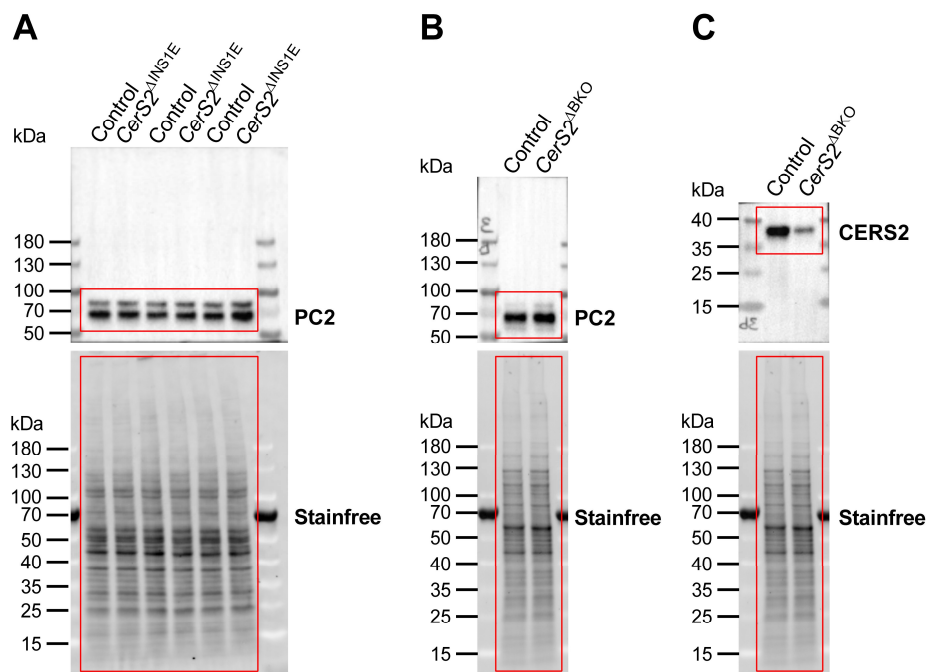

S.Figure 6 to Figure 17: Overlay of CERS2 immunoblot with protein marker image and Stainfree image, which was used for normalization to total protein. The molecular weight is shown in kDa and red boxes display regions of representative immunoblot images used in this thesis.

S.Figure 7 to Figure 19: Overlay of PC1 immunoblot with protein marker image and Stainfree image, which was used for normalization to total protein. The molecular weight is shown in kDa and red boxes display regions of representative immunoblot images used in this thesis. **A)** Immunoblot image with short exposure time. **B)** Immunoblot image with covered PC1 overexpression (OE) and long exposure time. **C)** Immunoblot image with covered PC1 OE as well as lower PC1 band and long exposure time.
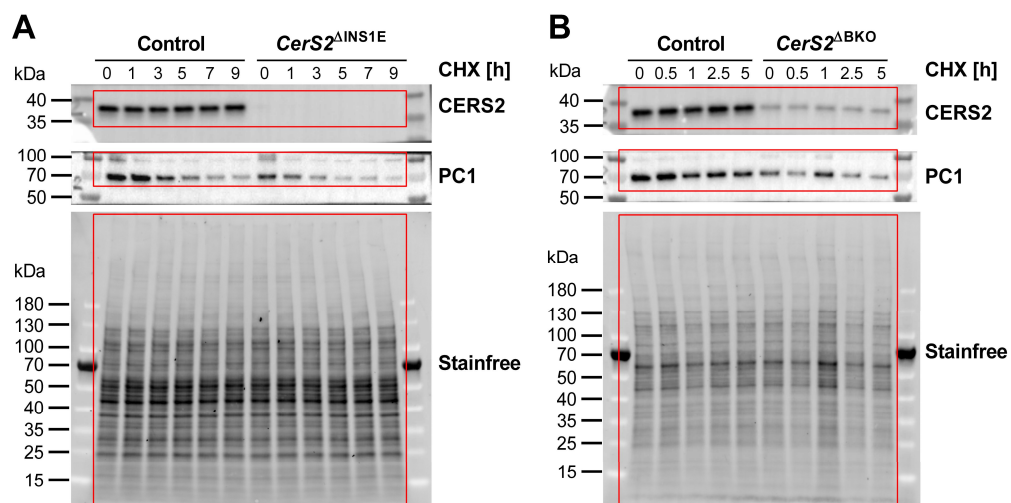

S.Figure 8 to Figure 20: A) Overlay of ANXA6 and **B)** PC1 immunoblot with protein marker image and Stainfree image, which was used for normalization to total protein. The molecular weight is shown in kDa and red boxes display regions of representative immunoblot images used in this thesis.
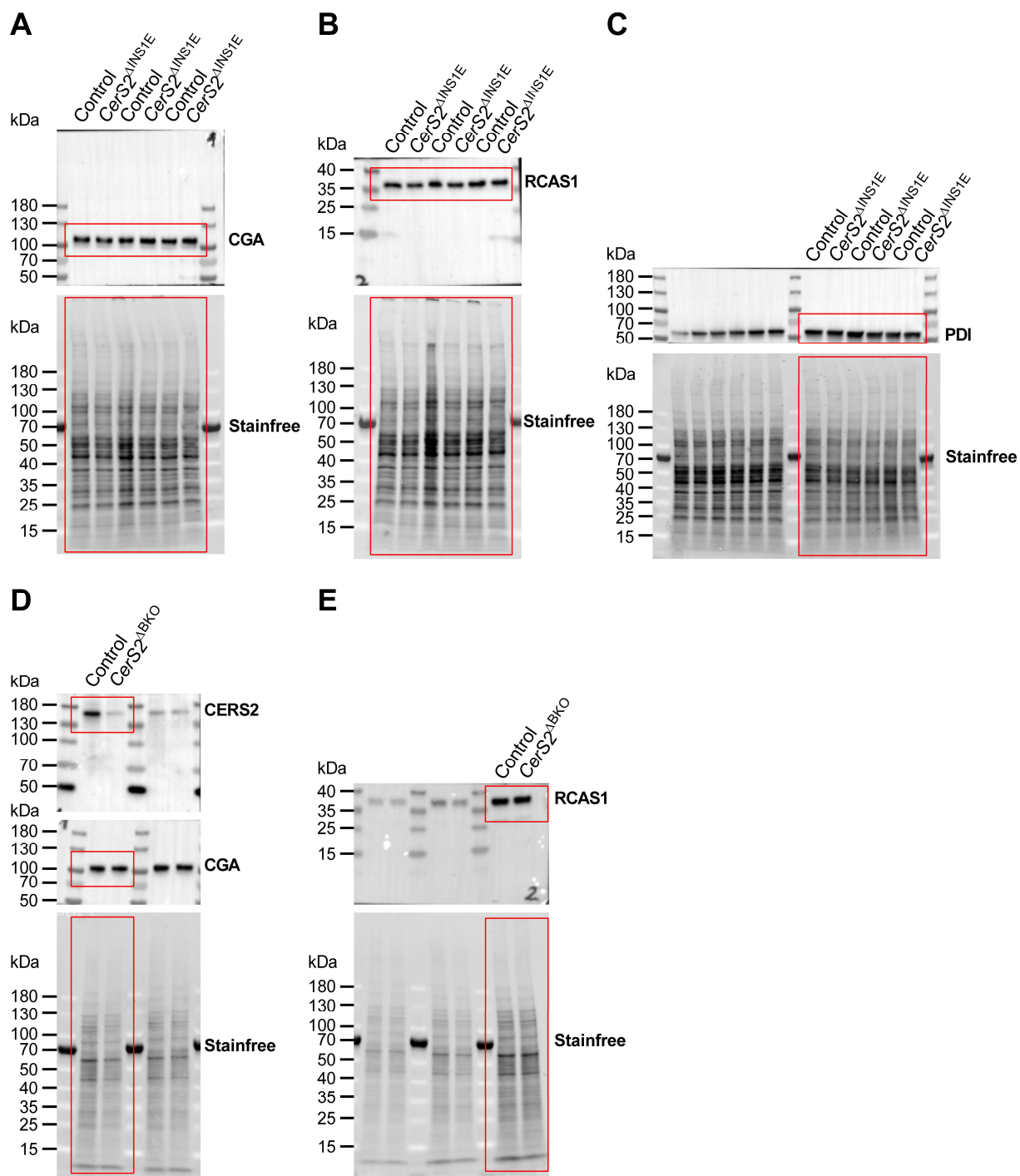
S.Figure 9 to Figure 21: A) Overlay of ANXA6 and **B)** PC1 immunoblot with protein marker image and Stainfree image, which was used for normalization to total protein. The molecular weight is shown in kDa and red boxes display regions of representative immunoblot images used in this thesis.

S.Figure 10 to Figure 22: A and B) Overlay of PC2 and **C)** CERS2 immunoblot with protein marker image and Stainfree image, which was used for normalization to total protein. The molecular weight is shown in kDa and red boxes display regions of representative immunoblot images used in this thesis.
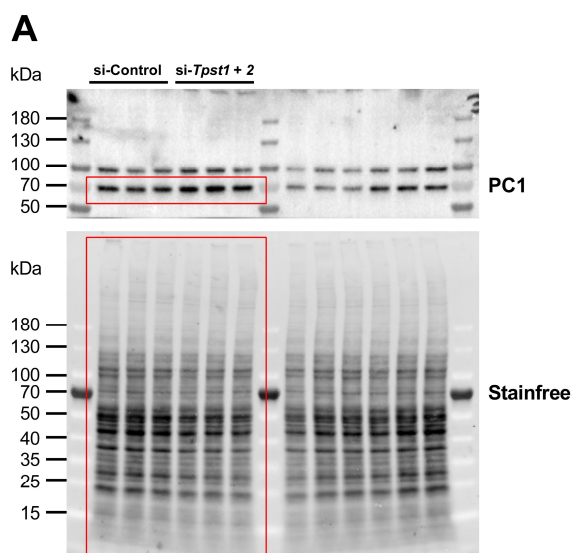
S.Figure 11 to Figure 23: A and B) Overlay of CERS2 and PC1 immunoblot with protein marker image and Stainfree image, which was used for normalization to total protein. The molecular weight is shown in kDa and red boxes display regions of representative immunoblot images used in this thesis.

S.Figure 12 to Figure 24: A and D) Overlay of CGA, **B and E)** RCAS1 and **C)** PDI immunoblot with protein marker image and Stainfree image, which was used for normalization to total protein. The molecular weight is shown in kDa and red boxes display regions of representative immunoblot images used in this thesis.

A

S.Figure 13 to Figure 25: Overlay of PC1 immunoblot with protein marker image and Stainfree image, which was used for normalization to total protein. The molecular weight is shown in kDa and red boxes display regions of representative immunoblot images used in this thesis.

12.   Acknowledgements

First, I would like to thank my supervisor Dr. Bengt-Frederik Belgardt for giving me the opportunity to write my thesis on this great project in his lab, very good scientific advice and ideas to push the project forward, a productive work environment and always taking time for discussions and support.

Furthermore, I thank Prof. Dr. Eckhard Lammert for supervision, great discussions in the labmeetings, good advice and ideas, as well as PD Dr. Volker Burkart for being my second referee.

I would like to thank all present and former lab members of the AG Belgardt for the nice atmosphere, insightful discussions, helpful suggestions and assistance. A special thanks to Michael Rieck, Caroline Schlegel, Angela Pelligra and Jessica Jablonskyj, the "CESYDE team", for your advices, reliability, commitment and active support on this project. I would also like to thank Jennifer Kuboth for your effort and assistance. I cordially thank Celina Uhlemeyer, Nadine Müller and Michael Rieck for your help, motivating words, friendship and funny times, even on long working days. I really enjoyed the time in the lab, the lunch times, coffee breaks and other activities outside the lab with all of you.

I would further like to thank all collaboration partners, especially Dr. Gergely Karsai, Prof. Dr. Thorsten Hornemann, Dr. Sonja Hartwig, Dr. Stefan Lehr, Dr. Jürgen Weiß, Kay Jeruschke, Sandra Cames and Prof. Dr. Oliver Kuß for all their help.

I especially thank my mother Dagmar Grieß for always supporting and believing in me, as well as my siblings Annika, Kathrin and Michael for listening and being around.

A very special thanks to Tobias Schürmann for your great support, encouragement, consolation, understanding and love during the last years. You are the Best.

All of you partially contributed to this doctoral dissertation and without your support, it would not have been possible. I am deeply indepted in you!

13.   Declaration

Eidesstattliche Erklärung

Ich versichere an Eides Statt, dass die Dissertation „Investigating the role of very long chain sphingolipids in pancreatic beta cell demise" von mir selbständig und ohne unzulässige fremde Hilfe unter Beachtung der „Grundsätze zur Sicherung guter wissenschaftlicher Praxis an der Heinrich-Heine-Universität Düsseldorf" erstellt worden ist. Ich habe keine anderen, als die angegebenen Quellen und verwendet. Aussagen, in denen ich Bezug zu der Arbeit Anderer nehme, wurden als solches kenntlich gemacht.
Ich versichere, dass die vorliegende Dissertation weder in dieser noch in einer ähnlichen Form von mir bei einer anderen Institution eingereicht wurde.
Vorherige Versuche zur Promotion wurden von mir nicht unternommen.

Gezeichnet

_____
Kerstin Grieß
Düsseldorf im September 2020

Declaration

I declare on oath that I have prepared the thesis „Investigating the role of very long chain sphingolipids in pancreatic beta cell demise" independently and without forbidden outside help and according to the „Good Scientific Practice of the Heinrich Heine University Düsseldorf". I did not use other sources than those indicated and I marked all positions, where I refer to the work of others.
I did not submit this thesis form or modified to any other institution.
I did not make any previous attempts to do a PhD.

Signed

_____
Kerstin Grieß
Düsseldorf in September 2020